



THE HONG KONG  
POLYTECHNIC UNIVERSITY

香港理工大學

Pao Yue-kong Library

包玉剛圖書館

---

## Copyright Undertaking

This thesis is protected by copyright, with all rights reserved.

**By reading and using the thesis, the reader understands and agrees to the following terms:**

1. The reader will abide by the rules and legal ordinances governing copyright regarding the use of the thesis.
2. The reader will use the thesis for the purpose of research or private study only and not for distribution or further reproduction or any other purpose.
3. The reader agrees to indemnify and hold the University harmless from and against any loss, damage, cost, liability or expenses arising from copyright infringement or unauthorized usage.

### IMPORTANT

If you have reasons to believe that any materials in this thesis are deemed not suitable to be distributed in this form, or a copyright owner having difficulty with the material being included in our database, please contact [lbsys@polyu.edu.hk](mailto:lbsys@polyu.edu.hk) providing details. The Library will look into your claim and consider taking remedial action upon receipt of the written requests.

Pao Yue-kong Library, The Hong Kong Polytechnic University, Hung Hom, Kowloon, Hong Kong

<http://www.lib.polyu.edu.hk>

**SYNTHESIS, CHARACTERIZATION,  
AND APPLICATIONS OF SMART AND  
BIOMIMETIC TEXTILE MATERIALS  
FOR MANIPULATION OF LIQUID**

**YUANFENG WANG**

**Ph.D**

**The Hong Kong Polytechnic University**

**2018**

**THE HONG KONG POLYTECHNIC UNIVERSITY**

**INSTITUTE OF TEXTILES AND CLOTHING**

**Synthesis, Characterization, and  
Applications of Smart and Biomimetic  
Textile Materials for Manipulation of  
Liquid**

**YUANFENG WANG**

**A Thesis Submitted in Partial Fulfillment of the Requirements  
for the Degree of Doctor of Philosophy**

**September 2017**

## **CERTIFICATE OF ORIGINALITY**

I hereby declare that this thesis is my own work and that, to the best of my knowledge and belief, it reproduces no material previously published or written, nor material that has been accepted for the award of any other degree or diploma, except where due acknowledgement has been made in the text.

\_\_\_\_\_ (Signed)

Yuanfeng WANG \_\_\_\_\_ (Name of student)

## **Abstract**

A series of textile based smart materials have been designed and fabricated in this thesis integrating a variety of bio-inspired concepts to manipulate different types of liquids on solid surface. The stimuli responsiveness endows the biomimetic materials or surfaces with better flexibility, adaptability, and controllability to achieve various on-demand applications. According to different manipulation mechanism towards liquid behaviors, this study is divided into four research systems: (i) manipulation of liquid wetting behavior between hydrophilic and hydrophobic states by a temperature-responsive nanofiber system and its application in smart separation of oil/water mixture at different temperature; (ii) manipulation of liquid wetting behavior between superhydrophilic and superhydrophobic states by a light/heat responsive nanofiber membrane and the application in reversible separation of oil/water mixtures; (iii) manipulation of the directional condensation and coalescence of water droplets on a superhydrophobic cotton fabric surface with light-induced superhydrophilic bumps and its application in water collection from fog; (iv) real-time manipulation of the coalescence and sliding of liquid droplets on a flexible slippery surface with tunable morphology along with external tensile stress and its practicability in wind-resistance water collection.

The above division of this thesis is according to the evolving manipulation mechanism towards liquid behaviors from static to dynamic, and also from simple

to complex. Specifically, the liquid wetting behavior is a basic property of a solid surface, and with simple and uniform modification of surface chemical composition or surface energy, a statically hydrophilic or hydrophobic surface can be obtained. By grafting stimuli-responsive polymer brushes with adjustable surface energy, a smart transition between wetting and non-wetting can be achieved. However, the single control of surface energy is not sufficient to fabricate surfaces with extreme wettability, such as superhydrophilicity and superhydrophobicity. A delicate construction of surface microstructure is also necessary to form hierarchical roughness. Therefore, stimuli-responsive change of surface energy accompanied by a highly roughened microstructure is required to design smart material with super-wetting/resistant surface. Further, dynamic manipulation of liquid behaviors such as directional condensation and coalescence requires higher level of material design. Driven force commonly generated from wettability gradient or shape gradient should be included to lead the mobility of liquid droplets. Meanwhile, the integral surface energy and roughness should still be well regulated to ensure the low friction during droplet movement. Thus, the more sophisticated design including both integral surface construction and detailed decoration with multiple ingredients make it possible to realize more complicated manipulation towards liquid behaviors. Finally, compared to those stimuli responding mechanism that needs long time exposure to certain stimuli or has slow response speed, a real-time stimulus response is considered to be of better controllability while giving rise to more sophistication towards material

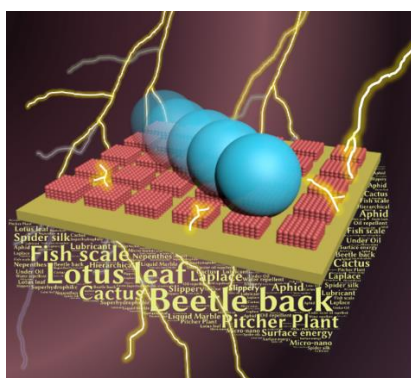
design. To achieve real-time manipulation of liquid behaviors such as coalescence and sliding, a material surface should show immediate change in surface property such as morphology, wettability, or friction along with external applied stimuli and should possess sufficient flexibility for both the substrate and modification agent, as well as the good coordination between each other.

In this thesis, we conducted in depth study for various basic mechanisms of liquid manipulation learning from creatures in nature and summarized a variety of design concepts of biomimetic materials from literature. Following this, we creatively designed different kinds of stimuli-responsive materials and strategies to develop smart and biomimetic composite materials or surfaces aiming to improve their controllability and expand their applications. Besides, the incorporation of diverse textile substrates with appropriate properties makes such kind of materials more readily available and easier to be scaled up. This attempt may facilitate the interdisciplinary studies among traditional textile technology and new branches of science, and possibly promote their industrialization.

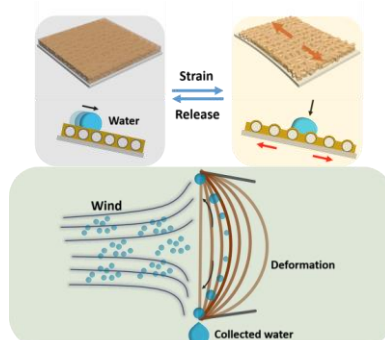
## Publications

### International Journal Papers:

1. **Wang, Y.**; Ma, K.; Xin, J. H\*, Stimuli-Responsive Bioinspired Materials for Controllable Liquid Manipulation: Principles, Fabrication, and Applications. *Advanced Functional Materials*, DOI: 10.1002/adfm.201705128

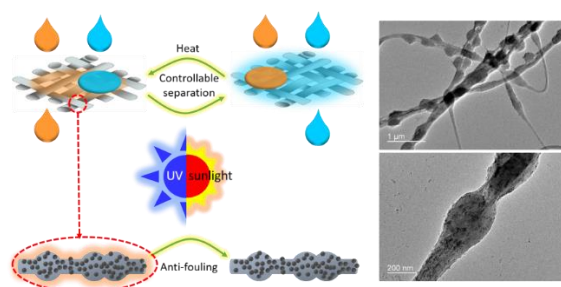


2. **Wang, Y.**; Qian, B.; Lai, C.; Wang, X.; Ma, K.; Guo, Y.; Zhu, X.; Fei, B.; Xin, J. H\*, Flexible Slippery Nanofiber Membrane to Manipulate Droplet Coalescence and Sliding, and Its Practicability in Wind-Resistant Water Collection. *ACS Applied Materials & Interfaces* 2017, 9 (29), 24428–24432.

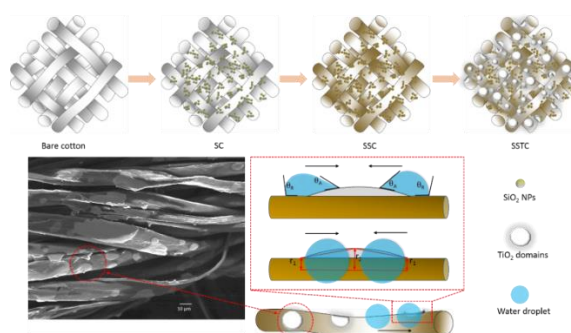


3. **Wang, Y.**; Lai, C.; Wang, X.; Liu, Y.; Hu, H.; Guo, Y.; Ma, K.; Fei, B.; Xin, J. H\*, Beads-on-String Structured Nanofibers for Smart and Reversible Oil/Water Separation with Outstanding Antifouling Property. *ACS Applied*

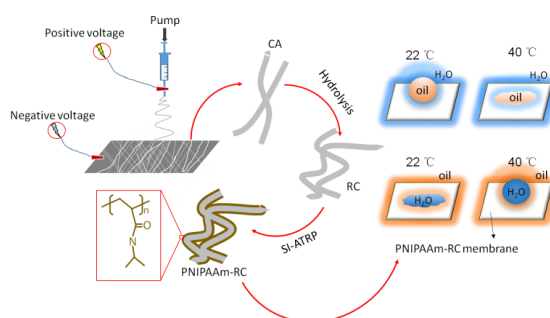
*Materials & Interfaces* 2016, 8 (38), 25612-25620.



4. **Wang, Y.**; Wang, X.; Lai, C.; Hu, H.; Kong, Y.; Fei, B.; Xin, J. H\*.,  
Biomimetic water-collecting fabric with light-induced superhydrophilic  
bumps. *ACS applied materials & interfaces* 2016, 8 (5), 2950-2960.



5. **Wang, Y.**; Lai, C.; Hu, H.; Liu, Y.; Fei, B.; Xin, J. H\*.,  
Temperature-responsive nanofibers for controllable oil/water separation. *RSC  
Advances* 2015, 5 (63), 51078-51085.

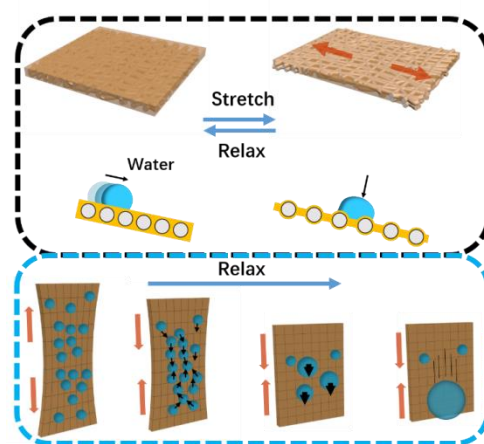


6. Hu, H.; Wang, X.; Miao, D.; **Wang, Y.**; Lai, C.; Guo, Y.; Wang, W.; Xin, J. H.;  
Hu, H., A pH-mediated enhancement of the graphene carbocatalyst activity for  
the reduction of 4-nitrophenol. *Chemical Communications* 2015, 51 (93),  
16699-16702.

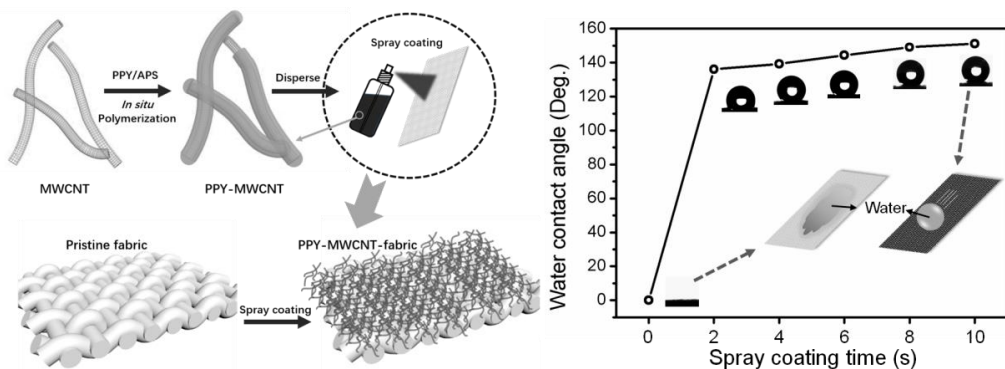
7. Wang, X.; Hu, H.; Wang, W.; Lee, K. I.; Gao, C.; He, L.; **Wang, Y.**; Lai, C.; Fei, B.; Xin, J. H., Antibacterial modification of an injectable, biodegradable, non- cytotoxic block copolymer-based physical gel with body temperature-stimulated sol-gel transition and controlled drug release. *Colloids and Surfaces B: Biointerfaces* 2016, 143, 342-351

### International Conference Papers:

1. **Yuanfeng Wang**, John H. Xin, Elastic slippery membrane to alter liquid mobility. *14th Asian Textile Conference Proceedings*, 2017, 2, 355.



2. **Yuanfeng Wang**, John H. Xin, Biomimetic water-repellent nanospray to prepare immediate superhydrophobic surface. *ISERD-140<sup>th</sup> International Conference on Science and Innovative Engineering*, 2017, 1, 6-9.



## Acknowledgements

Three years of my PhD study is coming to an end. There are many people who helped and supported me during the precious three years in both my life and learning, which should be thanked sincerely. First of all, I would like to convey my sincerest gratitude to my chief supervisor, Prof. John H. Xin, who gave me the opportunity to study under his supervision, has provided me with his invaluable advices, guidance, and insightful discussions about this research project. He always encourages me to explore novel ideas, gives ear to my thought, and corrects my mistakes in time. Also, I would appreciate him for supporting my visiting study in Nanyang Technological University, Singapore, which broadened my horizon.

I would like to thank my co-supervisor Prof. Bin Fei who has provided his continuous support and technical advices for my research. I also would like to thank my host co-supervisor in Nanyang Technological University for accepting me as his visiting student and offering me the liberty to do my research.

I am very grateful to my friend, Dr. Chuilin Lai, who offered me lots of help in experiments such as electrospinning and ATRP, as well as paper writing and submission. His professional advices and guidance have helped me solved critical problems for many times.

My special thanks are sent to Dr. Baitai Qian who usually offers me great enlightenment to generate new ideas. Also, he has provided precious advices and

instructions in polymer synthesis and material fabrication.

My sincere thanks also go to my friends and colleagues Yujuan Guo, Yadie Yang, Xiaowen Wang, Huawen Hu, Yang Liu, Yeeyee Kong, Jianming Chen, Peng Liu, Ben Wang, Kaikai Ma, Xingli Zhu, Pengpeng Yao, Jie Zhang, Chang Liu, Sha Li, Jie Luo, Haifeng Lu, Liang He, Xianxia Han, Chang Liu, Eelin Ng, Ying Xiong, Shengbo Shan, and Ziqiang Feng who gave me warm helps when I first came Hong Kong, supported me a lot in both life and learning, and offered useful discussions about my experiments.

Many thanks are sent to Ms. Mow Nin Sun, Dr. Wei Lu, Dr. Ngai Yui Chan, and Dr. Hardy Liu for the assistance in tests.

Sincerely thank my basketball team members Xufeng Yan, Zhenhua Dong, Jianming Chen, Chen Zheng, Qi Zhang, Zehua Peng, Zhiwei Ren, Wei Du, Pengwei Hu, Chenhao Lin, Ran Bi, Yifu Wang, Xuan Xuan, Cefang Gao, Lei Xu, Fei Xie, Wanjia He, Qin Qi, Lei Yang, Qingkai Wang, Yuze Zhang, and Junbo Chen who have brought great fun into my life in Hong Kong.

Sincerely thank my new friends Yanqin Yang, Chongyang Cai, Wen Li, Xin Zhao, Neng Xiong, Zhuangzhuang Li, Yi Sun and Jianqiang Luo in Nanyang Technological University. They helped me get familiar with the conditions in Singapore and gave lots of support in both life and learning.

Last but not least, I would like to appreciate my wife and my parents who have provided great encouragement for my PhD study, paid lots of efforts in raising my child, and have given me endless love.

# Table of Contents

Abstract .....	i
Publications .....	iv
Acknowledgements .....	vii
Table of Contents .....	ix
List of Abbreviations .....	xiii
Chapter 1 .....	1
Introduction .....	1
1.1 Research Background.....	1
1.2 Research Objectives .....	3
1.3 Overall Methodology .....	5
1.4 Framework of Thesis.....	7
Chapter 2 .....	9
Literature Review.....	9
2.1 Smart/stimuli-responsive materials.....	9
2.1.1 Temperature responsive materials.....	10
2.1.2 pH responsive materials .....	14
2.1.3 Electricity and light responsive materials .....	16
2.2 Liquid behavior on solid surface and examples in nature.....	17
2.2.1 Wettability .....	17
2.2.2 Directional transportation and condensation.....	27
2.2.3 Rolling and sliding .....	31
2.3 Biomimetic materials or surfaces for the manipulation of liquid behaviors .....	34
2.3.1 Biomimetic surfaces to manipulate liquid wetting.....	35
2.3.2 Biomimetic surfaces to manipulate directional transportation and condensation.....	38
2.3.3 Biomimetic surfaces with better manipulation of liquid sliding....	43

2.4 Textile based materials and surface modification .....	47
Chapter 3 .....	51
Temperature-Responsive Nanofibers Fabricated by Surface Grafting of Polymer Chains to Manipulate Liquid Wetting: Synthesis, Characterization, and Application.....	51
3.1 Introduction .....	52
3.2 Experimental .....	56
3.2.1 Materials.....	56
3.2.2 Characterization .....	56
3.2.3 Fabrication of electrospun RC nanofibers .....	57
3.2.4 Immobilization of the ATRP-initiator on the RC nanofibers .....	58
3.2.5 Surface-grafted with PNIPAAm.....	58
3.2.6 Investigation of water collection/release and separation of oil/water mixtures.....	59
3.2.7 Measurement of liquid absorption capacity and reusability .....	60
3.3 Results and discussion .....	61
3.3.1 Characterization and Morphology.....	61
3.3.2 Thermo-Responsive Behavior.....	64
3.3.3 Thermo-responsive Controllable oil/water Separation .....	69
3.4 Conclusions .....	73
Chapter 4 .....	75
Light-Responsive Nanoparticle/Polymer Composite Nanofiber Membrane to Manipulate Liquid Wetting with Antifouling Property: Synthesis, Characterization and Application .....	75
4.1 Introduction .....	76
4.2 Experimental .....	78
4.2.1 Materials.....	78
4.2.2 Synthesis of TiO <sub>2</sub> gel.....	79
4.2.3 Preparation of electrospun T-P nanofiber membrane.....	79
4.2.4 Characterization. ....	80

4.2.5 Smart oil/water separation. ....	81
4.2.6 Exact procedure for contact angle measurements.....	82
4.2.7 Investigation of self-cleaning property.....	82
4.2.8 Durability study.....	83
4.3 Results and discussion .....	83
4.4 Conclusions .....	103
Chapter 5 .....	105
Biomimetic Surface with Light-Induced Superhydrophilic Bumps to Manipulate the Directional Condensation of Water: Synthesis, Characterization and Application.....	105
5.1 Introduction .....	106
5.2 Experimental .....	109
5.2.1 Materials.....	109
5.2.2 Synthesis of SiO <sub>2</sub> and TiO <sub>2</sub> nanosol.....	109
5.2.3 Fabrication of superhydrophobic fabric with light-induced superhydrophilic domains .....	110
5.2.4 Characterization .....	111
5.2.5 Water collection measurement .....	112
5.2.6 Stability and durability study .....	113
5.3 Results and discussion .....	113
5.4 Conclusion .....	136
Chapter 6 .....	138
Flexible Slippery Surface to Manipulate Water Coalescence and Sliding in Real Time: Synthesis, Characterization and Application .....	138
6.1 Introduction .....	138
6.2 Experimental .....	140
6.2.1 Materials.....	140
6.2.2 Fabrication of electrospun TPU nanofiber membrane (NM) .....	141
6.2.3 Fabrication of poly(dodecafluoroheptyl methacrylate- co-isobornyl acrylate-co-lauryl methacrylate) (PDIL).....	141

6.2.4 Fabrication of PFPE-PDIL-TPU flexible slippery membrane (FSM)	142
6.2.5 Characterization	143
6.2.6 Investigation of controllable water sliding and condensation.....	144
6.2.7 Investigation of water collection in strong wind.....	145
6.3 Results and discussion	146
6.4 Conclusion	165
Chapter 7	166
Conclusions and Suggestions for Future Work	166
7.1 Conclusion	166
7.2 Suggestions for Future Work.....	168
References	172

## List of Abbreviations

AFM	Atomic force microscopy
ATRP	Atom transfer radical polymerization
AIBN	2,2'-azobis(isobutyronitrile)
BiB	2-bromoisobutyryl bromide
bare-C	bare cotton fabric
CA	Contact angle
CAH	Contact angle hysteresis
CNTs	Carbon nanotubes
CuBr	Copper(I) bromide
DMAc	Dimethylacetamide
DSC	Differential scanning calorimetry
DI	deionized
DMAP	4-(dimethylamino) pyridine
DMF	Dimethyl formamide
EDX	Energy-dispersive X-ray spectroscopy
FT-IR	Fourier transform infrared
FE-SEM	Field emission scanning electron microscopy
FSM	Flexible slippery membrane
FSS	Flexible slippery surface

HCl	hydrochloric acid
LCST	lower critical solution temperature
MB	methylene blue
MeOH	Methanol
NaOH	Sodium hydroxide
NIPAAm	N-isopropylacrylamide
NF	Nanofiber
NFM	Nanofiber membrane
NPs	Nanoparticles
OTES	n-octadecyltriethoxysilane
OCA	Oil contact angle
PEMDETA	Pentamethyldiethylenetriamine
PNIPAAm	poly(N-isopropylacrylamide)
PVDF	polyvinylidene fluoride
PDI	Polydispersity index
PS	Polystyrene
RC	Regenerated cellulose
RH	Relative humidity
SA	Sliding angle
SI-ATRP	surface-initiated atom transfer radical polymerization
SC	cotton fabrics treated with SiO <sub>2</sub> NPs
SSC	cotton fabrics treated with SiO <sub>2</sub> NPs/OTES

SSTC	cotton fabrics treated with SiO <sub>2</sub> NPs/OTES/TiO <sub>2</sub>
SEM	Scanning electron microscopy
SiO <sub>2</sub>	Silica
THF	Tetrahydrofuran
T-P	TiO <sub>2</sub> doped PVDF
TTIP	titanium tetraisopropoxide
TiO <sub>2</sub>	titanium dioxide/titania
TEA	triethylamine
TGA	thermogravimetric analysis
TC	Titania treated cotton fabric
TEM	transmission electron microscopy
UCST	Upper critical solution temperature
UV	ultraviolet
WCA	Water contact angle
HAc	acetic acid
XRD	X-ray diffraction
XPS	X-ray photoelectron spectroscopy
$\theta$	intrinsic contact angle on the smooth surface
$\theta_{ow}$	under-water OCAs
$\theta_{wo}$	Under-oil WCAs
$\theta_w$	WCA in air
$\theta_o$	OCA in air

$\theta^*$	apparent contact angle on the rough surface
$\gamma_{OA}$	interface tensions of oil/air
$\gamma_{wA}$	interface tensions of water/air
$\gamma_{ow}$	interface tensions of oil/water
$\gamma_{SV}$	Surface tension between solid and vapor
$\gamma_{SL}$	Surface tension between solid and liquid
$\gamma_{LV}$	Surface tension between vapor and liquid
$\gamma_c$	Critical Surface Tension
$r_f$	roughness ratio of the wet surface area
1 D	One dimensional
2 D	Two dimensional
3 D	three dimensional

# Chapter 1

## Introduction

### 1.1 Research Background

Liquid behavior on a solid surface has always been an interesting and in some cases important subject being investigated by material and chemical scientists. Technologies in manipulating liquid behaviors on solid surfaces are widely exploited and utilized in a great many of areas among research, industry, agriculture, daily life, and even environmental protection. For example, liquid wetting/non-wetting behavior is a fundamental factor to be considered in developing waterproof clothing, biomedical dressings, filtration membranes, oil/water absorbents, anti-water electronics, and so on. Liquid condensation is critical to applications such as water capturing systems, distillation towers, desalination, air conditioning, and thermal power generation. Liquid rolling, sliding and other mobile behaviors determine the efficiency of fuel transportation, microfluidics, water collection/drainage, self-cleaning, irrigation, and so on. Therefore, liquid behavior on a material surface sometimes determines the function and major application of this material.

Recently, along with the progress of science and technology, people are no longer content with single-functioned materials with fixed property and limited applications. In other words, for daily life, people tend to use or wear “smarter”

accessories or clothes that can provide flexible, adaptive, and controllable feedbacks and experiences. Also for research and industrial development, scientists tend to prepare versatile materials that can solely solve different kinds of problems or can be solely utilized in various applications after been given different orders or stimuli. As a result, a new branch of technology revolution named “smart” or “intelligent” technology appeared recently. Smart materials are generally defined as materials that can sense and react to surrounding conditions such as temperature and humidity, or applied stimuli such as chemical treatment, electricity, light irradiation, and stress. For liquid behavior manipulation strategies, smart concept seems to be a novel and potential direction to help develop materials with adaptive wettability, activatable condensation sites, and controllable liquid mobility on their surfaces.

On the other hand, our understanding towards manipulation of liquid behavior also largely benefits from nature creatures. Especially after the invention of microscopy with high magnification and other surface characterization technologies, many secrets hidden in the surface of animals or plants were uncovered finally. Complicated and sophisticated structures including micro- or nano-scaled ingredients and accompanied various chemical components and distributions contribute to diverse dominating strategies towards liquid behaviors, which enlightened us a lot to design similar surfaces. Furthermore, scientists have even developed numerous materials or surfaces by combining together two or more bio-inspired concepts to realize liquid manipulation with higher efficiency

and achieve more complicated manipulation.

However, while designing such biomimetic materials or surfaces, the fabrication of hierarchical structures including both micro- and nano-scaled components highly increased the difficulty and cost. Some of the fabrication processes are so time-consuming and usually require expensive facilities or raw materials. In this regard, textile materials that naturally consist of micro-scaled fibers gradually came into our vision and were considered as possible substrate to construct hierarchical structures on. Besides, the unique interlaced net work of textile not only makes it a stable supporter for applied chemicals or nano-particles but also provides necessary tunnels for some types of manipulation of liquid droplets. Furthermore, other advantages of textile material such as the light weight, flexibility, and low cost make it a promising material for massive transportation, bulk production and design of soft devices. Moreover, enormous new advanced techniques and facilities have enriched the approaches to fabricating diverse textiles and even offered customized production. From this, smart and biomimetic materials or surfaces can become more readily available and easier to be scaled up by integrating textile materials as linkers or substrates.

## **1.2 Research Objectives**

Based on the increasing research demand of the smart materials, valuable inspirations from nature creatures towards liquid manipulation and the relatively high-cost fabrication methodology of such smart and biomimetic materials, this

study aimed to meet the expectation of this emerging research area and provide effective response to its present problems. The effort of this study is directed to stepwise achieving the goals of designing and developing smart and biomimetic textile materials or surfaces to realize a variety of manipulation strategies towards liquid behaviors. To be specific, the research objectives of this study are described as follows:

- (i) To develop a novel, free standing, and nanofiber based stimuli-responsive material with smart and reversible superficial wettability transition between hydrophilicity and hydrophobicity.
- (ii) To provide a thorough investigation into the recyclable stimulus-responsive change of wetting behaviors of the as-prepared material along with the external stimulus and explore its advantage in certain applications.
- (iii) To design and fabricate nanofiber based materials with adjustable super-wetting or super-non-wetting behaviors on the surface.
- (iv) To offer a mechanism understanding of the requirement to achieve extreme wettability and wettability transition. To investigate the performance of the as-prepared material in selectively separating liquids and its recyclability.
- (v) To design and fabricate textile surface with certain integral wettability accompanied with additional construction of wetting gradient and shape gradient to achieve the manipulation of liquid condensation and coalescence.

- (vi) To investigate the performance of the prepared material in dynamic manipulation towards liquid condensation and coalescence and assess its efficiency in capturing fog droplets and the following drainage.
- (vii) To develop nanofiber based material surface with flexible and immediate change of surface property to achieve a real-time manipulation of liquid behaviors along with external stimulus.
- (viii) To conduct mechanism study on the surface property change and the exhibited performance of the real-time manipulation toward liquid sliding and condensation. Explore a self-adaptive application in liquid management.

### **1.3 Overall Methodology**

In this thesis, the design and fabrication of smart and biomimetic materials were all based on flexible and low-cost textile substrates including electrospun nanofibrous textiles using cellulose acetate, polyvinylidene fluoride, or thermoplastic polyurethane and traditional cotton fabrics.

A variety of surface modification methods were involved such as dip-pad-cure process, spray coating, surface initiated atom transfer radical polymerization (SI-ATRP), inner doping, lubricant infusion and dip-coating.

Various modification agents with different functions were utilized including metallic/nonmetallic oxide nanoparticles, temperature-responsive polymer chains, long chain silane, lubricant, fluorinated copolymers and so on.

After synthesis, comprehensive characterizations have been conducted to investigate the as-prepared materials or surfaces. Specially, the surface morphologies were studied mainly by scanning electron microscopy (SEM) and atomic force microscopy (AFM), wettability were assessed by contact angles (CAs), chemical compositions were detected mainly by Fourier transform infrared (FT-IR), phase transitions along with temperature were recorded by differential scanning calorimetry (DSC) and thermogravimetric analysis (TGA), the elementary composition and distribution were studied by (EDX) and X-ray photoelectron spectroscopy (XPS), X-ray diffraction (XRD) was performed to study the crystallization, transmission electron microscopy (TEM) was conducted to further investigate the inner structures of composite materials.

To further assess the manipulation performance towards liquid behaviors, some fluid samples simulating nature or industrial process were prepared. The artificial fog flows were generated by an ultrasonic humidifier with adjustable flow rate. Compressed air simulating the nature wind was generated by an industrial air blower, and the wind speed was measured by a digital anemometer. Two types of acidic fog flow were made from water solutions with pH values of 3 and 5 containing  $\text{H}_2\text{SO}_4$  and  $\text{HNO}_3$  (1.9:1 w/w) to simulate acid rain. Oil polluted water were prepared by mixing water with a variety of oils with different properties including n-hexane, chloroform, paraffin oil, silicone oil, peanut oil and gasoline and some of the mixtures were dyed for a easy detection.

All the tested data were repeated for three or five times to ensure reliability.

Corresponding check experiments were performed to show the performance improvement and advantages. The stability and durability of most of the materials were studied by recyclable exposure to stimuli or repeated consumption by mechanical friction, liquid washing or pollutant contamination.

## **1.4 Framework of Thesis**

The thesis is divided into seven chapters.

Chapter 1 introduces the background and research gap, research objectives, and methodology of this study.

Chapter 2 reviews and summarizes the typical work devoted to discovery and investigation of liquid management by nature creatures, exploration and development of biomimetic materials, structures and properties of smart materials, techniques of surface modification, and textile based technologies.

Chapter 3 focuses on the fabrication, structure and surface property analyses of a temperature-responsive nanofiber textile with manipulation ability towards liquid wetting behavior between hydrophobicity and hydrophilicity, followed by its assessment of applications in high-efficient oil/water absorption separation.

Chapter 4 presents the design and fabrication of a lotus leaf inspired nanofiber membrane doped with TiO<sub>2</sub> nanoparticles, and its performance in manipulation of liquid wetting behaviors which can reach superhydrophobicity and superhydrophilicity. Its light-heat triggered reversible oil/water separation and

anti-fouling performance was further investigated.

Chapter 5 concentrates on design and fabrication of an integral superhydrophobic cotton fabric with light-induced superhydrophilic bumps mimicking both desert beetle's back and spider silk. The enhanced water condensation and coalescence were studied during a fog collection process, as well as the effective drainage of the captured water benefitting from the integral water rolling property.

Chapter 6 describes the design and development of a flexible slippery membrane mimicking pitcher plants with real-time adjustable morphology along with external tensile stress. Various liquid mobility real-time controls were performed on the as-prepared membrane surface and its innovative application in wind-resistant water collection was studied.

Chapter 7 summarizes the whole work of this thesis and presents some suggestion for the future work.

## Chapter 2

### Literature Review

#### 2.1 Smart/stimuli-responsive materials

Smart or stimuli-responsive materials are defined as materials that can exhibit varied properties along with environmental stimuli and have present growing attraction for the use to support various applications (e.g., responsive moisture management, controlled agents release, and adaptive shape memory). Among all the reported or fabricated smart materials, smart polymers are the most common materials that could respond with an apparent property change to slight changes in their environment.<sup>1</sup> The unique macromolecule chain composed of smaller repeating structural subunits<sup>2</sup> endows polymers the possibility to present varied responsive property changes in chemistry or structure which thus results in macroscopical property changes such as wettability, mechanics, and conductivity. The stimuli they respond to and the responsive property variation are determined by the monomer type, and also can be tailored by adjusting their molecular structures. In addition to smart polymers, some transition metal oxides also show stimuli-responsive properties along with external environmental changes. The specific electron transport and energy level transition along with external stimuli make them significant materials used in semiconductor, catalysis, electromagnetism, and so on. Nowadays, smart materials have been studied and

applied into varied areas due to their controllability, high flexibility, and energy saving.

### **2.1.1 Temperature responsive materials**

To trigger the property change of smart materials, temperature is among the most widely used stimulus on account of the easy controllability and universality.<sup>3-5</sup> The lower critical solution temperature (LCST) is always used to evaluate temperature-responsive polymers. It is a critical temperature below which the components of a mixture are miscible for all compositions.<sup>6-7</sup> The phase behavior of polymer solutions around the LCST is an important property utilized to design temperature-responsive materials for certain applications. For the polymers with LCST, they are usually miscible and exhibit homogeneous phase in the solution below LCST, whereas above LCST partial liquid miscibility and a phase separation occurs. On the contrary, for polymers with High Critical Solution Temperature (HCST), they are usually miscible and exhibit homogeneous phase in the solution above HCST, whereas below HCST partial liquid miscibility and a phase separation occurs. The HCST is also named of Upper Critical Solution Temperature (UCST).<sup>8-11</sup> Some polymer solutions possess an LCST higher than the UCST, as shown in Figure 2.1, which means that there is a temperature interval of homogeneous phase or complete miscibility, with partial miscibility or phase separation occurring at both higher and lower temperatures.<sup>12</sup>

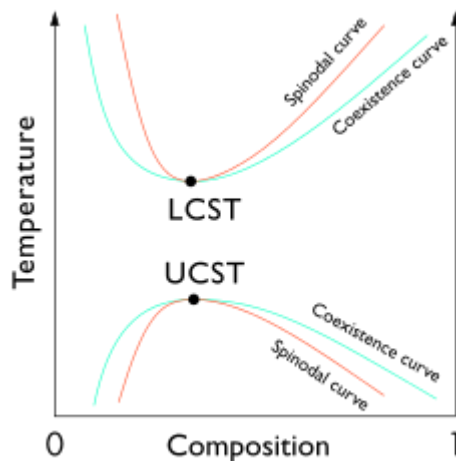


**Figure 2.1.** A plot of typical polymer binary solution phase behavior including both an LCST and a UCST.

Among all the temperature-responsive polymers, poly(N-isopropylacrylamide) (PNIPAAm) is the most famous one and has been extensively studied because of its sharp phase transition around 32 °C (below 32 °C it is soluble in water whereas insoluble above 32 °C).<sup>13</sup> Moreover, the LCST of it (32 °C) is very close to the temperature of human body, which can be well utilized in developing medicine related functional materials. At lower temperature, PNIPAAm is miscible with water due to the hydrogen bonds formed between amide groups and water. In contrast, at the temperature above 32 °C, it becomes hydrophobic and phase separation occurs immediately because the polymer chains coil up and form intramolecular hydrogen bonds between the amide groups (Figure 2.2).<sup>14</sup>

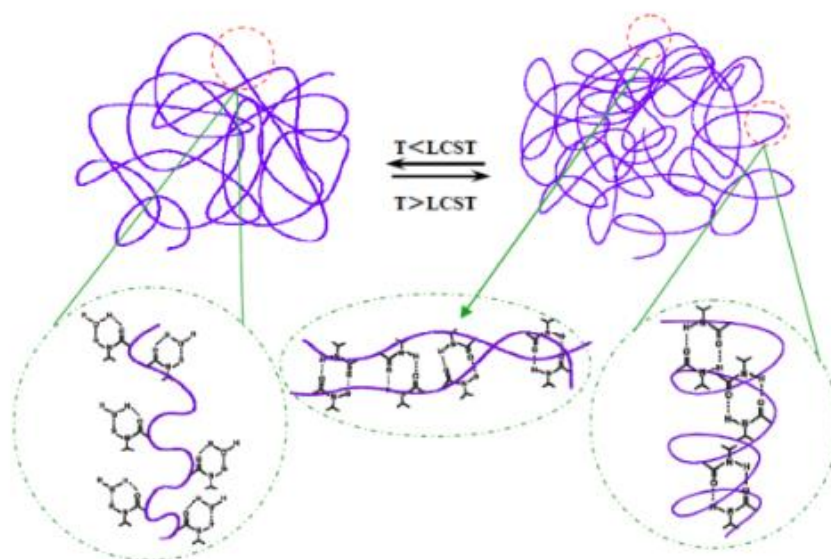


**Figure 2.2.** The transition of PNIPAAm molecule conformation in water at low (left) and high (right) temperatures.<sup>14</sup>

The unique thermal-responsive property of PNIPAAm in the presence of water makes it a potential material which can be used in drug delivery systems. By integrated with micropore-structures,<sup>15-17</sup> the as-developed drug delivery systems containing PNIPAAm progressively solved the conventional problems such as long responsive time and low permeability present in traditional drug delivery systems. Wu et al.<sup>15</sup> first carried out such work by crosslinking PNIPAAm with hydroxypropyl cellulose (HPC) achieving a large pore volume, homogeneous pore size distribution and faster velocity of permeability. Fabricating microgels is another strategy to shorten the responsive time.<sup>18</sup> The pioneering work was made by Pelton et al.<sup>19</sup> who prepared aqueous lattices with PNIPAAm and studied their morphology and temperature-responsive property, after which microgels were studied extensively and have been widely utilized in

other areas such as environment protection and photoelectric switch.<sup>20-21</sup>

In addition to hydrogels, PNIPAAm is also widely explored in the application of solid surface modification. By grafting PNIPAAm on substrates such as polymer, silicon and metal, the original surface property of the substrates can be altered.<sup>22-26</sup> For examples, Jiang et al.<sup>27</sup> grafted PNIPAAm on both a rough and a flat silicon substrate and realized a switch between superhydrophilic to superhydrophobic property which can be intelligently controlled by the change of temperature (Figure 2.3).

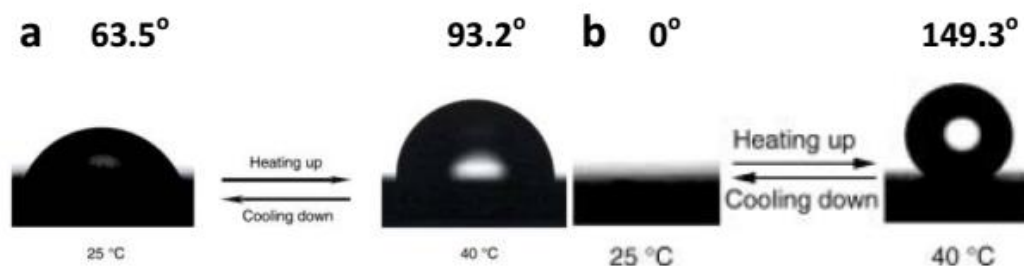


**Figure 2.3.** Thermal responsive wettability for a (a) smooth and (b) PNIPAAm-modified rough surface.<sup>27</sup>

Listed below are some examples of polymers which possess a LCST (Figure 2.4). The function group among these molecules is poly(N-substituted acrylamide).<sup>5, 13, 28-30</sup>

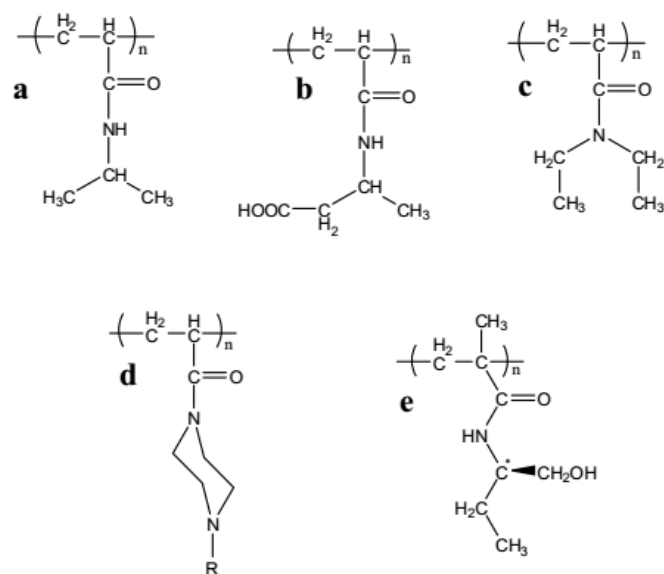


**Figure 2.4.** Temperature responsive polymers. (a) poly(N-isopropylacrylamide) (PNIPAAm); (b) poly(2-carboxyisopropylacrylamide) (PCIPAAm); (c) poly(N,N'-diethylacrylamide) (PDEAAm); (d) poly(N-acryloyl-N'-alkylpiperazine); (e) poly(N-(L)-(1-hydroxymethyl)propylmethacrylamide (P(L-HMPMAAm)).

## 2.1.2 pH responsive materials

Two types of functional groups may be included in a pH-responsive polymer: weak polyacids and weak polybases. The ionizable pendants existed in these groups can accept and donate protons induced by the pH change in the environment.<sup>31</sup> Along with the change of the degree of ionic concentration, the polymer network structure will be rearranged and thus the hydrogel swells due to the breakage of the the hydrogen bond inside polymer gels. The pH-responsive polymers have been widely used in drug release,<sup>32-33</sup> gene delivery,<sup>34-37</sup> and oil/water separation.<sup>38-40</sup> For examples, Li et al.<sup>38</sup> designed a smart fiber

membrane for pH-induced oil/water separation via synthesizing poly(methyl methacrylate)-block-poly(4-vinylpyridine) (PMMA-*b*-P4VP) copolymer solution and electrospinning. The pH-responsive polymer P4VP and the under-water oleophilic/hydrophilic PMMA endow the as-prepared fiber membrane with switchable wettability toward water or oil (Figure 2.5).

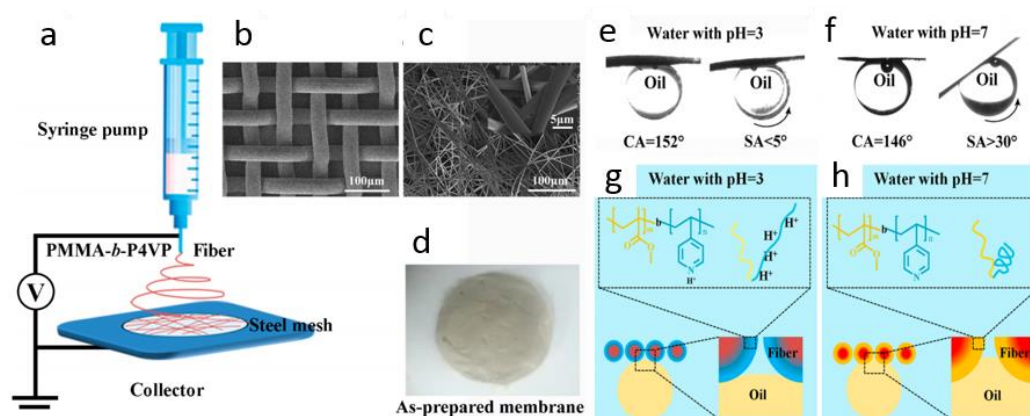


**Figure 2.5.** (a) Schematic showing the electrospun membrane fabrication process, (b) SEM image of the original stainless steel mesh, (c) SEM image of a fiber-coated stainless steel mesh with high and low magnification, and (d) photograph of the as-prepared PMMA-*b*-P4VP fiber membrane, Oil wettability of the as-prepared fiber membrane in aqueous media with different pH values: (e) images of an oil (n-hexane) droplet on the fiber membrane in acidic water (pH 3) with an OCA of  $\sim 152^\circ$  (left) and a sliding angle of  $\sim 4^\circ$  (right); (f) images of an oil (n-hexane) droplet on the as-prepared membrane in neutral water (pH 7) with an OCA of  $\sim 146^\circ$  in a horizontal state (left) and a tilted state (right); (g and h) schematic description of the oil wetting behavior on the fiber membrane surface in pH 3 and 7 water, respectively.<sup>38</sup>

### 2.1.3 Electricity and light responsive materials

The electro-responsive materials have attracted less attentions than pH- and thermal-responsive materials. The electro-sensitive polymers usually consist of polyelectrolyte. The deformation of this type of polymers may occur due to the directional movement of the free ions in solution under DC voltage.<sup>41-42</sup> Langer et al.<sup>43</sup> used hexadecanoic acid (MHA) to modify the gold surface, when the substrate is applied with negative electrical potential, the surface shows hydrophilic property, because the negative charged carboxylate groups will locate on the surface layer due to the electric repulsive force between the gold substrate and the negatively charged end group. However, the surface exhibited hydrophobic property when positive potential was applied onto the gold substrate due to the attractive force between negative end groups and the substrate (Figure 2.6).

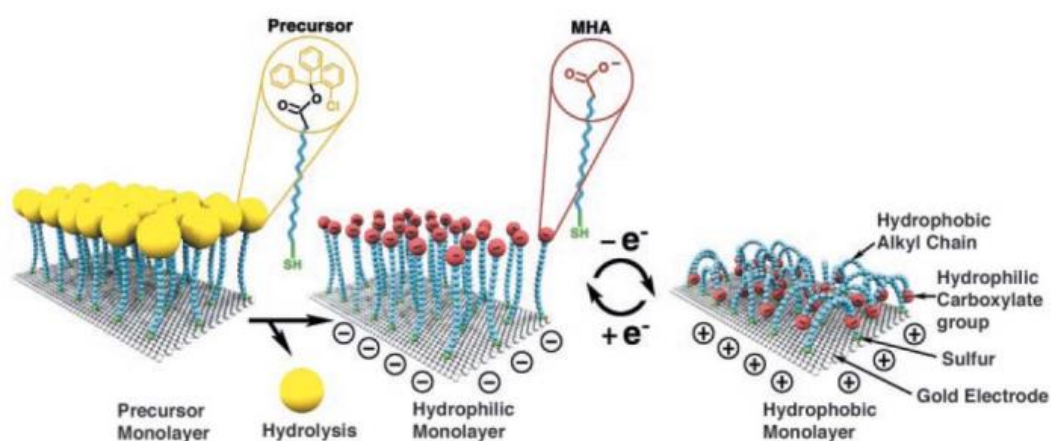


**Figure 2.6.** Schematic diagram of the switch from straight (hydrophilic) to bent (hydrophobic) molecular conformations.<sup>43</sup>

The light-responsive materials can be mainly divided into polymers and inorganic metal oxide. For polymers, two types of mechanism are most common: (1) the structure of the polymer changes after absorbing a certain wavelength of light;<sup>44-45</sup> (2) functional groups existed in the polymer can transfer the energy absorbed from light into enthalpy, and thus cause structure changes of the thermal-sensitive polymer chains.<sup>46</sup> For metal oxide, TiO<sub>2</sub> and ZnO are the most popular light-responsive materials. Fujishima et al.<sup>47</sup> first reported the amphiphilic transition of TiO<sub>2</sub> induced by UV light, after which the relevant research and its applications have been extensively explored.<sup>48-55</sup>

## **2.2 Liquid behavior on solid surface and examples in nature**

### **2.2.1 Wettability**

Wettability is a property assessing the ability or the extent to which can a solid surface be wetted by liquids, which is very important for both industry and daily life.<sup>56-63</sup> Liquid contact angle, defined as the angle that a liquid/vapor interface meets a solid surface, is always used to measure the wettability of a solid surface. The Young equation describing the balance of the contact angle and the surface tensions of interfaces is:<sup>64-65</sup>

$$\gamma_{SV} = \gamma_{SL} + \gamma_{LV} \cos\theta \quad (Eq. 2.1)$$

where  $\gamma_{SV}$ ,  $\gamma_{SL}$  and  $\gamma_{LV}$  represent surface tensions between solid and vapor, solid and liquid, and liquid and vapor, respectively. And  $\theta$  is the contact angle of the

liquid droplet.

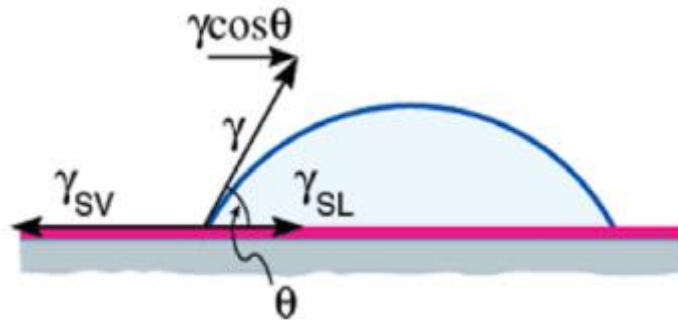


*Figure 2.7.* The forces balance of a liquid drop on a solid surface demonstrated by Eq. 2.1.<sup>64</sup>

According to Eq. 2.1, different wetting states with corresponding contact angles are listed below:

$\theta = 0$  completely wetting

$0 < \theta < 90^\circ$  wetting

$90^\circ < \theta < 180^\circ$  nonwetting

$\theta = 180^\circ$  completely nonwetting

There are two commonly accepted factors which will influence the wettability of a solid surface: surface free energy and surface micro-structure.

The value of surface free energy or surface tension ( $\gamma_{SV}$ ) determines the basic wettability or surface property of a material surface, i.e., hydrophilic or hydrophobic. To be specific, a larger value of  $\gamma_{SV}$  generally means a more hydrophilic surface whereas a smaller value of  $\gamma_{SV}$  usually means a more hydrophobic surface. The surface wettability is highly determined by the chemical

composition of the surface materials. For examples, the replacement of hydrogen atoms by halogen element fluorine will cause the decrease of  $\gamma_{SV}$ . However, the replacement of hydrogen atoms by oxygen or nitrogen will cause the increase of the  $\gamma_{SV}$ . The extent to which the  $\gamma_{SV}$  will decrease/increase is determined by the degree of replacement. The sequence of normal elements which will cause  $\gamma_{SV}$  increase is as follows:



An example of high degree of replacement of halogen element in the molecule is polytetrafluoroethylene (PTFE) which possesses critical surface tension lower than most of liquids (including organic solvent and water) and is thus referred to as amphiphobic material. It can be well applied in oil transmission pipe line because it can decrease the resistance of flow and minimize the deposition of salts crystallization when transporting crude oil.<sup>66</sup>

However, in order to achieve an extreme wetting or nonwetting state, only chemical modification of the surface is far not enough, which can be proved by the water contact angle of  $119^\circ$  on the flat surface composed of  $-CF_3$  groups.<sup>67</sup> According to the Wenzel's model proposed in 1936,<sup>68</sup> the surface roughness is also important in improving the surface wettability (Figure 2.8). To be specific, the relationship between the contact angle and the surface roughness can be qualified by:

$$\cos\theta^* = r\cos\theta \quad (\text{Eq. 2.2})$$

In the equation, is  $\theta^*$  the apparent contact angle on the rough surface,  $\theta$  is the intrinsic contact angle on the smooth surface, and  $r$  is the surface roughness ( $r \in (1, +\infty)$ ). Accordingly, when the  $\theta$  is below  $90^\circ$ , the increase of the roughness will lower the apparent contact angle  $\theta^*$ , whereas when  $\theta$  is above  $90^\circ$ , the increase of the roughness will enlarge the apparent contact angle  $\theta^*$ . In summary, the surface roughness increase will lead the wettability to extreme. In other words, a hydrophilic surface will become more hydrophilic along with increasing degree of surface roughness and a hydrophobic surface will be more hydrophobic when the degree of surface roughness is increased.<sup>69</sup>

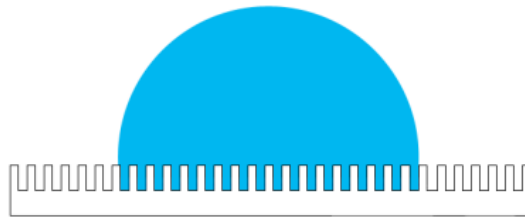


**Figure 2.8.** Wenzel model.

Wenzel model reveals the relationship between the roughness and the contact angle of the surface, but it is not sufficient to deal with a heterogeneous surface. When various materials are involved, a more complex model measuring the change of the apparent contact angle is needed. Cassie–Baxter equation is a widely accepted model to explain that phenomenon as below (Cassie's law):<sup>70</sup>

$$\cos\theta^* = r_f f \cos\theta_Y + f - 1 \quad (\text{Eq. 2.3})$$

Where the  $r_f$  is the roughness ratio of the wet surface area;  $f$  is the fraction of solid surface area wetted by the liquid. It is worth noting that when  $r_f = r$  and  $f = 1$ , the

Cassie–Baxter equation will become the Wenzel equation. On the other hand, if there are many different surface roughness ingredients involved, each ingredient of the total surface area can be denoted by  $f_i$ . Then the Cassie–Baxter equation will be recast as follows:

$$\gamma \cos \theta^* = \sum_{n=1}^N f_i (\gamma_{i,sv} - \gamma_{i,sl}) \quad (\text{Eq. 2.4})$$

Here  $\gamma$  is the Cassie–Baxter surface tension between liquid and vapor,  $\gamma_{i,sv}$  is the surface tension of solid-vapor interface of each component and  $\gamma_{i,sl}$  is the surface tension of solid-liquid interface of each component. It is worth noting that when the liquid drop is placed on the solid surface and the air is trapped underneath it, which forms the two-component system, the Cassie–Baxter equation can be denoted by:

$$\gamma \cos \theta^* = f_1 (\gamma_{1,sv} - \gamma_{1,sl}) - (1 - f_1) \gamma \quad (\text{Eq. 2.5})$$

This equation is based on an assumption that the exposed surface of air is under the liquid droplet and is the only other substrate in the system.

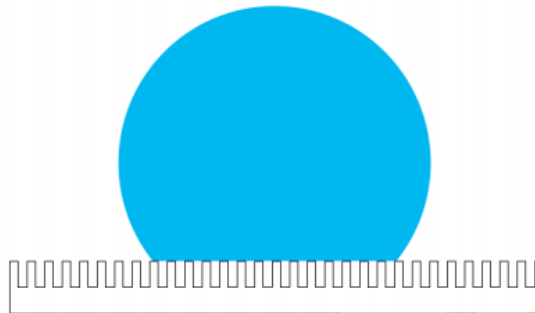


**Figure 2.9.** Cassie model.

The traditional boundary between hydrophilic and hydrophobic deduced from Young’s equation is the contact angle of  $90^\circ$ . But most recent researches

have shown a different point that a contact angle of  $65^\circ$  is considered as a more reasonable boundary above which a hydrophobic material surface is defined and below which a hydrophilic surface is defined.<sup>71</sup> The main reason of the difference is that one assumption in Young's equation, that the water molecules on the surface of liquid is the same as those in the bulk phase, is not true in the real case. The truth is that the structure and activity of the facial water molecules are highly different from those in the bulk phase. When studying the water structure at the surface, it is found that a water contact angle  $\theta < 65^\circ$  indicates a surface with adhesion tension  $> 30$  dyn/cm and a repulsive force can be detected at the interface, while a water contact angle  $\theta > 65^\circ$  indicates a surface with adhesion tension  $< 30$  dyn/cm and a long-range attractive force can be detected. Therefore, a more reasonable theory is proposed about the two kinds of structure and activity of water molecules at the surface: on the hydrophobic surface, the density of water molecules is relatively low with open hydrogen-bonded network, whereas on the hydrophilic surface, the density of water molecules is relatively high with collapsed hydrogen-bonded network. This study was also supported by Yoon<sup>72</sup> and Berg<sup>73</sup> that the boundary separate the hydrophilic and hydrophobic surface should be the contact angle of  $65^\circ$ .

The concept of super-wetting, including superhydrophilic and superhydrophobic, is also a very important property that has attracted extensive attentions in recent decades. As is known to all, a superhydrophobic surface requires a minimum water contact angle of  $150^\circ$ , and a superhydrophilic surface

means a water contact angle of which is less than  $10^\circ$ .<sup>74</sup> To fabricate surfaces with super-wetting property, a chemical modification with sufficiently low/high surface energy and a sufficient surface roughness are both required.

There are many examples with different types of wettability existing in nature. The most famous ones are the lotus leaf effect and rose petal effect. The self-cleaning function of the lotus leaf due to its superhydrophobicity make it “live in the silt but not imbrued”, which has attracted great interesting among researchers.<sup>75</sup> The first observation of the topography related hydrophobicity of many kinds of plant leave was conducted by Barthlott<sup>76</sup> and Neihuis<sup>77</sup>, and the widely accepted mechanism of the self-cleaning property was based on papillae’s micro-scale roughness and the water-repellent wax. Later, Jiang et al.<sup>78</sup> proposed a novel viewpoint that the nanostructure on the micro- papillae, which forms a hierarchical structure, is the main reason leading to the final superhydrophobic surface of lotus leaf. Figure 2.10 shows the hierarchical structure by SEM images with different resolutions. This extreme non-wetting property of lotus leaf makes the water droplets on it easy to roll off and meanwhile take the stain off the leaf.

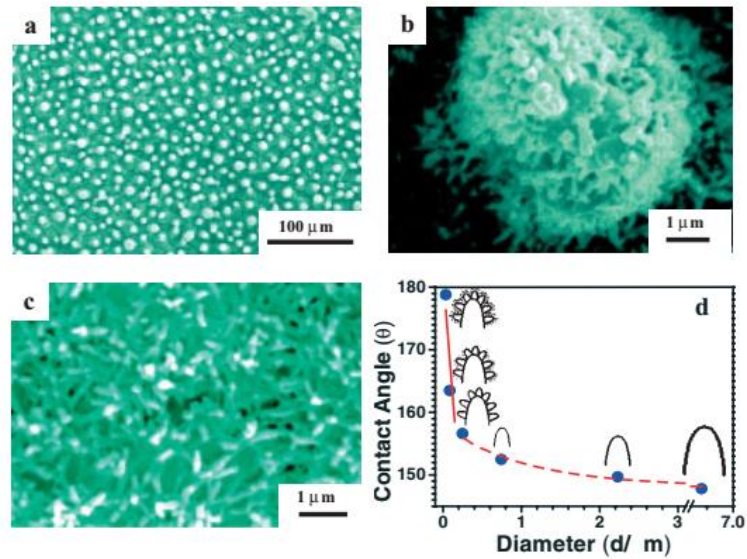


**Figure 2.10.** (a-c) are the SEM images of lotus leaf; (d) is the fitted curve based on the calculated data (contact angle, in degrees, against the mean outer diameter of protruding structures, in micrometers).<sup>79</sup>

The other famous example of superhydrophobicity in nature is rose petal.<sup>80</sup> However, different from lotus leaf, even though the rose petal surface also exhibits superhydrophobic property, the small water droplets on it can hardly roll off even the petal is turned upside down. When observing the structure of rose petal (Figure 2.11), cuticular folds about 730 nm in width on each top can be detected on the micropapillae, forming a micro- and nano-scale hierarchical structure, which results in the spherical shape of the water droplets on it (with water contact angle of 152.4°). The difference in water-rolling property of these two kinds of plants is attributed to the diverse design, the different sizes of the micro- and nano-structure and the different chemical compositions (Figure 2.12). To be specific, the triple (three phase) lines on the wax-covered and randomly roughened hydrophobic lotus leaf surface are considered to be contorted and

extremely unstable, which prevent water from intruding into the spaces between micropapillae.<sup>81-85</sup> Therefore, the drop moves easily due to the constant advancing and receding behavior at different contact line point on the lotus leaf. However, compared to the lotus leaf, the rose petal has larger size of both micropapillae and nanostructures. Hence, water droplets are expected to intruding into the larger scale grooves but not into the smaller ones, forming the Cassie impregnating wetting regime.<sup>86-88</sup> As a result, a higher contact angle hysteresis is expected owing to that the water sealed in the microstructures is clinged to the rose petal surface, which leads to a non-rolling phenomenon when the petal is tilted or even turned upside down.

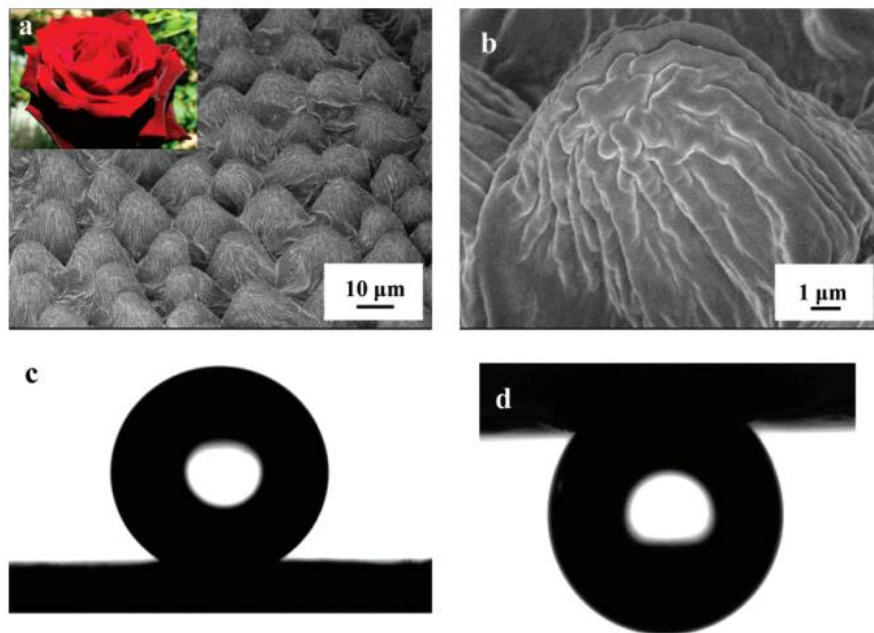


**Figure 2.11.** (a, b) SEM images of the surface of a red rose petal, showing a periodic array of micropapillae and nanofolds on each papillae top. (c) Shape of a water droplet on the petal's surface, indicating its superhydrophobicity with a contact angle of  $152.4^\circ$ . (d) Shape of water on the petal's surface when it is turned upside down.<sup>80</sup>

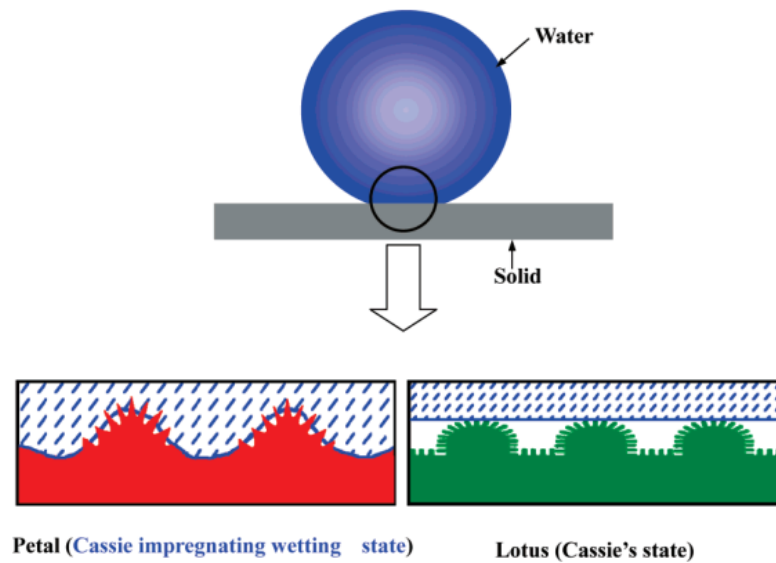


**Figure 2.12.** Schematic illustrations of a drop of water in contact with the petal of a red rose (the Cassie impregnating wetting state) and a lotus leaf (the Cassie's state).<sup>80</sup>

Besides the plants, many animals have been found to utilize their superhydrophobic organs in life. For examples, the special superhydrophobic structures composed of stepwise stacked stripes of duck and butterfly can realize easy rolling of water along the radial outward of the central axis of the body and tight pinning along the opposite direction.<sup>89-90</sup> Another instance is for Water striders Gerridae, a common insect reside on the surface of rivers, was found supporting their weight by the superhydrophobic legs with numerous oriented setae and nanoscale grooves on each setae which constructs a hierarchical structure to trap air and form a cushion that support their bodies on the water surface (Figure 2.13).<sup>91</sup>

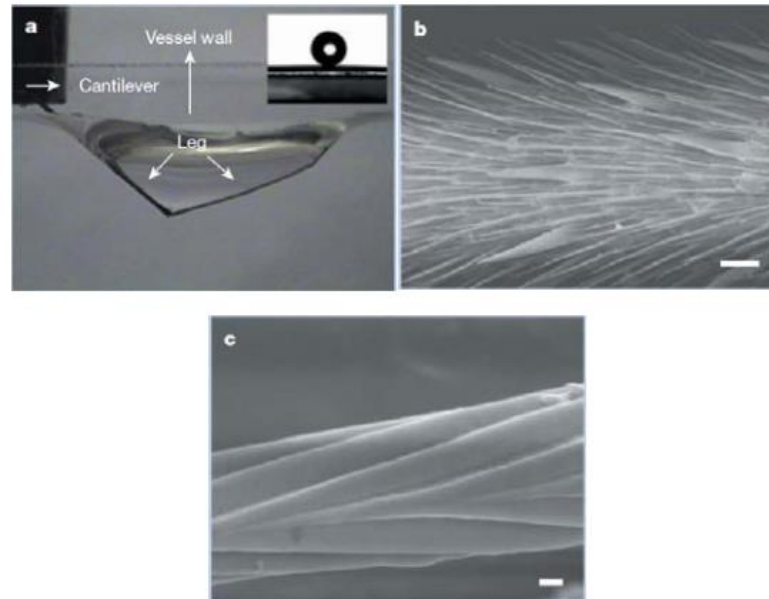


**Figure 2.13.** (a) side view of Gerridae's leg in water; (b), (c) SEM images of micro-, nanostructure on a leg.<sup>91</sup> Scale bars: b, 20  $\mu\text{m}$ ; c, 200 nm.

## 2.2.2 Directional transportation and condensation

In addition to the wetting property, some nature creatures have been found with excellent ability to manipulate the directional transportation and condensation of water droplets. They are commonly seen in those inhabited deserts and arid regions. The rainfalls in such areas are scarce, some animals and plants rely on fog and humid air as the major source of water. Stenocara beetle from Namib Desert can harvest water from the mist and direct the drops into its mouth, because its carapace has a hydrophobic surface with a random array of hydrophilic bumps (Figure 2.14 a-b). The fog droplets contact with the beetle back will condense primarily on the hydrophilic bumps, after which the coalesced water drop will roll down to beetle's mouth after they reach enough volume.<sup>92-94</sup> Cribellate spiders rely on their silks, on which alternated spindle-knots and joints

lead to both wettability<sup>95-96</sup> and curvature gradients,<sup>97-98</sup> to collect water from humid air (Figure 2.14 c-d). To be specific, the spindle-knot has larger radius of curvature and the joints has smaller one, and the spindle-knot part shows a rough and random conformation while the joint structure is smoother. The two driven forces formed on the silk, surface energy gradient and the Laplace pressure gradient, is the reason why the water droplets can move directionally.<sup>99</sup> Additionally, some plants have also been found with water collection properties. For instance, *Cotula fallax*, a plant in South Africa, can collect water from fog and channel the drops to its stems due to the hydrophobic surface and 3D hierarchical structure of its leaves (Figure 2.14 e-g).<sup>100</sup> The increasing radius of curvature from the tip to the bottom generates a Laplace pressure gradient driving the water moving from tip to the bottom. The surface energy generating driven force can be calculated by:<sup>96, 101</sup>

$$F = \int_{L_1}^{L_2} \gamma(\cos \theta_A - \cos \theta_R) dl \quad (Eq. 2.6)$$

Where  $\gamma$  is the surface tension of water,  $\theta_A$  and  $\theta_R$  are the advancing and receding contact angles respectively,  $l$  is the integration variable along the length between two areas with different surface energy. The Laplace gradient between different radius of curvature can be denoted by:<sup>97, 99</sup>

$$\Delta P = - \int_{r_1}^{r_2} \frac{2\gamma}{(r+R)^2} \sin \beta dz \quad (Eq. 2.7)$$

Where  $\gamma$  denotes the local mean radius of the fiber,  $r_1$  and  $r_2$  are the radii of the substrate at the two sides of a droplet,  $\beta$  denotes half of the apex angle of the conical shape,  $z$  is the integration variable along the diameter of the fiber. Besides,

in some extremely droughty areas, cactaceae species can efficiently capture fog benefiting from the well-distributed spines and trichomes on their stems (Figure 2.14 k-l).<sup>102</sup> A unique water capturing and direction behaviour was also found in green bristlegrass due to the barb-groove structure of its bristles (Figure 2.14 h-j).<sup>103</sup> These two kinds of plants also rely mainly on the Laplace pressure gradient or shape gradient as the driven force to lead the transportation of the water droplets from the tip to the bottom of the barbs or the spines, then the coalesced water on the stem or the bristle which also possesses the shape gradient was further led to the needed organs. In summary, the relatively more hostile environment such as desert drives the plants or animals living there to evolve more sophisticated organs or implements to adapt and survive. That is, compared to the strategies only adjusting the wetting behaviour utilized by lotus or rose, the directional transportation or condensation utilized by Cribellate spiders and cactus seems to be more high-level because it requires diverse or heterogeneous design to form hybrid wettability or shape in different areas on a single surface or organ instead of a uniform property. This undoubtedly raises higher demand to scientists when developing bio-inspired materials to manipulate liquid behaviours.

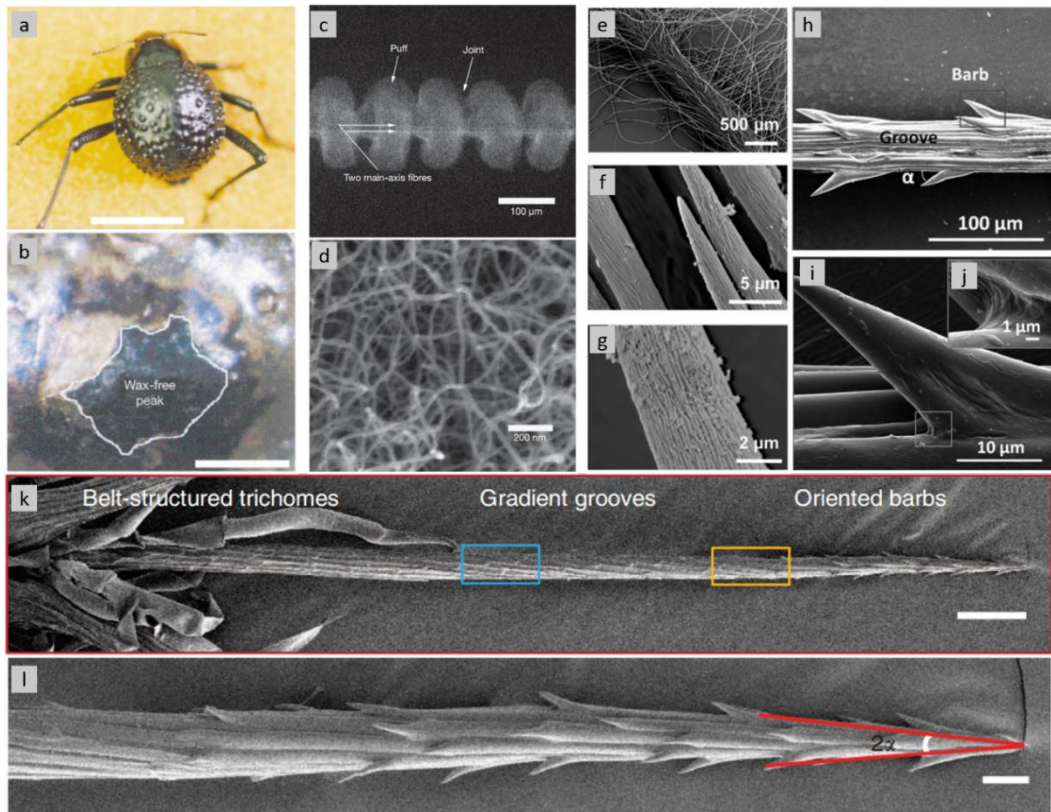


**Figure 2.14.** Images depict the structures of water collection units of nature creatures. (a) Adult female of desert beetle *Stenocara sp.*, dorsal view; peaks and troughs are evident on the surface of the elytra. (b) A ‘bump’ on the elytra, stained with Red O for 15 min and then with 60% isopropanol for 10 min, a procedure that tests for waxes. (c) Lowmagnification environmental SEM image of periodic puffs and joints surrounding two main-axis fibres on dry capture silk of cribellate spider. (d) Magnified image of puff composed of countless nanofibrils. (e) A single leaf covered in hairs of *Cotula fallax*. (f) individual hairs, (g) midsection of a single hair at high resolution. The bristle has aligned micro-grooves and oriented barbs (h), the magnified image of barb (i), and nano-fold structure at the bottom of the barb (g). (k) SEM image of a single spine of the cactus, the tip (l) with an apex angle ( $2\alpha$ )

and oriented barbs.<sup>92, 99-100, 102-103</sup>

### 2.2.3 Rolling and sliding

In manipulation of liquid behaviors, the rolling or sliding of the liquid out of the surface is a very important factor or even fundamental to some applications such as water collection, self-cleaning or desalination. The rolling or sliding property of a surface is always measured by sliding angle (SA), an inclination angle of the surface above which the liquid droplet can start to roll or slide. According to Furmidge,<sup>104</sup> the SA was defined as a function of advancing and receding contact angles. If a drop is placed on a tilted solid surface (Figure 2.15), the contact angles at the front and back of the direction of droplet movement represent the advancing and receding contact angle respectively. The SA can be calculated by:<sup>104</sup>

$$\frac{mg(\sin \alpha)}{\omega} = \gamma(\cos \theta_{adv} - \cos \theta_{rec}) \quad (Eq. 2.8)$$

Wherein  $m$  is the mass of water,  $\alpha$  is sliding angle (SA),  $\gamma$  is the surface tension of water,  $\theta_{adv}$  and  $\theta_{rec}$  are the advancing and receding contact angles respectively,  $g$  is the acceleration of gravity,  $\omega$  is the width along the movement direction of the contact area between the droplet and the surface.

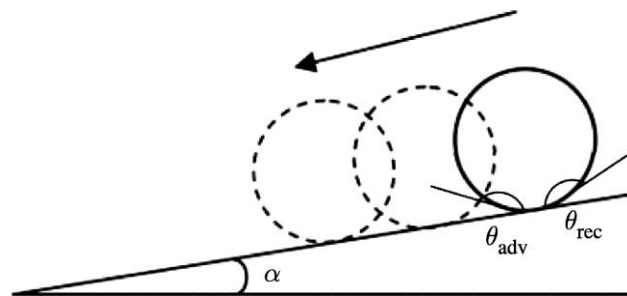


**Figure 2.15.** Tilted surface profile (tilt angle,  $\alpha$ ) with a liquid droplet; advancing and receding

contact angles are  $\theta_{adv}$  and  $\theta_{rec}$ , respectively.<sup>105</sup>

Even though the sliding or rolling property of surfaces can uniformly measured by SA, but these two concepts are recently considered different from each other, especially after the discovery of the slippery surface on the pitcher plant (Figure 2.16).<sup>106</sup> It is found that the *Nepenthes* can capture insects with high efficiency especially after a rainfall. The insects that step on the peristome helplessly slip on the surface and fall into the pitcher. The main mechanism of the slipperiness of the peristome of *Nepenthes* is based on the presence of lubricating water or nectar film as well as on the microstructure of the peristome surface (Figure 2.16 D-E). To be specific, after rainfall, the peristome is wetted by rain water which spread and forms a fluid film integrating nectar. The fluid film generates an aquaplaning, i.e., lubricating effect between the peristome surface and adhesive pads of insects, which highly decrease the friction force. Then, the microscopic cavities with opening pointing inside of the pitcher can provide anchorage for insect claws pointing outside of the pitcher.

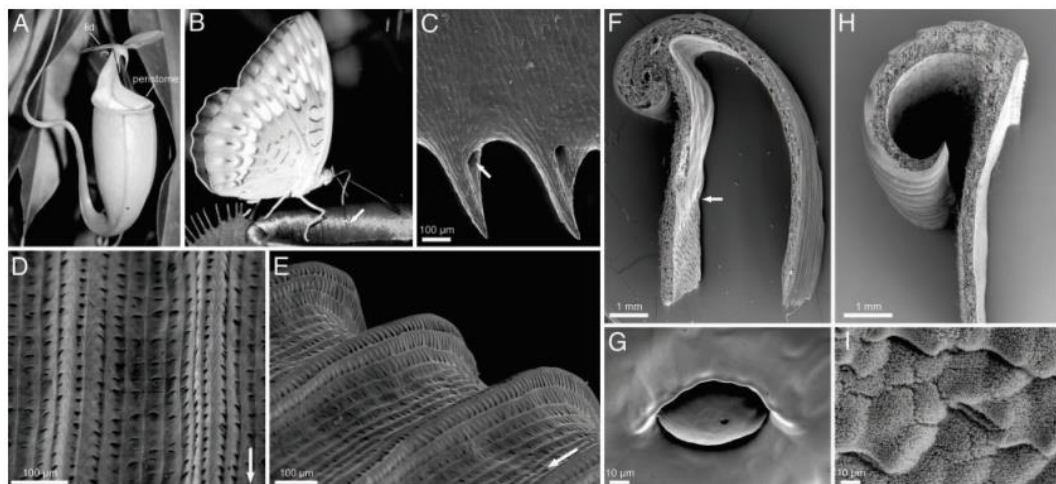


**Figure 2.16.** *Nepenthes* pitcher and peristome morphology. (A) Pitcher. (B) Butterfly

(probably *Tanaecia pelea pelea*) harvesting nectar from the peristome surface. (C) Underside of inner margin of peristome with tooth-like projections and nectar pores (arrow). (D and E) Peristome surface with first- and second-order radial ridges. Arrows indicate direction toward the inside of the pitcher (F) Transverse section of peristome. Note the transition from the digestive zone to the smooth surface under the peristome (arrow). (G) Inner pitcher wall with digestive gland at the height of the inner peristome margin (H and I) *N. alata*. (H) Transverse section of peristome. (I) Waxy inner pitcher wall at the height of the inner peristome margin.<sup>106</sup>

Different from the lotus leaf with high surface roughness, low surface energy and thus very large water contact angle which make the water droplets easily to roll off the surface, the capturing activity of *Nepenthes* with the help of the slippery peristome provide a novel thinking towards liquid drainage, i.e., sliding off. Note that the slippery surface on which liquid can slide off does not mean a highly roughened surface morphology and a large liquid contact angle. On the contrary, a slippery surface with lubricating film always requires sufficient smoothness and shows a relatively lower contact angle.<sup>107</sup> In the other words, the mechanism of the lubricating slippery surface is not based on the lower liquid spreading and higher air trapping on the highly roughened solid surface: it is based on the higher flexibility of movement of molecules in the layer of the liquid lubricant, which is like transportation with help of wheels underneath. There is a similarity between a slippery and a superhydrophobic surface that the contact

angle hysteresis (CAH) on both surface, which is denoted by<sup>105</sup>  $\theta_{adv} - \theta_{rec}$ , is very small.

## **2.3 Biomimetic materials or surfaces for the manipulation of liquid behaviors**

Inspired by nature creatures, many materials have been designed to realize the manipulation of liquid behaviours. Inspired by lotus leaf or other prototypes with special surface wettability, materials or surfaces with elaborate surface modifications integrating the promotion of the surface roughness or altering the surface energy have been developed to manipulate the wetting behaviour of the liquid. Along with the increasingly profound understanding of the desert beetle or cactus by scientists and the fast development of the science and technology, more sophisticated materials or surfaces have been fabricated integrating hybrid wettability components and unique structures or shapes to realize the manipulation of the directional transportation or condensation of liquid. With deep study of the pitcher plant species, a novel slippery surface to further decrease the friction of liquid mobility has been reported and has enlightened the development of lubricating surfaces to improve the efficiency of manipulating liquid condensation, transportation and drainage. The detailed introduction of these progresses is listed below.

### 2.3.1 Biomimetic surfaces to manipulate liquid wetting

Jiang et al.<sup>108</sup> fabricated a lotus-leaf-like superhydrophobic surface via the electrohydrodynamics (EHD) technique with fine adjusting of the polystyrene/dimethyl formamide (PS/DMF) solution concentration (Figure 2.17). A porous microsphere/nanofiber composite film (PMNCF) was obtained from a 7 wt % PS/DMF solution and it showed a water contact angle of  $160.4 \pm 1.2^\circ$ . The obtained superhydrophobicity of this film is attributed to the high roughness of the microspheres and the interweaved nanofibers formed a 3D network that reinforced the composite film.

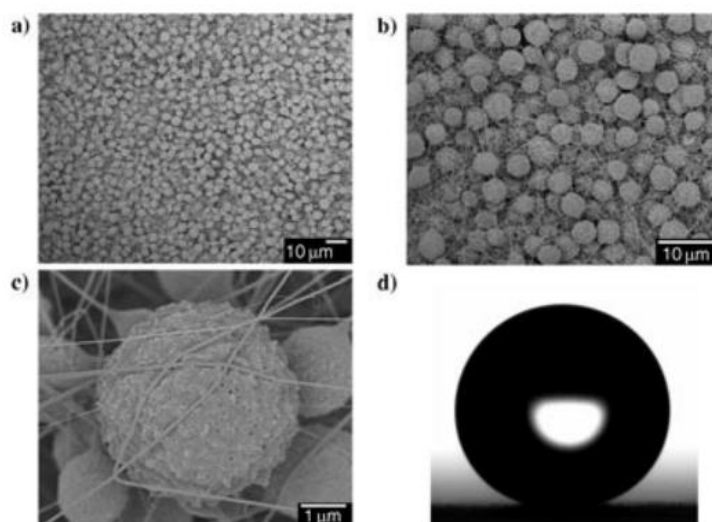


**Figure 2.17.** a) SEM image of porous microsphere/nanofiber (PMNCF) prepared from a 7 wt % PS/DMF solution; b) 3D network structure of PMNCF; c) surface nanostructure of a single porous microsphere; d) water droplet on PMNCF.<sup>108</sup>

Liu et al.<sup>109</sup> developed a CNTs–Teflon composite coating to repellent hot

liquid (Figure 2.18) because they found that many so-called superhydrophobic surfaces, which exhibited high repellency towards cool water, showed remarkably decreased repellency to hot water (Figure 2.18E). This can be attributed the decreased surface tension of the hot water which make it easier to intrude into the pores and fissures of surfaces with high roughness. They also argued that the surface energy is more dominant than the surface roughness in improve the repellency to hot liquids of the surface. The as-prepared CNTs–Teflon coating showed better repellency towards hot liquid with temperature above 50 ° than just a layer of Teflon coating. This paper pointed the challenge faced by scientists that hot liquid with high pressure is more difficult to repel by present superhydrophobic materials.

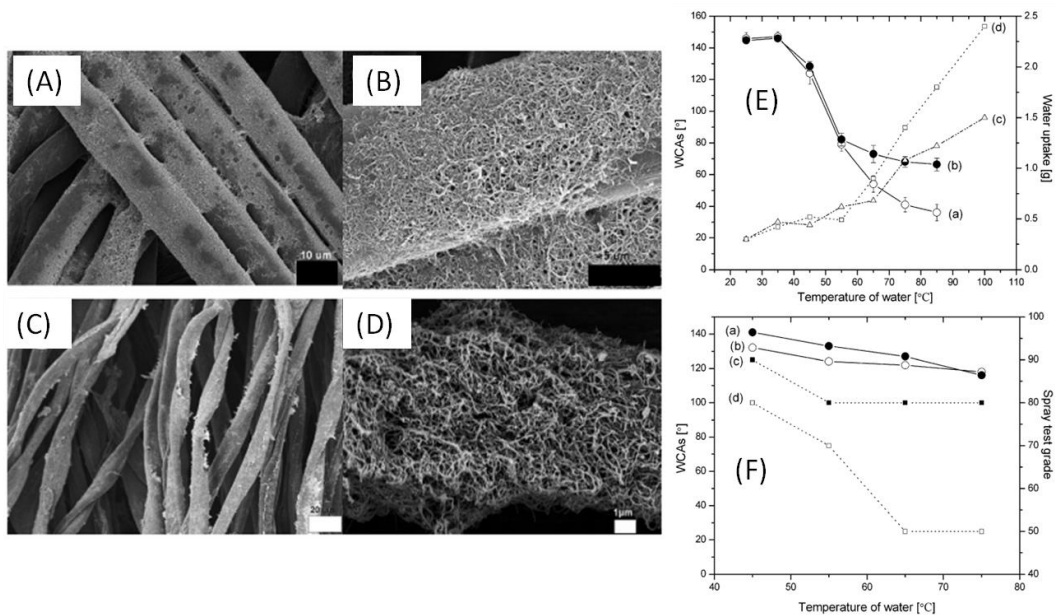


**Figure 2.18.** SEM images of CNT–Teflon hybrid treated fabrics: (A) and (B), 80/20 cotton/polyester blend weaved fabrics; (C) and (D), 100% cotton knitted fabrics. (E)

Repellent properties of fluorine-containing (silica-F, b and c) and non-fluorine-containing (silica-C, a and d) composite coatings to water with different temperatures. (F) Repellent

properties of CNT–Teflon composite (a and c) and Teflon (b and d) treated fabrics to hot water.<sup>109</sup>

Wang and his group<sup>110-111</sup> proposed general methods in fabricating stable superhydrophobic fabrics combining dip coating and chemical in-situ growth of transition metal or metal-oxide nanocrystals (including Fe, Ni, Co, Ag and Cu) with modification by n-octadecylthiol (Figure 2.19). The nanoparticles of metal/metal oxide provide the roughness of surfaces, long chain thiol offers the low surface energy. Due to the strong covalent bond formed between the transition-metal element and sulfur, thiols with a strong tendency in reacting with the transition-metal element are applied as modifying agents. The combination reaction between metal/metal oxide nanoparticles and n-octadecylthiol enhances the synergy of the two important factors to fabricate oil/water separation materials.

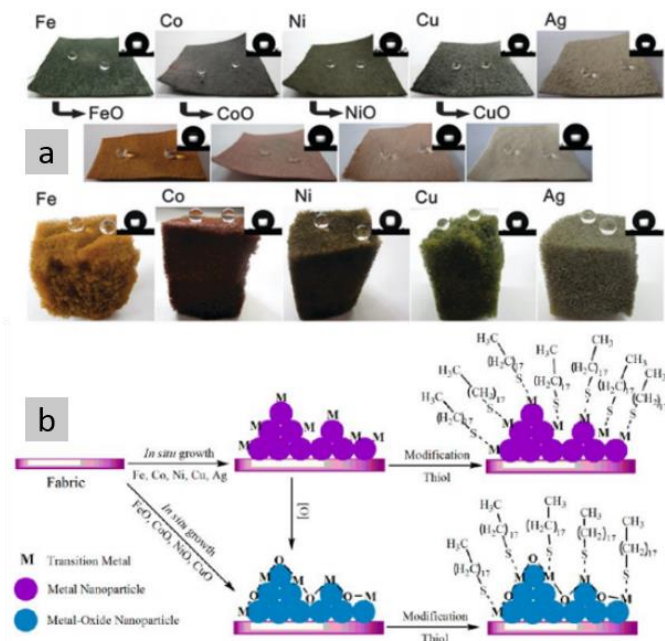


**Figure 2.19.** Optical images of the superhydrophobic fabric/sponge from the in situ growth of

Group VIII and IB metal/metal oxide nanoparticles (a); Schematic illustration of the preparation procedure of the superhydrophobic and superoleophilic fabric from the in situ growth of transition-metal/metal oxide nanocrystals with thiol modification (b).<sup>110-111</sup>

### **2.3.2 Biomimetic surfaces to manipulate directional transportation and condensation**

Spider silks have both micro- and nanoscale composite structures, for example, nanofibrils and nanocrystals. The nano- and micro-scale structure of spider silks plays a pivotal role in achieving the unique physical and chemical properties of spider silks. In addition, the spindle-knots and joints structure that possessing wettability and curvature gradients gives us a biomimetic revelation to fabricate 1-D bioinspired fibers to realize water drops capture. Based on fiber material, 1-D water collection materials have been developed imitating spider silks,<sup>112-119</sup> on which condensed small water drops were transported from joints to spindle-knots and coalesce to form larger drops.

Hou et al.<sup>120</sup> fabricated porous hump fibers using the Rayleigh instability technique and breath figure method. The structures of the pores can be adjusted by changing the reaction conditions of the resin (Figure 2.20a). Jiang et al.<sup>121</sup> developed periodic, screw-shaped cracks on core-shell spindle-knots by a first-step dip-coating and subsequent calcination (Figure 2.20b). Hou et al.<sup>122</sup> further studied the water collection performance related to the periodicity of

structural geometry on artificial humped fiber. They investigated two water collection mode, i.e., water collected by a single spindle-knot (Figure 2.20c) and by two spindle-knots together (Figure 2.20d), in terms of different conjunction mode of three-phase contact line with threshold volume.

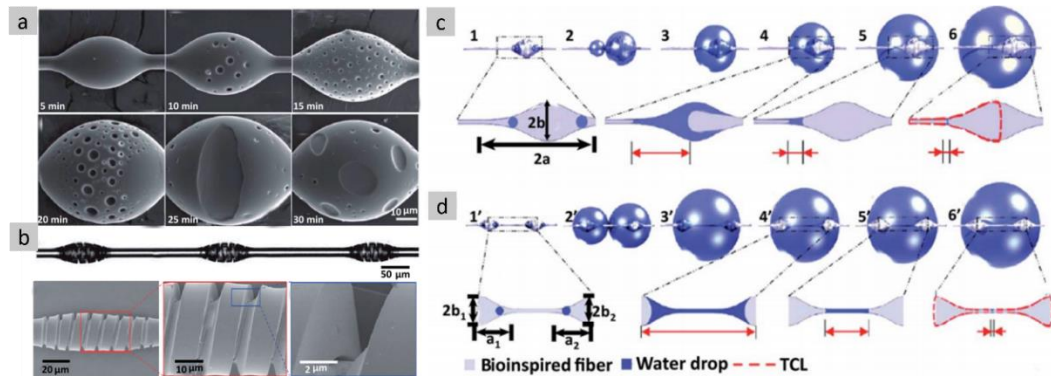


**Figure 2.20.** (a) SEM images of the polymer bioinspired fibers fabricated after different reaction times.<sup>120</sup> (b) Intact and helically cracked spindle knots after calcination.<sup>121</sup>

Illustrations of water droplet formation on bioinspired fibers with spindle-knots on (c) Fiber with one spindle-knot, (d) fiber with two spindle-knots.<sup>122</sup>

A type of smart water drops direction fiber was developed by combine hydrogel and N-isopropylacrylamide (NIPAAm), which is a thermo-responsive polymer.<sup>123</sup> Features of different curvature, roughness and wettability were also adopted. By changing the surrounding temperature (above or below the LCST of PNIPAAm), the water droplets can be driven towards and away from the spindle-knots accordingly. This innovation is promising to fabricate smart fibers with controllable water collection function, which can provide solutions towards liquid collection in various surrounding conditions.

Inspired by cactus, Luo et al.<sup>124</sup> fabricated a type of ZnO wire with an array

of small ZnO wires on it motivated by the approach used in cactus to harvest fog. All these wires possess conical shapes, with a gradually increasing diameters from tip to root of the wire. Therefore, water droplets condensed on the tip of each wire are driven into the root by the capillary force generated from the curvature gradient. The as-prepared ZnO wires exhibit an excellent water collection performance exceeding its counterparts in the case of cactus.

Jiang's group<sup>125</sup> developed a cactus spine like water collection material by gradient electrochemical corrosion and investigated the directional water transportation and condensation on the as-prepared artificial cactus inspired spines.

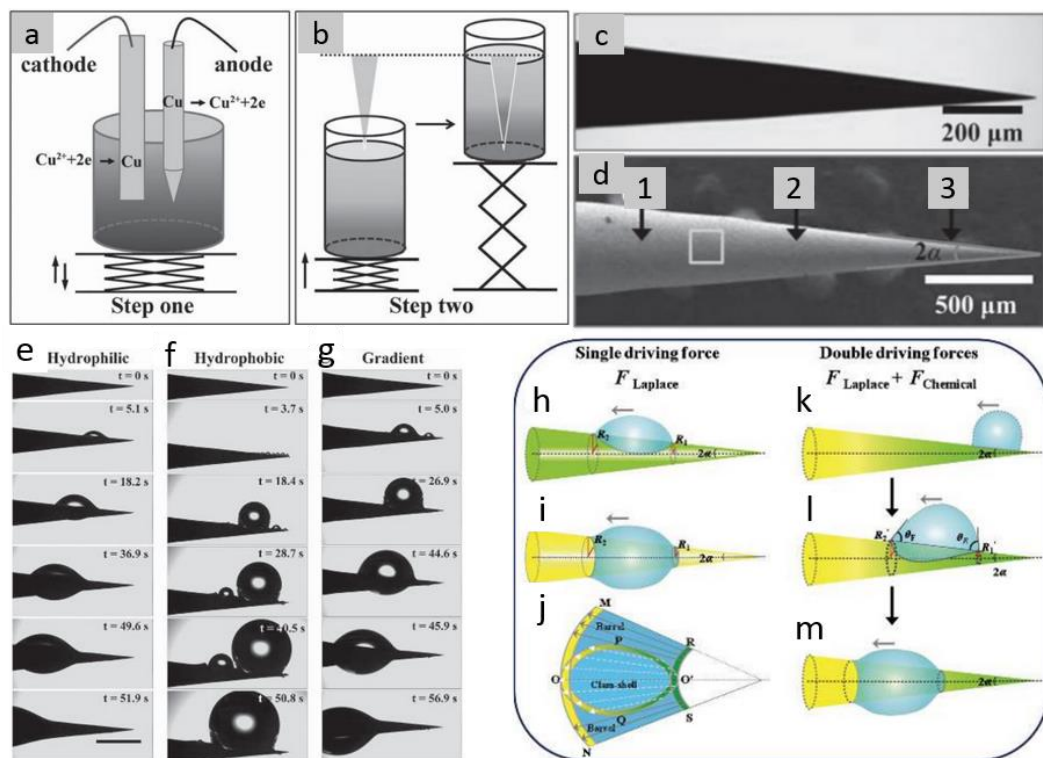


**Figure 2.21.** Sketch of step 1 (a) and step 2 (b) of preparation of conical copper wire

(CCW) through gradient electrochemical corrosion. (c-d) Structure of the CCW. (e-g)

Microscopic observations of typical fog-collection processes on three kinds of CCWs with

different wettability. (h-m) Mechanism of the distinct velocity of water drop motion on CCWs with different wettability.<sup>125</sup>

By mimicking the desert beetles' back, a variety of strategies have been explored to fabricate 2-D surfaces consisting of both hydrophobic and hydrophilic ingredients.<sup>126-129</sup> However, some of the approaches are very difficult to be generalized due to the laborious and tedious synthetic procedures. In spite of this, some innovations have been attempted to simplify the synthesis procedures.

Wang et al.<sup>130</sup> reported a simple route to make fabric with a superhydrophobic-superhydrophilic hybrid (SSH) surface based on the selective reactivity of thiol with Fe and Co nanoparticles. Through an evenly distribution of Fe and Co nanoparticles, and a subsequent treatment of n-Octadecyl thiol, an integral superhydrophobic surface mixing alternately distributed superhydrophilic sites was prepared mimicking the desert beetle, and was investigated on the water collection process.

Bai et al.<sup>131</sup> prepared a superhydrophobic surface with star-shaped superhydrophilic patterns to create a combination of a wettability gradient and a shape gradient to improve the water collection efficiency. By integrating a wettability gradient and shape gradient, the hydrophobic surface with star-shaped superhydrophilic patterns can be more efficient in driving water droplets into bigger ones and avoid the water being lost in wind (Figure 2.22).

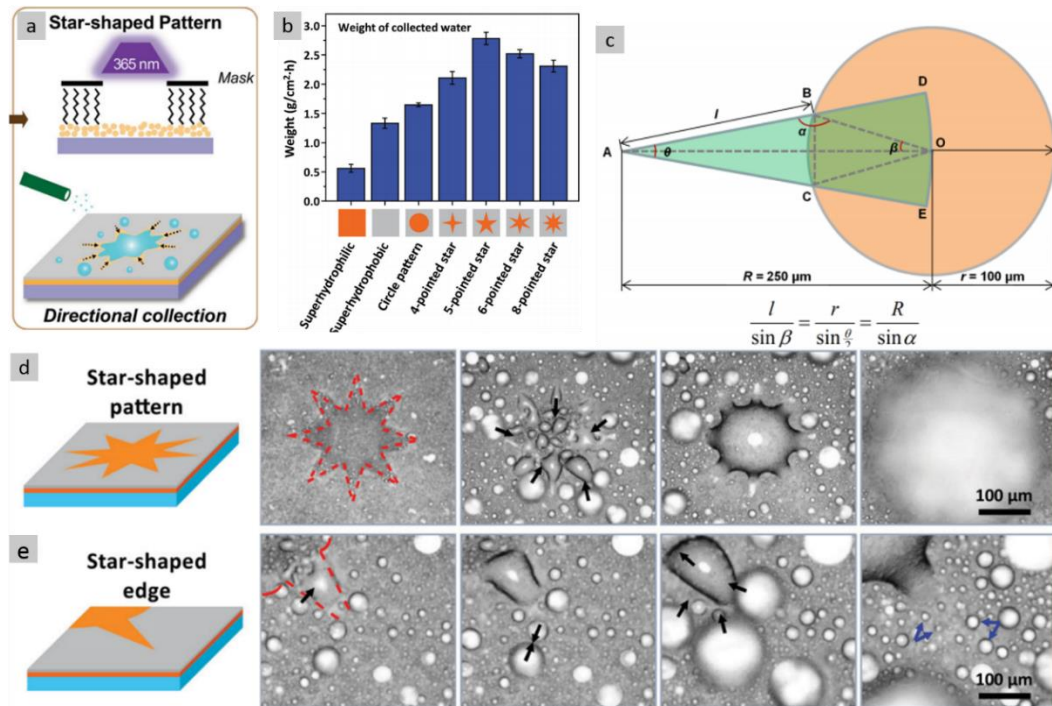


**Figure 2.22.** (a) Bioinspired gradient surface with a star-shaped wettability pattern. (b)

Star-shaped pattern are more efficient than that with circle-shaped pattern. (c) Calculation of the hydrophilic area of star-shaped patterns as shown by the in-Figure equation. Detailed directional collecting processes on the border of (d) star-shaped wettability patterns and (e) star-shaped edge.<sup>131</sup>

Compared to water collection materials or surfaces inspired by spider silk or cactus, desert beetle bio-inspired water collection materials or surfaces have a better drainage system as the integral hydrophobic surface prepared can let the captured water drops roll down to a designated device to improve the conveniences of human utilization. Also, the small space occupation and the relatively strong mechanical strength of this type of 2-D materials can suit better for a mass production and transportation.

### 2.3.3 Biomimetic surfaces with better manipulation of liquid sliding

Inspired by pitcher plant, numerous kinds of materials with slippery surface have been developed and applied in some areas such as biomedicine,<sup>132-134</sup> self-cleaning,<sup>135-136</sup> anti-icing,<sup>137-142</sup> and self-repairing.<sup>107, 143-145</sup> There are mainly two strategies to fabricating such lubricating slippery surface: covalently surface grafting and liquid infusing.

For surface grafting method, McCarthy et al.<sup>146</sup> reported the development of an instant omniphobic surface with unprecedented repellency by grafting a layer of covalently attached liquid on the surface of glass slide. The as-prepared surface is smooth, stable and temperature-durable, and also exhibit extremely low contact angle hysteresis (CAH) ( $<1^\circ$ ) as well low sliding angle (SA) for liquids even with low surface energy (18.4 mN/m) as shown in Figure 2.23.

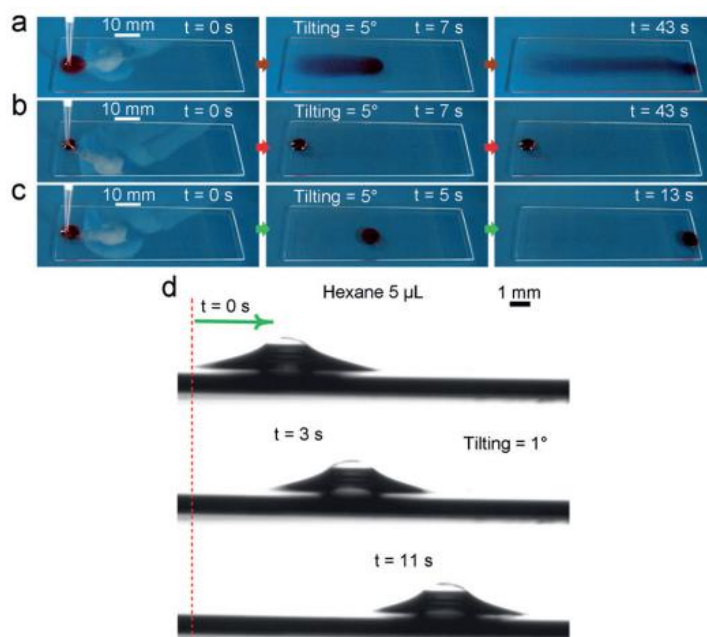


**Figure 2.23.** Time-sequence images for comparison of the mobility of 20  $\mu\text{L}$  toluene drops

(containing Oil Red O) on a clean glass slide surface (a), on a clean glass slide modified with  $\text{CF}_3\text{-(CF}_2)_5\text{CH}_2\text{CH}_2\text{SiMe}_2\text{Cl}$  (b), and on a clean glass slide coated with a SOCAL PDMS layer (c). d) Time-sequence images for a hexane drop sliding down a tilted SOCAL PDMS surface.<sup>146</sup>

Yao et al.<sup>147</sup> grafted a liquid-like copolymer with reactive groups via a layer-by-layer covalently immobilization. The grafted nano-coating is oil-repellent to a broad range of organic liquids and can be further modified by functional molecules because of the reactive sites. This approach may have technical implications in surface modifications and biomedical technologies.

For liquid infusing method, there are three principles:<sup>107</sup> (1) the infused lubricating fluid must wick into, wet and stably adhere within the substrate, (2) the solid substrate must be preferentially wetted by the lubricating fluid rather than by the liquid one wants to repel, and (3) the lubricating and impinging test liquids must be immiscible. The first criterion can be satisfied by utilizing micro/nanostructured, highly roughened substrates with large surface area, integrating chemical affinity towards the liquid to facilitate its wetting and adhesion by the lubricant. The second criterion should be satisfied by determining the required chemical and physical properties to ensure the combinations of substrates and lubricants. To be specific,  $\Delta E_1 = E_A - E_1 > 0$  and  $\Delta E_2 = E_A - E_2 > 0$  should be satisfied in order to ensure the solid is wetted preferentially by the lubricating fluid, wherein the total interfacial energies of textured solids that are completely wetted by arbitrary immiscible liquid ( $E_A$ ), or a lubricant with ( $E_1$ ) or

without ( $E_2$ ) a completely wetted immiscible testing liquid above it. The equations can be expressed as:<sup>148</sup>

$$\Delta E_1 = R(\gamma_B \cos \theta_B - \gamma_A \cos \theta_A) - \gamma_{AB} > 0 \quad (\text{Eq. 2.9})$$

$$\Delta E_1 = R(\gamma_B \cos \theta_B - \gamma_A \cos \theta_A) + \gamma_A - \gamma_B > 0 \quad (\text{Eq. 2.10})$$

In the equations,  $\gamma_A$  and  $\gamma_B$  are the surface tensions of the testing liquid and the lubricant,  $\gamma_{AB}$  is the interfacial tension at the interface of two liquids,  $\theta_A$  and  $\theta_B$  are the equilibrium contact angles of the testing liquid and the lubricant on a flat solid surface respectively,  $R$  is the surface roughness factor.

Based on these principles, a smart slippery membrane with tunable transparency and wettability has been developed via infusing lubricant into a porous film.<sup>149</sup> Along with the change of external stretching force, the morphology of the membrane tunes from smooth to rough which thus results in its ability to control the transparency and manipulate various low-surface-tension droplets from sliding to pinning.

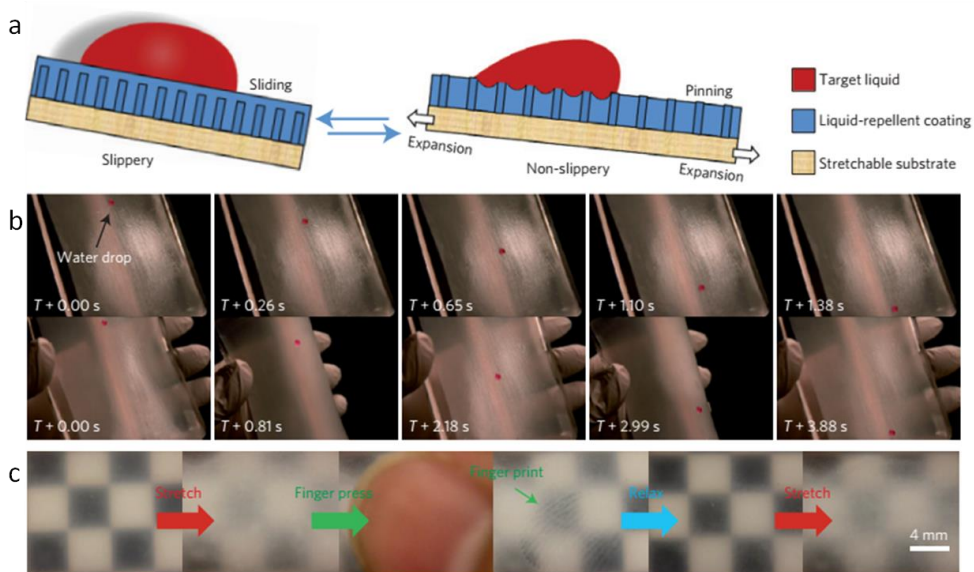


**Figure 2.24.** (a) Scheme showing the control mechanism: a droplet of test liquid changes

from sliding to pinning under external stretching. (b) Comparison of water drops sliding on a tilted slippery surface without (upper row) and with (lower row) bending. (c) Change of transparency and anti-fingerprint ability.<sup>149</sup>

Besides, due to the highly decreased friction of droplet mobility on a solid surface by introduction of a layer of lubricant, the efficiency of liquid transportation or condensation can be highly improved. For example, a type of asymmetric bumps has been designed by 3D-printing combining three concepts inspired by desert beetle, cactus and pitcher plant to enhance the water condensation on solid surface (Figure 2.25).<sup>150</sup> The droplets condense on the bumps grow much faster than on the flat surface and can slide along the slope even its direction is opposite the gravity. This strategy can be applied on a wide range of areas such as water collection, phase-change heat-transfer applications and droplet transportation.

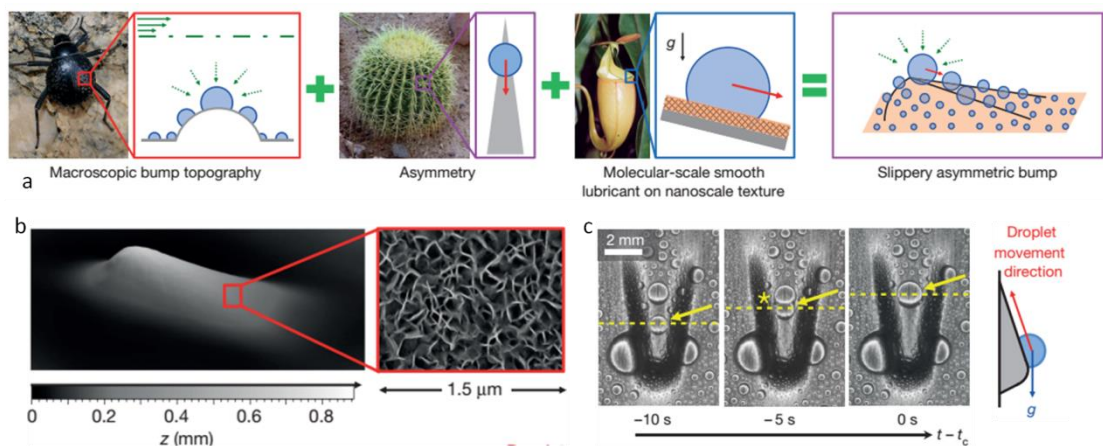


**Figure 2.25.** (a) The design concept of the approach. (b) A profilometer image (oblique view) showing nanostructure (inset) infused with lubricant, and the tangentially connected bottom slope. (c) Time-lapsed optical images of condensed water droplets on an asymmetric bump rotated 180° relative to gravity.<sup>150</sup>

## 2.4 Textile based materials and surface modification

A textile is a flexible material consisting of natural or artificial fibers. In the process of the development of functional, biomimetic or intelligent materials, textile has always been one of the most popular substrates due to its light weight, flexibility, and low cost, which make it a promising material for massive transportation and bulk production. For designing materials or interfaces with special wettability, the interlaced fibers of the textile can provide a micro- or even nano-scaled roughness, which is highly needed when fabricating hierarchical structures. Traditionally, textiles are formed mainly by knitting, weaving, crocheting, knotting, and felting. As technology advances, more types of artificial textile materials with adjustable fiber diameters have been developed by various techniques such as melt-spinning,<sup>151</sup> wet-spinning,<sup>152</sup> dry-spinning,<sup>153</sup> electro-spinning,<sup>154</sup> and micro-channel spinning<sup>155</sup> to satisfy increasingly diverse applications.

Strategies to modify textile surface are also diverse. The most widely used methods to treat textiles are surface coating by dip-coating or dip-pad coating.<sup>156-157</sup> For example, Kong et al.<sup>54</sup> developed a cotton fabric with light-dark triggered self-adaptive wettability to realize moisture management and directional transportation of water through cotton fabric. The TiO<sub>2</sub> nano-sol were dip-pad coated on the surface of cotton fabric and adhered by hydrogen bonds between the oxide network of TiO<sub>2</sub> and hydroxyls of cellulose. However, most of the surface modifications by dip-coating or dip-pad coating will form a coating layer that is

adhered onto the substrate by physical force, which usually means a poor adhesion strength and durability. Similar modification methods also include spray coating, spin coating, doctor blading, and so on.

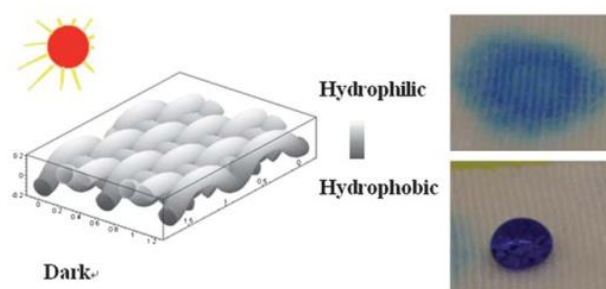


**Figure 2.26.** Fabric with self-adaptive wettability controlled by “light and dark”.

Two-dimensional wetting phenomenon on a cotton substrate with one side having hydrophilic and other side having hydrophobic properties.<sup>54</sup>

The other strategy of surface modification is to form chemical bonding between the textile substrate and the coating agent. In order to fabricate functional textile materials with special surface structure and property, surface grafting of polymers with a variety of functional groups have been widely explored. The traditional polymer grafting method can be performed by a couple of techniques such as cationic, anionic, living free radical, and open-ring metathesis polymerization.<sup>158-160</sup> There are some shortage of the above grafting method that the end group of those polymer chains should be functioned with high active anchors such as chlorosilyl group which can be deactivated by some groups such as amine, hydroxyl and carboxylic acid groups, and the thickness of the grafted polymer are always limited to 1 to 5 nm because of the kinetic and thermodynamic characteristic of such technique. To solve the above problems, a

more advanced grafting strategy called “grafting from” method has been explored involving a functional initiator immobilization process in the first step for subsequent polymer brush growing. The grafting methods include ionic, ring-opening metathesis, free radical, and controlled radical polymerization.<sup>161-166</sup> Among above techniques, the controlled radical polymerization is regarded to be to be superior to others for the reason that it can generate uniform brush layer, controllable brush thickness, layer of homopolymer or diblock copolymer. The surface initiated atom transfer radical polymerization (SI-ATRP) is the most popular technique that has been widely utilized in modifying textile materials. For instance, Yang et al.<sup>167</sup> proposed a method to develop smart water absorbing cotton with high efficient. In this work, a temperature-responsive polymer PNIPAAm was grafted from a pre-initiated cotton fabric, and formed a layer of uniform structured, highly roughened polymer brushes on the surface of the cotton fibers. It is worth noting that the as-prepared sponge-like cotton fiber can automatically collect and release water just triggered by temperature change which is consistence with the typical day-and-night range of desert.

In summary, the development and study of biomimetic liquid-manipulating materials is of great significance in both academic research and industrial application. The introduction of smart materials and chemicals endows such materials with higher controllability, adaptability, and flexibility. In terms of lowering the synthetic cost and meanwhile further promote the flexibility, textiles materials show their great advantages due to their low cost, light weight, and

unique interlaced structures with micro- or even nano-scaled roughness. In this thesis, therefore, the design and development of textile-based stimuli-responsive biomimetic materials for liquid manipulation is targeted, with an in-depth study of the correlations among material structures, stimuli, and liquid manipulation performances.

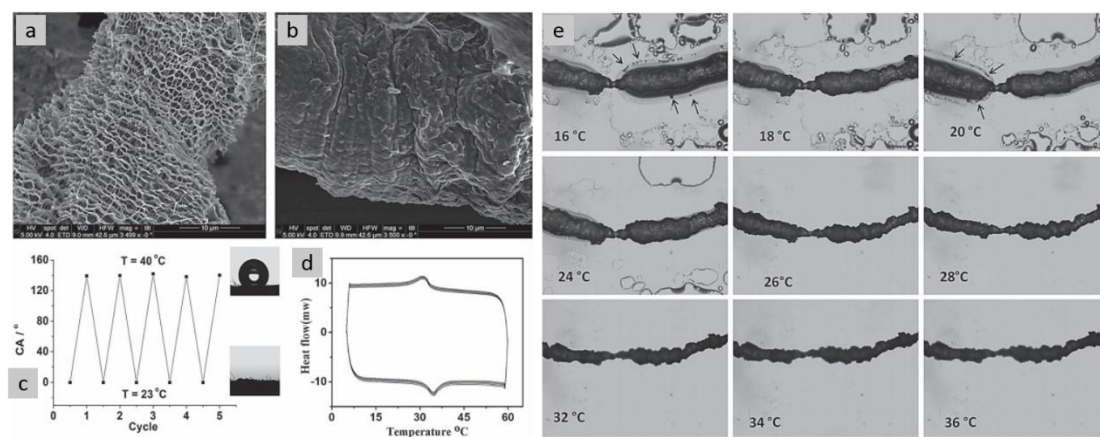


**Figure 2.27.** Reversible responsive behavior of PNIPAAm-cotton fabric (a-d) and water

collection/release by the PNIPAAm-cotton fiber upon temperature changes.<sup>167</sup>

## Chapter 3

# Temperature-Responsive Nanofibers Fabricated by Surface Grafting of Polymer Chains to Manipulate Liquid Wetting: Synthesis, Characterization, and Application

Surface functionalization with stimuli-responsive materials can turn an ordinary material into a smart one that shows adaptive properties upon external stimuli. In this study, an electrospun regenerated cellulose (RC) nanofibrous membrane was firstly prepared; subsequently, Poly (N-isopropylacrylamide) (PNIPAAm), a thermo-responsive polymer, was surface grafted to form the polymer chains/brushes on the surface of RC nanofibers via the surface-initiated atom transfer radical polymerization (SI-ATRP) method. Thereafter, the PNIPAAm-modified RC nanofibrous membrane was investigated for its temperature-responsive surface wettability at temperature below/above the lower critical solution temperature (LCST). Furthermore, the nature of the hydrophilic/hydrophobic transitions of the modified nanofibrous membrane was also investigated through the water up-taking and release experiment at various temperatures. Especially, as responses to different temperatures, the PNIPAAm-grafted nanofibrous membrane exhibits switchable super-lyophilic/super-lyophobic property at a water-oil-solid three-phase interface. With the large surface area and switchable surface wettability, the as-prepared

PNIPAAm-grafted nanofibrous membrane exhibits excellent property of controllable oil/water separation, and possesses great potential towards both wastewater treatment and oil purification.

### **3.1 Introduction**

Oil/water separation technology attracts much attention in recent years due to the increasing problems of industrial oily waste water discharge, offshore oil spillage, and the high cost of treating domestic waste water. Therefore, a large number of oil/water separation materials have been fabricated based on polymer membranes,<sup>168-169</sup> metal nets,<sup>170-171</sup> nanoparticles,<sup>172-173</sup> or textiles<sup>174-175</sup> with special surface wettability. In addition to fixed surface wettability, materials with switchable surface wettability have also been developed for controllable oil/water separation triggered by pH value,<sup>176</sup> electric field,<sup>177</sup> thermo-treatment,<sup>178</sup> or multiple stimuli.<sup>39</sup> Considering the recycling and anti-fouling properties of the separation materials, some responsive hydrophilic/underwater superoleophobic membranes were developed with self-cleaning or anti-fouling function.<sup>179-180</sup> Overall, materials with the stimuli-responsive property, which are generally defined as ‘smart materials’, have shown great potential to offer on-demand treatments towards liquid pollution.

Among the various fabrication methods of all the smart materials mentioned above, surface modification is the most popular one, which can turn an ordinary material into a smart one with certain stimulus sensibility. Usually, the

modification agent determines the stimulus a material responds to, while the substrate determines the functional efficiency and capacity of the material. Specifically, with the purpose of waste water treatment or oil purification, high adsorption efficiency and capacity of the material is greatly required.<sup>181-182</sup> Nanofibers with the diameter in submicron range or even nanoscale have shown great promise to serve as substrates of functional materials,<sup>183-185</sup> because the large surface area provided by nanofibers means more chemical reaction sites and a higher degree of physical contact, which can result in improved adsorption efficiency.<sup>186</sup> To fabricate nanofibers with such advantages, electrospinning has been considered as a versatile technique.<sup>183</sup>

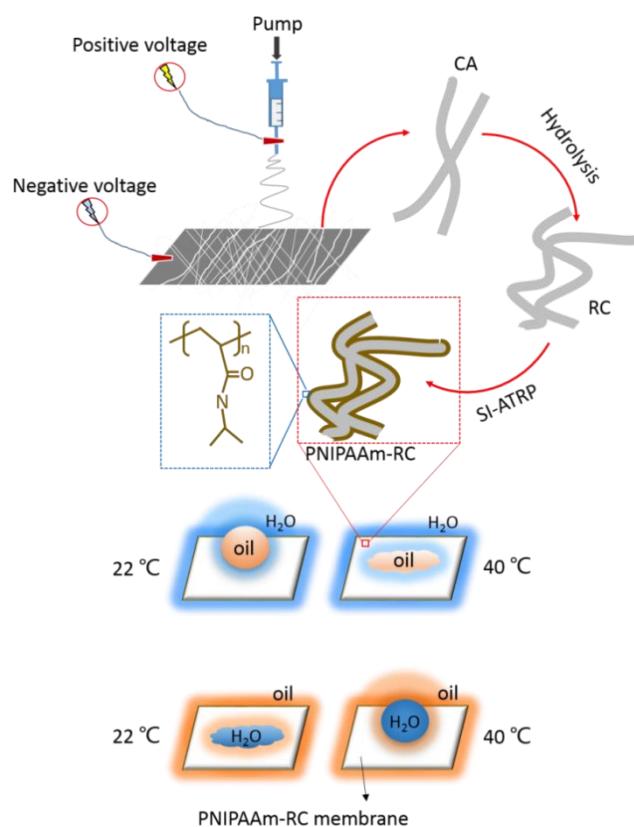
In our experiments here, regenerated cellulose (RC) nanofibers were modified with Poly (N-isopropylacrylamide) (PNIPAAm) via surface-initiated atom transfer radical polymerization (SI-ATRP).<sup>187-189</sup> PNIPAAm, as a temperature-responsive polymer, has attracted more attention, because of the transition between coil and globule with the change of wettability (hydrophilic and hydrophobic, respectively) in an aqueous solution at lower critical solution temperature (LCST, +32 °C).<sup>13, 190</sup> As suggested, the grafted temperature-sensitive PNIPAAm brushes can turn the RC nanofiber into a smart material, the surface wettability of which can be switched between hydrophilic and hydrophobic with the change of temperature of the environment.

The switchable wettability, triggered by temperature, enables the material to provide specific solutions towards the separation of various oil/water mixtures. To

be specific, at room temperature, the PNIPAAm-RC nanofiber presents a hydrophilic and under-water superoleophobic property. As a result, water can pass through and the oil will be blocked by the pre-wetted PNIPAAm layer. Therefore, in a water-in-oil mixture, the PNIPAAm-RC nanofiber can clean the oil phase by removing water drops out without much oil adhering. In contrast, the PNIPAAm layer can let the oil pass through and block the water due to the oleophilic and under-oil superhydrophobic property at temperature above the LCST. This enables the PNIPAAm-RC nanofibers to treat the oil polluted water by drawing the oil drops out at a high temperature. With the combination of responsive wettability and high adsorption efficiency, the PNIPAAm-RC nanofiber shows outstanding potential in various types of oil/water separation situations, for instance, wastewater treatment and oil purification. Scheme 1 shows the fabrication procedures and the thermo-responsive wettability at a water-oil-solid interface of PNIPAAm-RC nanofibers.

In this chapter, RC nanofibers were fabricated through electrospinning method from a cellulose acetate (CA) solution, followed by hydrolysis in strong base. Hydrolysis of CA was referred to in Menkhaus's work,<sup>182</sup> and had no damage on well-defined cylindrical morphology of the nanofibers. Thereafter, through SI-ATRP, the RC nanofibers were surface functionalized by PNIPAAm brushes, which introduced a thermal-responsive wettability at oil-water-solid interfaces. The results indicate that the prepared PNIPAAm-RC nanofibers show excellent water absorption from water/oil mixture at 22 °C and oil absorption

from oil/water mixtures at 40 °C. To date, most of the existing oil/water separation materials can hardly have versatile applications due to the fixed wettability;<sup>191-193</sup> and even if some stimuli-responsive materials have been designed for selective oil/water separation, few of them are qualified for the in situ oil/water removal because of the poor adsorbability.<sup>194-195</sup> Innovatively, the study presented here can lead to a simple method to realize controllable oil/water separation in situ.



**Scheme 3.1.** Fabrication process of PNIPAAm-RC nanofibers undergoing electrospinning, hydrolysis and SI-ATRP; and the temperature-responsive super-lyophobic/super-lyophilic property at water-oil-solid interface of the prepared PNIPAAm-RC nanofiber membrane.

## **3.2 Experimental**

### **3.2.1 Materials**

Cellulose acetate (CA, ACROS, Mn~100000 g/mol), acetone (VWR International 99.8%), dimethylacetamide (DMAc, Duksan Chemical 99.5%), sodium hydroxide (NaOH, VWR International 99%), 2-bromisobutyryl bromide (BiB, Aldrich 98%), triethylamine (TEA, Aldrich 99%), 4-(dimethylamino) pyridine (DMAP, Aldrich 99%), tetrahydrofuran (THF, J&K 99.9%), N-isopropylacrylamide (NIPAAm, J&K 99%), methanol (MeOH, Duksan Chemical 99.9%), pentamethyldiethylenetriamine (PEMDETA, Aldrich 99%), copper (I) bromide (CuBr, J&K 98%).

### **3.2.2 Characterization**

Field emission scanning electron microscopy (FE-SEM, JSM-6335F, Japan) was used to observe the surface morphologies of the electrospun CA nanofibers, RC nanofibers and PNIPAAm-grafted RC nanofibers, with a gold sputtering prior to imaging. All the samples were dried at 40 °C under vacuum and then fixed on the sample stub by electroconductive double-tape at room temperature before the FE-SEM test. Then, the samples were observed at room temperature under vacuum condition by FE-SEM.

Atomic force microscopy (AFM, Veeco, USA) was utilized to observe topography of the RC nanofibers before and after SI-ATRP.

Differential scanning calorimetry (DSC, PerkinElmer Diamond DSC, USA) was employed to investigate the interaction between polymer and water. The test was performed in the temperature range of 23 °C to 60 °C using a heating rate of 5 °C/min. Prior to the test, 5 mg of as-prepared PNIPAAm-RC nanofibers were soaked with 5 mg of distilled water.

Fourier Transform Infrared (FT-IR, PerkinElmer Spectrum 100, USA) was used to characterize the functional groups of the CA, RC and PNIPAAm-grafted nanofibers.

Static oil/water contact angle (CA) measurements were carried out with OCA20 (Data Physics, Germany) using a sample chamber to control the test temperature. The data of each contact angle were calculated averagely from five repeated measurements.

### **3.2.3 Fabrication of electrospun RC nanofibers**

Prior to electrospinning, 15 g of CA was dissolved in 100 mL mixture of acetone and DMAc (3:1, v/v). The electrospinning setup was purchased from Micro & Technologies Expert (TL-Pro), Shenzhen, China. During electrospinning, a positive high voltage of 15 kV was applied to the needle, and the flow rate of 0.5 mL/h was maintained. The CA nanofibers were collected as an overlaid membrane on a roller covered with aluminium foil. The rotational speed of the collector was set at 10 rpm during electrospinning. The ambient relative humidity in the chamber was around 55%.

The as-electrospun CA nanofibrous membrane was hydrolysed upon immersion into 0.05 M NaOH aqueous solution for 24 hrs to obtain the RC nanofibrous membrane. The RC nanofibrous membrane was then rinsed with deionized (DI) water for three times and dried in a vacuum oven.

### **3.2.4 Immobilization of the ATRP-initiator on the RC nanofibers**

The dried electrospun RC nanofibrous membrane was immersed into a mixture solution containing 15 mL anhydrous THF, 10 mg DMAP and 0.2 mL TEA, and then 0.2 mL of BiB was added into the mixture. Subsequently, the reaction mixture was kept at room temperature for 12 hrs under stirring in a nitrogen atmosphere. After reaction, the initiator-modified electrospun RC nanofibrous membranes were rinsed thoroughly with THF, acetone, and DI water and finally dried at 40 °C under vacuum for 24 hrs.

### **3.2.5 Surface-grafted with PNIPAAm**

4 mL of the mixture of MeOH and DI water solution (3:1, v/v) was added into a Schlenk flask and deoxygenated by a nitrogen flow for 15 minutes. The initiator-modified RC nanofibers (35 mg), NIPAAm (1.2 g), CuBr (16 mg), and PMDETA (0.05 mL) were then added into the deoxygenated mixture. Subsequently, the mixture was degassed by three vacuum-nitrogen cycles under an ice-salt bath to remove the oxygen from the system, followed by being sealed for 6 hours (Products with grafting duration of 2 hours and 10 hours have also

been made as shown in Figure 3.2) with slow magnetic stirring at room temperature. Next, the PNIPAAm-RC nanofibers were sequentially rinsed by MeOH and DI water to remove the residual monomers, unbonded polymers, and catalyst complex. Finally, the PNIPAAm-RC nanofibers were dried under vacuum overnight.

### **3.2.6 Investigation of water collection/release and separation of oil/water mixtures**

In order to further illustrate the temperature-responsive behavior of the modified nanofibers and the accompanied interfacial phenomenon with water, water collection and release performance of the as-prepared PNIPAAm-RC nanofibers was investigated, using the unmodified RC nanofibers as reference. Water collection of the as-prepared PNIPAAm-RC nanofibers was firstly conducted at room temperature (22 °C) and in an artificial humid atmosphere generated by an ultrasonic humidifier (Midea S40U-T, China). Typically, the PNIPAAm-RC nanofibers were placed in the generated fog (with relative humidity, RH, around 95% and the sprayed flow being 1/3 of maximum to avoid vast water condensation in short time), and the water uptake (weight percent) along with the humidity exposure time was recorded. Then, the water release rate of the modified samples were also investigated by measuring the water loss along with the exposure time in an oven at 40 °C. It is noted that the samples had a 375% (weight percent to the samples) initial water uptake prior to the water release test.

The water collection and release of the unmodified RC nanofibers were also studied for reference.

Oil/water separation was carried out through the absorption of methylene blue (MB) dyed deionized (DI) water, in n-hexane and the absorption of chloroform drops, colored by oil-based ink, in DI water. Typically, the as-prepared PNIPAAm-RC nanofibers were placed into the mixtures under magnetic stirring for 30 seconds.

### **3.2.7 Measurement of liquid absorption capacity and reusability**

In order to investigate the absorption capacity of the modified RC nanofibers for water and common oils (including N-hexane, paraffin oil, silicone oil, peanut oil and gasoline), the experiments were performed in the water/hexane mixture (with a weight ratio of 10:90) and oil/water mixture (with a weight ratio of 10:90) for water absorption and for oil absorption, respectively, and the final absorption capacity was generated by average value of 5 times experiments. Noted that, the water absorption capacity was measured at room temperature (22 °C); while the oil absorption capacity was measured at 40 °C. In a typical absorption measurement, the samples were immersed in the mixture for 30 seconds. After removed from the mixtures, the adherent excess of water or oil on the samples was cleaned with a tissue paper. The weight of the sample before and after absorption (defined as  $W_{\text{initial}}$  and  $W_{\text{final}}$ , respectively) were used for the calculation of absorption capacity  $C$ , defined as  $C=(W_{\text{final}}-W_{\text{initial}})/W_{\text{initial}}$ .

The reusability of the PNIPAAm-RC nanofibers was evaluated by repeated absorption-clean process. Normally, the absorbate saturated PNIPAAm-RC nanofibers were cleaned using ethanol and acetone, and dried in an oven before the next absorption-clean cycle. The absorption-clean cycle was repeated for 5 times.

### **3.3 Results and discussion**

#### **3.3.1 Characterization and Morphology**

As shown in Figure 3.1a, the electrospun CA nanofibrous membrane consisted of overlaid nanofibers with diameters of ~200-500 nm, and the nanofibers were relatively uniform without obvious beads and beaded nanofibers. After hydrolysis with 0.05 M NaOH aqueous solution, the RC nanofibers maintained well-defined cylindrical morphology and the diameter had no obvious change (as shown in Figure 3.1b). After the surface modification for 6 hours via the ATRP method, the RC nanofiber was fully covered by a concentric and rough PNIPAAm layer causing the increase of diameter by ~50 % (Figure 3.1c). The grafting reactions proceeding for shorter and longer time were also considered, but it was found that the long-time reaction led to the clogging of fibrous pores (see Figure 3.2c and f), while the short-time one resulted in an insufficient grafting content (the fiber base could not be evenly covered by a continuous polymer coating, as shown in Figure 3.2a and d). The atomic force microscopy (AFM) was further applied for characterization of the electrospun RC nanofibers

before and after PNIPAAm modification (as shown in Figure 3.1d and e). Additionally, Figure 3.1c and e reveal the hierarchical structure of the materials, which possesses submicro-scaled roughness from the nanofibers and nano-scale roughness due to the formation of PNIPAAm layer on RC nanofibers. Wenzel<sup>68</sup> reported that surface morphology or roughness assists in determining the macroscopic wettability of solid surface by magnifying the wettability levels to their extreme. As a result, the apparent surface wettability of PNIPAAm layer, either hydrophilicity or hydrophobicity, can be raised to a higher degree by the increased surface roughness.

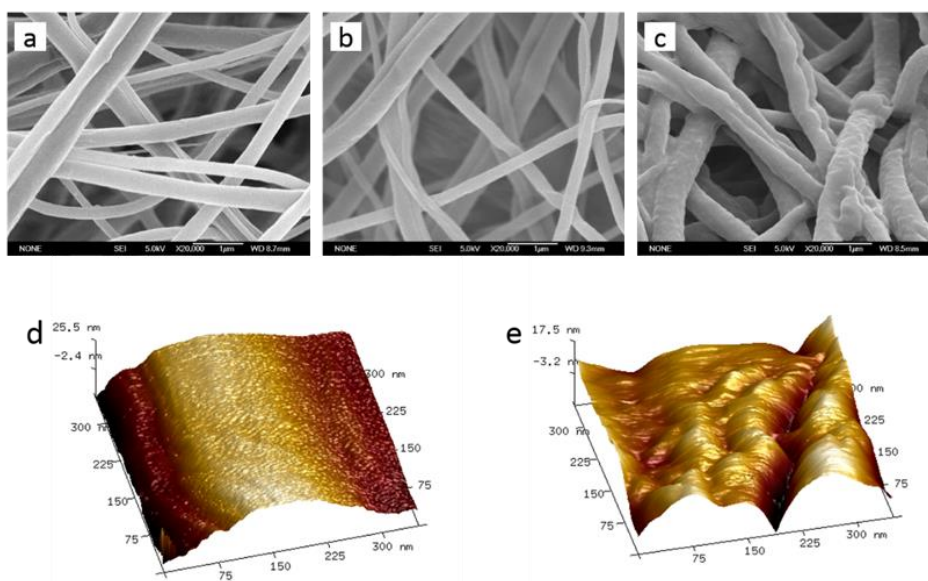


**Figure 3.1.** SEM images of CA nanofibers (a), RC nanofibers (b), and PNIPAAm-RC nanofibers (c); and AFM topography images of RC nanofibers before (d) and after (e)

PNIPAAm modification.

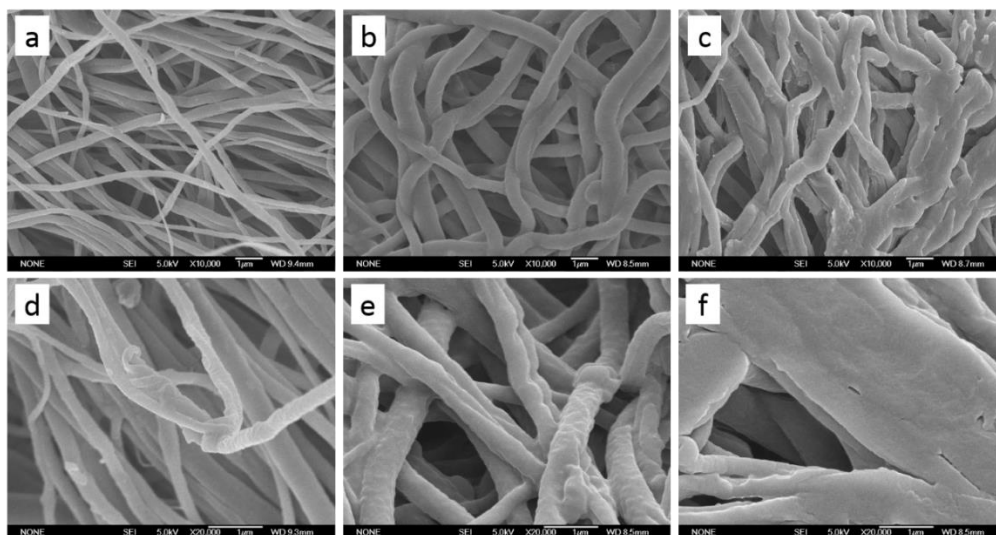


**Figure 3.2.** SEM images of PNIPAAm-modified nanofibers with different grafting duration: 2 h (a,d), 6 h (b,e), 10 h (c,f); a-c are SEM images with lower magnification (x10,000) and d-f are SEM images with higher magnification (x20,000).

FT-IR was employed to study differences among the CA, RC, and PNIPAAm-RC nanofibrous membranes (Figure 3.3). After hydrolysis, the characteristic ester band of CA at  $1750\text{ cm}^{-1}$  completely disappeared, which indicates that CA was thoroughly converted into RC.<sup>196</sup> After SI-ATRP, the primary amide band ( $-\text{C}=\text{O}$ ) at  $1640\text{ cm}^{-1}$  and the secondary amide band ( $-\text{N}-\text{H}$ ) at  $1540\text{ cm}^{-1}$  can be clearly identified in the spectrum, which means that the PNIPAAm has been successfully grafted onto the RC nanofibers.<sup>197-198</sup>

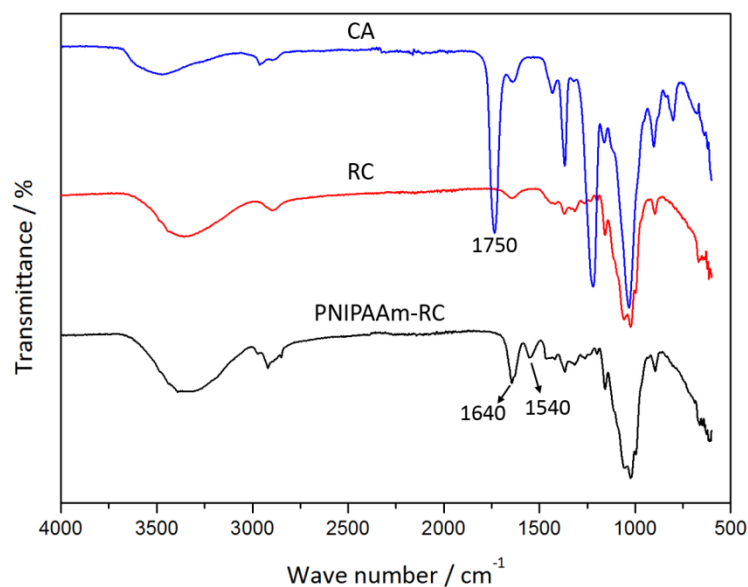


**Figure 3.3.** FTIR spectra of CA nanofibers, RC nanofibers, and PNIPAAm-RC nanofibers.

### 3.3.2 Thermo-Responsive Behavior

The pre-wetted PNIPAAm-RC nanofibers were further investigated by DSC for consecutive heating/cooling cycles, and the results were shown in Figure 3.4a. Repeated LCST transition was detected by the presence of the typical endothermic peaks at 29 °C on cooling experiment and exothermic peaks at 32 °C on heating experiment. These thermal transitions are mainly attributed to the forming and breaking of hydrogen bonds between polymer and water molecules along with the change of polymer configuration.<sup>13, 199-200</sup> When the PNIPAAm-RC nanofibers are heated to the LCST, the hydrogen bonds between PNIPAAm and water start to be broken due to the aggregating and collapse of the polymer chains. When temperature is lower than the LCST in the presence of water, the polymer chains stretch and the amide groups on the polymer brushes bind to the surrounding

water molecules by forming hydrogen bonds. The responsive stretching/shrinking behavior and the interaction with surrounding water of the grafted PNIPAAm brushes can be simulated as the illumination in Figure 3.4b. These structural changes occurring around the LCST directly cause the reversible change of surface wettability of the PNIPAAm-RC nanofibers, which can be observed from the static water contact angle (WCA) measured by switching the temperature at 22 °C and 40 °C. As shown in Figure 3.4c, the WCA was  $\sim 0^\circ$  at 22 °C, while a WCA of  $\sim 113^\circ$  could be observed at 40 °C. The phenomena of WCA oscillation between  $0^\circ$  and  $113^\circ$  indicated a transition between hydrophilic and hydrophobic, which is consistent to previous research.<sup>13</sup>

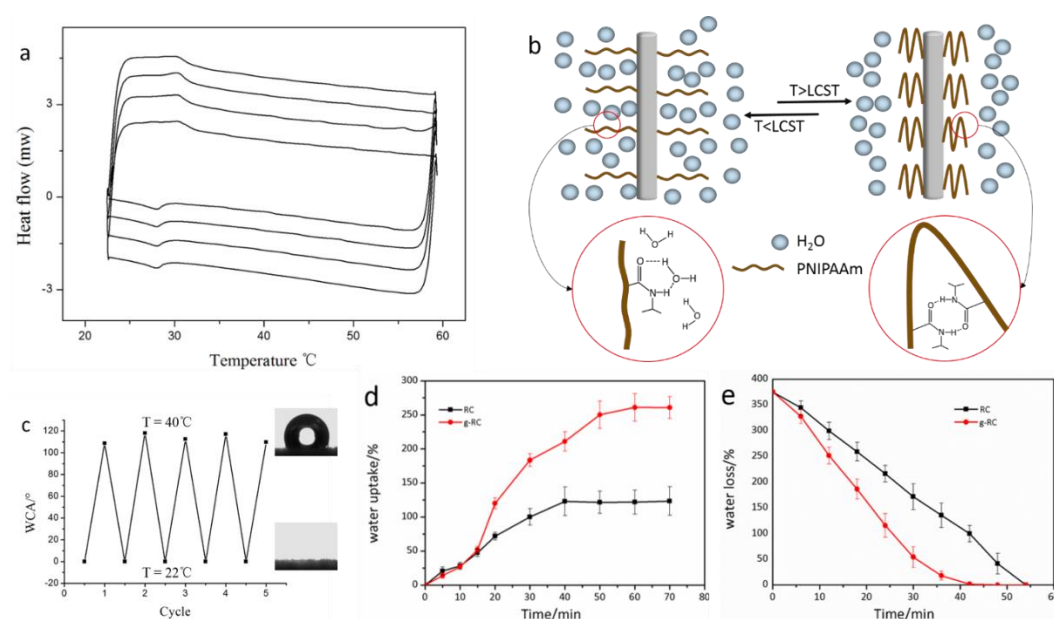


**Figure 3.4.** Reversible responsive behavior of PNIPAAm-RC nanofibers: DSC thermogram showing the thermo transition around the LCST in continuous cycles (a). Mechanism graph of the responsive interfacial phenomenon with water (b). Reversible WCA of PNIPAAm-RC nanofibrous membrane at 22 °C and 40 °C (inset: images of the droplets at the respective temperatures) (c). Water collection (d) and release (e) efficiency of the PNIPAAm-RC

nanofibers at 22 °C and 40 °C respectively (with unmodified RC nanofibers as reference).

The water collection/release performance of the as-prepared PNIPAAm-RC nanofibers was investigated to further illustrate the responsive polymer behavior and accompanied interfacial phenomenon with water. Water collection performance was studied in an artificial humid atmosphere (RH: ~95%) at room temperature (22 °C), and the water uptake along with the exposure time under humid atmosphere was plotted in Figure 3.4d. At the beginning of humidity exposure, the bare and PNIPAAm grafted RC nanofibers had the same weight increasing rate due to physical water adsorption from the fog. About 15 min later, water adsorbed by the PNIPAAm-RC nanofibers became enriched and formed hydrogen bonds with PNIPAAm brushes (referring to Figure 3.4b). And the hydrogen bonds between polymer chains and water molecules could limit the water lost in wind, which resulted in an increase of water uptake speed. Finally, under the experimental condition of this study (a small fog flow), the PNIPAAm-RC nanofibers showed a high water uptake of approximately 260% only after around one hour adsorption. While, the water uptake of bare RC nanofibers gradually tended to be stable at about 123% indicating the equilibration between physical water adsorption and evaporation lost in the wind. The high capacity of water collection of PNIPAAm-RC nanofibers at room temperature is attributed to the rough surface modified nanofibers and the hydrogen bonding between water molecules and polymer chains. Moreover, the PNIPAAm-RC nanofibers also showed fast water release when the temperature

was above LCST. Compared with the unmodified RC nanofibers, the PNIPAAm grafted RC nanofibers had a much higher water loss rate at 40 °C, as shown in Figure 3.4e. The easier water release of PNIPAAm-RC nanofibers is attributed to the shrinkage of the PNIPAAm brushes and the formation of intra-polymer hydrogen bonds when the temperature is above LCST, which squeezes the water molecules out of the PNIPAAm layer and thus increase the water evaporation rate.

The in-air oil contact angles (OCA) were measured at different temperatures. Figure 3.5a and 3.5b shows that the PNIPAAm-RC nanofibers are always oleophilic ( $\sim 0^\circ$ ) in air at both 22 °C and 40 °C. Therefore, the wettability of PNIPAAm-RC nanofibers at oil-water-solid interface (Figure 3.5 c-f) was mainly determined by the in-air WCA at different temperature. As shown in Figure 3.5c and 3.5d, the PNIPAAm-RC nanofibers exhibit a transition from superoleophobic ( $\sim 160.2^\circ$ ) to superoleophilic ( $\sim 0^\circ$ ) under water when the temperature increases from 22 °C to 40 °C. This apparent OCA ( $\theta_{OW}$ ) transition with temperature variation in aqueous environment can be explained by:<sup>201</sup>

$$\cos\theta_{OW} = \frac{\gamma_{OA}\cos\theta_O - \gamma_{WA}\cos\theta_W}{\gamma_{OW}} \quad (\text{Eq. 3.1})$$

Where  $\theta_W$  and  $\theta_O$  represent the WCA and OCA in air, respectively;  $\gamma_{OA}$ ,  $\gamma_{WA}$  and  $\gamma_{OW}$  are interface tensions of oil–air, water–air and oil–water interfaces, respectively. According to Eq. 3.1, it is reasonable that the in-air hydrophilic and oleophilic PNIPAAm-RC nanofibers show oleophobic property under water at the solid–water–oil interface at room temperature. This can be attributed to the generally much lower surface tension of oil/organic liquids than that of water,

which results in a commonly negative value of  $\gamma_{OA}\cos\theta_O - \gamma_{WA}\cos\theta_W$ . However, at a temperature above the LCST, the PNIPAAm-RC nanofibers become hydrophobic in air, which in turn makes the right hand of Eq. 3.1 always larger than 0, thus, makes the surface oleophilic. Similarly, the Eq. 3.1 can be transformed to Eq. 3.2 to predict the WCA ( $\theta_{WO}$ ) altering of the PNIPAAm-RC nanofibrous membrane in an oily environment, i.e., superhydrophilic ( $\sim 0^\circ$ ) at 22 °C but superhydrophobic ( $\sim 156.3^\circ$ ) at 40 °C (Figure 3.5 e, f).

$$\cos\theta_{WO} = \frac{\gamma_{WA}\cos\theta_W - \gamma_{OA}\cos\theta_O}{\gamma_{WO}} \quad (\text{Eq. 3.2})$$

As mentioned above, when the temperature is below the LCST,  $\gamma_{WA}\cos\theta_W$  and  $\gamma_{OA}\cos\theta_O$  are both positive and the value of the former one is normally larger than that of the latter one, which makes the  $\theta_{WO}$  always less than  $90^\circ$ . In contrast, at a high temperature of 40 °C,  $\theta_{WO}$  is always larger than  $90^\circ$  because of a definite negative value of the right hand of Eq. 3.2 resulting from the hydrophobicity and oleophilicity of PNIPAAm-RC nanofibers in air. Furthermore, combining the high surface roughness of the PNIPAAm layer, the PNIPAAm-RC nanofibers ultimately exhibit extreme dual-scale wettability at temperatures below/above the LCST, including under-water superoleophobic/superoleophilic and under-oil superhydrophilic/superhydrophobic.

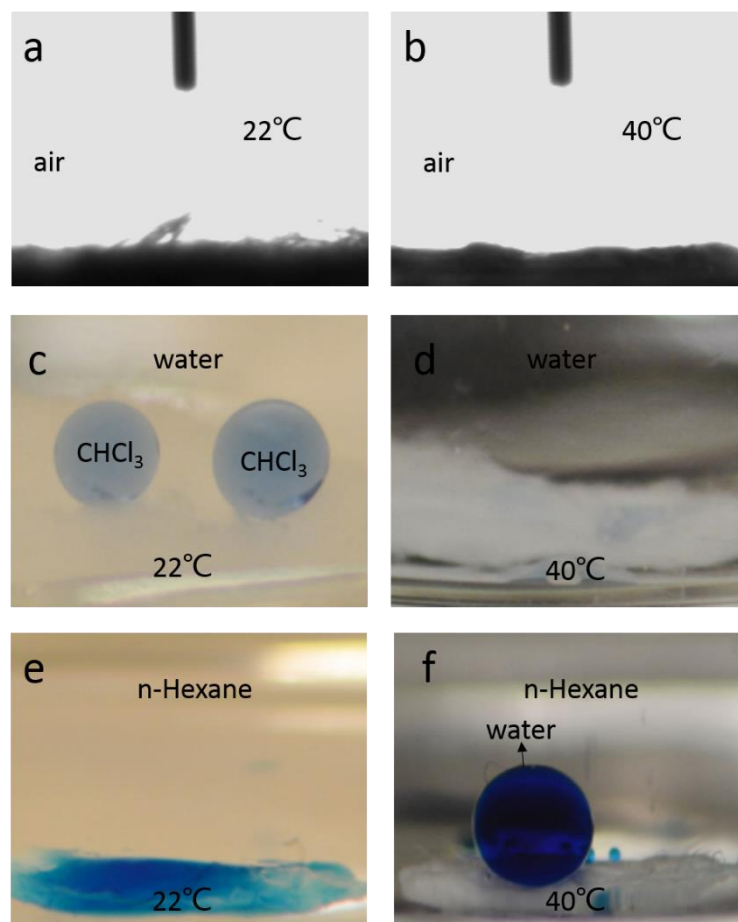


**Figure 3.5.** In-air OCA of the PNIPAAm-RC nanofibrous membrane at 22 °C (a) and 40 °C

(b). Oil and water wettability of the PNIPAAm-RC nanofibrous membrane at the oil-water-solid interface: under-water superoleophobic ( $\sim 160.2^\circ$ ) at 22 °C (c), under-water superoleophilic ( $\sim 0^\circ$ ) at 40 °C (d); under-oil superhydrophilic ( $\sim 0^\circ$ ) at 22 °C (e), under-oil superhydrophobic ( $\sim 156.3^\circ$ ) at 40 °C (f).

### 3.3.3 Thermo-responsive Controllable oil/water Separation

The obtained PNIPAAm-RC nanofibers were further used to absorb either oil or water from different oil-water mixture due to their temperature-responsive wettability. In a water-in-oil mixture, MB colored DI water was dropped into n-hexane. As shown in Figure 3.6a, after the PNIPAAm-RC nanofibers were

placed in the mixture under magnetic stirring at room temperature, blue water drops gradually disappeared and the nanofibers turned blue, indicating the efficient water absorption by PNIPAAm-RC nanofibers. To remove 0.04g of water, less than 0.01g of PNIPAAm-RC nanofibers were needed (Referring to Table 3.1). Additionally, the PNIPAAm-RC nanofibers absorbed with water can be easily recycled by being dried in an oven. Analogously, the oil removal from water by PNIPAAm-RC nanofibers was performed at 40 °C, and the procedure is shown in Figure 3.6b. Hence, by simply adjusting the operating temperature (below or above the LCST), the as-prepared PNIPAAm-RC nanofibers can be applied in dual-mode oil/water separation due to its responsive transition of wettability.

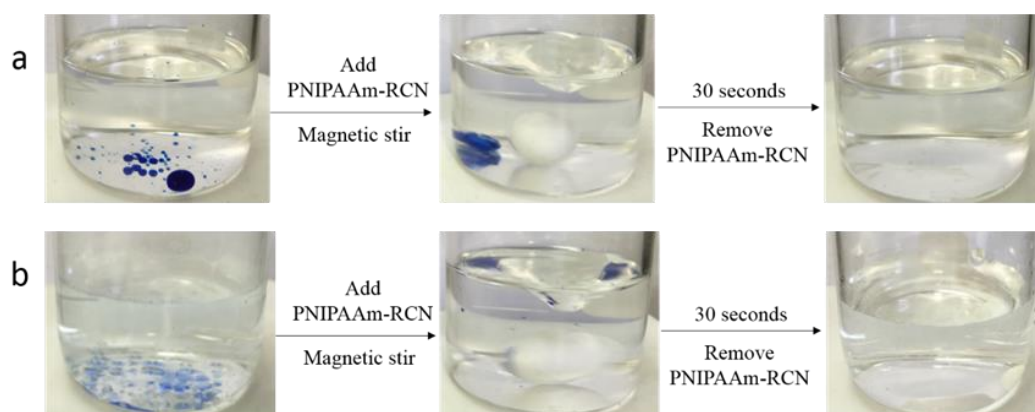


**Figure 3.6.** Water removal from water-in-oil mixture at 22 °C (a) and oil removal from oil-in-water mixture at 40 °C (b) by using the as-prepared PNIPAAm-RC nanofibers.

Moreover, the oil/water absorption capacities of the PNIPAAm-RC nanofibers were studied by measuring the absorption weight in five cycles. The water-in-oil mixture was made with DI water and n-hexane. Varied oils (including n-hexane, CHCl<sub>3</sub>, paraffin oil, silicone oil, peanut oil and gasoline) were used for preparing the oil-in-water mixtures, which were used to investigate the oil

absorption capacity and recycling property of the PNIPAAm-RC nanofibers. These mixtures were chosen to represent common pollutions from industrial drainage and daily emission. Table 3.1 shows the water and oil absorption capacities of the PNIPAAm-RC nanofibers (water uptake from water-in-oil mixture at 22 °C and oil uptake from varied oil-in-water mixtures at 40 °C) in weight percentage. It is obvious that the PNIPAAm-RC nanofibers show an excellent absorption capacity of about 4 times of its own weight for water from the water/hexane mixture at 22 °C, and also exhibit significant absorption capacities of about 3-5 times of its own weight for oils from oil/water mixture at 40 °C. Overall, the as-prepared PNIPAAm-RC nanofibers can be suitable for a wide range of oil/water separation with good capabilities. The specific absorption amount of the PNIPAAm-RC nanofibers may be determined by density, viscosity, or other physic-chemical properties of the absorbate.

**Table 3.1.** Absorption capabilities of the as-prepared PNIPAAm-RC nanofibers from different oil/water mixtures at 22 °C and 40 °C.

Mixture	Water-in-	Oil-in-water (40°C)					
	oil (22°C)	n-hexane	CHCl <sub>3</sub>	Paraffin oil	Silicone oil	Peanut oil	Gasoline
Absorbate	water						
Absorption capacity/%	440±22.0	346±22.1	496±29.8	318±20.3	332±29.3	295±21.0	276±19.8

It is noted that the PNIPAAm-RC nanofibers could also be reused for absorbing water and various oils with high capacities, which is significant for practical applications. After absorption, the PNIPAAm-RC nanofibers were rinsed using ethanol and acetone to remove the absorbates for the next absorption cycle. The varied absorption capacities are shown in Figure 3.7. As shown in curve A (water absorption at 22 °C), the water absorption had no remarkable decrease after five cycles, indicating an excellent reusability for water absorption from water-oil mixture. Significantly, oil absorption could be negligible in this process due to the superoleophobicity of the water absorbed PNIPAAm-RC nanofibers at room temperature. Additionally the PNIPAAm-RC nanofibers also showed great recycling properties for varied oil (curve B-G in Figure 3.7). For oils with strong volatility (n-hexane, CHCl<sub>3</sub> and gasoline, showed by curve B, C and D, respectively), the absorption capacities remained almost constant after five absorption cycles. For absorbates with poor volatility and high viscosity—paraffin oil, silicone oil and peanut oil (curve D, E and G, respectively), the absorption capacities had reduction after each absorption cycle. But still the absorption capacities can remain over 75% of the original after five absorption cycles.

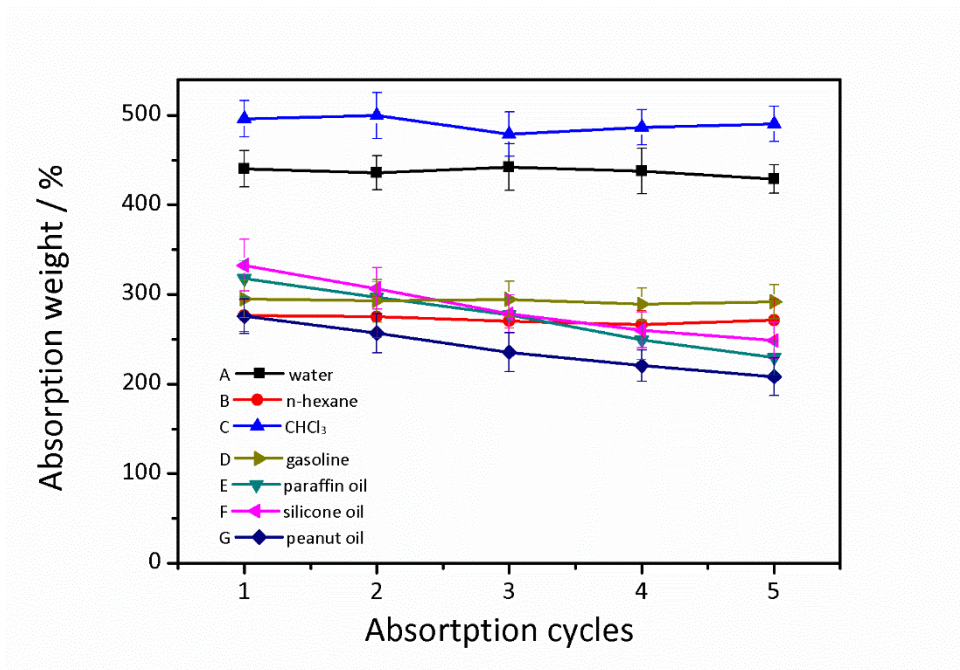


**Figure 3.7.** Absorption capacities of PNIPAAm-RC nanofibers in different cycles of absorption-desorption from varied mixtures.

As suggested by the results above, the as-prepared PNIPAAm-RC nanofiber can be suitable for the separation of various types of oil/water mixtures with both high absorption efficiency and easy recycling. This makes it a promising material to treat either oil-polluted water or water-polluted oil from both industrial drainage and daily emission.

### 3.4 Conclusions

In summary, the preparation of a thermo-responsive nanofibrous membrane through grafting PNIPAAm chains/brushes on the electrospun RC nanofibers via a surface-initiated atom transfer radical polymerization method has been demonstrated. The as-prepared PNIPAAm-RC membrane shows a switchable

wettability, which makes it a smart material with controllable oil/water separation function. As reported, the oil/water separation mode can be switched by simply changing the operating temperature. Benefiting from the large surface area provided by electrospun nanofibers, the efficiency and capacity of oil/water absorption were highly improved.

In addition, PNIPAAm brushes with more adaptive LCST can be synthesized by fine-adjusting the polymer characteristics, e.g., Mn and PDI, or grafting density.<sup>199, 202</sup> Furthermore, by copolymerization with other polymers or synergy with other molecules, the reported method may be extended to a variety of applications (e.g., drug delivery, chemical separation, ion exchange, and molecule detection).

## **Chapter 4**

# **Light-Responsive Nanoparticle/Polymer Composite Nanofiber Membrane to Manipulate Liquid Wetting with Antifouling Property: Synthesis, Characterization and Application**

It is challenging to explore a unified solution for the treatment of oily wastewater from complex sources. Thus membrane materials with flexible separation schemes are highly desired. Herein, a smart membrane was fabricated by electrospinning TiO<sub>2</sub> doped polyvinylidene fluoride (PVDF) nanofibers. The as-formed beads-on-string structure and hierarchical roughness of the nanofibers contribute to its super-wetting/resisting property to liquids, which is desirable in oil/water separation. Switched simply by UV (or sunlight) irradiation and heating treatment, the smart membrane can realize reversible separation of oil/water mixtures by selectively allowing water or oil to pass through alone. Most importantly, the as-prepared nanofiber membrane possesses outstanding anti-fouling and self-cleaning performance resulting from the photocatalytic property of TiO<sub>2</sub>, which has practical significance in saving solvents and recycling materials. This work provides a route for fabricating cost-effective, easily scaled up, and recyclable membranes for on-demand oil/water separation in versatile

situations, which can be of great usage in the new green separation technology.

## 4.1 Introduction

Oily wastewater yielded from offshore drilling, industrial production or household sewage poses threats to both the environment and humans.<sup>203-204</sup> Materials with effective oil/water separating capability are therefore strongly needed.<sup>205-206</sup> Based on interfacial science, materials with unique wettability, especially with hydrophobic/oleophilic<sup>192, 207-211</sup> or hydrophilic/underwater superoleophobic<sup>212-214</sup> surfaces, have been produced to offer solutions for separating oil/water mixtures without energy consumption. But the fixed wettability patterns of these materials do not have any flexibility in separation, which limits their application in the treatment of oily wastewater from diverse sources of pollution. Very recently, smart materials with surface wettability switch triggered by various stimuli such as pH value,<sup>38, 176</sup> electric field,<sup>177</sup> temperature,<sup>178</sup> light illumination,<sup>215</sup> and multiple stimuli<sup>39</sup> have attracted increasing attention. With elaborate design, extreme wettability switch can be realized for more efficient separation. However, fouling problems of smart materials during oil-removing processes were always intractable. Among various smart materials, titanium dioxide (TiO<sub>2</sub>) has been widely studied due to its photocatalytic property,<sup>216-217</sup> self-cleaning,<sup>218-219</sup> and photo-induced wettability change,<sup>47, 54</sup> all of which are desirable functions in smart oil/water separation.<sup>180</sup>

However, the less extreme wettability switch and the insecure coating adhesion may restrict its practical application. Blending nanoparticles into polymer matrix has been explored as one of the strategies to anchor nanoparticles from leaching out,<sup>220-221</sup> but the photocatalytic property of TiO<sub>2</sub> nanoparticles may cause damage to polymer matrix.<sup>222</sup> Polyvinylidene fluoride (PVDF) is among the most commonly used polymer incorporating with TiO<sub>2</sub> because of its outstanding antioxidation property, excellent resistance to chemicals and irradiation, favorable thermal stability, and good mechanical property.<sup>223-224</sup> Many studies have proved the anti-fouling ability of TiO<sub>2</sub>/PVDF composites under UV treatment,<sup>225-227</sup> but the extreme wettability switch between superhydrophobic/superoleophilic and superhydrophilic/underwater superoleophobic of TiO<sub>2</sub>/PVDF composites has rarely been realized. In chemical composition, both TiO<sub>2</sub> and PVDF have intrinsic hydrophobic properties but not extremely.<sup>54, 223</sup> To overcome this, the surface asperity should be designed skillfully for more extreme wetting or anti-wetting property. In this regard, electrospinning as a simple and low-cost technique can construct polymeric surface with various levels of roughness by regulating the fiber diameter which can be controlled by the polymer solution concentration, applied voltage and receipt distance.<sup>154, 183, 228</sup> Moreover, combined with doping of nanoparticles in an appropriate proportion, the surface can be further roughened to achieve super-wettability. Herein we report a unique structural design of TiO<sub>2</sub> doped PVDF (T-P) nanofiber membrane fabricated by electrospinning to realize a smart and reversible oil/water separation, triggered by UV (or sunlight) irradiation

and heating treatment. This is attributed to the light/heat-induced wettability switch of anatase  $\text{TiO}_2$ <sup>47, 54, 229-230</sup> combined with the as-formed highly roughened beads-on-string structure, which generate an extreme wetting state switching between superhydrophobic/superoleophilic and superhydrophilic/underwater superoleophobic. This switch is triggered by light and heat, and can be repeated for many cycles. To the best of our knowledge, the unique beads-on-string structure and the wetting state transition between superhydrophobicity and superhydrophilicity of such an electrospun  $\text{TiO}_2$ /PVDF binary composite has not been reported before. Likewise, the light-heat triggered reversible oil/water separation which requires such super-wetting/resisting switching behavior on a  $\text{TiO}_2$ /PVDF binary composite has also not been realized prior to our study. Moreover, the composite nanofiber membrane possesses excellent self-cleaning or anti-fouling property after a simple UV (or sunlight) treatment, which significantly improves its practical applicability. In this study, nano-sized  $\text{TiO}_2$  particles were precisely synthesized via a sol-gel process and evenly dispersed into a PVDF electrospinning solution. An appropriate proportion of  $\text{TiO}_2$  nanoparticles to PVDF plays an important role in fabricating T-P nanofiber membrane with satisfactory structure and efficient light responsiveness.

## **4.2 Experimental**

### **4.2.1 Materials**

Titanium tetraisopropoxide (TTIP, Aldrich 97%), polyvinylidene fluoride

(PVDF, Arkema, Kynar 761A), acetic acid (HAc, Aldrich 99%), hydrochloric acid (HCl, Aldrich 37%), dimethylacetamide (DMAc, Duksan Chemical 99.5%), and acetone (VWR International 99.8%) were used as received. Copper mesh (pore size: 75  $\mu\text{m}$ ) was firstly cleaned by ethanol and acetone in ultrasonic bath before use.

#### **4.2.2 Synthesis of $\text{TiO}_2$ gel**

The  $\text{TiO}_2$  nano-gel was prepared by the condensation of  $\text{TiO}_2$  nano-sol which was obtained by the hydrolysis of a TTIP hydrosol. TTIP (4 g) was firstly added dropwise into distilled water solution (10 ml) which contained HCl (1 wt.%) and HAc (0.5 wt.%) under vigorous stirring to form a hydrosol. Then, the obtained TTIP hydrosol was dropped into a beaker slowly along with adding of water (with temperature of 90  $^\circ\text{C}$ ) for 4h. The prepared milk-like sol was then cooled to 60  $^\circ\text{C}$ . Subsequently, a violent stirring was applied for 15 h until a transparent bluish sol was obtained. The mixture was then cooled to room temperature and stored for two weeks, after which the final  $\text{TiO}_2$  nano-sol was obtained with a 10 wt.% solid content of  $\text{TiO}_2$ . Finally, the above  $\text{TiO}_2$  sol was condensed by the heat evaporation of water to produce  $\text{TiO}_2$  nano-gel with a 32 wt.% solid content of  $\text{TiO}_2$ .

#### **4.2.3 Preparation of electrospun T-P nanofiber membrane**

Firstly, the prepared  $\text{TiO}_2$  nano-gel (0.25 g) was dispersed into 10 ml

DMAC/Acetone (3/1, w/w) solvent and the solution was treated by ultrasonic for 2 h. Then, 1 g of PVDF powder was added into the solution under a magnetic stirring which lasted for 12 h at room temperature (23 °C) to produce the electrospinning solution. An electrospinning setup (Micro & Technologies Expert, TL-Pro, Shenzhen, China) was used to fabricate nanofibers at room temperature (23 °C) with a positive voltage of 15 kV applied on the needle and a negative voltage of 2 kV applied on the collecting copper mesh. The distance between the spinneret and the collector was 20 cm. The solution flow rate was set at 1 ml/h through a syringe pump, and the ambient relative humidity was around 60%. The as-spun nanofiber membrane (the weight ratio of TiO<sub>2</sub> to PVDF is 8%) was dried at 80 °C for 30 min followed by a 12 h air-dry in dark to remove the residual solvent. T-P nanofiber membranes with TiO<sub>2</sub>/PVDF weight ratio of 2%, 4% and 6% were also prepared according to the same procedures. Pure PVDF nanofibers without TiO<sub>2</sub> doping were prepared as reference with strictly the same PVDF concentration of the electrospinning solution and operating conditions as above. The diameters of nanofibers of all the prepared samples were measured from their SEM images using the software ImageJ and the average diameter of each sample was calculated from the measurements of 20 nanofibers.

#### **4.2.4 Characterization**

The morphology of the as-prepared PVDF nanofiber with and without TiO<sub>2</sub> doping was observed using a field emission scanning electron microscopy

(FE-SEM, JSM-6335F, Japan) with a prior gold sputtering. The topography of the PVDF/TiO<sub>2</sub> nanofiber was observed utilizing atomic force microscopy (AFM, Veeco, USA) with pure PVDF nanofiber as reference. Transmission electron microscopy (TEM, Jeol JEM-2011, Japan) was used to observe the distribution of TiO<sub>2</sub> in PVDF nanofiber. Contact angle (CA) measurements were conducted with OCA20 (Data Physics, Germany). Fourier transform infrared (FT-IR, PerkinElmer Spectrum100, USA) was utilized to evaluate the anti-fouling and self-cleaning performance of the prepared PVDF/TiO<sub>2</sub> nanofiber membrane. Energy dispersive X-ray spectroscopy (EDX) detector attached to the scanning electron microscope was used to detect the surface Ti content on the membrane along with repeated UV-heat cycles.

#### **4.2.5 Oil/water separation**

To conduct the oil/water-removing process using the as-prepared T-P membrane before and after UV irradiation (in air, by 3 paralleled UV lamps, PHILIPS TL-D 18W, with a distance of 20 cm from the membrane), n-Hexane (dyed by solvent red) and deionized water (DI water, dyed by methylene blue) were mixed as oily water. The as-prepared T-P nanofiber membrane was anchored between two glass apparatuses to form a filter. A flask was placed under the filter to collect the liquid that can pass through the membrane. The layered oil/water mixture was poured slowly on the membrane directly (the pouring should be controlled at slow speed during the oil-passing process to avoid that too much

water is poured down first and blocks the oil passing through). The approximate fluxes of water and oil through the tested membrane were  $\sim 2.63 \times 10^4$  L/ m<sup>2</sup>h and  $\sim 3.12 \times 10^4$  L/ m<sup>2</sup>h respectively. Note that the membrane need a prior wetting by water before conducting the water passing/removing process after UV irradiation.

#### **4.2.6 Exact procedure for contact angle measurements**

The sample for contact angle measurement of the PVDF or T-P nanofiber membrane was prepared by attaching one piece of the as-spun membrane (with size 1x2 cm<sup>2</sup>) on a cleaned glass slide by double sided adhesive tape. The spin-coated T-P membrane was fabricated on a cleaned glass slide with rotate speed of 1600 rpm for 15 s followed by 3000 rpm for 5 s. The droplet volume of the testing liquid (DI water or chloroform) for contact angle measurements was 2  $\mu$ L. For the measurement of oil-in-water contact angle, the as-spun T-P nanofiber membrane was attached on the bottom of a quartz cuvette containing DI water, then 2  $\mu$ L of chloroform droplet was dragged by the needle tip to contact the surface of the T-P nanofiber membrane under water. Each value of the contact angle was averagely calculated from 5 repeated measurements.

#### **4.2.7 Investigation of self-cleaning property**

A piece of the prepared T-P nanofiber membrane with size of 2x2 cm<sup>2</sup> was stained by 0.1 ml of the ethanol solution (to ensure the even distribution and spreading on the membrane surface) of oleic acid (with concentration of 10 vol.%).

The stained membrane was then dried in an oven at 80 °C. The UV or sunlight irradiation was performed in a dry state in air. No rinse step was carried out by any solvent. The samples after UV or sunlight irradiation were directly used in the following observation.

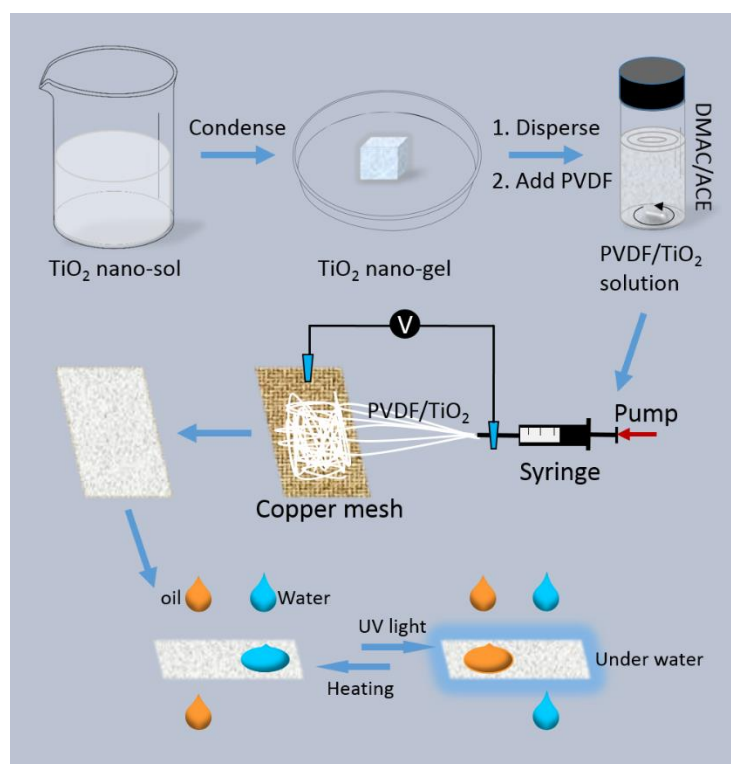
#### **4.2.8 Durability study**

The durability of the prepared T-P nanofiber membrane was studied by applying repeated UV and heating treatment on it. The gradual change of membrane morphology, hydrophobicity and Ti content after each light-heat cycle were recorded through SEM, WCA and EDX tests, respectively. The average diameter of the beads on the nanofibers were calculated from 20 measurements using the software ImageJ. The Ti content on the surface of the T-P membrane after each cycle of light-heat treatment were averagely calculated from 3 measurements in different areas.

### **4.3 Results and discussion**

Scheme 1 demonstrates the fabrication process of the TiO<sub>2</sub> doped PVDF (T-P) nanofibrous membrane and its smart oil/water separation triggered by UV irradiation and heating treatment. The electrospinning solution was prepared by simply mixing PVDF into TiO<sub>2</sub> dispersion which was treated beforehand by ultrasonic. The electrospinning process was conducted by a commercially

available setup. The fabrication process of T-P nanofibrous membrane is extremely simple and low-cost, which is easy to be scaled up.



**Scheme 4.1.** Illustration of the fabrication process of T-P nanofibrous membrane and its smart oil/water separation performance triggered by UV irradiation and heating.

The morphology of the prepared T-P nanofibrous membrane was studied by FE-SEM and AFM with the pure PVDF nanofibers as reference. Without TiO<sub>2</sub> doping, the PVDF nanofibers have an average diameter of ~795 nm (Figure 4.1a). Also, a mulberry-like surface of the PVDF nanofiber can be observed from Figure 4.1b and e. This formed highly roughened surface is attributed to the crystallization process of PVDF determined by thermal history, solvent, deposition method, et al.<sup>223, 231-234</sup> The low surface energy and the hierarchical surface roughness of PVDF nanofibrous membrane corporately lead to an outstanding hydrophobicity with a water contact angle (WCA) of ~140.6° (shown

by the inset in Figure 4.1b). Even so, the roughness is not sufficient to achieve superhydrophobicity which is generally defined with a WCA above  $150^\circ$ . However, after  $\text{TiO}_2$  doping ( $\text{TiO}_2/\text{PVDF}$  weight ratio is 8%), a superhydrophobic surface is obtained on T-P nanofiber membrane with a WCA of  $\sim 152.1^\circ$  (see the inset in Figure 4.1d). The WCA increase of  $\sim 8^\circ$  is possibly attributed to the increased surface roughness resulting from the decreased nanofiber diameter (with an average of  $\sim 120$  nm) and the unique beads-on-string structure. To be specific, the import of  $\text{TiO}_2$  lowers the entanglement and the spinnability of PVDF chains, thus caused a decreased diameter and an increased surface roughness, which lead to an improved air-trapping and a better water repellence.<sup>70, 235</sup> Moreover, a unique beads-on-string structure caused by the crystallization of PVDF and the lowered chain entanglement further increase the surface roughness and the hydrophobicity.<sup>236</sup> In additions, as shown by Figure 4.1f, a nano-scale roughness can be observed after the import of  $\text{TiO}_2$  NPs, which forms a hierarchical structure combined with the submicro-scale roughness provided by the T-P nanofibers and generated another possible factor for the hydrophobicity increase.<sup>68</sup> An apparent WCA comparison between T-P membranes produced by electrospinning and spin-coating is also shown by Figure 4.2. A narrower range of WCA switch between  $\sim 90^\circ$  and  $\sim 50^\circ$  can be observed on the smoother surface of spin-coated T-P membrane, which indicates the critical role played by surface spacial structure in constituting super-wetting surfaces. Compared to electrospun T-P nanofiber membrane, the spin-coated one exhibited a narrower range of WCA switch (only

between  $\sim 50^\circ$  and  $\sim 90^\circ$ ) and longer duration needed until it can be restored to hydrophobicity or hydrophilicity upon heating or UV treatment. The smoother morphology (or lower roughness) of the spin-coated T-P membrane compared to the electrospun one might be responsible for its narrower range of wetting state switch. Similarly, the lower sensibility of it towards UV and heating treatment might also be attributed to the less reception and internal reflection of the applied light and heat due to its lower exposed surface area and smoother morphology compared to the 3D porous structure formed on the electrospun T-P membrane.

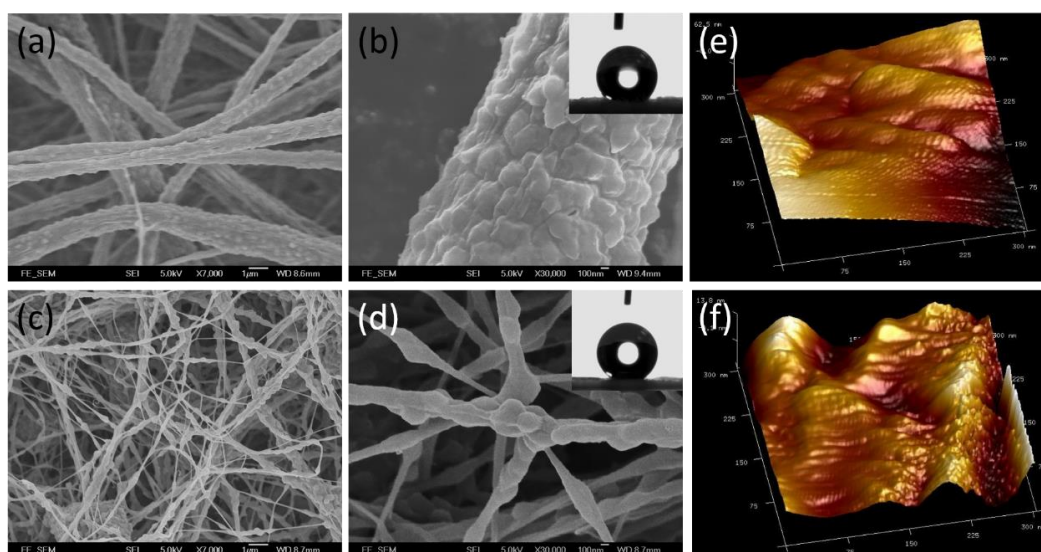


**Figure 4.1.** Morphology characterizations and WCAs of electrospun PVDF and T-P nanofibers. FE-SEM images of electrospun PVDF nanofibers with magnifications of x7,000 (a) and x30,000 (b); FE-SEM images of electrospun T-P nanofibers with magnifications of x7,000 (c) and x30,000 (d); AFM images of electrospun PVDF (e) and T-P (f) nanofibrous membrane; insets are the WCAs ( $\sim 140.6^\circ$  in b and  $\sim 152.1^\circ$  in d) of corresponding membranes.

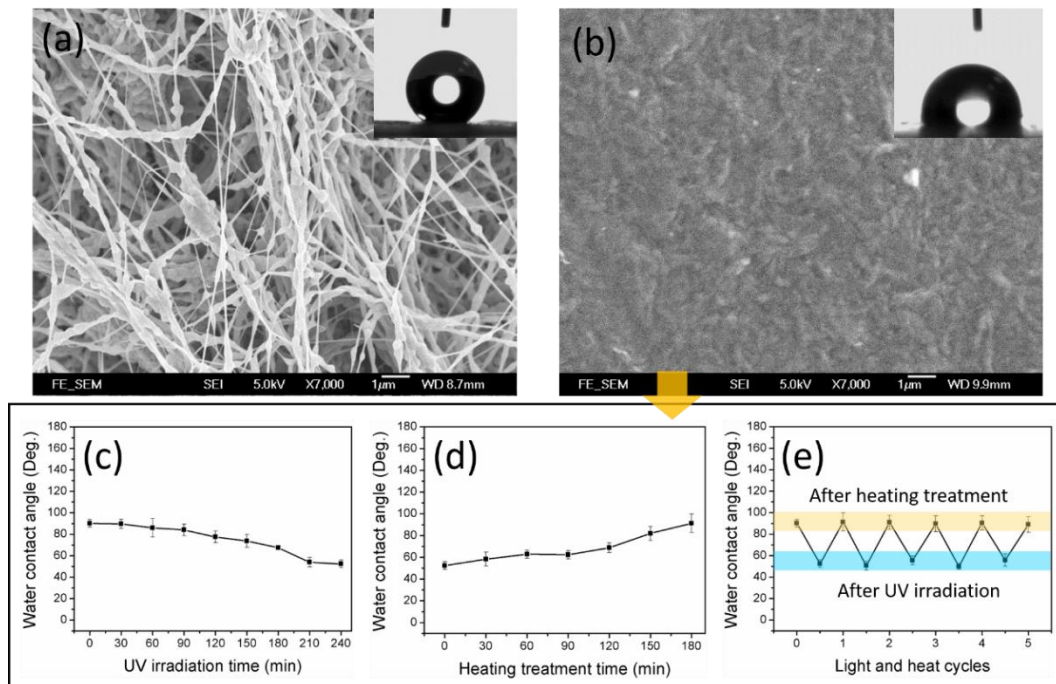


**Figure 4.2.** The morphology and WCA comparison between TiO<sub>2</sub>/PVDF membranes produced by electrospinning (a) and spin-coating (b); (c) WCA changes on the spin-coated T-P membrane with increasing time of UV irradiation; (d) hydrophobicity recovery indicated by WCAs of the spin-coated T-P membrane along with increasing time of heating treatment at 110 °C; (e) reversible WCA changes of spin-coated T-P membrane along with repeated light and heat cycles.

To observe the TiO<sub>2</sub> distribution in T-P nanofiber better, TEM was conducted. Figure 4.3 shows a series of TEM images of T-P nanofibers (with TiO<sub>2</sub> of 8%) with increasing magnifications. In Figure 4.3 b-d, the even distribution of TiO<sub>2</sub> can be observed both inner and on the surface of the nanofiber. The evenly distributed TiO<sub>2</sub> NPs in a polymer nanofiber can not only generate a nano-scale roughness on the surface (showed by Figure 4.1f), but also be anchored against leaching. In Figure 4.3e, fingerprint-like lattice of TiO<sub>2</sub> can be recognized with

diameters less than 10 nm (marked with white circles). XRD spectrum (Figure 4.4) of T-P nanofiber indicates the anatase phase of  $\text{TiO}_2$  which possesses superior light-induced superhydrophilicity and photocatalytic property.<sup>47</sup>

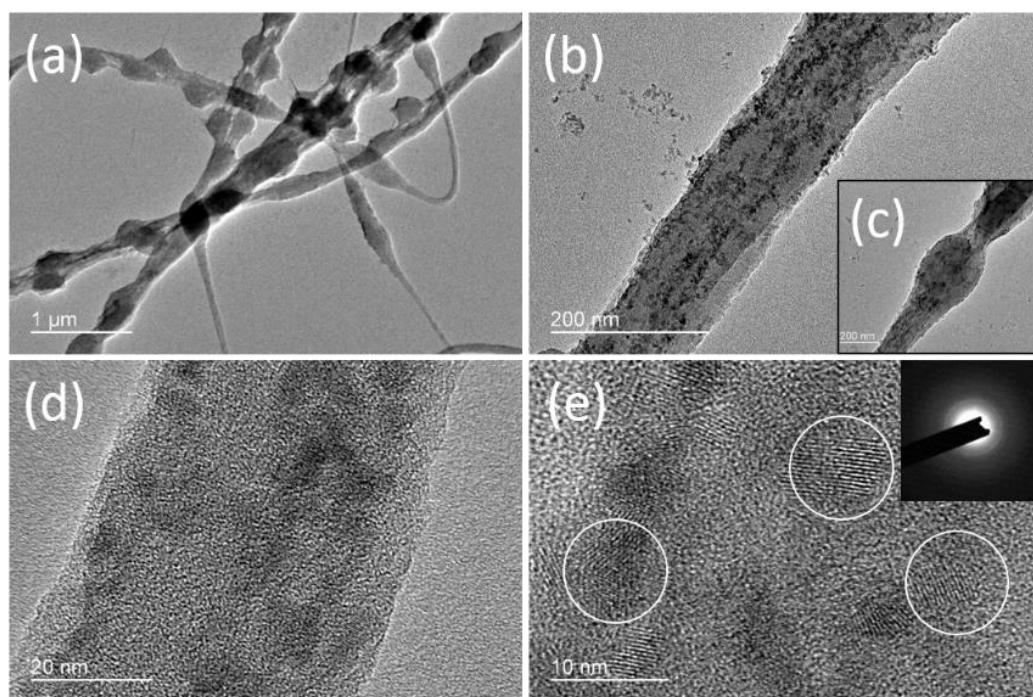


**Figure 4.3.** TEM images of T-P nanofiber with increasing magnifications (a, b, d and e). TEM

images showing the  $\text{TiO}_2$  distribution in a “string” (b) and a “bead” (c). Inset in (e) is the

SAED pattern of the observed  $\text{TiO}_2$  particles.

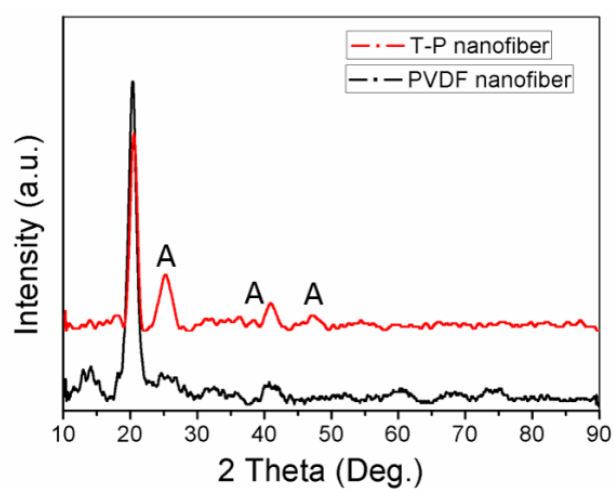


**Figure 4.4.** XRD spectrum of T-P nanofiber with pure PVDF nanofiber as reference. Letter ‘A’

marks the three peaks ( $25.4^\circ$ ,  $37.8^\circ$  and  $48.1^\circ$ ) of anatase  $\text{TiO}_2$ .

The UV-induced wettability change of T-P nanofibrous membrane (with TiO<sub>2</sub> doping ratio of 8%) was detected by measuring the WCAs along with increasing UV irradiation time, which is shown in Figure 4.5a. The prepared T-P nanofibrous membrane exhibited decreasing hydrophobicity along with the increasing UV irradiation time and turned superhydrophilic with a WCA of 0° after 90 min of UV irradiation, while the pure PVDF nanofibrous membrane showed no responsive change in WCA. It is worth noting that the UV-triggered superhydrophilic status can last several days in dark, which can ensure the stable performance in water passing separation. The UV-triggered water passing efficiency is also determined by the membrane thickness besides the UV irradiation time. As shown in Figure 4.6, thicker membrane showed slower flux increase along with the increasing UV irradiation, which suggests extended UV treatment for membranes with higher thickness. In addition to UV lamps, sunlight can also serve as the inducer to turn the T-P membrane into superhydrophilic. Under the exposure of sunlight with an average UV intensity of ~1 mW cm<sup>-2</sup>, the T-P membrane became superhydrophilic after ~189 min (Figure 4.7). Therefore, the conversion to superhydrophilic of T-P nanofiber membrane is easily accessible even in situations without handy artificial UV sources. To recover the superhydrophobicity of the prepared T-P nanofiber membrane, heating treatment in an oven was adopted. As shown in Figure 4.5b, a fast recovery of WCA from 0° to ~152° can be realized by heating treatment at 110 °C for around 70 min. This heat-induced transition from superhydrophilicity to superhydrophobicity is

attributed to the dehydration process triggered by heat and thus the decreased concentration of Ti-O-H bonds on the TiO<sub>2</sub> surface.<sup>230</sup> The switching ability of wetting state on the spin-coated T-P membrane was also investigated as a comparison to the electrospun T-P membrane. As shown in Figure 4.2 c-e, longer duration was needed until the spin-coated T-P membrane can be restored to hydrophobicity or hydrophilicity upon heating or UV treatment, which might be attributed to the less reception and internal reflection of the applied light and heat due to its lower exposed surface area and smoother morphology compared to the 3D porous structure formed on the electrospun T-P membrane. Therefore, the facile and time-saving features of the reversible transitions between water-soaking and water-resistant behaviors on the as-prepared T-P nanofiber membrane have favorable significance in practical or industrial applications.

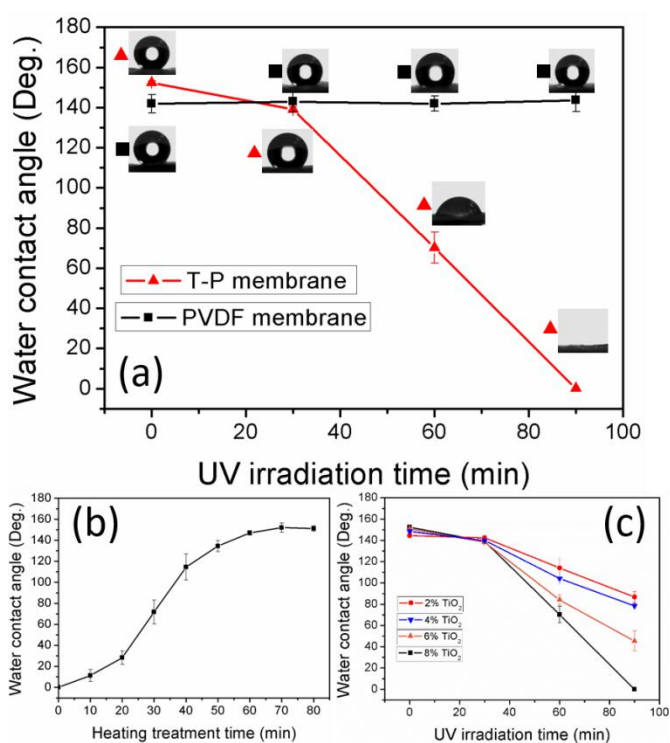


**Figure 4.5.** (a) UV-induced WCA change of T-P nanofibrous membrane (with TiO<sub>2</sub> of 8%)

after different UV irradiation time with pure PVDF nanofibrous membrane as reference. (b)

Heat-induced restoration of superhydrophobicity of T-P nanofibers (with TiO<sub>2</sub> of 8%). (c)

UV-induced WCA decrease of T-P nanofibers with different doping ratio of TiO<sub>2</sub>.

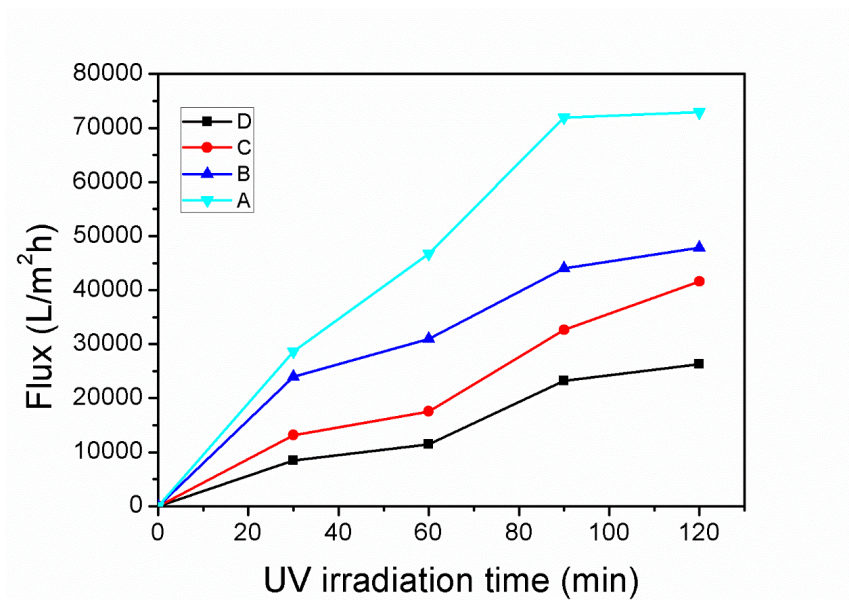


**Figure 4.6.** Water fluxes passing through the T-P membranes with different thicknesses along with increasing UV irradiation time. The membrane thicknesses are: A~5.6  $\mu\text{m}$ , B~9.7  $\mu\text{m}$ , C~17.6  $\mu\text{m}$ , D~32.1  $\mu\text{m}$ .

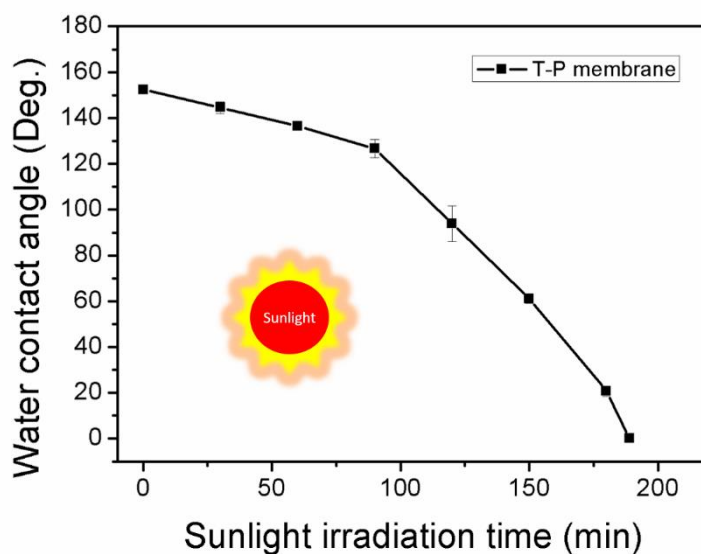


**Figure 4.7.** Sunlight-induced WCA change of T-P nanofibrous membrane (with TiO<sub>2</sub> of 8%)

after different sunlight irradiation time.

To fabricate T-P nanofiber membrane with satisfactory surface structure and sensitive wettability transition, the weight ratio of TiO<sub>2</sub> to PVDF should be set in perspective. As shown in Figure 4.8, weight ratio of TiO<sub>2</sub>/PVDF has an apparent effect on the morphology of electrospun T-P nanofibers. With a low doping ratio (2%, Figure 4.8a) of TiO<sub>2</sub>, the entanglement of PVDF polymer chains has not been distinctly lowered, which retains large diameter of the obtained nanofibers. Along with the increasing doping ratio (4% and 6 % from Figure 4.8b,c respectively), more nanofibers with small diameters (around 100 nm) and structured with beads and strings could be observed, but in both images there were still large portions of tangled polymer chains that were difficult to form separated nanofibers. However, when 8% of TiO<sub>2</sub> was doped, the obtained T-P nanofibers were mostly separated and had more homogeneous diameter distribution (Figure 4.8d). With further raised TiO<sub>2</sub> doping ratios (more than 10%), continuous jetting behavior from spinneret could hardly be observed, which indicates the thoroughly jeopardized entanglement of polymer chains due to the excess doping ratio of TiO<sub>2</sub> NPs. For the feature of sensitive wettability transition, T-P nanofiber membrane with TiO<sub>2</sub> doping ratio of 8% showed the fastest UV response, namely, shortest UV irradiation time was needed to reach superhydrophilic status compared to samples with TiO<sub>2</sub> doping ratio of 2%, 4% and 6% (Figure 4.5c). Therefore, with consideration of both qualified structure and efficient wettability

manipulation, the doping ratio of TiO<sub>2</sub> towards PVDF should be controlled around 8%.

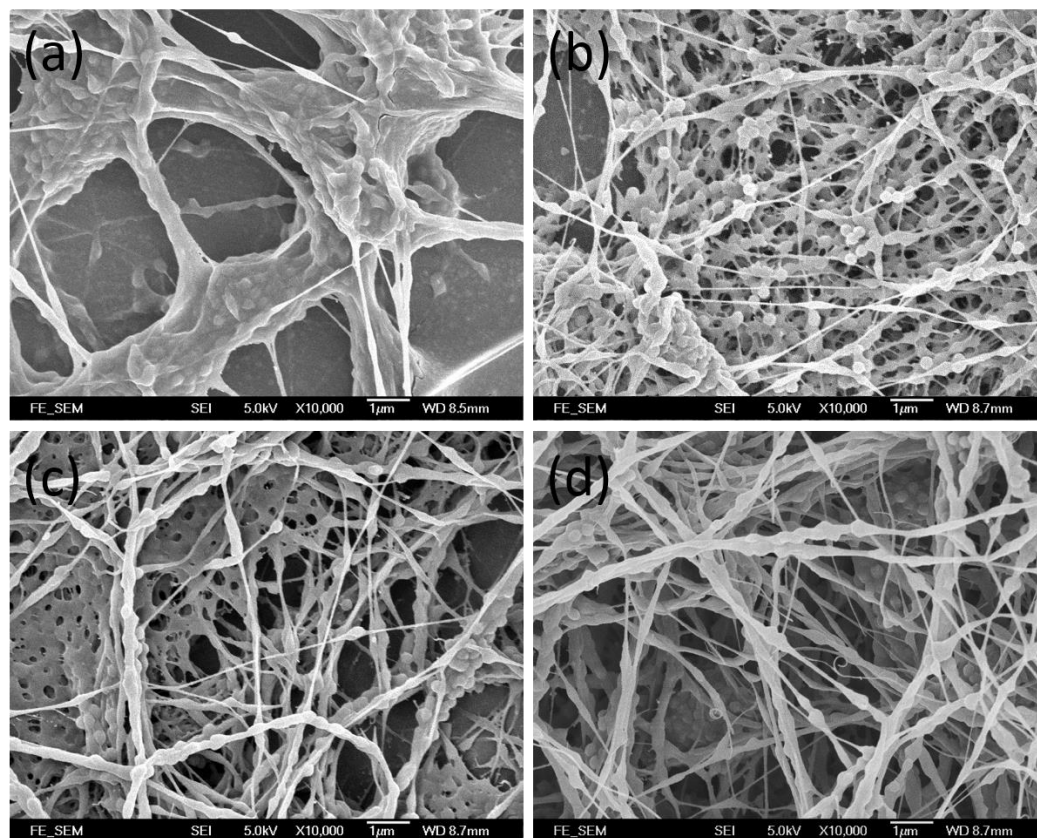


**Figure 4.8.** FE-SEM images showing the morphologies of T-P nanofiber membranes with TiO<sub>2</sub>/PVDF weight ratio of 2% (a), 4% (b), 6% (c), 8% (d).

The light and heat triggered, extreme wettability change of the prepared T-P nanofiber membrane between superhydrophobicity (>150°) and superhydrophilicity (0°) can sustain for many cycles of UV irradiation and heating treatment (Figure 4.9a). Before UV irradiation or after heating treatment for sufficient time, a formed nearly spherical shape of water droplet with a WCA of ~152.1° (the left photo in Figure 4.9b) and a thoroughly disappeared oil droplet with an OCA of 0° (the middle photo in Figure 4.9b) on the surface illustrates a

superhydrophobic and superoleophilic property of the prepared T-P nanofiber membrane in air. This high affinity of the prepared T-P membrane towards oil in air is mainly attributed to the lower surface tension of oil (generally below 30 mN/m) compared to PVDF (with surface energy of 33.8 mN/m).<sup>237-238</sup> Furthermore, the 3D roughness formed by the beaded nanofibers and the hierarchical structure of the T-P membrane lead to its superoleophilicity. Even under water, the similar superoleophilicity can be observed on the T-P membrane (the right photo in Figure 4.9b). In contrast, a superhydrophilic property can be detected after UV irradiation by a fully penetrated water droplet into the membrane. Meanwhile, a spherical oil (chloroform) droplet with an OCA of  $\sim 158.3^\circ$  formed on the membrane under water indicates an under-water superoleophobicity. The optical under-water OCAs ( $\theta_{OW}$ ) on the T-P membrane can be explained by:<sup>201</sup>

$$\cos\theta_{OW} = \frac{\gamma_{OA}\cos\theta_O - \gamma_{WA}\cos\theta_W}{\gamma_{OW}} \quad (\text{Eq. 4.1})$$

Wherein  $\gamma_{OA}$ ,  $\gamma_{WA}$  and  $\gamma_{OW}$  represent interface tensions of oil–air, water–air and oil–water interfaces, respectively;  $\theta_W$  and  $\theta_O$  are the WCA and OCA in air, respectively. According to equation (1), when the membrane is hydrophobic and oleophilic,  $\gamma_{OA}\cos\theta_O - \gamma_{WA}\cos\theta_W$  is always positive indicating an under-water oleophilic property shown in the right photo of Figure 4.9b. However, when the membrane is both hydrophilic and oleophilic (with both the WCA and OCA of  $0^\circ$  shown in the top row of Figure 4.9c),  $\gamma_{OA}\cos\theta_O - \gamma_{WA}\cos\theta_W$  is almost always negative because of the generally much lower surface tension of oil than that of

water. Therefore, the under-water oleophobicity (the top-right photo in Figure 4.9c) can be expected. Combined with the highly roughened surface of the T-P nanofibrous membrane, the extreme oil repellence or superoleophobicity under water is also reasonable. Moreover, the repeated contacting and leaving motion of the oil droplet dragged by the needle tip indicates an extremely low adhesion force between the oil droplet and the prepared T-P membrane (see the bottom row of Figure 4.9c). The excellent under-water oil repellence not only ensures a strict separation of the oil/water mixture but also minimizes the fouling effect caused by oil adhesion. The stability regarding the TiO<sub>2</sub>-catalyzed photochemical oxidation (or ageing) of the PVDF host fibers was also under our consideration. As shown by Figure 4.10, the overall morphology and superhydrophobicity could be well retained after 5 cycles of UV-heat cyclic treatment, but showed apparent damage after 10 cycles. However, frequent UV or heat treatments are hardly needed in practical use because each of the wetting status (superhydrophilicity or superhydrophobicity) can last for a long time once triggered.

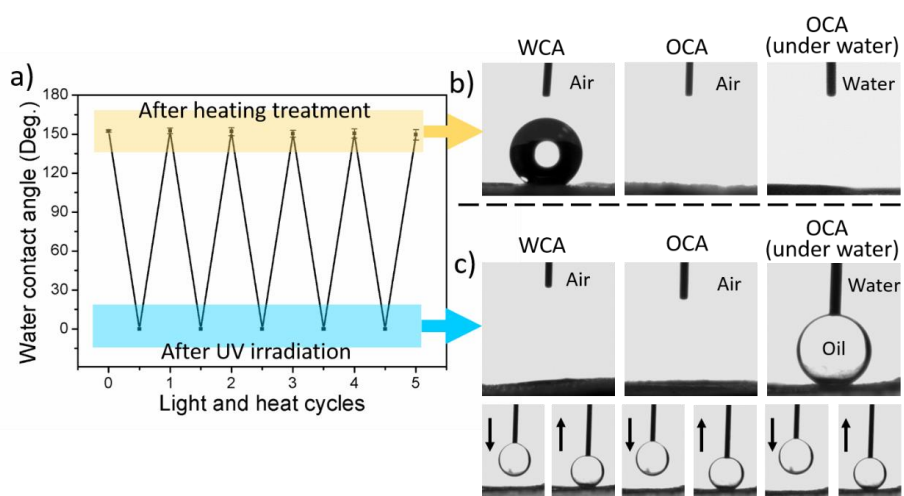


**Figure 4.9.** Light-heat induced wettability change of the prepared T-P nanofiber membrane. (a)

Reversible WCAs of the T-P nanofiber membrane in 5 cycles of UV irradiation and heating treatment; (b) the static shape of water and oil droplets on the T-P nanofiber membrane after heating; (c) the static shape of the water droplet and the under-water oil droplet on the T-P nanofiber membrane; the bottom row in (c) demonstrates three cycles of contacting and leaving motion of the oil droplet dragged by the needle tip under water.

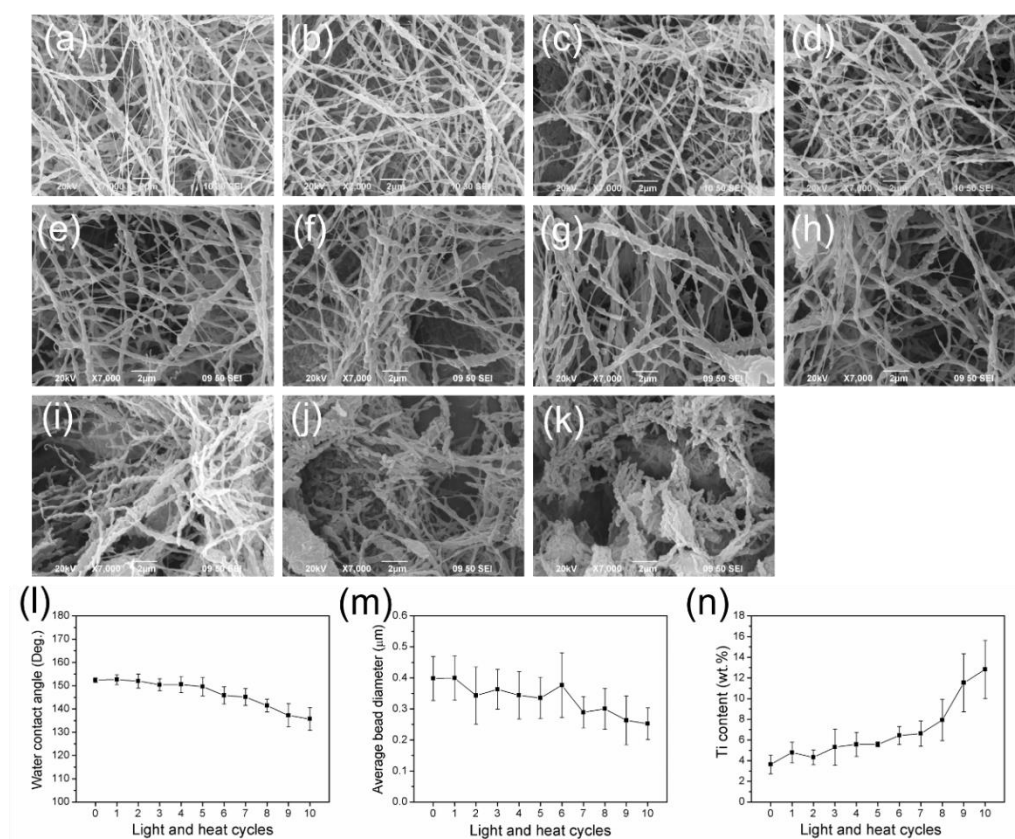


**Figure 4.10.** SEM images showing the UV-induced TiO<sub>2</sub>-catalyzed photochemical oxidation (or aging) of the T-P nanofiber membrane after 0-10 cycles (a-k, respectively) of UV-heat cyclic treatments, and (l-n) shows the corresponding changes of WCA, average bead diameter, and Ti content on the surface of the T-P nanofiber membrane.

The fracture of the T-P nanofibers caused by UV-induced photochemical oxidation occurs from thinner nanofibers to thicker ones. After 5 cycles of UV-heat treatment, the overall morphology (with only a few of thin nanofibers

fractured) and superhydrophobicity (with WCA of  $\sim 150.3^\circ$ ) of the T-P nanofiber membrane can be well retained. However, apparent damage can be observed on the morphology (with the fracture of thick nanofibers shown in Figure 4.10 i-k) after 8-10 cycles of UV-heat treatments. The decrease of WCA and bead diameter along with increased UV-heat cycles (Figure 4.10 l-m) can indirectly indicate the damage of T-P nanofibers. The increasing Ti content obtained from EDX test indicates the increasing exposure of  $\text{TiO}_2$  NPs on the nanofiber surface caused by  $\text{TiO}_2$ -catalyzed photochemical oxidation induced by UV. In practical use, nevertheless, frequent UV or heat treatments are hardly needed because each of the wetting status (water-wetting or water-resisting) can last for a long time once triggered.

The light and heat induced smart oil/water separation of the as-prepared T-P nanofibrous membrane was investigated using n-Hexane (red)/D.I. water (blue) as the oil/water mixture. As shown in Figure 4.11a, the oil/water mixture was separated with the oil phase passing through and the water phase being blocked before UV irradiation or after heating restoration. A reverse separation occurred with the water phase passing through and the oil phase being blocked after the T-P membrane underwent a UV irradiation (Figure 4.11b). Both types of separation, water passing or oil passing, are highly efficient without any leakage of unexpected liquid, which can be distinguished by the complete separation of the two purely colored liquids. This smart passing control of water and oil switched by UV and heat endows the prepared T-P nanofibrous membrane an on-demand

oil/water separation function to adapt to different separation situations and requirements such as separation of water- or oil-upper mixtures, separation of oil-in-water or water-in-oil mixtures, and recycling requirements of either water or oil. Furthermore, two pieces of the same T-P membranes with different treatment (UV or heating) and thus opposite wetting preference can be combined in one separation system to recycle both water and oil as reported by Liu et al<sup>239</sup> with the advantage that only one fabrication technique is needed.

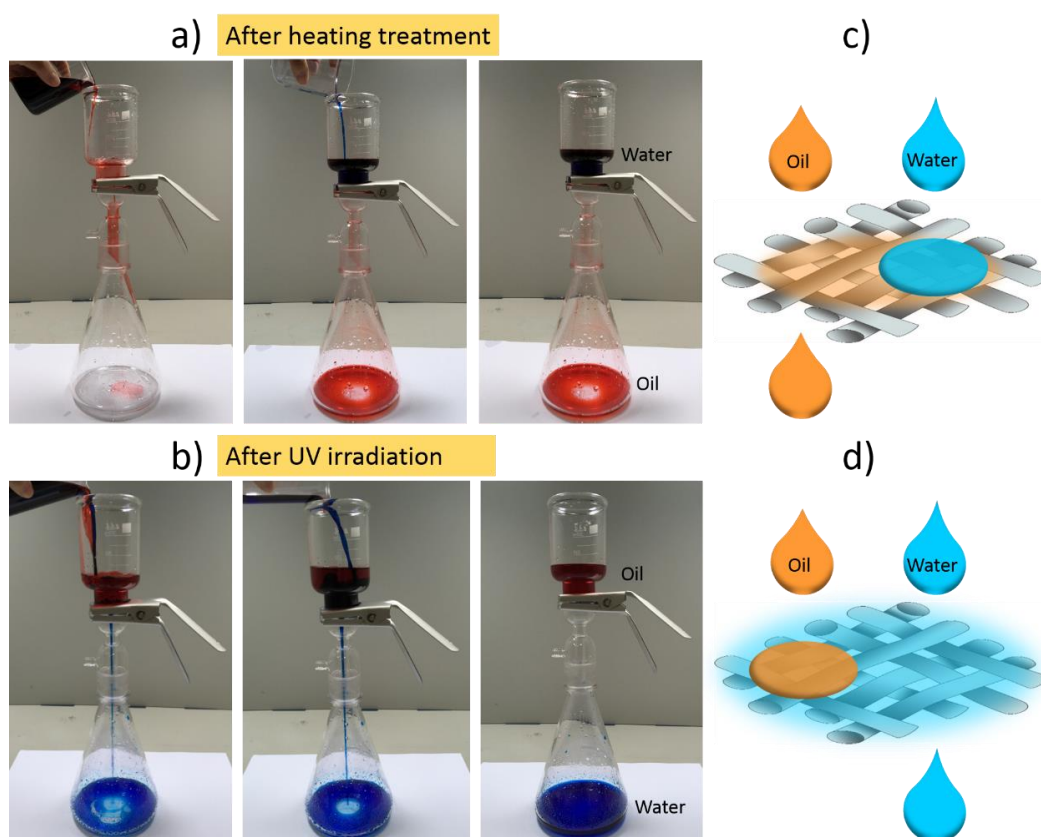


**Figure 4.11.** Light (b) and heat (a) induced oil/water separation by the T-P nanofiber membrane. (c) Schematic demonstration of the oil/water separation process before UV irradiation or after heating treatment; (d) schematic demonstration of the oil/water separation process after UV irradiation.

The self-cleaning behavior of the prepared T-P nanofiber membrane under UV irradiation was also studied. As for traditional oil/water separation membranes, fouling issues arise from the oil adhesion severely restrict the repeated and long-term use of the membranes.<sup>240-242</sup> In contrast, the TiO<sub>2</sub> used in our study endows the T-P membrane a feature of excellent anti-fouling and self-cleaning due to its photocatalytic degradation property towards organic compounds. In this study, oleic acid was used as the oily pollutant to detect the anti-fouling property of the T-P nanofiber membrane. As shown in Figure 4.12a, after stained by oleic acid, peaks at 2923, 2852 (ascribed to the stretching vibration of –CH<sub>3</sub> and –CH<sub>2</sub> respectively), and 1746 cm<sup>-1</sup> (characteristic ester band) appeared in the FTIR spectrum. However, when the stained membrane was irradiated by UV-light for 3 h, these three peaks of oleic acid disappeared completely, which indicates a photocatalytic decomposition behavior of TiO<sub>2</sub> towards the oleic acid. A gradual elimination of oleic acid on the surface of the stained T-P membrane with increasing time of UV irradiation from 0 h to 3 h was also recorded by FTIR (see Figure 4.13). It is shown that with the increasing time of the UV irradiation, a gradually declining intensity of the characteristic peaks of oleic acid can be observed. As a reference, pure PVDF nanofiber membrane exhibited no self-cleaning property with all the characteristic FTIR peaks of oleic acid retained (see Figure 4.14) on the membrane surface after the UV irradiation for the same time. Moreover, FE-SEM was also conducted to observe the difference presented on the top surface of the contaminated T-P nanofiber membrane before and after

UV irradiation. As can be seen in Figure 4.12b and c, the oleic acid that nearly covered the membrane was mostly cleared only by the photocatalytic degradation behavior of TiO<sub>2</sub> without rinsed by any solvent. Similar to superhydrophilic conversion, the self-cleaning property can also be triggered by sunlight. As shown in Figure 4.15, it takes 3.5 h for T-P membrane to degrade the same amount of adherent oleic acid under sunlight with average UV intensity of  $\sim 1 \text{ mW cm}^{-2}$ . The underlying mechanism of the pollutant (such as organic oil) degradation is the photocatalytic property of TiO<sub>2</sub> NPs. After UV irradiation, reactive oxygen species with strong redox activity are generated due to the electron excitation and transition. These as-formed reactive oxygen species can degrade organic compounds into H<sub>2</sub>O, CO<sub>2</sub> and other small molecule compounds (as illustrated by Figure 4.12d). This smart anti-fouling and self-cleaning behavior of the T-P membrane may be of great significance for practical application by reducing the use of solvent and decreasing the recycling cost. Therefore, the light/heat-induced wettability change and the photocatalysis property, which are considered as the two most attractive features of TiO<sub>2</sub>, were utilized conjunctively in this study.

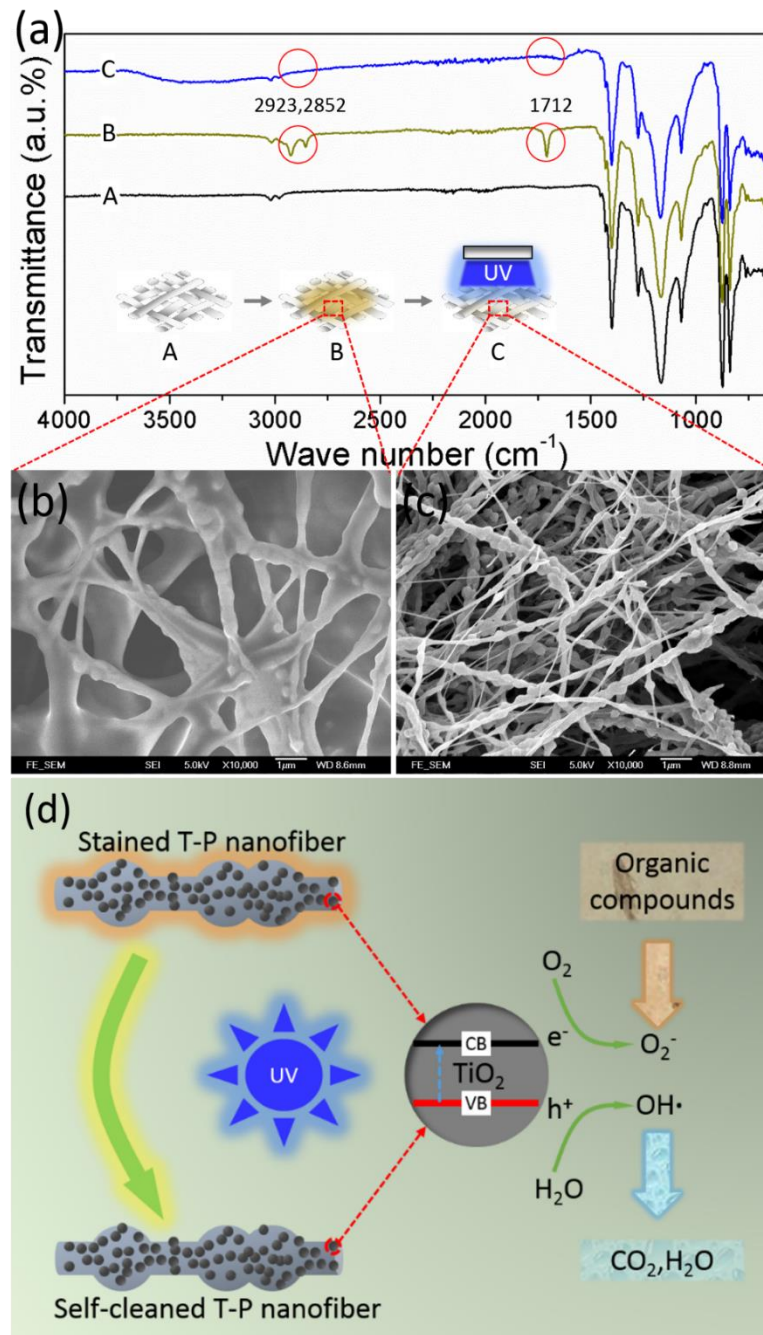


**Figure 4.12.** Anti-fouling and self-cleaning behavior of the prepared T-P nanofiber membrane.

(a) FTIR spectrum showing the chemical component difference among the T-P membrane before stained, after stained by oleic acid, and the stained T-P membrane treated by UV irradiation; FE-SEM images showing the top surface of the stained T-P membrane before (b) and after (c) UV irradiation. (d) Illustration of the under-UV self-cleaning behavior of the prepared T-P nanofibers and the photocatalytic mechanism of TiO<sub>2</sub> NPs.

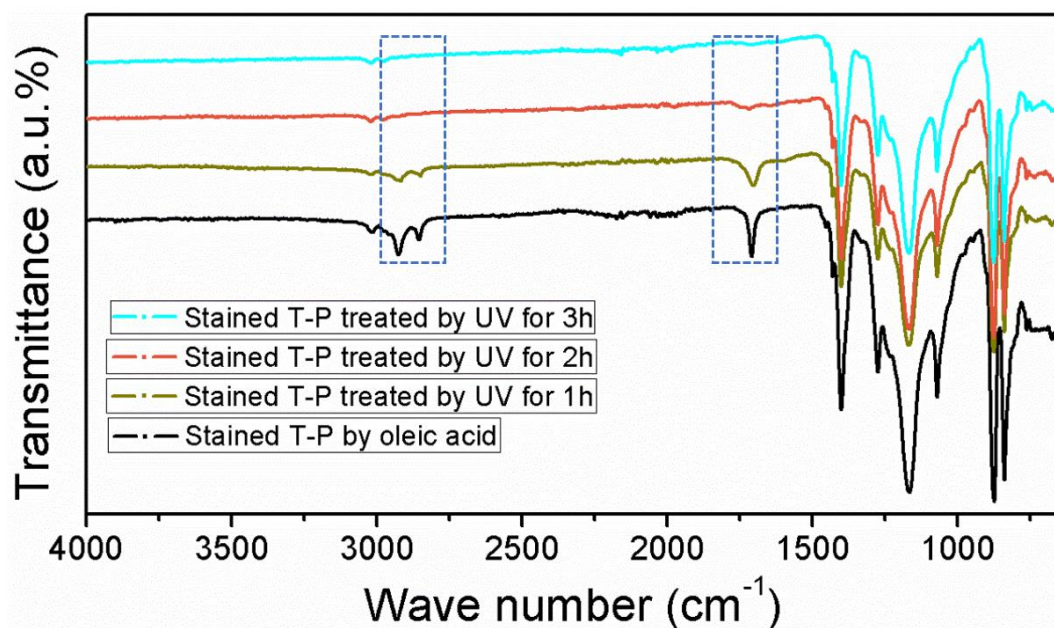


*Figure 4.13.* FTIR spectrums of the stained T-P nanofibers with subsequent UV irradiation for 0-3 hours.

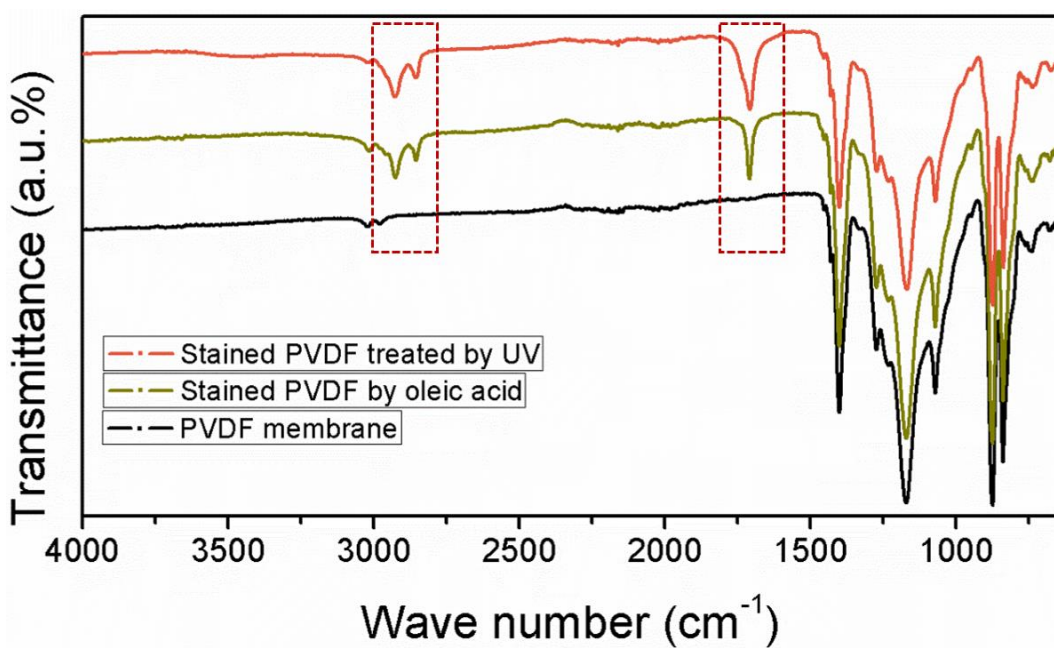


*Figure 4.14.* FTIR spectrums of PVDF nanofiber membrane, oleic acid stained PVDF nanofiber membrane, and oleic acid stained PVDF nanofiber membrane with subsequent UV irradiation for 3 hours.

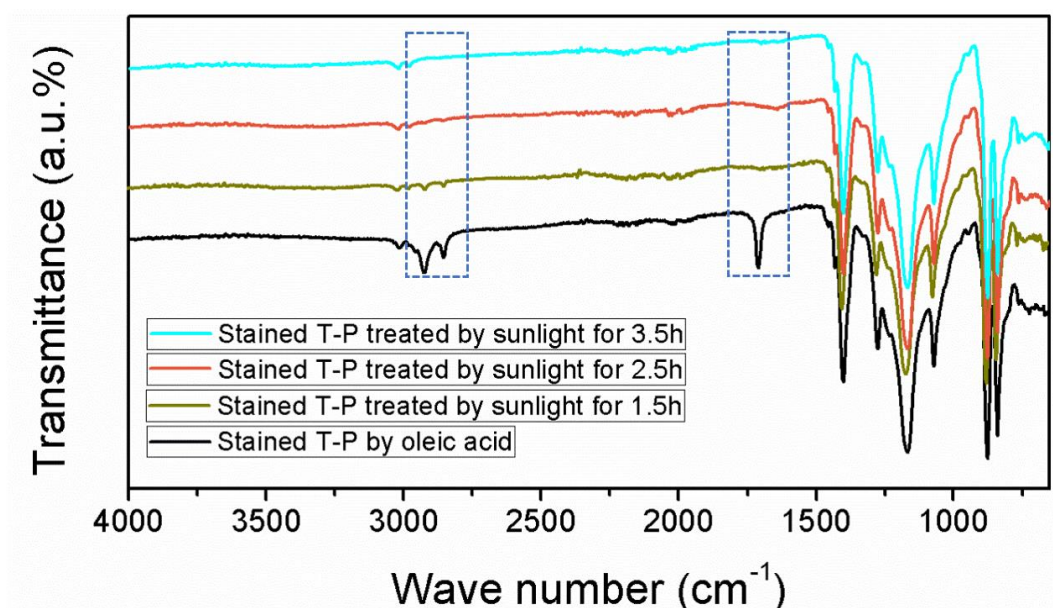


*Figure 4.15.* FTIR spectrums of the stained T-P nanofibers with subsequent sunlight irradiation for 0-3.5 hours.

## 4.4 Conclusions

In this chapter, a cost-effective TiO<sub>2</sub> doped PVDF nanofiber membrane has been successfully fabricated by electrospinning. The as-prepared nanofibers had unique beads-on-string structure and formed highly roughened top surface. Switched by simple UV irradiation and heating treatment, the TiO<sub>2</sub>/PVDF membrane can exhibit transition between superhydrophobic/superoleophilic and superhydrophilic/underwater superoleophobic states, which can realize an on-demand oil/water separation by controlling the passing of water or oil. The transitions are easily manipulated, sensitive and reversible for many times. More importantly, this TiO<sub>2</sub>/PVDF membrane possesses excellent anti-fouling property under UV irradiation by automatically removing the oil stain from the surface,

which is significant in saving solvents and recycling materials. Hence, this recyclable, easily scaled-up, and controllable smart nanofiber membrane can provide solutions to complex and industry-scale oily water treatment.

## Chapter 5

### **Biomimetic Surface with Light-Induced Superhydrophilic Bumps to Manipulate the Directional Condensation of Water: Synthesis, Characterization and Application**

To develop an efficient water collecting surface that integrates both fast water capturing and easy drainage properties is of high current interest for addressing global water issues. Herein, a superhydrophobic surface was fabricated on cotton fabric via manipulating both the surface roughness and surface energy. This was followed by a subsequent spray coating of TiO<sub>2</sub> nano-sol that created light-induced superhydrophilic bumps with a unique raised structure as the result of interfacial tension of the TiO<sub>2</sub> nano-sol sprayed on the superhydrophobic fiber surface. These raised TiO<sub>2</sub> bumps induce both wettability gradient and shape gradient, synergistically accelerating the water coalescence and water collection. The in depth study revealed that the quantity and the distribution of the TiO<sub>2</sub> had a significant impact on the final water collection efficiency. This inexpensive and facilely fabricated fabric biomimicks the desert beetle back and the spider silk that are capable of fog harvesting without additional energy consumption.

## 5.1 Introduction

Increasing attention has been paid to water capturing technology since 20<sup>th</sup> century because of more serious water shortage problems throughout the world, especially in those inhabited deserts and arid regions. The rainfalls in such areas are scarce, some animals and plants rely on fog and humid air as the major source of water. *Stenocara* beetle from Namib Desert can harvest water from the mist and direct the drops into its mouth, because its carapace has a hydrophobic surface with a random array of hydrophilic bumps.<sup>92-94</sup> Cribellate spiders rely on their silks, on which alternated spindle-knots and joints lead to both wettability<sup>96, 101</sup> and curvature gradients,<sup>97-98</sup> to collect water from humid air.<sup>99</sup> Additionally, some plants have also been found with water collection properties. For instance, *Cotula fallax*, a plant in South Africa, can collect water from fog and channel the drops to its stems due to the hydrophobic surface and 3D hierarchical structure of its leaves.<sup>100</sup> In some extremely droughty areas, cactaceae species can efficiently capture fog benefiting from the well-distributed spines and trichomes on their stems.<sup>102</sup> A unique water capturing and direction behaviour was also found in green bristlegrass due to the barb-groove structure of its bristles.<sup>103</sup>

Inspired by nature creatures, some materials have been designed to realize the function of water collecting from humid air.<sup>124-125, 243-244</sup> Based on fiber material, 1-D water collection materials have been developed imitating spider silks,<sup>112-114</sup> on which condensed small water drops were transported from joints to spindle-knots and coalesce to form larger drops. However, these coalesced water

drops collected by intricate silks or fibers can be expediently utilized by spiders rather than by human beings because they are separately distributed and difficult to be collected directly and in bulk. With this consideration, the aligned barb-groove structure of some plants or the vertically raised carapace of desert beetles, which have a uniform direction, can be imitated to transport collected water into a designated device. Despite the fact that, motivated by cactus, some attempts have been made to develop spine-like water collection materials,<sup>124-125,</sup><sup>244</sup> some of their synthetic procedures were too complicated to be expanded, and these approaches did not include any effective drainage system. Fortunately, the hydrophobic carapace with hydrophilic domains of desert beetle offers an idea on draining the collected water. By mimicking the desert beetles' back, a variety of strategies have been explored to fabricate 2-D surfaces consisting of both hydrophobic and hydrophilic ingredients.<sup>126-129</sup> However, some of the approaches are still difficult to be generalized due to the laborious and tedious synthetic procedures. Wang *et al.*<sup>130</sup> reported a simple route to make fabric with a superhydrophobic- superhydrophilic hybrid surface based on the selective reactivity of thiol with Fe and Co nanoparticles. Bai *et al.*<sup>131</sup> prepared a superhydrophobic surface with star-shaped superhydrophilic patterns to create a combination of a wettability gradient and a shape gradient to improve the water collection efficiency. According to these previous reports, a water harvesting surface should include both hydrophilic sites, where water is easy to condense, and a slippery surface for water to roll off with gravity as the driven force. Herein,

inspired by both 1-D spider silk and 2-D beetle back, we created a superhydrophobic fabric surface with light-induced superhydrophilic bumps via a simple and efficient process including first-step hydrophobization by SiO<sub>2</sub> nanoparticles (NPs) and an alkylsilane and subsequent spray coating with TiO<sub>2</sub> nano-sol. It is worth pointing out that the deposited TiO<sub>2</sub> can form raised shape due to the difficulty for sol drops to spread on the superhydrophobic cotton fibers before water evaporation. The hydrophilic spots with convex structure generate both a surface energy gradient and Laplace pressure gradient, which can accelerate the coalescence of water droplets on them. Meanwhile, by consisting of interlaced fibers, a fabric-based material provides not only channels for water drops to coalesce but also a surface for coalesced water drops to roll off. Also, the light weight, flexibility and low cost of fabric make it a promising material for massive transportation and bulk production. In this chapter, we eliminated the inherent water-absorbing property of cotton fabric by making it superhydrophobic through both increasing the surface roughness and decreasing the surface energy.<sup>68</sup>

To be specific, silica nanoparticles (NPs) was applied onto the cotton fabrics firstly to form hierarchical structure including both micron-scale and nano-scale roughness. Then, octadecyltriethoxysilane was applied to lower the surface energy, resulting in the superhydrophobic cotton fabric. Similar procedures in creating superhydrophobic surfaces integrating NPs and hydrophobic agents have been reported before.<sup>109, 245</sup> The prepared superhydrophobic fabric efficiently block the water absorption, thus improve the water drainage. Finally, TiO<sub>2</sub> NPs was

introduced onto the pre-treated fabric as hydrophilic sites via a simple spray coating method. As demonstrated in previous reports, TiO<sub>2</sub> exhibits superhydrophilic after light irradiation, which has been widely explored in changing surface wettability.<sup>47, 54-55, 246</sup> This light-induced superhydrophilic property can be utilized conveniently under the adequate sunlight of nature. In this chapter, the coating amount of TiO<sub>2</sub> was controlled by the spraying distance and the spraying time. Moreover, the effect of the size and density of hydrophilic spots distributed on the fabric on the final water harvesting efficiency was analysed.

## **5.2 Experimental**

### **5.2.1 Materials**

Cotton fabric (twill, 202 g/m<sup>2</sup>, provided by China Dye Ltd., Hong Kong), water glass (UNI-CHEM, 12% Na<sub>2</sub>O and 30% SiO<sub>2</sub>), hydrochloric acid (HCl, Aldrich 37%), n-octadecyltriethoxysilane (OTES, Accuchem 95%), titanium tetraisopropoxide (TTIP, Aldrich 97%) and acetic acid (HAc, Aldrich 99%) were used as received.

### **5.2.2 Synthesis of SiO<sub>2</sub> and TiO<sub>2</sub> nanosol**

The SiO<sub>2</sub> nanosol was prepared by the following procedures: firstly, water glass (10 g) was added into 100 mL of distilled water under magnetic stirring at room temperature for 10 min, and 2 M hydrochloric acid solution was added dropwise into the water glass solution under a magnetic stirring until the pH value

of the mixture reaching 8-9.

The TiO<sub>2</sub> nanosol was prepared by the hydrolysis of a TTIP hydrosol. Firstly, TTIP (40 g) was added dropwise into 100 ml distilled water solution containing HAc (0.5 wt.%) and HCl (1 wt.%) under vigorous mechanical stirring. The prepared TTIP hydrosol was then dropped slowly with a simultaneous adding of water at 83~90 °C for 4h to produce a milk-like sol. Subsequently, the sol was cooled to 60 °C, and stirred violently for 15 h until a transparent bluish sol was obtained. Finally, the mixture was cooled in air to room temperature and aged for two weeks, resulting in the final TiO<sub>2</sub> nanosol with TiO<sub>2</sub> solid content being 10 wt.%. The above TiO<sub>2</sub> sol was diluted by 10 times before use.

### **5.2.3 Fabrication of superhydrophobic fabric with light-induced superhydrophilic domains**

The cotton fabrics were immersed into the prepared SiO<sub>2</sub> sol for 1 min, and then padded with an automatic padder at a pressure of 2 kg/cm<sup>2</sup> to ensure the uniform coating of SiO<sub>2</sub> NPs. After dried at 80 °C for 3 min, the fabrics were dipped in a OTES/ethanol solution with the OTES concentration of 5 wt.% for 30 min. Then, the fabrics were washed using ethanol, and dried at 80 °C for 3 min, followed by curing at 160 °C for another 3 min.

A spraying equipment (RUIYI, HD-130, Taiwan) was applied to spray TiO<sub>2</sub> nanosol onto the as-prepared superhydrophobic cotton fabrics. The spray coating time was controlled at 5 seconds for all the samples, and the distances were varied

at 3, 5, 7, 9, 11, 13 and 15 cm to make different samples. A simultaneous heat treatment was conducted using a hot plate during the spraying process to facilitate the evaporation of water. After the spray coating, the cotton fabrics were dried at 80 °C for 3 min.

For comparison, a piece of pristine cotton fabric was also treated directly by spray coating of TiO<sub>2</sub> sol according to the above procedures (with a spraying distance of 11 cm).

#### **5.2.4 Characterization**

Scanning electron microscopy (SEM, Jeol 6490) was used to observe the bare cotton fabric (bare-C) and cotton fabrics treated with SiO<sub>2</sub> NPs, SiO<sub>2</sub> NPs/OTES, SiO<sub>2</sub> NPs/OTES/TiO<sub>2</sub>, and only TiO<sub>2</sub> (defined as SC, SSC, SSTC, and TC, respectively). Before applied on fabrics, SiO<sub>2</sub> NPs and TiO<sub>2</sub> NPs were observed by transmission electron microscopy (TEM, Jeol JEM-2011). To make SiO<sub>2</sub> and TiO<sub>2</sub> NPs, 10 μL of SiO<sub>2</sub> and TiO<sub>2</sub> sols with concentration of 0.1 wt.% were dripped onto the copper mesh and dried. X-ray diffraction spectroscopy (XRD, Rigaku SmartLab) was performed to study the crystallinity of TiO<sub>2</sub>. The morphology of bare-C and SC were recorded on atomic force microscopy (AFM, Veeco NanoScope V) in a tapping mode. X-ray photoelectron spectroscopy (XPS, Sengyang SKL-12) was performed to distinguish the surface chemical composition of SC, SSC and SSTC. The elementary composition and distribution were further studied by an energy dispersive X-ray spectroscopy (EDX) detector

attached to SEM. Water contact angles (WCA) of all the samples were measured by OCA20 (Data Physics). The thermal weight loss of SSTC samples with different spraying distances were investigated by thermogravimetric analyser (PerkinElmer Diamond TGA).

### **5.2.5 Water collection measurement**

An artificial fog flow (200 ml/h) horizontally generated by an ultrasonic humidifier (Midea, S20U-A) was used to simulate the fog of nature. All prepared samples (bare-C, TC, SSC, and SSTC with various spraying distances) with a uniform size of  $3 \times 3 \text{ cm}^2$  were firstly exposed to a UV irradiation (the wavelength is 365 nm and the light intensity of the lamp is  $0.46 \text{ mW/cm}^2$ ) for 30 min (the same result can be obtained by 1 h of sunlight irradiation with a light intensity of  $\sim 1 \text{ mW/cm}^2$ ) and subsequently fixed vertically to the direction of fog flow at room temperature ( $23 \text{ }^\circ\text{C}$ ). A beaker was placed under the sample to receive the collected water. The time was recorded when the first water drop dripped off each fabric sample. Also, the weight of the first water drop was measured. Finally, the water-collecting capacity of each sample was evaluated after 30 and 60 min. Moreover, in order to observe the water condensing and coalescing process, a fog flow was directed vertically to the horizontally placed fabrics. A digital camera was used to capture pictures.

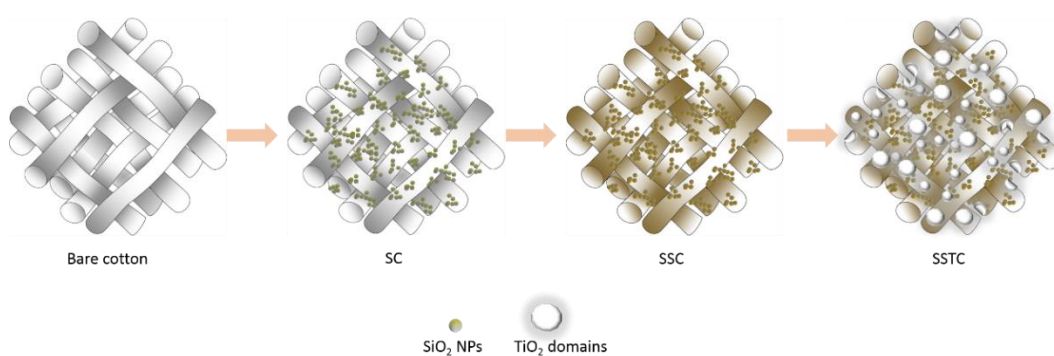
### **5.2.6 Stability and durability study**

The durability of the superhydrophobic coating and TiO<sub>2</sub> bumps was studied by repeated water collection and abrasion test. One cycle of water collection included a prior UV irradiation for 30 min, 1 hour of water-collecting process using method as previously mentioned, followed by an airdry. WCA and water collection performance of SSTC-11 fabric were recorded after 5, 10, and 15 cycles. SEM and EDS mapping were used to observe the surface morphology and element distribution respectively after 15 cycles of water collection. The abrasion test was conducted using a Martindale abrasion tester based on standard ASTM D4966-12. 100 and 500 times of friction was performed, after which WCA (after UV irradiation), water collection performance, SEM and EDS mapping were recorded. Two types of acidic fog flow was made from water solution with pH values of 3 and 5 containing H<sub>2</sub>SO<sub>4</sub> and HNO<sub>3</sub> (1.9:1, wt/wt) simulating the acid rain.<sup>246</sup> Water collection stability and morphology of SSTC-11 fabric was studied under acidic fog flow by 15 cycles. Water collection performance of the prepared SSTC-11 fabric at different temperature (20, 25, and 40 °C) was also investigated by conducting the experiments in a constant temperature laboratory, a common laboratory without air-condition, and an oven respectively.

## **5.3 Results and discussion**

The fabrication procedure from bare-C to SSTC is demonstrated in Scheme 5.1. SiO<sub>2</sub> NPs were first synthesized beforehand by a sol-gel process with water

glass as the precursor and then applied onto the fabric via a simple dip-pad-dry method. Then, the SC was treated by OTES to form a superhydrophobic SSC fabric. Finally, the TiO<sub>2</sub> sol was sprayed onto the surface of SSC fabric to create raised hydrophilic domains after dried at 80 °C.



**Scheme 5.1.** Illustration of the fabrication process for SC, SSC and SSTC fabrics.

In order to investigate the crystallinity of titania particles by XRD, the titania solid powders were extracted from the TiO<sub>2</sub> sol. As shown in Figure 5.1a, the characteristic peaks of TiO<sub>2</sub> in anatase phase (25.4 °, 37.8 ° and 48.1 °) can be detected from XRD spectrum (Figure 5.1a). Anatase TiO<sub>2</sub> has been reported to have strong photocatalytic property and light-induced superhydrophilicity.<sup>47</sup> The light-responsive wettability change of TiO<sub>2</sub>-treated cotton fabric (TC) was studied. As shown in Figure 5.2, the introduction of TiO<sub>2</sub> would lengthen the time to wick the water droplet indicating the decrease of hydrophilicity of cotton fabric. However, after UV irradiation for 30 min (or sunlight irradiation for 1 h), much shorter time was needed for WCA to become 0 ° than that before UV irradiation, indicating a wettability transformation of TiO<sub>2</sub> to superhydrophilicity. Note that this superhydrophilic status can be maintained for at least 12 h in absence of light (the top column in Figure 5.3), which can ensure a good fog capturing in next

morning even after a whole night storage. After about 48 h of dark-storage, however, TiO<sub>2</sub> turns hydrophobic (the bottom column in Figure 5.3) because of the dehydration-induced decrease in -OH groups and the readsorption of airborne organics on TiO<sub>2</sub> surface. Hence, in cloudy and rainy days, TiO<sub>2</sub> bumps can turn hydrophobic and have a better resistance to the damage by flush rainwater. TEM was also performed to characterize TiO<sub>2</sub> and SiO<sub>2</sub> NPs which were deposited from TiO<sub>2</sub> and SiO<sub>2</sub> nano-sols with concentration being both 0.1 wt.%. From Figure 5.1c, a diameter of around 10 nm could be measured for each TiO<sub>2</sub> NP, but an aggregation phenomenon of TiO<sub>2</sub> NPs could also be found in Figure 5.1b in the absence of water. The aggregation instinct of TiO<sub>2</sub> NPs is conducive to the formation of scattered hydrophilic TiO<sub>2</sub> domains. Conversely, SiO<sub>2</sub> NPs had a much better dispersibility after the evaporation of water (Figure 5.1d), which may be responsible for the homogeneous coating of SiO<sub>2</sub> NPs and even roughness increase on the SC fabric.

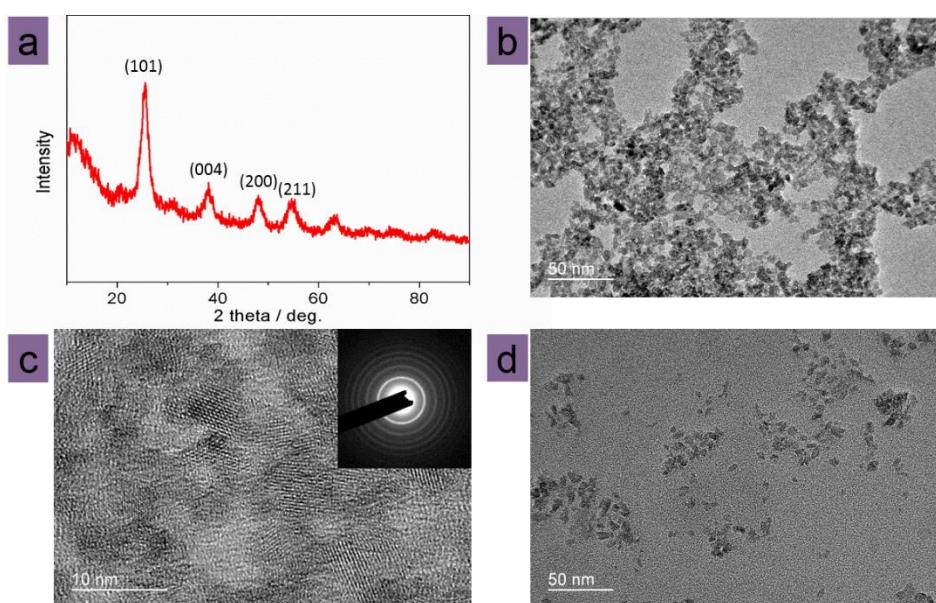


**Figure 5.1.** a-c) Characterization of TiO<sub>2</sub> NPs by XRD (a), and low resolution (b) and high

resolution (c) TEM; d) TEM observation of SiO<sub>2</sub> NPs. The inset in (c) is the SAED pattern for the observed TiO<sub>2</sub> NPs.

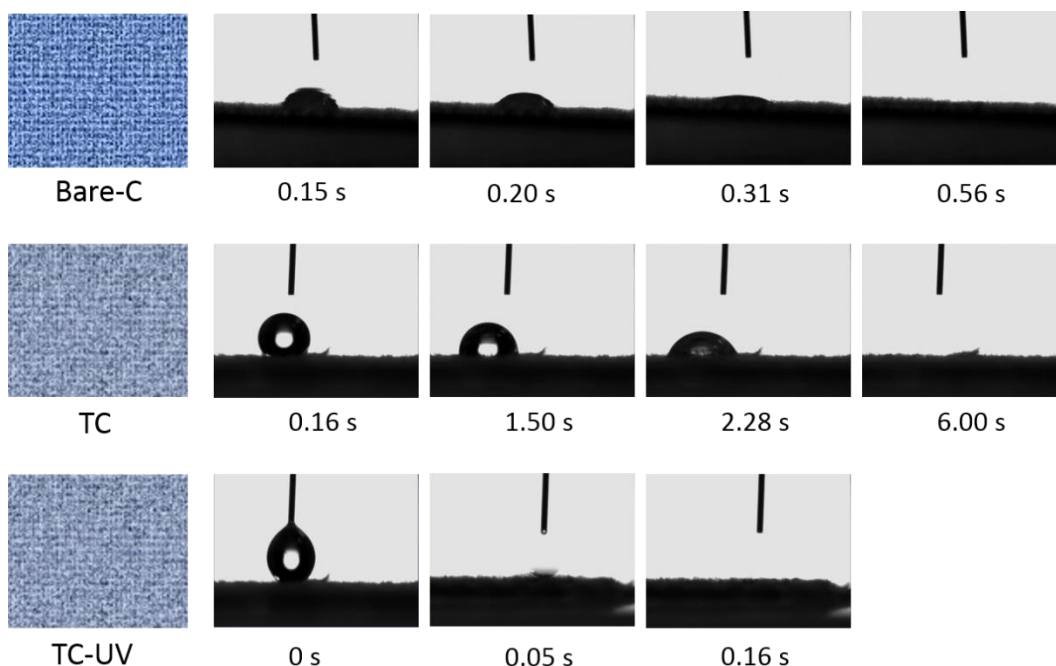


**Figure 5.2.** Illustration of the hydrophilicity of bare-C, TC, and UV-treated TC (TC-UV).

Time needed for water droplets to become 0° on bare-C, TC and TC-UV is 0.56 s, 6 s and 0.16 s respectively. A sunlight irradiation of 1 h was confirmed to have the same result (with a light intensity being 1 mW/cm<sup>2</sup>).

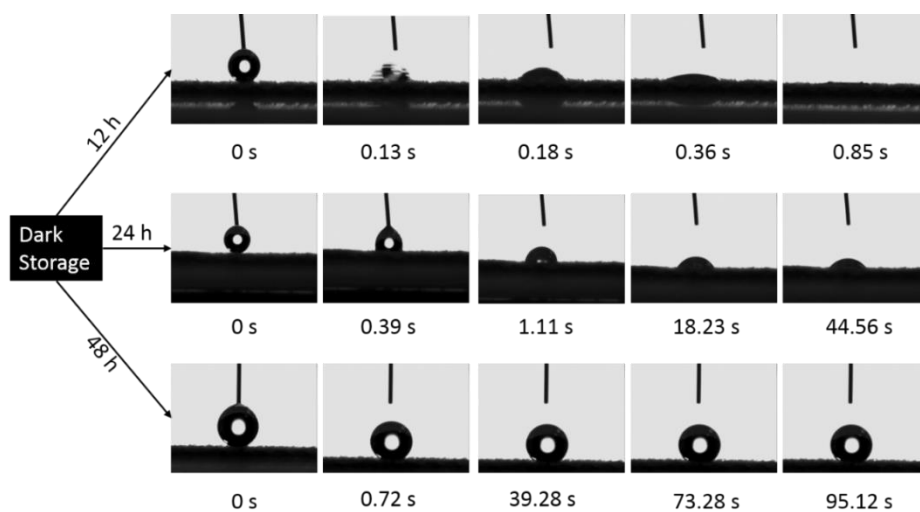


**Figure 5.3.** Pictures of water droplets on TC fabric after UV irradiation and following

dark-storage for 12 h, 24 h and 48 h. After 12 h dark-storage, TiO<sub>2</sub> maintains superhydrophilic and only 0.85 s is needed for water droplets to infiltrate into the TC fabric. The hydrophilicity of TC fabric decreases apparently after more than 24 h dark-storage, and even turn hydrophobic with a WCA around 144.6 ° after 48 h of dark-storage.

SEM was conducted to observe the surfaces of bare-C, SC, and SSC (Figure 5.4 a-f). In Figure 5.4a and d, a flat and smooth surface of bare cotton fiber can be seen. After padding with SiO<sub>2</sub> sol and drying, the surface of cotton fiber was covered by a layer of SiO<sub>2</sub> NPs, which introduced a nano-scale roughness onto the surface (see the AFM images of bare-C and SC in Figure 5.5a and b, respectively). The increase of the surface roughness can maximize the surface wettability levels.<sup>68</sup> Therefore, after treated by OTES, with low surface energy, the fabric surface turned superhydrophobic (Figure 5.4g) with the WCA of about 155.6 ° (Figure 5.4h). This superhydrophobic fabric surface ensures efficient water drainage by accelerating the rolling off of water droplets.

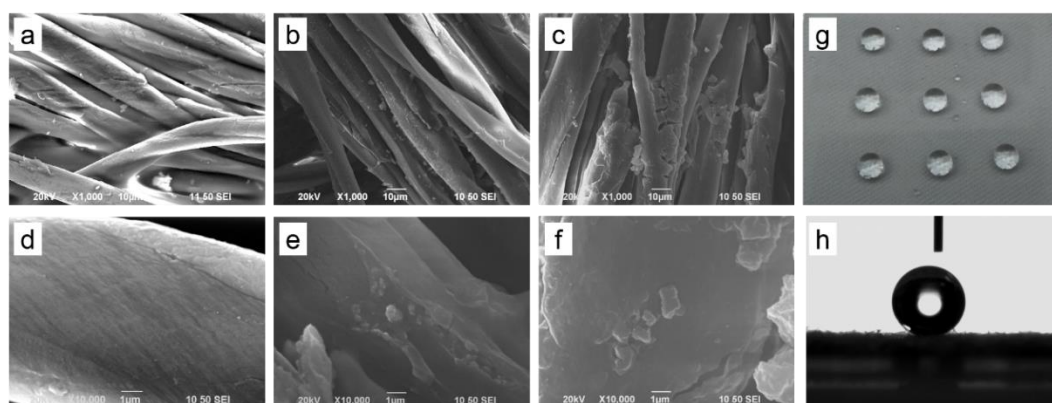


**Figure 5.4.** SEM images of bare-C (a, d), SC (b, e), and SSC (c, f) fabrics with different magnification (a, b, c with 1,000 times and d, e, f with 10,000 times); optical image of water macro-droplets on the as-prepared SSC fabric (g); WCA of ~155.6 ° on the as-prepared SSC

fabric (h).

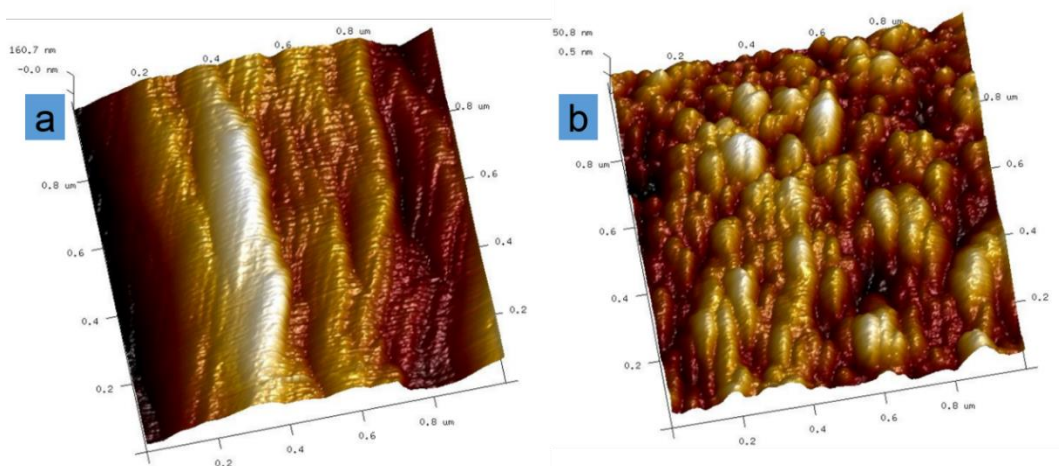
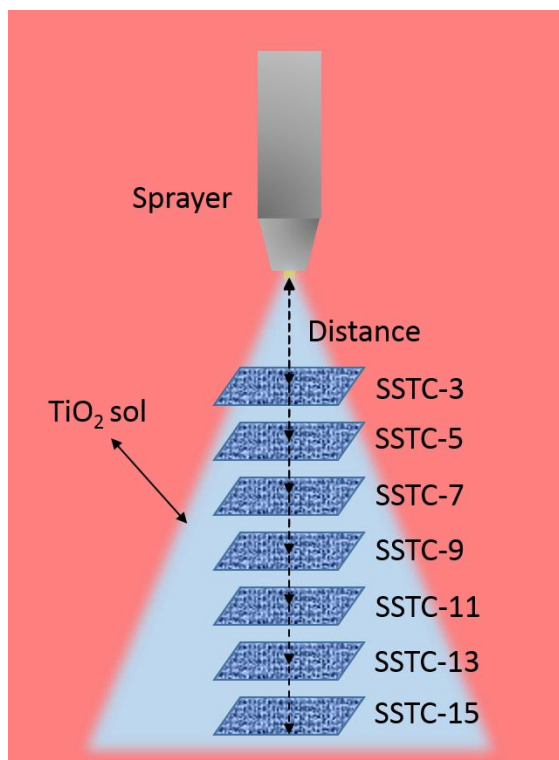


**Figure 5.5.** AFM images of bare-C (a) and SC (b) fabrics in tapping mode.

After the fabrication of the superhydrophobic fabric, hydrophilic domains were introduced by simply spraying  $\text{TiO}_2$  sol onto the as-formed superhydrophobic surface. The coating amount of  $\text{TiO}_2$  and the domains size was generally determined by the spraying distance. Specially, SSTC fabricated with a different spraying distance: 3, 5, 7, 9, 11, 13, or 15 cm is defined as SSTC-3, SSTC-5, SSTC-7, SSTC-9, SSTC-11, SSTC-13, and SSTC-15, respectively. Note that the spraying time for all the SSTC samples were maintained the same (5 s). The spraying process is demonstrated in Scheme 5.2. A longer spraying distance can lead to smaller and more scattered  $\text{TiO}_2$  domains and a lower  $\text{TiO}_2$  coating percentage, which is demonstrated detailedly in the following section. The distribution of the light-induced superhydrophilic domains has a complicated influence on the water collection efficiency of SSTC fabrics, which will be discussed in the subsequent section.



**Scheme 5.2.** Illustration of spray coating of  $\text{TiO}_2$  sol on SSC fabrics with varying the distance between the nozzle and the fabrics.

The elementary composition and distribution of the prepared samples were studied by XPS and EDX. The elementary change during the synthesis process from SC fabric to SSTC fabric was recorded by XPS curves. As shown in Figure 5.7a and b, Si2p peak was detected on SC fabric around 103.4 eV indicating the successful preparation of  $\text{SiO}_2$  and the coating of  $\text{SiO}_2$  on the cotton fabric. After treated with OTES, the C1s peak intensity relative to that of the O1s peak was greatly increased due to the existence of long aliphatic carbon chain of OTES. With subsequent spray coating of  $\text{TiO}_2$  sol (Figure 5.6 a-c), Ti2p 3/2 peak (Figure 5.6b) started to appear around 458.5 eV denoting the presence of  $\text{TiO}_2$  on the fabric. To further demonstrate the composition of SSTC fabric (SSTC-11), EDX spectrum and mapping are given in Figure 5.6d and e. The result confirms the

presence of C, O, Ti, Si elements and displays the distribution of Ti, Si and C. Note that Si and C are both uniformly distributed along with the corresponding SEM image, while Ti is distributed as scattered domains with irregular shapes. The discrete distribution of TiO<sub>2</sub> is attributed to the superhydrophobic surface, on which the sprayed TiO<sub>2</sub> sol beads up and this will be the key factor to fog trapping and coalescence.

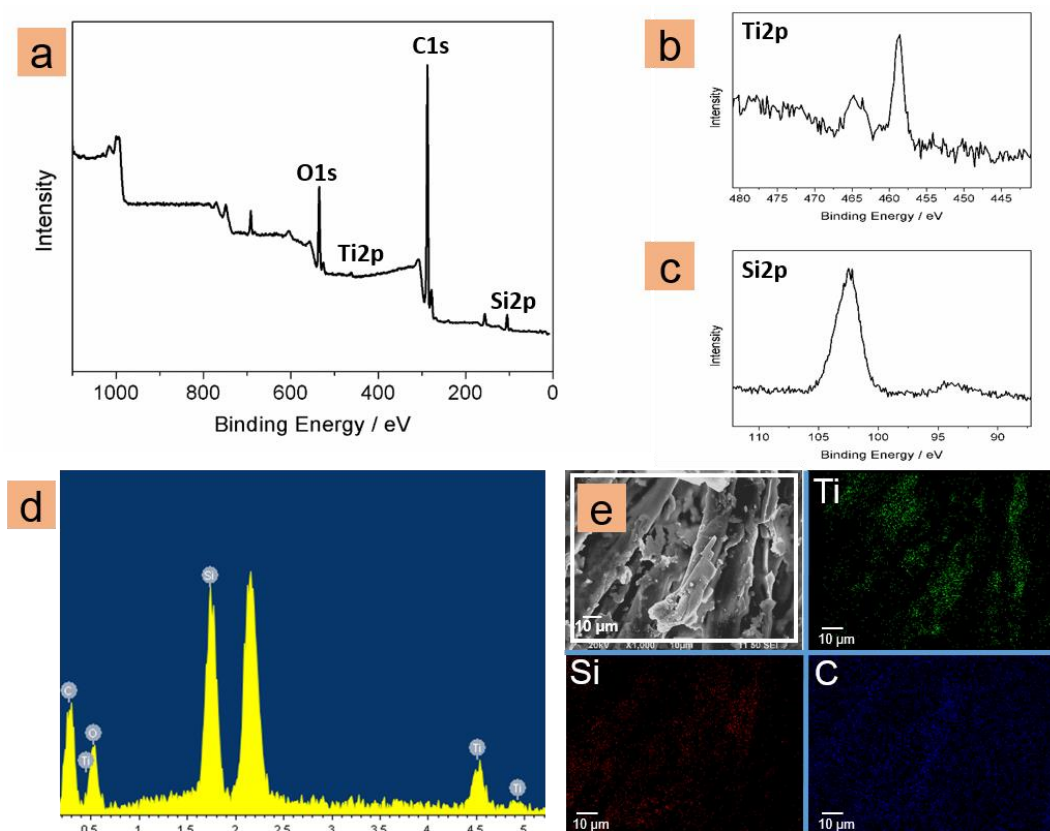


**Figure 5.6.** Elementary composition and distribution of the as-prepared SSTC fabric. (a)-(c) are XPS survey spectrum, high-resolution spectrum of Ti2p and high-resolution spectrum of Si2p, respectively; (d) EDX spectrum of the resultant SSTC fabric; (e) EDX mapping images of Ti, Si and C elements on the SSTC fabric corresponding to the SEM image.

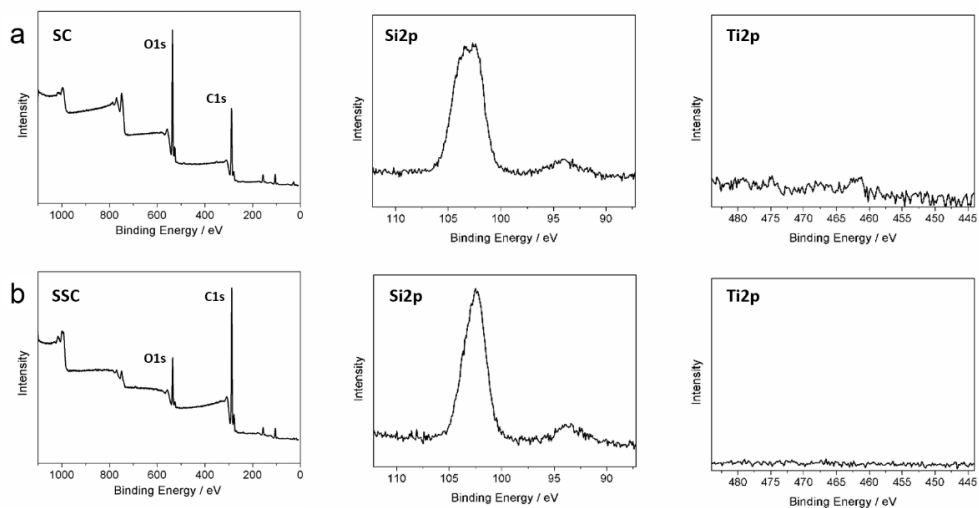


**Figure 5.7.** XPS results of the prepared SC (a) and SSC (b) fabrics. The far left column are integral spectra of the fabrics and the others are spectra with high-resolution denoting Si and Ti elements as labeled in the spectra.

To study the water-collecting efficiency, bare-C, TC, SSC and SSTC were compared with the weight of collected water after 30 and 60 min. The starting-time for collection and the weight of the first drop off each sample were also recorded. Before water collection, all the samples were exposed to a UV light (365 nm) for 30 min, and the comparison result of water collection is presented in Figure 5.8. As shown in Figure 5.8a and b, SSTC samples have a generally higher water collecting efficiency than bare-C, TC and SSC. The poor water collection capacity of bare-C and TC can be explained by their inherent hydrophilic and water-absorbing properties. Condensed water on bare-C or TC can wet and saturate the fabric before dripping, so the starting time for collection of bare-C and TC are much longer than other samples with superhydrophobic modification. Furthermore, Figure 5.8c and d shows that TC took the longest time until the first drop dripped, and the weight of its first water drop was the largest. This can be

attributed to the superhydrophilicity of TiO<sub>2</sub> treated cotton fabric after UV irradiation, which leads to high water absorption capacity and strong water adhesion property, and thus an inefficient water collection property.

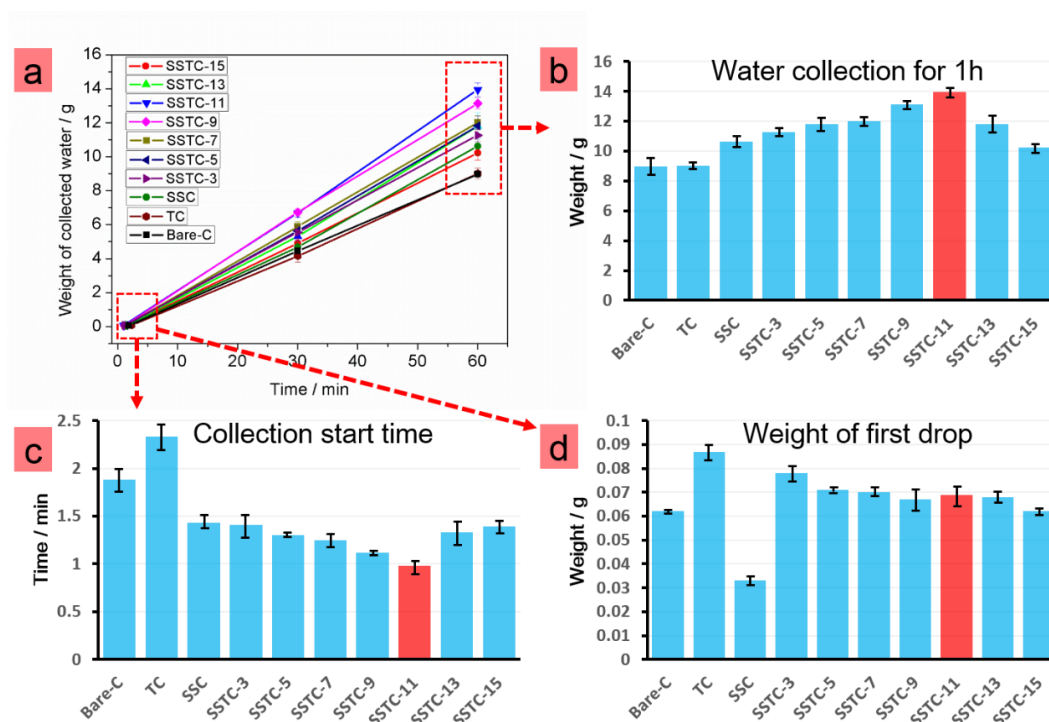


**Figure 5.8.** Water collection performance of various fabrics. (a) Water collection amount of each sample along with the collection time; (b) total amount of collected water of each sample after 1 h; (c) starting time for collection, i.e., time needed for each fabric to drip the first water drop in the fog environment; (d) the weight of the first water drop at the starting time for collection.

On the contrary, the superhydrophilic property of TiO<sub>2</sub> can play a positive role in water collection when combined with superhydrophobic substrate. After introduced with TiO<sub>2</sub> domains, the water collection efficiency of superhydrophobic fabrics was generally increased except SSTC-15 (see Figure

5.8b), indicating an increase of water condensation on the surfaces with superhydrophilic domains. However, more hydrophilic domains do not mean higher water collection efficiency. The incorporation of too much hydrophilic ingredient will destroy the original superhydrophobicity of the fabric, which may lead to a poor water collection property, such as SSTC-3, SSTC-5 and SSTC-7 (Figure 5.8b). The effect of TiO<sub>2</sub> coating amount upon hydrophobicity of fabrics is indicated by Figure 5.9. After UV irradiation, SSTC fabrics with more TiO<sub>2</sub> coating had a higher degree of WCA decrease. As for SSTC-3~SSTC-7 with too much TiO<sub>2</sub> coverage, a hydrophilic property appeared after UV exposure. However, when the spraying distance was more than 9 cm, the decline of superhydrophobicity seemed not that obvious. Note that the SSTC-11 fabric, which had the best water collection efficiency among all the samples (see Figure 5.8b), exhibited a WCA close to 150 ° (Figure 5.9) indicating a good maintenance of the superhydrophobic property. The gradual decrease of WCA along with increasing UV irradiation time was also recorded on SSTC-11 fabric (see Figure 5.10a). The corresponding ascent of water collecting amount (Figure 5.10b) indicates the important role the superhydrophilic TiO<sub>2</sub> bumps play in water pinning. In summary, water collection efficiency is mainly determined by the combined effect of hydrophobicity of the surface and the amount of hydrophilic ingredient. To be specific, an efficient water collection surface should possess not only sufficient superhydrophilic sites to adhere and fix fog droplets but also an integral superhydrophobic property to accelerate the rolling of water drops.

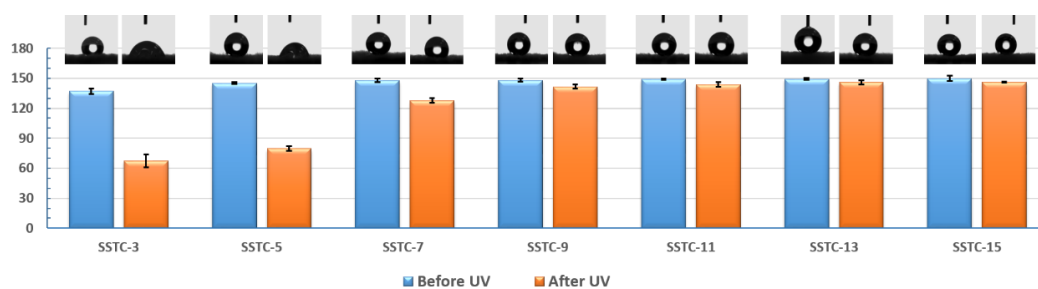


**Figure 5.9.** WCA of SSTC fabrics with various spraying distances before and after UV

irradiation (insets on the top of the histogram are the corresponding shapes of water drops on the fabrics).

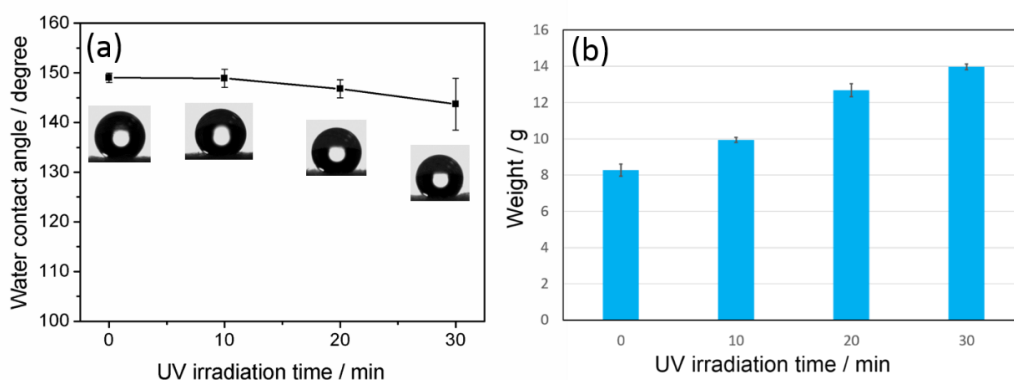


**Figure 5.10.** (a) Gradual WCA decrease on SSTC-11 fabric surface along with an increasing time of UV irradiation; (b) Water collection performance (for 1 h) of SSTC-11 fabric after different time of UV irradiation.

SEM images of SSTC fabrics with various spraying distances are displayed in Figure 5.11 (a-g). The top surfaces of SSTC-3 and SSTC-5 are almost fully covered by contiguous titania bumps, each of which extends across the width of one or two fibers (Figure 5.11a and b). With the increase of spraying coating distance, TiO<sub>2</sub> bumps seem less dense on surfaces of SSTC-7 and SSTC-9, but still have large sizes with a width equal to a fiber (Figure 5.11c and d). When the spraying distance reaches to 11 cm and 13 cm, smaller and scattered titania domains appear with diameters ranging from one to a few tens of micrometers

(Figure 5.11e and f). Finally on the surface of SSTC-15 fabric, very scarce titania domains could be seen (Figure 5.11g), which may be responsible for its poor water collection performance because of the insufficient hydrophilic sites for fog to condense on. Additionally, SEM image of TC fabric is shown in Figure 5.11h for a better comparison with SSTC fabrics. No raised  $\text{TiO}_2$  domains could be found on the surface of TC fabric because the sprayed sol can spread evenly on the pristine cotton fabric.

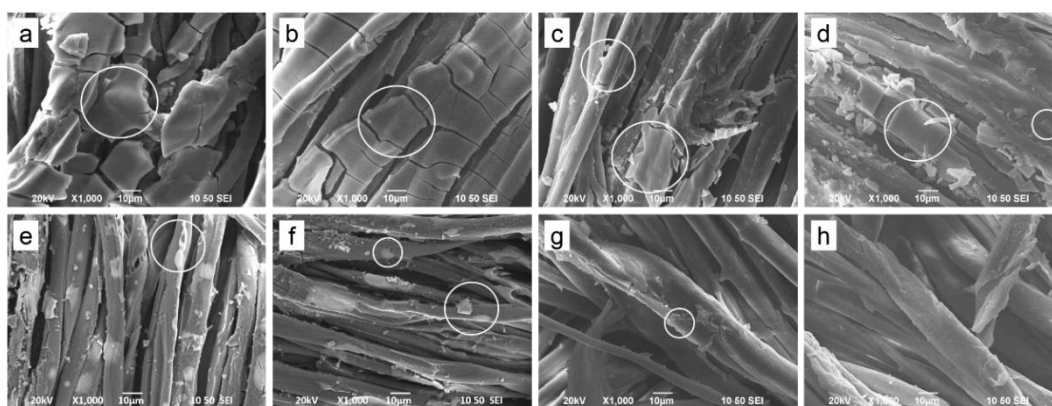


**Figure 5.11.** SEM images of TC (h) and SSTC with various spraying distances (a-g): SSTC-3 (a); SSTC-5 (b); SSTC-7 (c); SSTC-9 (d); SSTC-11 (e); SSTC-13 (f); SSTC-15 (g). The white circles in a-g mark the  $\text{TiO}_2$  domains. No obvious  $\text{TiO}_2$  domains can be seen in TC samples (h).

In order to further study the relationship between the spraying distance and the coating amount of  $\text{TiO}_2$ , TGA was performed to study the percentage of  $\text{TiO}_2$  on weight of SSTC fabrics with a series of spraying distances (see Figure 5.12). Bare-C and SSC samples was chosen as references. The pyrolysis of the samples started at about 350 °C due to the decomposition of cellulose fibers.<sup>247-248</sup> Finally, the weight gain percentage of  $\text{TiO}_2$  on each SSTC fabrics was calculated from the

difference between the residue percentages of SSC and SSTC fabrics. As can be seen from Figure 5.12, a shorter spraying distance indicates a higher percentage of TiO<sub>2</sub> coating. This result has also been supported by EDX detection of Ti content on the fabric surface, which is shown in Figure 5.13. Specifically, with the TiO<sub>2</sub> gain percentage of ~0.92 % (by TGA), SSTC-11 sample achieved the best water collecting performance in our study owing to its sufficient hydrophilic sites with no obvious damage effect on the integral superhydrophobicity.

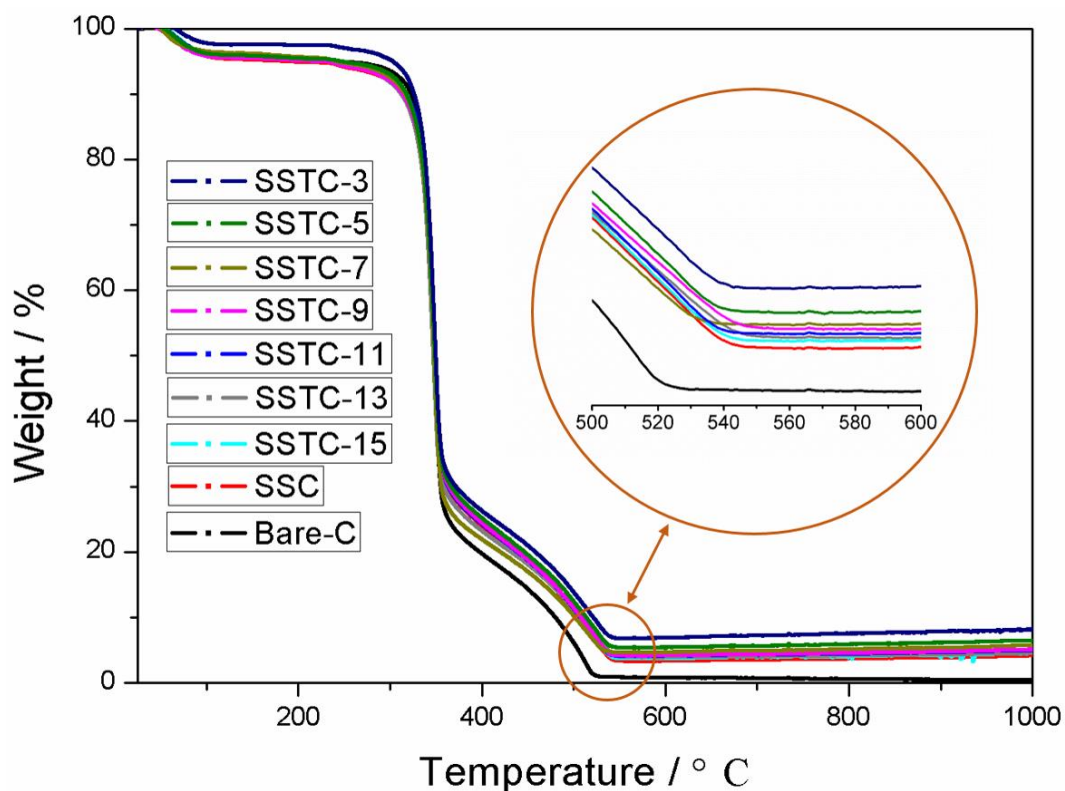


**Figure 5.12.** TGA spectra of SSTC fabrics under various spraying coating distances with bare-C and SSC fabrics as references.

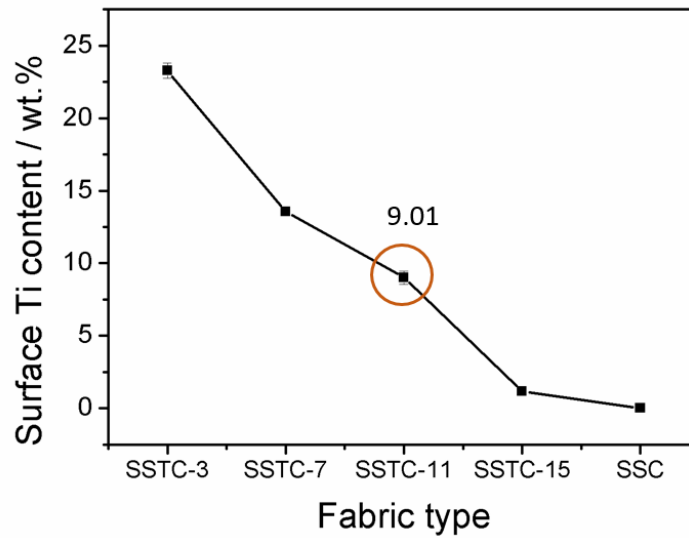


*Figure 5.13.* Surface Ti content of SSTC-3, SSTC-7, SSTC-11, SSTC-15, and SSC fabric detected by EDX.

To investigate how the superhydrophilic  $\text{TiO}_2$  domains influence the water condensing velocity on a superhydrophobic fabric surface, the water condensation and coalescence process of SSTC-11 was recorded by a digital camera discretely from 30 s to 4 min with SSC and TC fabrics as references. A prior UV light exposure was conducted for 30 min to switch the  $\text{TiO}_2$  coating to be superhydrophilic. A fog flow (200 ml/h) was then directed vertically onto the horizontally placed fabrics. As shown in Figure 5.14a, during the fog condensation process, no spherical water droplets can be formed because water is easy to spread on a superhydrophilic TC fabric surface with strong water absorption. In contrast, coalesced water forms visible spherical droplets on the integral superhydrophobic surfaces of SSC and SSTC-11 fabrics as shown in Figure 5.14b and c, respectively. However, in the presence of superhydrophilic

spots, SSTC-11 fabric harvested more and larger water droplets than SSC fabric with the same harvesting time. This fog pinning and overall superhydrophobic property of SSTC-11 fabric can well explain the results shown in Figure 5.8c and d that it have the earliest starting time for water collection and a biggish weight of the first drop collected.

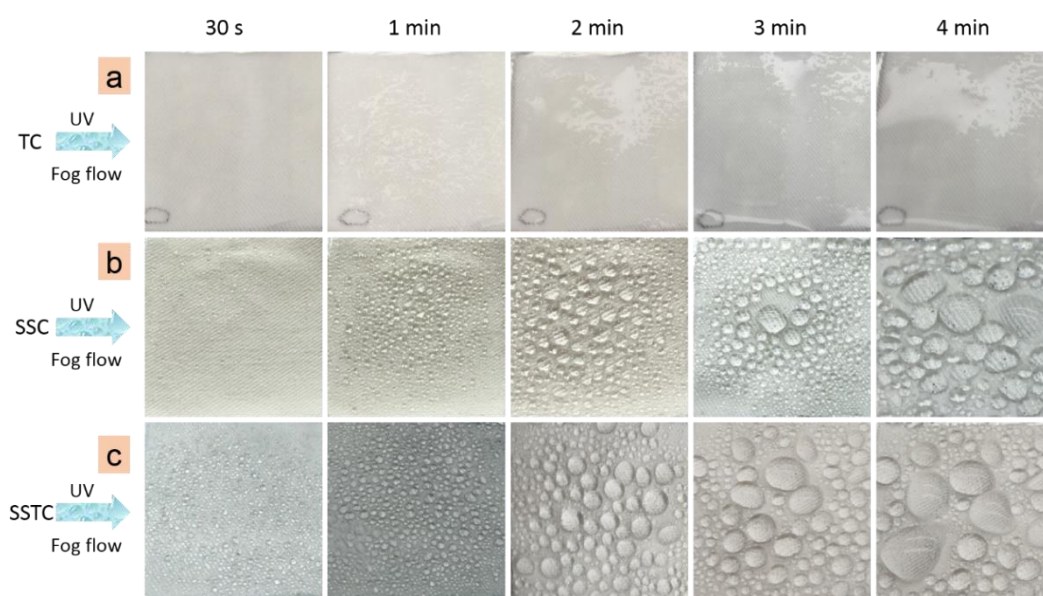


**Figure 5.14.** Water condensation and coalescence process along with time on TC (a), SSC (b), and SSTC-11 (c) fabrics (the UV treatment was conducted before atomizing the fog).

The mechanism of how the sprayed  $\text{TiO}_2$  bumps accelerate the water condensation and coalescence on SSTC fabrics was analyzed in detail (see Figure 5.15). After a light irradiation, the sprayed  $\text{TiO}_2$  bump becomes superhydrophilic, which means that it has a much higher apparent surface energy and smaller WCA than surrounding superhydrophobic fiber. The driven force generated by the surface energy gradient can be calculated by<sup>96, 101</sup> Eq. 2.6. As predicted by Eq. 2.6, the water droplets will move from superhydrophobic fiber surface to

superhydrophilic TiO<sub>2</sub> bump driven by the surface gradient. Moreover, there is another possible driven force generated by Laplace pressure gradient. From Figure 5.11 and Figure 5.15a, raised TiO<sub>2</sub> domains can be seen because of the difficulty for spreading the TiO<sub>2</sub> sol droplets on superhydrophobic fabric. The raised TiO<sub>2</sub> spots lead to a local increase of fiber radius (from  $r_1$  to  $r_2$  in Figure 5.15c), and can be thought of as two partial conical shape. The Laplace pressure gradient ( $\Delta P$ ) arises from the curvature gradient can be approximately calculated by:<sup>97, 99</sup>

$$\Delta P = - \int_{r_1}^{r_2} \frac{2\sigma\gamma}{(r+R_0)^2} \sin \beta \, dz \quad (\text{Eq. 4.1})$$

where  $r$  denotes the local mean radius of the fiber;  $\beta$  denotes half of the apex-angle of the conical shape;  $dz$  is the integrating variable along the diameter of fiber;  $\sigma$  is the proportion that TiO<sub>2</sub> domain versus the whole cone (because the TiO<sub>2</sub> domain partially encircle the local fiber surface, the formed cone is not integrated, namely,  $\sigma < 1$ ). Overall, as a result of these two cooperative driven force, surface energy gradient and Laplace pressure difference, water droplets are more prone to coalesce from superhydrophobic fiber to superhydrophilic TiO<sub>2</sub> domains.

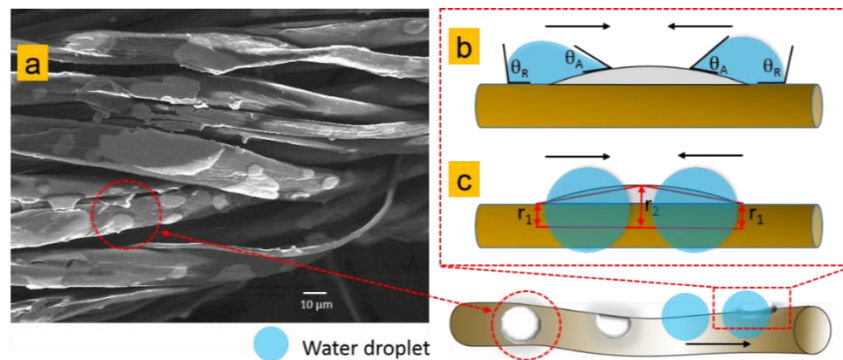


**Figure 5.15.** Structure and distribution of raised TiO<sub>2</sub> domains on SSTC-11 fabric and

mechanism of directional water coalescence. (a) SEM image showing the shape and distribution of raised TiO<sub>2</sub> domains on SSTC-11 fabric; (b) illustration of driven force caused by surface energy difference between superhydrophilic TiO<sub>2</sub> domains and superhydrophobic fiber; (c) illustration of Laplace pressure gradient between fiber and the thickened TiO<sub>2</sub> area.

Besides the significance of the water capturing (condensation and coalescence) process, the drainage of captured water is also important. An effective water drainage system means larger water release in a shorter time. To simulate the growing and release of water drops during the water collection, the water drops were added on each horizontal UV-irradiated fabric (the bottom side of the fabric was adhered to a glass slide by double sided adhesion tape) and then the fabric was rotated to upright. The growing of the water drop was conducted by using a microsyringe to add water to the initial drop. The growing process was recorded by a digital camera discretely until the drop started to roll off. Figure 5.16 a-c show different mechanisms of water drainage of TC, SSC, and SSTC fabrics, while Figure 5.16 d-f are their corresponding simulations displayed by photos, respectively. Figure 5.16a and d display the poor water drainage on superhydrophilic TC fabric. Water undergoes a thorough spread and is absorbed by the fabric before dripping down from the bottom end (Figure 5.16d-4). Also, the strong adhesion force between water drops and the superhydrophilic surface makes water difficult to drip down. Therefore, the drainage time is long because the captured water need to spread thoroughly and coalesce to be large enough to

overcome the strong adhesion force, which can also explain the results (TC) shown in Figure 5.8c and d. In contrast, water drainage in SSC and SSTC fabrics are favoring because their overall superhydrophobic property. Water drops form almost perfect spheres with a tiny contact area with fabric surface and a low adhesion force, which may lead to rapid water release (Figure 5.8c and d). Note that the SSTC fabric (Figure 5.16f) had a little higher critical roll-off volume than SSC fabric (Figure 5.16e), which can be attributed to the incorporation of  $\text{TiO}_2$  causing a slight reduction in hydrophobicity. However, it does not lower the overall water collection efficiency (Figure 5.8b) because the  $\text{TiO}_2$  bumps could accelerate the pinning and growing of water drops on the fabric surface, as has been discussed above. Overall, the as-prepared SSTC fabric exhibits an effective water collection function attributed not only to the enhanced water capturing and growing, but also an efficient drainage.

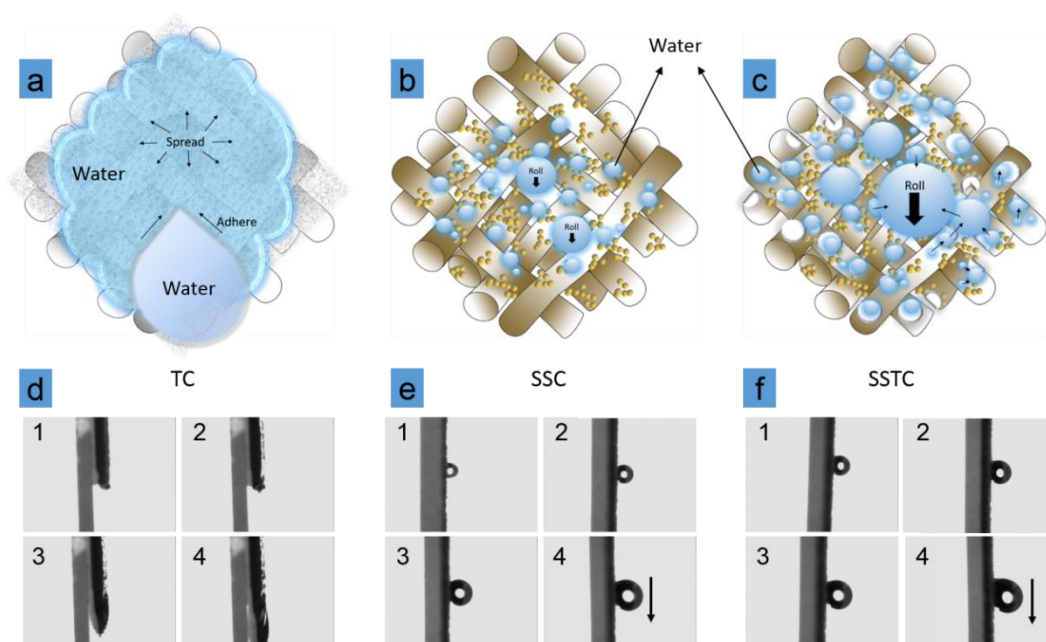


**Figure 5.16.** Graphic illustration of different water drainage systems on TC (a), SSC (b), and

SSTC(c) fabrics; photos of simulations of water growing and rolling processes corresponding different drainage mechanisms with (d)-(f) representing TC, SSC and SSTC fabrics, respectively.

Finally, the stability and durability of the SSTC-11 fabric was studied by repeated water collection and abrasion test. As shown in Figure 5.17a and b, there was no obvious impairment in WCA or water collection performance even after 15 cycles of water collection repetition. This is attributed to the well conservation of silica/silane superhydrophobic coating and the raised  $\text{TiO}_2$  bumps, which can be observed in SEM image and EDS mapping shown in Figure 5.17 c-e.

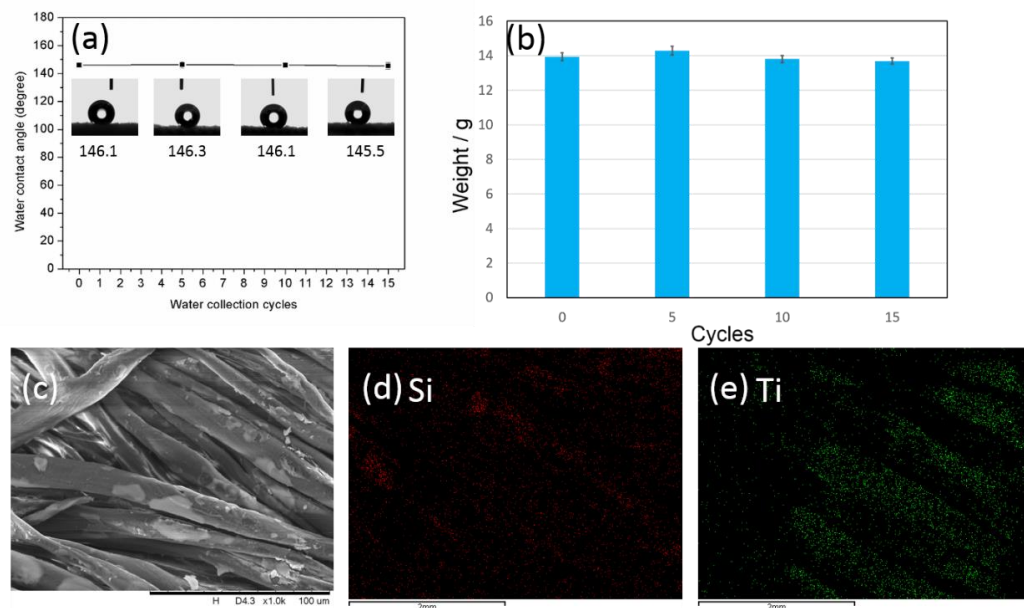


**Figure 5.17.** (a) Line graph displaying the relationship between WCA and water collection cycles (insets show the WCAs after 0, 5, 10, and 15 cycles of water collection); (b) Water collection performance/weight after 0, 5, 10, and 15 cycles of water-collecting repetition; (c) SEM image of the SSTC fabric surface after 15 cycles of water collection; (d) and (e) are EDS mappings of Si and Ti, respectively, on SSTC fabric after 15 cycles of water collection.

Even in acidic fog flow, a stable water collection performance and a well retaining of the functional coating (after 15 cycles) can also be observed (Figure 5.18). Abrasion test was also conducted to evaluate the adhesion strength of the functional coating against the friction during transportation.

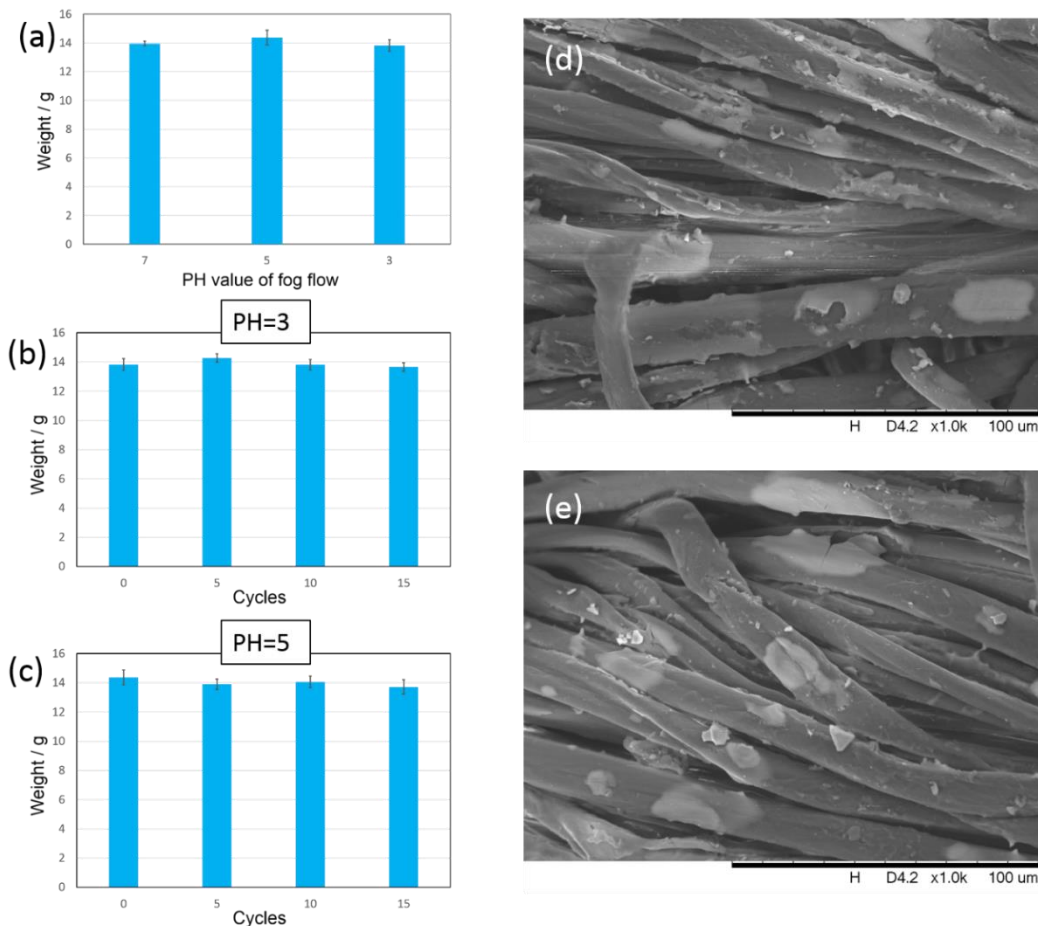


**Figure 5.18.** (a) Water collection stability of the as-prepared SSTC-11 fabric under acidic fog flow with pH values of 3 and 5 (with DI water generated fog as reference); (b) Water collection stability after 0, 5, 10, and 15 cycles under fog flow with pH values of 3; (c) Water collection stability after 0, 5, 10, and 15 cycles under fog flow with pH values of 5; (d) SEM image of the SSTC-11 fabric surface after 15 cycles of water collection under fog flow with pH values of 3; (e) SEM image of the SSTC-11 fabric surface after 15 cycles of water

collection under fog flow with pH values of 5.

It can be seen from Figure 5.19 that 100 times of friction scarcely generates damage to the surface coating and the WCA (after UV irradiation). 500 times of friction causes a slight decrease of the density of TiO<sub>2</sub> bumps, but it is hardly that products undergo such high-strength friction in the practical transport. Hence, the adhesion between cotton fabric and the surface finishing can withstand repetitive water (including acidic water) flush and friction, which ensures a stable water collection performance. In additions, the impact of temperature on water collection performance was also investigated. As shown in Figure 5.20, along with the increase of temperature, a decrease of water collection happens, which might be attributed to the easier condensation of fog at lower temperature and the faster water (including fog and the collected water) evaporation at higher temperature. Therefore, in areas at high latitudes where the morning temperature is very low, a better water collection performance of the as-prepared SSTC fabric can be expected.

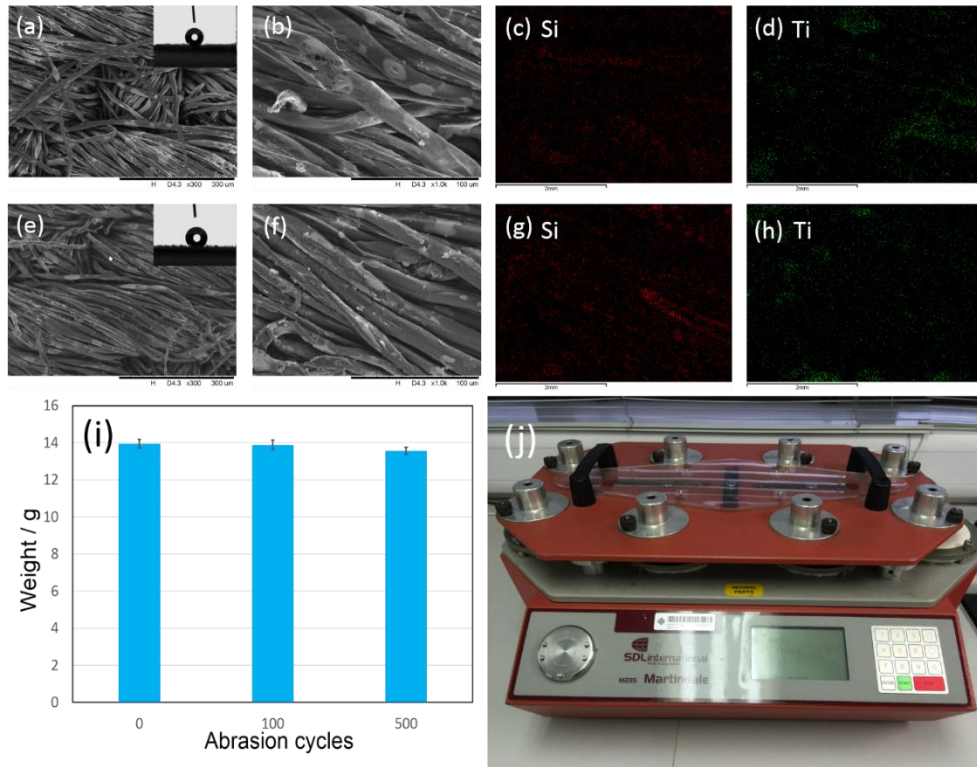


**Figure 5.19.** Rub resistance testing results of the superhydrophobic coating and the TiO<sub>2</sub> bumps on the SSTC-11 fabric. (a)-(d) are SEM images with magnification of x300, x1000, EDS mapping of Si, and Ti on SSTC fabric surface after 100 times of friction respectively; (e)-(h) are SEM images with magnification of x300, x1000, EDS mapping of Si, and Ti on SSTC fabric surface after 500 times of friction respectively, insets in (a) and (e) show the after-UV WCAs of SSTC after 100 and 500 times friction respectively; (i) shows the water collection performance/weight after 0, 100, and 500 times abrasion; (j) is the picture of Martindale abrasion-testing machine used in this chapter.

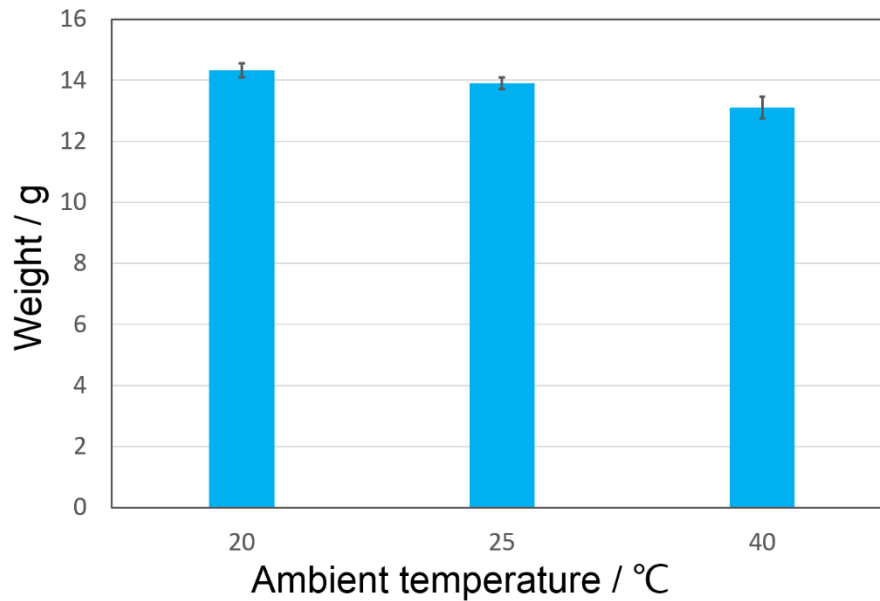


*Figure 5.20.* Water collection performance at different ambient temperature.

## 5.4 Conclusion

An efficient water collecting fabric with a superhydrophobic surface integrated with light-induced superhydrophilic bumps has been successfully fabricated by a simple method. Utilizing the beads forming feature of TiO<sub>2</sub> sol on a superhydrophobic surface, raised TiO<sub>2</sub> bumps are obtained, which may provide surface energy gradient and Laplace pressure gradient cooperatively accelerating the directed coalescence of water droplets. The spraying distance of TiO<sub>2</sub> sol (the spraying time is fixed) had significant effect on the water collecting efficiency through controlling the coating amount and distribution of TiO<sub>2</sub>. In order to attain an efficient water collection, sufficient scattered TiO<sub>2</sub> bumps should be formed on the basis of an overall superhydrophobicity. The as-prepared SSTC fabric can thereby be regarded as an inspiration of both 1-D spider silk and 2-D beetle back

with water collecting function. Simply triggered by sunlight, a sustainable energy source, the superhydrophilicity of  $\text{TiO}_2$  can be achieved without additional effort, which may provide ideas to developing smart water collection device. Furthermore, the self-cleaning or anti-bacterial property of  $\text{TiO}_2$  makes it a more competitive material applied in water harvesting and recycling.

## Chapter 6

# Flexible Slippery Surface to Manipulate Water Coalescence and Sliding in Real Time: Synthesis, Characterization and Application

A flexible slippery membrane with tunable morphology and high degree of affordable deformation upon external tensile-stress is developed by infusing perfluoropolyether into a fluorinated-copolymer modified thermoplastic polyurethane nanofibrous membrane. A controllable liquid condensation enhancement on the surface can thus be realized, as well as a creative solution to ensure an efficient water collection in strong wind.

### 6.1 Introduction

The manipulation of the wettability, condensation, and motion of liquids on solid surfaces is fundamental to many applications, such as self-cleaning,<sup>249-250</sup> oily water treatment,<sup>251-252</sup> water collection,<sup>243, 253</sup> moisture management,<sup>54, 254</sup> desalination,<sup>255</sup> microfluidics transportation,<sup>256-257</sup> directional water transport,<sup>258</sup> and anti-icing.<sup>259</sup> For water collection in particular, the condensation and sliding behavior of water droplets should be conjunctively addressed through adjusting surface wettability and constructing spacial structure. The mainstream design concepts for materials and surfaces with water-collecting function were inspired

by creatures in nature living in arid regions and capturing water from mist air for surviving. In particular, *Stenocara* beetle's back,<sup>92</sup> cribellate spider's silk<sup>99</sup> and Cactaceae species' leave<sup>102</sup> are the three most popular models that have been widely studied and imitated.<sup>131, 243-244, 253</sup> Through sophisticated design of shape and wettability gradients, these bio-inspired materials or surfaces can accelerate the water condensation or facilitate the sliding/drainage of the captured water droplets. Recently, Aizenberg and coworkers designed a slippery lubricated surface with asymmetric bumps and reported its highly improved water condensation and drainage performance compared with conventional superhydrophobic based surfaces.<sup>150</sup> In their work, the concept of the designed asymmetric bumps is derived from Namib desert beetles and cacti, and the slippery coating is inspired by *Nepenthes* pitcher plants<sup>106</sup> with lubricated peristome on which insects aquaplane and are captured. Based on the slippery coating with negligible friction of pitcher plants, a new concept of manipulating the motion of liquid droplets has been pointed out, i.e., creating a "liquid-like" surface between solid surface and target liquids, which has been adopted in fabricating a wide range of omniphobic surfaces.<sup>107, 132, 146, 260</sup> Integrating such slippery surfaces, the efficiency of water collection can be highly improved due to the enhanced water condensation and shedding. Although recent progress is remarkable in realizing beyond-nature water collection efficiency on account of the highly decreased water adhesion and sliding friction, water captured on such surfaces is easy to be blown away in nature wind. Few works have considered to

eliminate the wind-caused loss of the captured water because it is incompatible to simultaneously improve the water drainage/sliding and increase the water adhesion to resist wind force, especially for rigid solid surfaces on which drastic wind impact occurs and wind direction sharply changes. Herein we developed a flexible slippery surface and studied its deformation-triggered manipulation of water sliding and condensation. The membrane is developed by infusing perfluoropolyether into a fluorinated-copolymer modified thermoplastic polyurethane nanofibrous membrane. A controllable liquid condensation enhancement on the surface can thus be realized, as well as a creative solution to ensure an efficient water collection in strong wind.

## **6.2 Experimental**

### **6.2.1 Materials**

Thermoplastic polyurethane (TPU,  $M_w \sim 600,000$ ) was purchased from Hong Kong Hi-Tech Enterprises Ltd. Dimethylacetamide (DMAc, Duksan Chemical 99.5%), dodecafluoroheptyl methacrylate (DFMA, XEOGIA 96%), lauryl methacrylate (LMA, Aldrich 96%), isobornyl acrylate (IBOA, Aldrich, technical grade), 1-dodecanethiol (DDET, Aldrich 98%), 2,2'-azobis(isobutyronitrile) (AIBN, IL, 99%), propylene glycol butyl ether (PGBE, Aldrich 99%), Perfluoropolyether (PFPE, Fomblin® Y, Aldrich) were used as received.

### **6.2.2 Fabrication of electrospun TPU nanofiber membrane (NM)**

The TPU electrospinning solution was made by dissolving 15 g of TPU chips in 100 mL of DMAC. A commercial electrospinning setup (TL-Pro, purchased from Micro & Technologies Expert, Shenzhen, China) was used to fabricate nanofibers at room temperature (23 °C) with the ambient relative humidity around 55%. A positive voltage of 15 kV was applied on the needle and a negative voltage of 2 kV was applied on the collecting aluminum foil (anchored on a rotating drum with rotating speed of 10 rpm during the electrospinning process). The distance between the needle tip and the aluminum foil was 20 cm. The solution flow rate from the spinneret was controlled at 1 mL/h through a syringe pump. The as-spun TPU NM (~46  $\mu\text{m}$ , Figure 6.3) was placed in an oven at 80 °C for 10 min followed by a 12 h air-dry in dark to remove the residual solvent. Finally, the TPU NM was peeled off the aluminum foil and flattened before the following treatment.

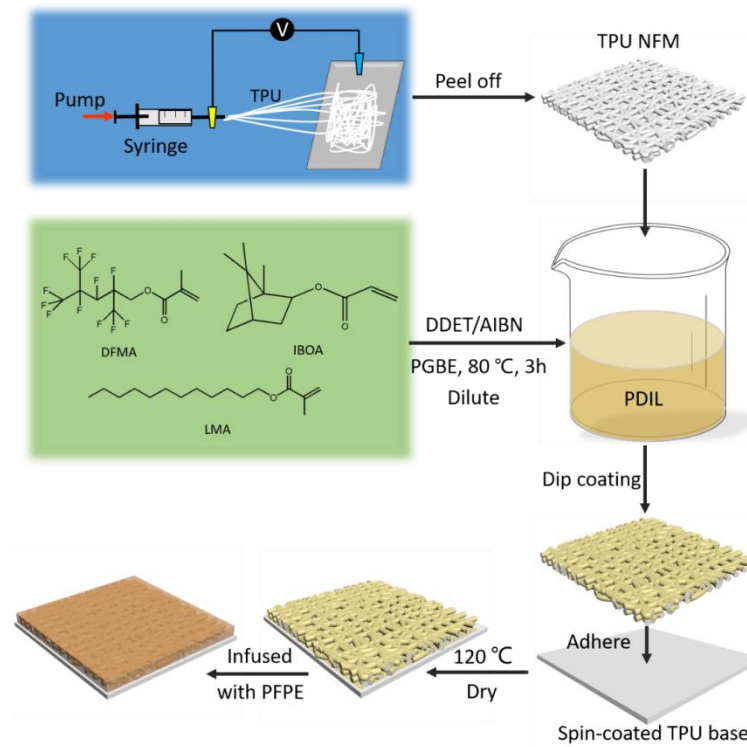
### **6.2.3 Fabrication of poly(dodecafluoroheptyl methacrylate-co-isobornyl acrylate-co-lauryl methacrylate) (PDIL)**

PDIL was synthesized by the random copolymerization of DFMA, IBOA and LMA with weight ratio of 1:2:1. First, 10 g of DFMA, 20 g of IBOA and 10 g of LMA were dissolved in 60 g of PGBE. The initiator AIBN (0.4 g) and polymerization regulator DDET (0.1 g) were then added into the solution. The reaction was kept at 80 °C for 3 hours without sealing because of the generation

of N<sub>2</sub> from the system. The resultant PDIL solution (40 wt %) was stored overnight at room temperature and then diluted into solutions with five concentration gradients: 1 wt %, 3 wt %, 5 wt %, 7 wt %, and 9 wt %.

#### **6.2.4 Fabrication of PFPE-PDIL-TPU flexible slippery membrane (FSM)**

The as-prepared TPU NM was firstly dipped into the PDIL solution for 5 seconds, then it was extracted and the excess solution was removed by tissue paper. Subsequently, the TPU NM was attached flatly onto a piece of TPU thin film (~50 μm, Figure 6.3) made by spin-coating method (15 wt % of TPU/DMAC solution with spin-coating rate of 1600 rpm for 10 s and 3000 rpm for 6 s in succession). The composited membrane was then dried at 120 °C in an oven for 10 min. The liquid-infused FSM was prepared by infusing PFPE onto the as-prepared membrane and the infusing amount was controlled by the volume of liquid versus a known surface area.



**Scheme 6.1.** Fabrication procedure of the PFPE-PDIL-TPU FSM.

## 6.2.5 Characterization

The morphology of the as-prepared TPU NM, TPU-PDIL NM, and TPU-PDIL-PFPE FSM were observed using a field emission scanning electron microscope (FE-SEM, JSM-6335F, Japan). Contact angle (CA), sliding angle (SA) and contact angle hysteresis (CAH) measurements were conducted using OCA20 (Data Physics, Germany). The CAH ( $\Delta\theta$ ) was calculated by the difference between advancing CA ( $\theta_A$ ) and receding CA ( $\theta_R$ ) which were measured from the water droplet (4  $\mu$ L) while the probe was added to and withdrawn from the drop:  $\Delta\theta = \theta_A - \theta_R$ . The chemical compositions of the samples were compared utilizing Fourier transform infrared (FT-IR, PerkinElmer Spectrum 100, USA). The tensile

stress-strain curves of the samples were recorded using an INSTRON 5566 (USA) universal tensile tester. The water or oil sliding on the tilted (45°) FSM was investigated (for Figure 6.1 f, g) using deionized water (DI water, colored by methylene blue) and n-hexane (colored by solvent red).

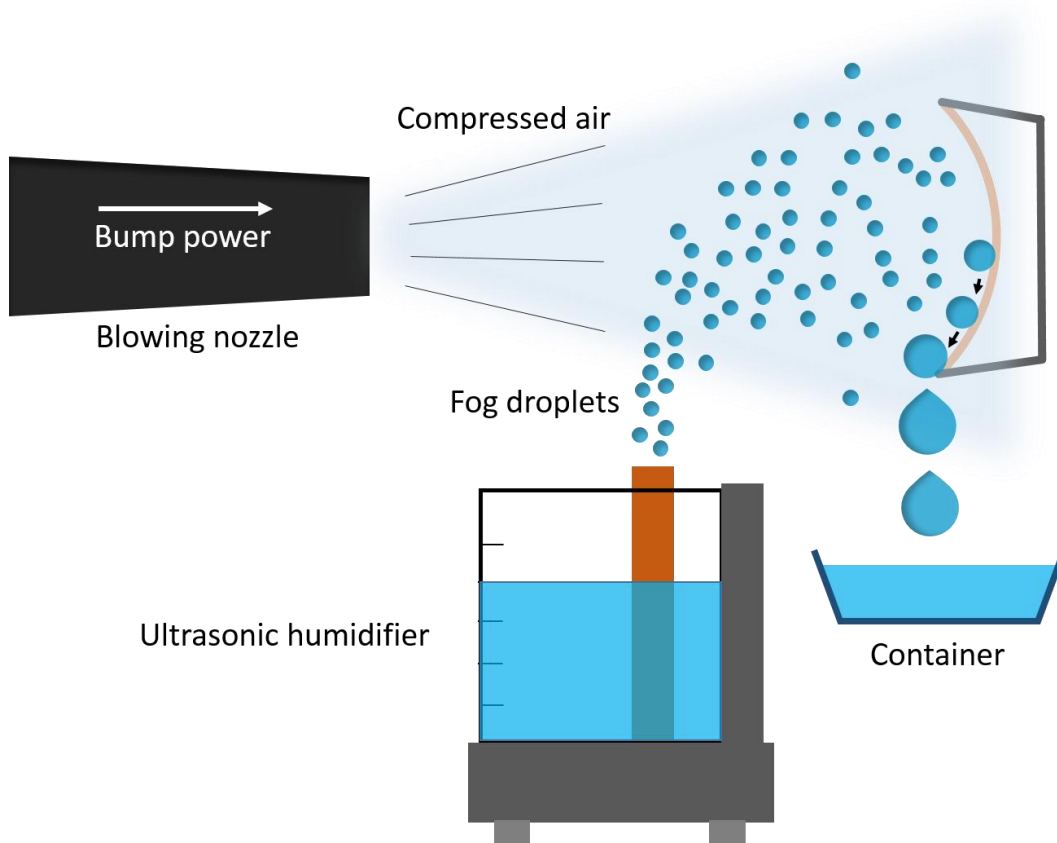
### **6.2.6 Investigation of controllable water sliding and condensation.**

The strain-release responsive water pinning and sliding was observed on the as-prepared TPU-PDIL-PFPE FSM. A water droplet of 4  $\mu\text{L}$  was placed on the inclined FSM (with both sides attached on hard plastic sheets), and the strain-release behavior was controlled by dragging or release the mobile side.

The enhanced water condensation behavior on the FSM along with its release process from the strained status was investigated with both in-plane and out-plane deformation. The in-plane deformation (strain) was conducted by the same method as above, and the water droplets were placed on the horizontal and strained FSM, then the FSM was put vertically and gradually released. The out-plane deformation was conducted by attaching one terminal of a glass rod onto the midpoint of the back face of the rounded FSM (anchored on a hollow circle) using double faced adhesive tape and dragging the other terminal of the glass rod. Fog droplets generated from an ultrasonic humidifier were directed onto the vertically placed and strained FSM, after sufficient droplets were pinned, the FSM was released gradually.

### **6.2.7 Investigation of water collection in strong wind**

The as-prepared TPU-PDIL-PFPE FSM was anchored onto a hollow circle with a diameter of 5 cm. An industrial air blower (1200 W, ZHIPU, China) with adjustable wind speed generated was used as the artificial wind source. The distance between the blowing nozzle and the membrane was 20 cm. An ultrasonic humidifier (Midea S20U-A, China) was utilized to generate fog droplets and was placed between the air blowing nozzle and the membrane. A glass petri dish was placed under the membrane to receive the collected water. The experimental setup was demonstrated in Scheme 6.2. As comparison, another piece of TPU-PDIL-PFPE FSM was anchored onto a top surface of a bottle cap with a diameter of 5 cm to form a rigid slippery membrane (RSM). The wind speed was measured by a digital anemometer (TA8161 0.3-30 m/s, TASI, China). For the demonstration presented in Figure 6.11 a-b, the wind speed was set at 12 m/s. To record the data in Figure 6.11e, each collection duration is set at 5 minutes. To observe the water splashing during water collection by both the FSM and the RSM, the membranes were placed near a background wall with a distance of 15 cm to collect part of the splashed water from the membranes.



*Scheme 6.2.* Experimental setup for water collection test.

### 6.3 Results and discussion

By infusing lubricant perfluoropolyether (PFPE) into an electrospinning thermoplastic polyurethane (TPU) composite membrane, an elastic surface with tunable topography was obtained (Figure 6.1a). To overcome the low chemical affinity between TPU and PFPE, a layer of fluorinated polymeric coating (Figure 6.1c) was introduced on the surface of electrospun nanofibers (Scheme 6.1). By adjusting monomer proportion (1:2:1, weight ratio) among dodecafluoroheptyl methacrylate (DFMA), lauryl methacrylate (LMA) and isobornyl acrylate (IBOA),

a random copolymer poly(DFMA-co-IBOA-co-LMA) (PDIL) was synthesized with low surface energy, high chemical affinity to PFPE (with strong C-F stretching vibration appeared at 1100-1300  $\text{cm}^{-1}$  in the FTIR spectrum of PDIL, Figure 6.4), adequate flexibility and strong physical adhesion on TPU, which is one of the critical innovations in this work. To be specific, the long carbon chains contained in LMA and their interaction<sup>261-262</sup> can lower the surface energy and improve the molecular arrangement for a better exposure of the fluorine groups in DFMA, the rigid side group of IBOA ensures the film-forming property and the strong physical adhesion.<sup>263-264</sup> The stable adhesive property of PDIL on solid surfaces (Figure 6.2 shows a good adhesive property on metal surface) make it a desirable linker between the lubricant PFPE and matrixes that naturally have no affinity towards PFPE, which broadens the selection of matrixes with varied mechanical properties.

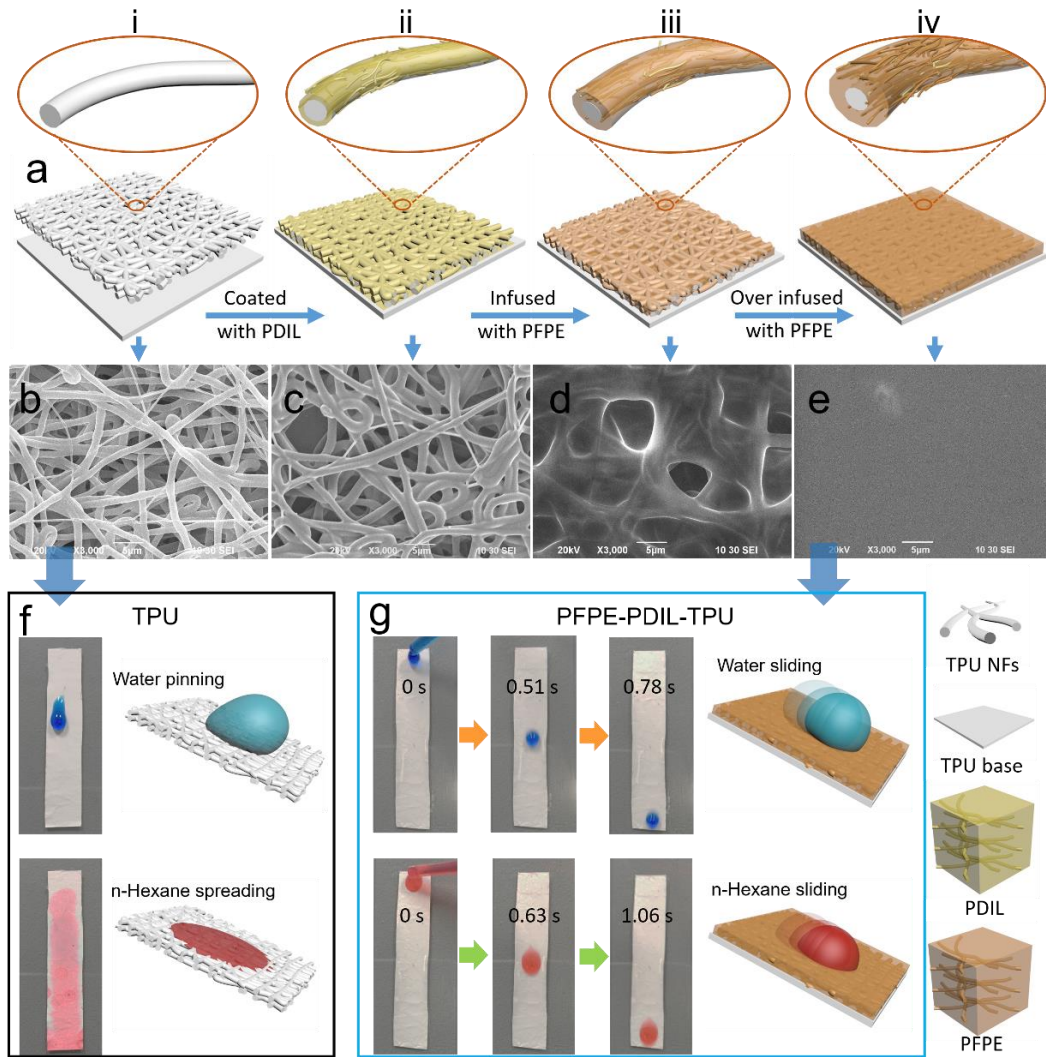


**Figure 6.1.** (a) Illustration of the fabrication process of the PFPE-PDIL-TPU composite membrane; (b-e) FE-SEM image showing the top view of the corresponding prepared membrane after each fabrication step; observation of movement of water and n-hexane drops on the pure TPU NM (f) and on the PFPE-PDIL-TPU membrane (g).

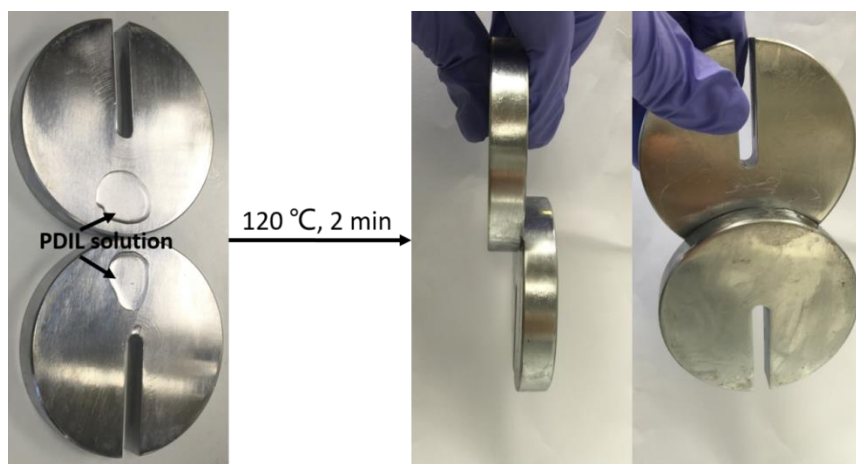


**Figure 6.2.** The strong adhesion of two weights (450 g) with the assistance of PDIL.

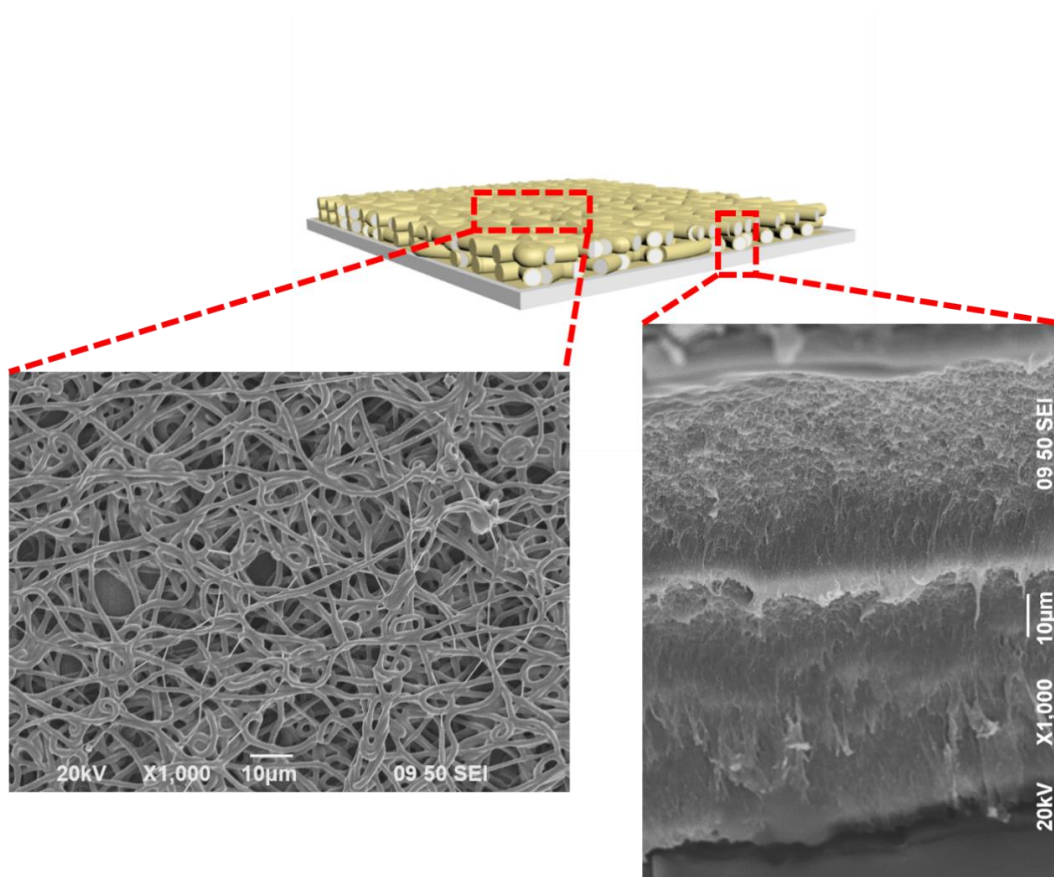


**Figure 6.3.** FE-SEM images of the top view (left) and the section view (right) of the

TPU-PDIL NM attached on a TPU thin film before PFPE infusion.

The as-spun TPU nanofiber membrane (NM) was dip-coated with the synthesized PDIL solution and then attached to a spin-coated TPU base film

without porous texture before drying (Figure 6.3). The coated PDIL polymer chains can be wetted and infiltrated by PFPE chains more easily than TPU due to the chemical affinity between fluorine groups, which ensures a more stable immobilization and more even distribution of the lubricant PFPE. The coating amount of the PDIL should be well controlled, for that the insufficient coating is incapable of lowering the surface energy (Figure 6.5b) and the excessive coating would block the porous texture for lubricant wicking as well as weaken the elastic recovery of the membrane (Figure 6.5a and 5.6 c-e). The PDIL solution with concentration of 3 wt % was used because the as-coated TPU NM exhibited the best water repellency and a well retaining of elastic recovery. Following the over infusion of PFPE, the membrane possesses a slippery surface on which water drops and n-hexane drops can slide easily (Figure 6.1g) whereas water drops are pinned and n-hexane drops will spread and penetrate on a pure TPU NM (Figure 6.1f). The formed smooth and flawless liquid surface (Figure 6.1e) on the membrane with over infused PFPE ( $2.8 \mu\text{L cm}^{-2}$ ) and the low surface energy of PFPE ( $17.4 \text{ mN m}^{-1}$ ) is the key to the fluent sliding of the testing water and even oil. As a comparison, a rough and porous surface can be observed (Figure 6.1d) on the membrane with an insufficient lubricant infusion ( $1.6 \mu\text{L cm}^{-2}$ ), and as a result, a higher contact angle hysteresis was detected (Figure 6.7f).

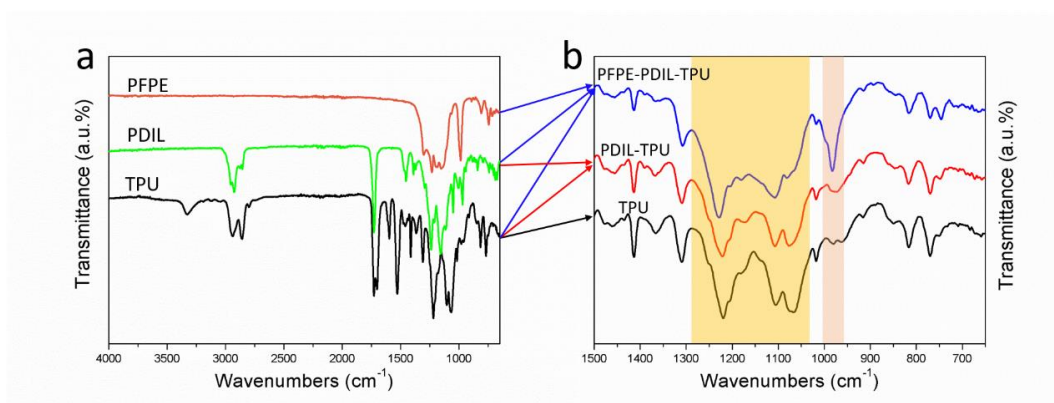


**Figure 6.4.** (a) Separate FTIR spectra of the as-spun TPU NM, as-synthesized PDIL, and the purchased PFPE; (b) composite FTIR spectra of the TPU NM, PDIL-TPU NM, and the PFPE-PDIL-TPU FSM. The peak appeared at 950-1000  $\text{cm}^{-1}$  on PFPE-PDIL-TPU spectrum represents the stretching vibration of the ether bond in PFPE.

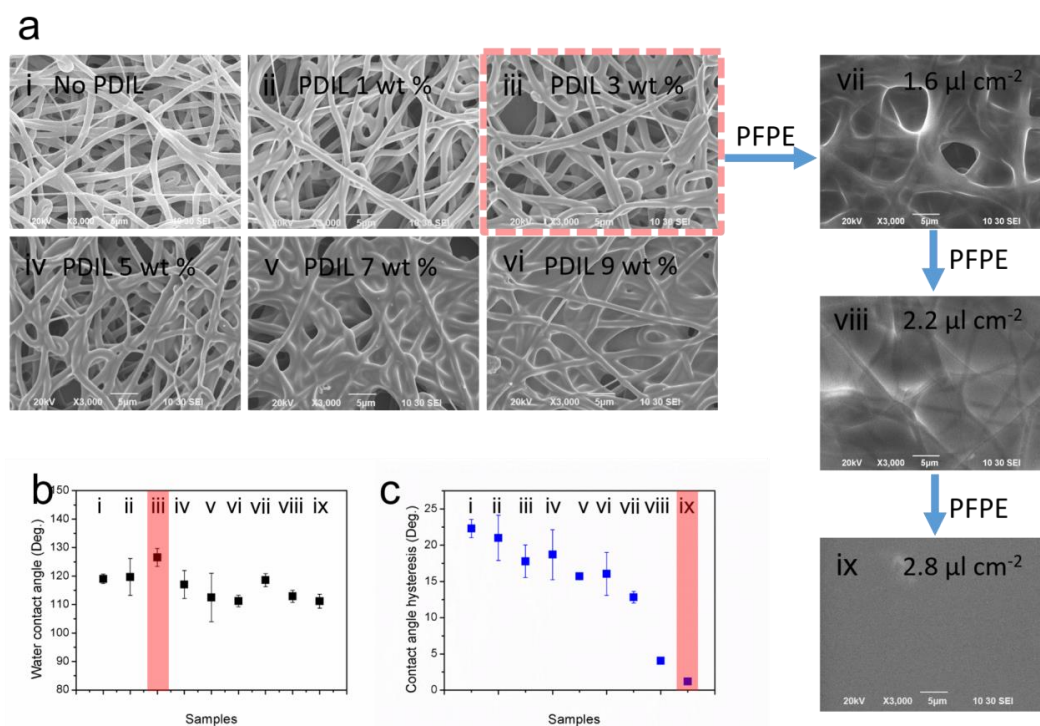


**Figure 6.5.** (a) SEM images of TPU NM (i), TPU NMs coated with PDIL solutions of varied concentrations (ii-vi are 1, 3, 5, 7, and 9 wt % respectively), PFPE-PDIL-TPU FSMs with varied PFPE infusion amount (vii-ix are 1.6, 2.2, and 2.8  $\mu\text{L}/\text{cm}^2$ ); (b) and (c) are their corresponding water contact angle (WCA) and contact angle hysteresis (CAH).

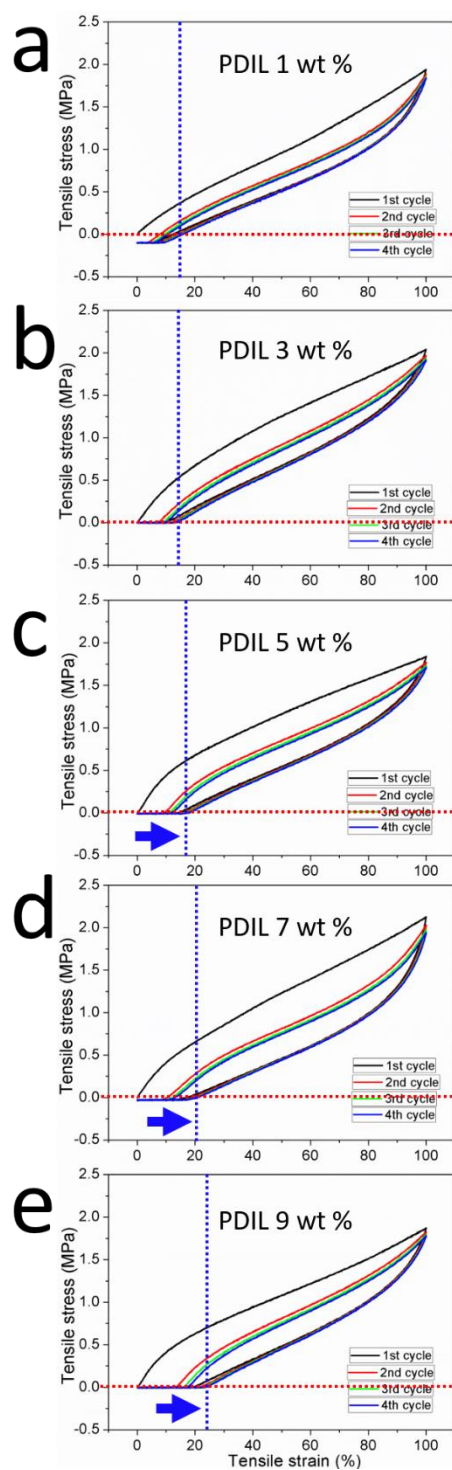


**Figure 6.6.** Stress-strain diagrams (including four strain-release cycles with a maximum tensile strain of 100 %) of the TPU NMs coated with PDIL solutions with different concentrations (a-e are 1, 3, 5, 7, 9 wt %, respectively). The red dotted line shows the status that the tensile stress of the membrane returns to 0, and the blue dotted line indicates the

elastic recovery value.

The formed smooth and flawless topography on the PFPE-PDIL-TPU flexible slippery membrane (FSM) is not in a steady state due to the easy deformation of the TPU-PDIL composite substrate and the flow ability of the liquid lubricant. As shown by Figure 6.7 a-d, the flat surface topography turns into rough and porous upon an external tensile stress. It is because that the stretch-triggered deformation reduces the pressure in the porous matrix and drives the lubricant to flow and retreat into the pores.<sup>149</sup> As a consequence, the free water-sliding behavior on the flat and lubricated surface will be decelerated and even halted after a sufficient tensile strain is reached. Figure 6.7e demonstrates the sliding-control of a water droplet (~30  $\mu$ l) on the tilted FSM. To be specific, the water droplet slides freely on the undeformed FSM, but slows down and nearly stops when a tensile stress is applied (with tensile strain of ~50 %). Meanwhile, the droplet shape changes apparently from a regular hemisphere to an irregular one (Figure 6.7f) with advancing angle much bigger than receding angle indicating an increased sliding resistance force encountered. After the stress is removed, the high-speed sliding behavior is started again and the droplet shape converts back to a regular hemisphere indicating the recovery to the smooth topography of the FSM (Figure 6.7d). In agreement with this performance, the recorded contact angle hysteresis (CAH) and the sliding angle (SA) change along with different tensile strain (0-100 %) shows that the difficulty of water sliding increases with enhanced deformation (Figure 6.7 g-h).

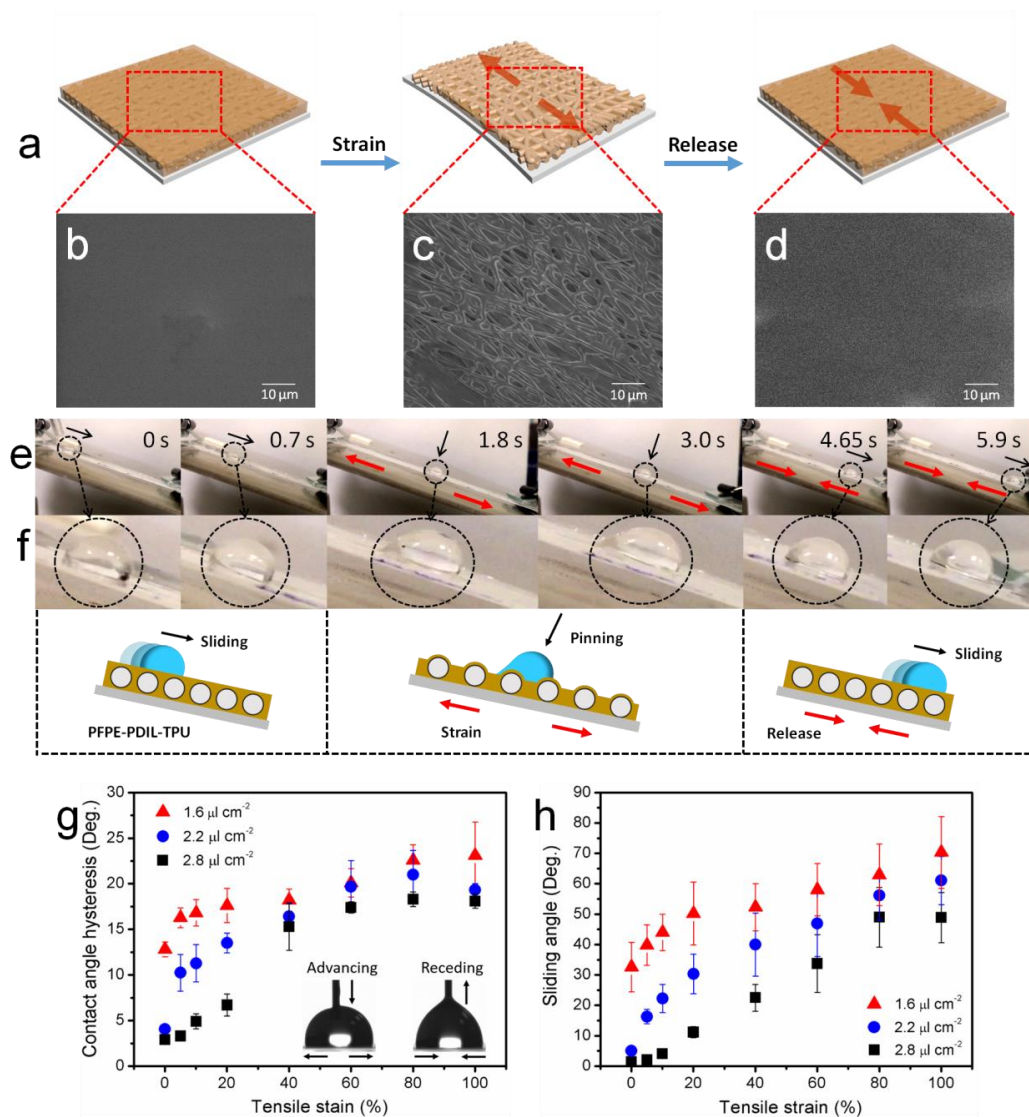


**Figure 6.7.** Stain/release triggered topography change and corresponding water sliding control on the as-prepared PFPE-PDIL-TPU FSM. (a) The topography transition between smooth and rough along with the relaxing and straining of the FSM, respectively, shown by FE-SEM images (b-d); (c) shows the topography of the FSM with tensile strain of 100 %; (e) sliding control of a water droplet ( $\sim 30 \mu\text{l}$ ) on the tilted ( $\sim 18^\circ$ ) FSM by straining and relaxing (with maximum tensile strain of  $\sim 50\%$ ); (f) shows the magnified images of the droplet shapes corresponding to the different sliding states in (e); (g-h) CAH and SA change along with increasing tensile strain (the inset in f shows the measurement method of the advancing/receding CAs).

A more detailed topography change along with varied tensile strain extracted from an integral strain-release cycle is shown in Figure 6.8. Namely, the roughness and the surface pore ratio increases gradually with the increasing tensile strain, which is responsible for the gradually raised water sliding obstruction force. Note that a sufficient infusion amount of PFPE should be ensured, otherwise it is difficult to obtain a water-sliding surface even without external stress because of the incomplete filling of the pores (Figure 6.5a vii-ix). Similar PFPE infused flexible system for the control of droplet mobility was reported before integrating a Teflon porous matrix.<sup>149</sup> However, in this work, the creative synthesis of PDIL make it possible to infuse PFPE into a TPU nanofiber matrix, which has low chemical affinity towards PFPE itself, and thus to fabricate a membrane that can afford higher tensile strain (the elongation at break is ~220 %, Figure 6.9). Moreover, as a result of the high tensile strain or great degree of deformation, a new function can be developed on the prepared FSM: enhanced condensation triggered by the relaxation of the imposed strain.

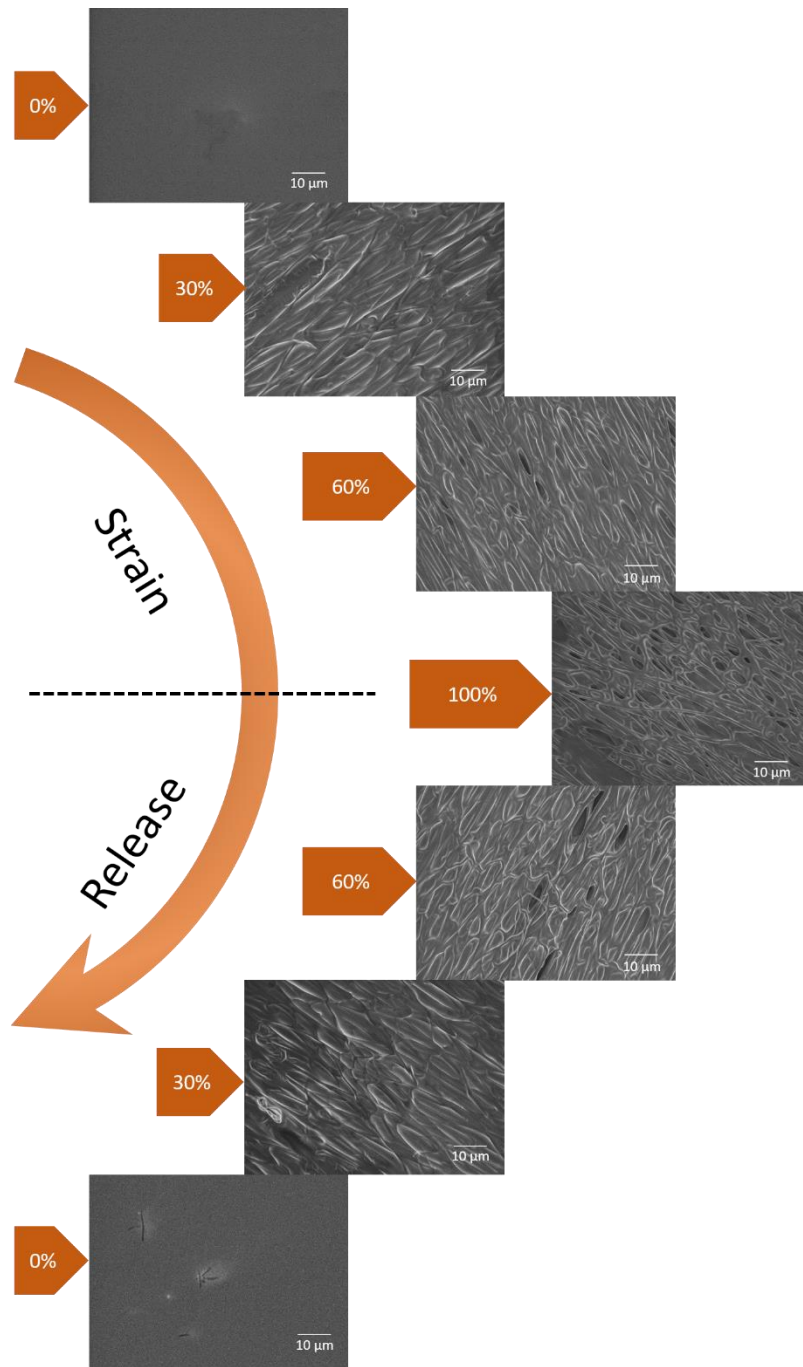


**Figure 6.8.** FE-SEM images showing the topographies of the as-prepared FSM with different tensile strain (0, 30, 60, 100 %) extracted from an integral strain-release cycle.

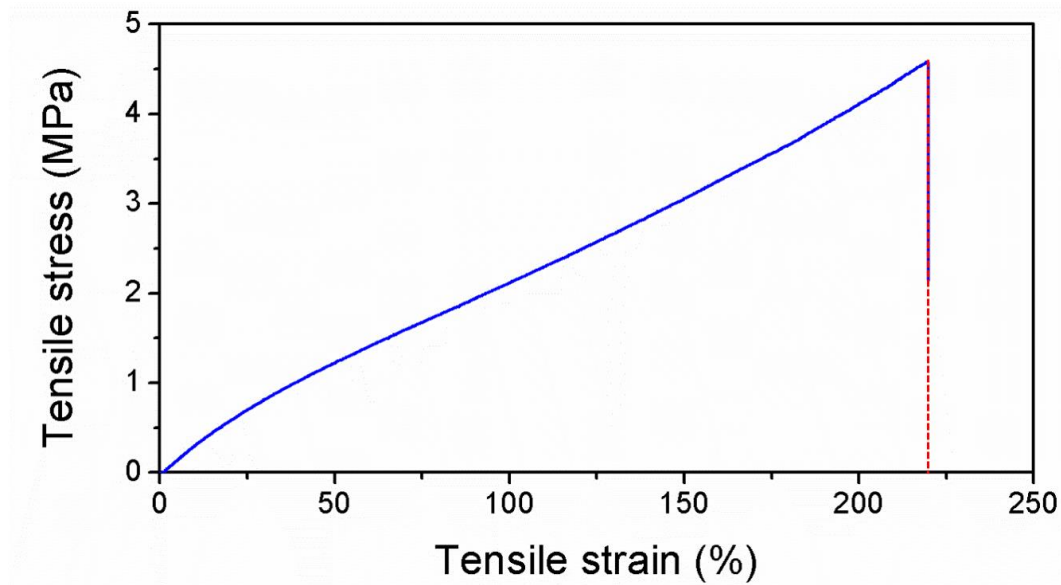


*Figure 6.9.* Stress-strain diagram showing the elongation at break of the prepared PFPE-PDIL-TPU FSM.

In addition to the controllable sliding and pinning of water droplets, which is one critical feature to enhance the water condensation and shedding, the affordable high deformation degree of the FSM is another advantage to further enhance the water condensation and drainage. To be specific, water droplets are more easily to be pinned on the surface when the FSM is strained, which contributes to the formation of the initial condensation nucleus to capture more water droplets to condense. Upon relaxing of the FSM, some droplets may start to slide due to the topography transition of the surface from rough to smooth. Furthermore, those smaller droplets that are unable to slide can coalesce together owing to the significant distance decrease or even the position overlap between two adjacent droplets along with the high degree of surface reversion. The sizes of those coalesced droplets are more likely to exceed the sliding

threshold value and start to shed. The enhanced water condensation and sliding along with release of the FSM has been investigated in two situations. As shown in Figure 6.10a, several adjacent water droplets were firstly added onto the top surface of the bi-directionally stretched FSM. During the decrease of the tensile stress, the membrane reverted gradually with adhered water droplets coalescing together along the reverting direction until they start sliding. Also, during the out-plane deformation from strained to relaxed state by dragging the center of the circular FSM, some adhered fog droplets coalesced along the spoke direction and achieved a drastic size increase for shedding (Figure 6.10c, d). In theory, a higher degree of deformation of the FSM means more coalescence among adjacent droplets, which in turn lead to more efficient liquid drainage. Comparing to the complicated design of wettability or shape gradients on rigid surface, which is a common strategy to improve liquid condensation and drainage, the method introduced here provides another solution with improved controllability and flexibility.

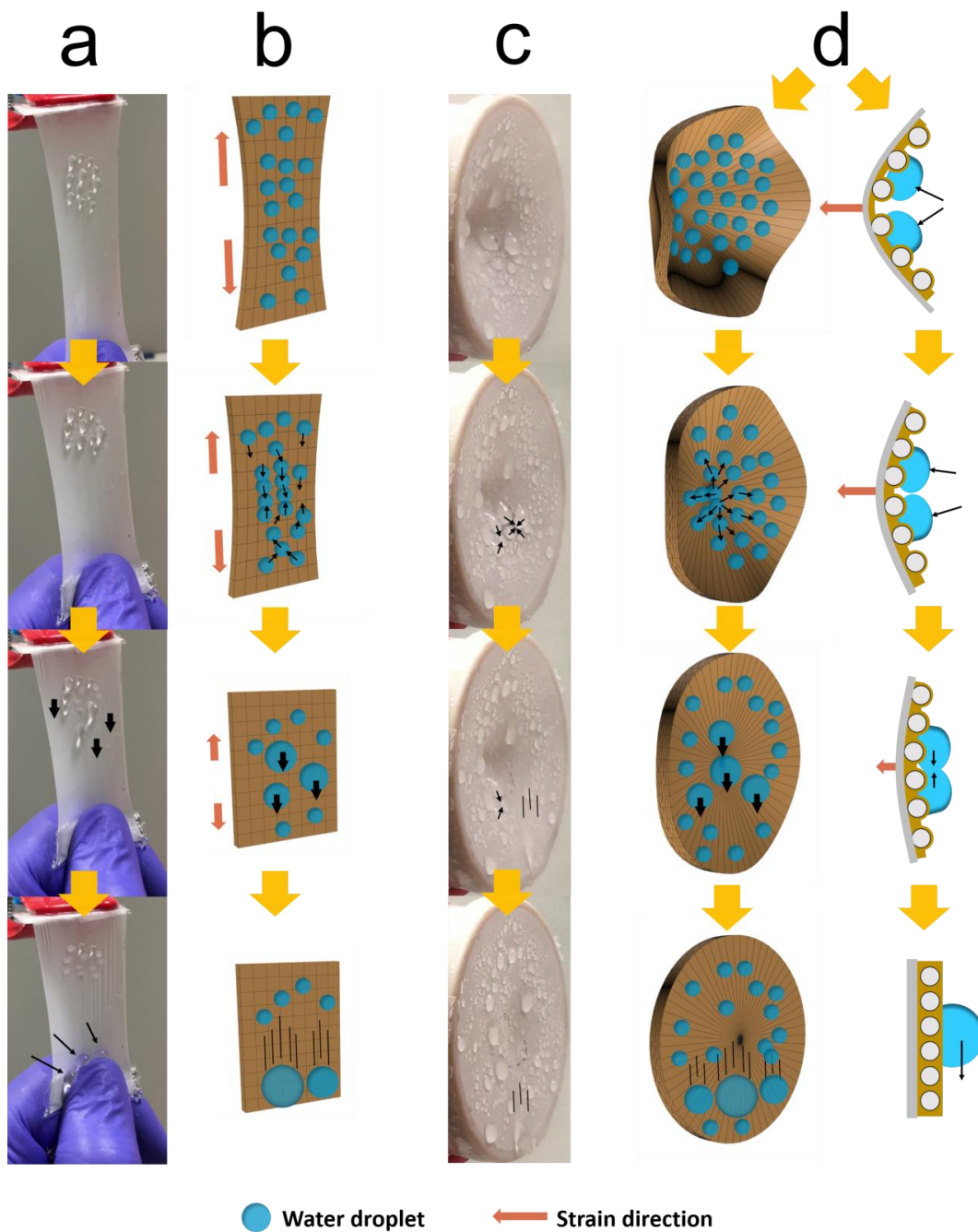


**Figure 6.10.** Demonstration of the enhanced condensation of pinned water drops along with the relaxation of the FSM from a strained status. (a-b) Water condensation during the relaxation from a bilateral and in-plane stretching; (c-d) water condensation during the relaxation from an out-plane stretching (the right column of d illustrates the side view of the coalescence of two adjacent droplets located around the dragging point).

The strain responsive water sliding control and the remarkably high deformation ability possessed by the prepared FSM make it a potential water collector that is more suitable to be used in an environment with strong wind. The wind in nature has pro and con for the efficiency of water collecting. First, the accelerated fog droplets in soft wind are more readily to be captured by a solid surface because of the increased impact force. Consistent with this point, our investigation of the distinct improvement of the water collection efficiency on both the flexible and rigid slippery membrane (RSM) in wind with speed from 0 to  $2 \text{ m s}^{-1}$  (Figure 6.11e) also indicates the obvious advantage brought by a soft wind. Therefore, even without deliberate modification with wettability or shape gradients on the surface, water condensation can be highly enhanced by only strengthening the directional impact. However, as the wind power increases, more captured water droplets are blown away because of the easy-sliding property of the slippery surface, especially the rigid one (grey columns in Figure 6.11e), on which water collection efficiency has a sharp decrease with the increasing wind power. This is because that there is no deformation occurred on the RSM even under increasingly strong wind and thus the surface can hardly prevent the splash of water (Figure 6.11d). From Figure 6.11b, water splashing can be observed along varied directions off the RSM and the captured droplets can hardly coalesce together and shed to the collecting container. Also in the rightmost image of Figure 6.11b, splashed water from the RSM can be observed everywhere on the background wall near the membrane indicating the severe water loss on the RSM

in strong wind. Compared to that, the FSM retains the water collection efficiency with a significant degree: as wind power increases, the decrease of collected water amount is much more moderate (Figure 6.11e, red columns). Meanwhile, an interesting water collection process can be observed on the FSM (Figure 6.11a): at early stage, the water droplets pinned on the membrane are driven to slide to the boundary and fixed; then with more droplets coalesce at the boundary, larger drops are formed and start to slide down along the boundary until they reach the bottom; finally, the accumulated drops drip down when they have adequate volumes. During the process, very few droplets splash out of the surface (it can also be observed from the rightmost image in Figure 6.11a that almost no splashed water is collected on the background wall), which ensures the efficient collection of water. The better performance of the FSM at water collection in strong wind can be mainly attributed to the sensitive deformation increment induced by increasing wind power, which consequently generates increasing sliding resistance force and thus effectively reduces the water splashing. In additions, splashing on soft substrates is harder than that on rigid substrates due to energy losses caused by immediate deformations of soft substrates after impact, which was recently investigated by Howland et al.<sup>265</sup>

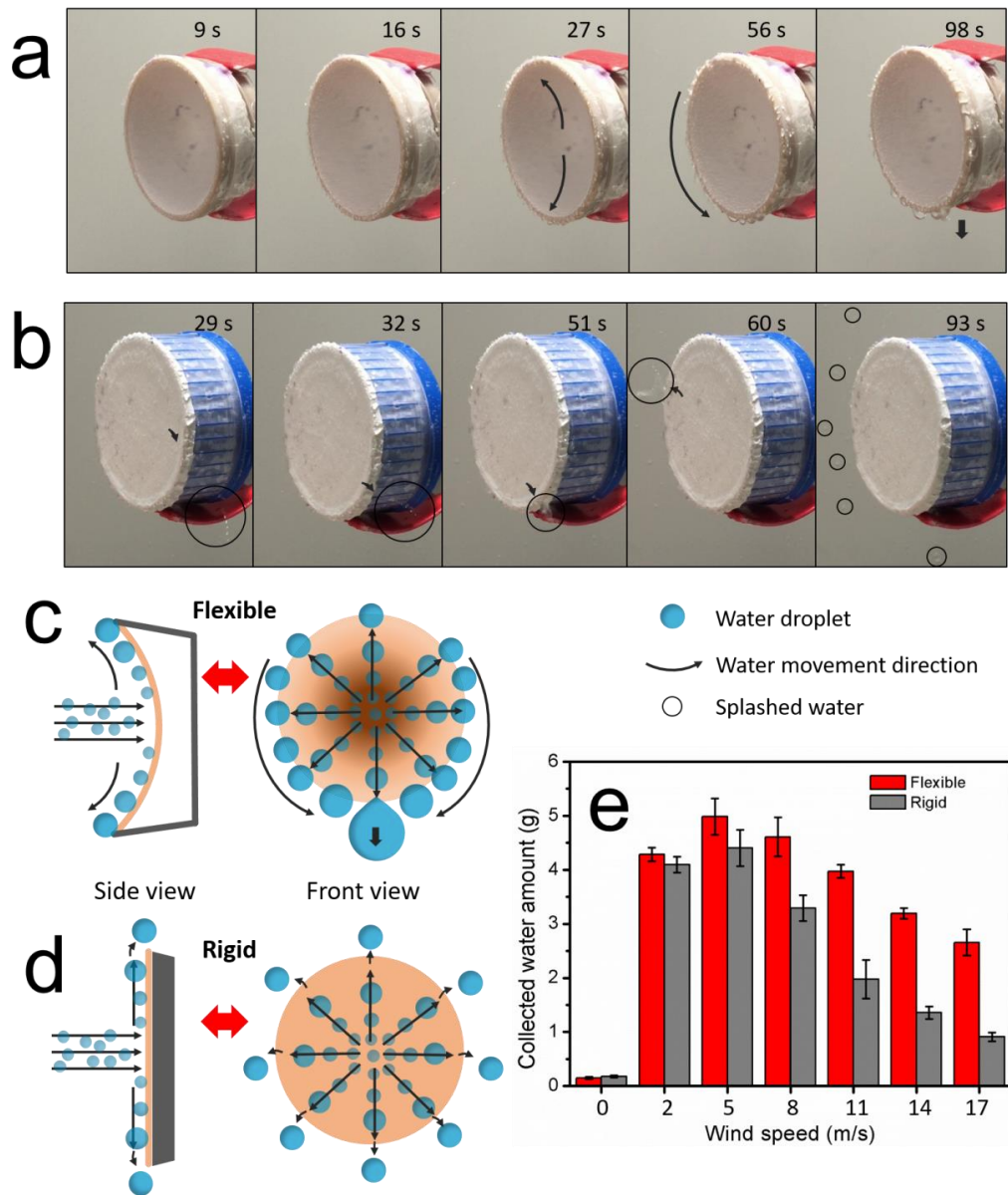


**Figure 6.11.** Investigation of the water collection process on the prepared FSM (a) in a strong wind ( $12 \text{ m s}^{-1}$ ) with the RSM (b) as reference (the rightmost images of both indicating the water splashing extent by the quantity of the splashed water droplets collected on the background wall). (c-d) Illustration of the water droplets movement on the prepared FSM and the RSM respectively during the water collection process in strong wind. (e) Comparison of the amount of collected water in 5 minutes by the FSM and the RSM in different wind power.

Moreover, through wind force analysis (Figure 6.12), there is another possible reason for the droplets-fixing at the boundary of the FSM that the composite wind force of the incoming and the backflow wind has the opposite direction to the movement of the water droplets and thus impeding the water splashing off the boundary of the FSM. In contrast, the composite wind force at the boundary of the RSM can aggravate the water splashing due to its small intersection angle ( $< 90^\circ$ ) with droplet movement, which also results in the poor water collection efficiency of the rigid surface in strong wind. To be specific, the wind directed to the membrane surface will change direction and form backflow wind which is the driven force leading the water droplets to move to the boundary and even splash out. At the boundary of the RSM, the direction of the backflow wind is vertical to that of the incoming wind, which would generate a force enhancing the splashing of the water droplets off the surface. In contrast, the backflow wind at the boundary of the FSM is in opposite direction with the incoming wind (with vector angle  $>90^\circ$ ). Therefore, the generated composite force will hinder the water from splashing out of the surface.

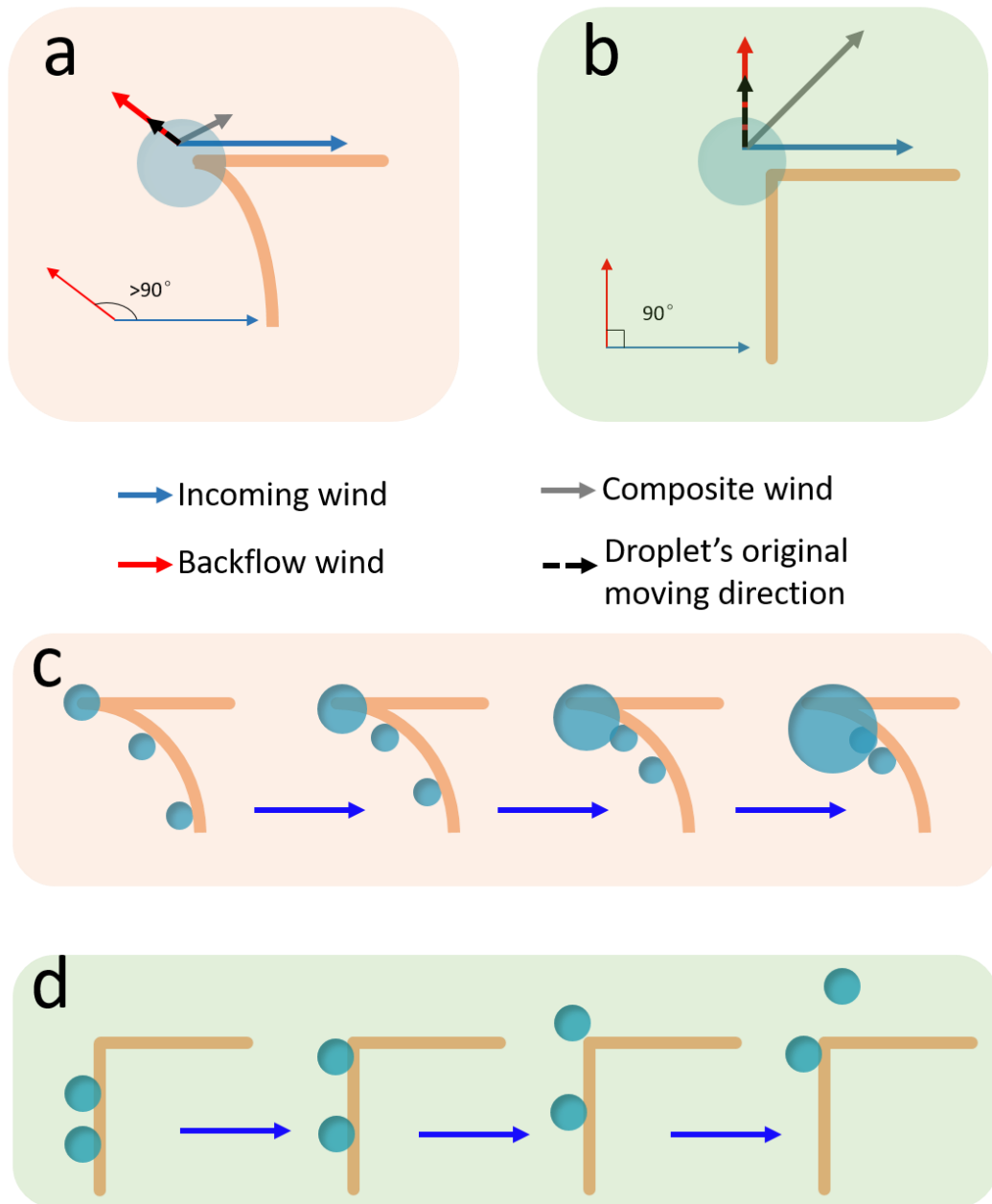


**Figure 6.12.** The driven force analysis and the droplet movement at the boundary of the FSM and the RSM (all the images are presented in side view). (a-b) The analysis of the interaction between the incoming wind force and the backflow wind force, and whether the composite wind force is enhancing the splashing of water droplets off the surface at the boundary of the FSM and the RSM, respectively. (c-d) Illustration of the water droplets movement at the boundary of the FSM and the RSM, respectively.

## 6.4 Conclusion

In conclusion, a flexible slippery membrane has been fabricated by infusing PFPE into a PDIL coated electrospun TPU nanofiber matrix. The innovative production of the coating agent PDIL with low surface energy, high chemical affinity to PFPE, sufficient flexibility and strong physical adhesion broadens the selection of porous matrix that can immobilize PFPE. The strain/release induced manipulation of water pinning/sliding, integrated with the high degree of deformation make the prepared FSM a potential material to enhance water/liquid condensation and collection. Besides, due to the deformation sensitive water sliding resistance change and the wind direction adjustment, the FSM exhibits the ability to preserve the captured water from being blown away by strong wind. This concept may provide solutions to develop water-collecting devices that are more suitable to be used in the real nature.

## Chapter 7

### Conclusions and Suggestions for Future Work

#### 7.1 Conclusion

In this thesis, a systematic study has been presented on design and development of textile based smart materials integrating biomimetic concepts to manipulate liquid behaviors including wetting/non-wetting, condensation/coalescence, rolling/sliding, and real-time mobility. The stimuli-responsive feature of the as-prepared materials endows the manipulation of liquid behavior with flexibility, adaptivity, reversibility, and controllability. For wetting behaviors manipulation, transition between non-extreme wetting states—hydrophilicity and hydrophobicity, and extreme wetting states—superhydrophilicity and superhydrophobicity have been both achieved inspired by lotus leaf. Mechanism insights into the wettability transition and the wetting degree have been provided in view of the surface energy and structure. For manipulation of liquid condensation and coalescence, both the wettability gradient and shape gradient have been considered inspired by desert beetle back and spider silk in designing the smart textile surface. The enhanced water condensation and coalescence have been investigated by a variety of assessment methods. For the real-time mobility manipulation, a pitcher plant inspired slippery surface has been fabricated by the incorporation of a flexible membrane. Mechanism insights into

the tensile stress-responsive and real-time control towards the liquid mobility have been provided.

The conclusive contributions of this thesis are detailedly summarized as follows. Firstly, the preparation of a thermo-responsive nanofibrous membrane through a SI-ATRP method has been introduced. The as-prepared PNIPAAm-RC membrane shows a switchable wettability, which makes it a smart material with controllable oil/water separation function. As reported, the oil/water separation mode can be switched by simply changing the operating temperature. Also, benefiting from the large surface area provided by electrospun nanofibers, the efficiency and capacity of oil/water absorption were highly improved. Secondly, a cost-effective TiO<sub>2</sub> doped PVDF nanofiber membrane has been successfully fabricated by one-step electrospinning. The as-prepared nanofibers had unique beads-on-string structure and formed highly roughened top surface. Switched by simple UV irradiation and heating treatment, the TiO<sub>2</sub>/PVDF membrane can exhibit transition between superhydrophobic/superoleophilic and superhydrophilic/underwater superoleophobic states, which can realize an on-demand oil/water separation by controlling the passing of water or oil. More importantly, this TiO<sub>2</sub>/PVDF membrane possesses excellent anti-fouling property under UV irradiation by automatically removing the oil stain from the surface, which is significant in saving solvents and recycling materials. This recyclable, easily scaled-up, and controllable smart nanofiber membrane can provide solutions to complex and industry-scale oily water treatment. Thirdly, a

superhydrophobic surface integrated with light-induced superhydrophilic bumps has been successfully fabricated by a simple method. Utilizing the beads forming feature of  $\text{TiO}_2$  sol on a superhydrophobic surface, raised  $\text{TiO}_2$  bumps are obtained, which provides surface energy gradient and Laplace pressure gradient cooperatively accelerating the directed coalescence of water droplets. Simply triggered by sunlight, a sustainable energy source, the superhydrophilicity of  $\text{TiO}_2$  can be achieved without additional effort, which may provide ideas to developing smart water collection device. Finally, a flexible slippery membrane has been fabricated by infusing PFPE into a PDIL coated electrospun TPU nanofiber matrix. The strain/release induced manipulation of water pinning/sliding, integrated with the high degree of deformation make the prepared FSM a potential material to enhance water/liquid condensation and collection. Besides, due to the deformation sensitive water sliding resistance change and the wind direction adjustment, the FSM exhibits the ability to preserve the captured water from being blown away by strong wind. This concept may provide solutions to develop water-collecting devices that are more suitable to be used in the real nature. The textile based smart and biomimetic materials presented in this thesis can shed light on the future exploration of low-cost, multifunctional, and easy-manipulate materials or devices that can be applied on environmental technology.

## **7.2 Suggestions for Future Work**

Materials or surfaces design for manipulation of liquid behaviors is an

ever-lasting research topic. Although great research progress in laboratory level has been made in developing smart or biomimetic materials with functions of manipulating liquid behaviors, the industrial production or application of such materials only stays in primary stage. Therefore, developing low-cost, easy-prepare, and durable materials with efficient performance is the most important target from the industrial process point of view. Based on the progress achieved and the shortages exist in design and fabrication of materials for liquid manipulation, some future works are suggested as follows.

- (1) The SI-ATRP method used in the temperature-responsive system is not so cost-effective to be scaled up because the reaction condition involving two steps isolating from water or oxygen is extremely demanding which will highly increase the production cost. Seeking reaction with less-demanding condition or other cheaper polymer substitute to simplify the fabrication process and lower the cost is the an important issue.
- (2) PNIPAAm brushes with more adaptive LCST can be synthesized by fine-adjusting the polymer characteristics, e.g., Mn and PDI, or grafting density. Also, by copolymerization with other polymers or synergy with other molecules, the reported method in Chapter 3 may be extended to a variety of applications (e.g., drug delivery, chemical separation, ion exchange, emulsion separation, and molecule detection).
- (3) The response rate of the membrane reported in Chapter 4 along with the stimuli such as UV light exposure or heat treatment is not fast enough, which

may limit its efficiency and practicability. Other elements doping or incorporating with the TiO<sub>2</sub> nanoparticles can be explored to narrow the energy gap between valence band and conduction band, and thus to shorten the response time.

- (4) Fabricate more stable textile substrates to hold TiO<sub>2</sub>. The high photocatalytic activity of TiO<sub>2</sub> will cause damage to the substrate and shorten the usage period. Oxidation, UV, and aging resisting agents or polymers should be utilized to reinforce the PVDF substrate to increase the service cycles of the material.
- (5) For the method presented in Chapter 5, more hydrophobic fabrics such as polyester or polystyrene should be explored to fabricate superhydrophobic substrate with better water drainage performance. Evaluate the associativity between the fabric and the SiO<sub>2</sub> nanoparticles as well as the long chain silane. Further study the water condensation or coalescence efficiency, and establish a balance between water capturing and drainage performance.
- (6) Try to shorten the activation time needed to turn the TiO<sub>2</sub> bumps superhydrophilic. Further study the adhesion mechanism of TiO<sub>2</sub> bumps onto the superhydrophobic layer.
- (7) Further improve the elastic recovery of the TPU substrate reported in Chapter 6 by modifying the monomers, fabricating copolymers or doping other materials.
- (8) Applying the PDIL onto other substrates such as metal or glass to immobilize

PFPE and design appropriate device which can transform wind power to condensation driven force to collect more water in wind.

## References

1. Galaev, I.; Mattiasson, B., *Smart polymers for bioseparation and bioprocessing*. CRC Press: 2001.
2. Pearce, E. M., *Polymers: Chemistry and physics of modern materials*. Wiley Online Library: 1992.
3. Hoffman, A. S.; Stayton, P. S.; Bulmus, V.; Chen, G.; Chen, J.; Cheung, C.; Chilkoti, A.; Ding, Z.; Dong, L.; Fong, R., Really smart bioconjugates of smart polymers and receptor proteins. *Journal of Biomedical Materials Research Part A* **2000**, *52* (4), 577-586.
4. Galaev, I. Y.; Mattiasson, B., 'Smart' polymers and what they could do in biotechnology and medicine. *Trends in biotechnology* **1999**, *17* (8), 335-340.
5. Ebara, M.; Yamato, M.; Hirose, M.; Aoyagi, T.; Kikuchi, A.; Sakai, K.; Okano, T., Copolymerization of 2-carboxyisopropylacrylamide with N-isopropylacrylamide accelerates cell detachment from grafted surfaces by reducing temperature. *Biomacromolecules* **2003**, *4* (2), 344-349.
6. Atkins, P. W.; De Paula, J., *Atkins' Physical chemistry*, volume 8. ed. Oxford: 2006.
7. White, M. A., *Properties of materials*. Oxford University Press: 1999.
8. Ganapathy, S.; Rajamohanam, P. R.; Badiger, M. V.; Mandhare, A. B.; Mashelkar, R. A., Proton magnetic resonance imaging in hydrogels: volume phase transition in poly (N-isopropylacrylamide). *Polymer* **2000**, *41* (12), 4543-4547.
9. Zeng, F.; Tong, Z.; Feng, H., NMR investigation of phase separation in poly (N-isopropyl acrylamide)/water solutions. *Polymer* **1997**, *38* (22), 5539-5544.
10. Tanaka, N.; Matsukawa, S.; Kurosu, H.; Ando, I., A study on dynamics of water in crosslinked poly (N-isopropylacrylamide) gel by nmr spectroscopy. *Polymer* **1998**, *39* (20), 4703-4706.
11. Tokuhito, T.; Amiya, T.; Mamada, A.; Tanaka, T., NMR study of poly

- (N-isopropylacrylamide) gels near phase transition. *Macromolecules* **1991**, 24 (10), 2936-2943.
12. Cowie, J. M. G., *Polymers: Chemistry and Physics of Modern Materials*, 2nd edn; Blackie. *New York* **1991**, 236.
  13. Schild, H. G., Poly (N-isopropylacrylamide): experiment, theory and application. *Progress in polymer science* **1992**, 17 (2), 163-249.
  14. 夏帆, 仿生多尺度智能界面材料的构筑及研究. **2008**.
  15. Kishi, R.; Hirasa, O.; Ichijo, H., Fast responsive poly (N-sopropylacrylamide) hydrogels prepared by  $\gamma$ -ray irradiation. *Polymer Gels and Networks* **1997**, 5 (2), 145-151.
  16. Wu, X. S.; Hoffman, A. S.; Yager, P., Synthesis and characterization of thermally reversible macroporous poly (N-isopropylacrylamide) hydrogels. *Journal of Polymer Science Part A: Polymer Chemistry* **1992**, 30 (10), 2121-2129.
  17. Zhang, X.-Z.; Zhuo, R.-X., Preparation of fast responsive, thermally sensitive poly (N-isopropylacrylamide) gel. *European Polymer Journal* **2000**, 36 (10), 2301-2303.
  18. Pelton, R., Temperature-sensitive aqueous microgels. *Advances in colloid and interface science* **2000**, 85 (1), 1-33.
  19. Pelton, R. H.; Chibante, P., Preparation of aqueous latices with N-isopropylacrylamide. *Colloids and Surfaces* **1986**, 20 (3), 247-256.
  20. Morris, G. E.; Vincent, B.; Snowden, M. J., Adsorption of Lead Ions onto N-Isopropylacrylamide and Acrylic Acid Copolymer Microgels. *Journal of colloid and interface science* **1997**, 190 (1), 198-205.
  21. Saunders, B. R.; Vincent, B., Microgel particles as model colloids: theory, properties and applications. *Advances in colloid and interface science* **1999**, 80 (1), 1-25.
  22. Liang, L.; Feng, X.; Liu, J.; Rieke, P. C.; Fryxell, G. E., Reversible surface properties of glass plate and capillary tube grafted by photopolymerization of N-isopropylacrylamide. *Macromolecules* **1998**, 31 (22), 7845-7850.

23. Liang, L.; Rieke, P. C.; Liu, J.; Fryxell, G. E.; Young, J. S.; Engelhard, M. H.; Alford, K. L., Surfaces with reversible hydrophilic/hydrophobic characteristics on cross-linked poly (N-isopropylacrylamide) hydrogels. *Langmuir* **2000**, *16* (21), 8016-8023.
24. Liang, L.; Rieke, P. C.; Fryxell, G. E.; Liu, J.; Engehard, M. H.; Alford, K. L., Temperature-sensitive surfaces prepared by UV photografting reaction of photosensitizer and N-isopropylacrylamide. *The Journal of Physical Chemistry B* **2000**, *104* (49), 11667-11673.
25. Kuckling, D.; Harmon, M. E.; Frank, C. W., Photo-cross-linkable PNIPAAm copolymers. 1. Synthesis and characterization of constrained temperature-responsive hydrogel layers. *Macromolecules* **2002**, *35* (16), 6377-6383.
26. Yakushiji, T.; Sakai, K.; Kikuchi, A.; Aoyagi, T.; Sakurai, Y.; Okano, T., Graft architectural effects on thermoresponsive wettability changes of poly (N-isopropylacrylamide)-modified surfaces. *Langmuir* **1998**, *14* (16), 4657-4662.
27. Sun, T.; Wang, G.; Feng, L.; Liu, B.; Ma, Y.; Jiang, L.; Zhu, D., Reversible switching between superhydrophilicity and superhydrophobicity. *Angewandte Chemie* **2004**, *116* (3), 361-364.
28. Qiu, Y.; Park, K., Environment-sensitive hydrogels for drug delivery. *Advanced drug delivery reviews* **2001**, *53* (3), 321-339.
29. Aoki, T.; Muramatsu, M.; Torii, T.; Sanui, K.; Ogata, N., Thermosensitive phase transition of an optically active polymer in aqueous milieu. *Macromolecules* **2001**, *34* (10), 3118-3119.
30. Gan, L. H.; Gan, Y. Y.; Deen, G. R., Poly (N-acryloyl-N '-propylpiperazine): A new stimuli-responsive polymer. *Macromolecules* **2000**, *33* (21), 7893-7897.
31. Gil, E. S.; Hudson, S. M., Stimuli-reponsive polymers and their bioconjugates. *Progress in polymer science* **2004**, *29* (12), 1173-1222.
32. Brannon-Peppas, L.; Peppas, N. A., Dynamic and equilibrium swelling

behaviour of pH-sensitive hydrogels containing 2-hydroxyethyl methacrylate. *Biomaterials* **1990**, *11* (9), 635-644.

33. Khare, A. R.; Peppas, N. A., Release behavior of bioactive agents from pH-sensitive hydrogels. *Journal of Biomaterials Science, Polymer Edition* **1993**, *4* (3), 275-289.
34. Godbey, W. T.; Wu, K. K.; Mikos, A. G., Poly (ethylenimine) and its role in gene delivery. *Journal of Controlled Release* **1999**, *60* (2), 149-160.
35. Godbey, W. T.; Mikos, A. G., Recent progress in gene delivery using non-viral transfer complexes. *Journal of Controlled Release* **2001**, *72* (1), 115-125.
36. Urtti, A.; Polansky, J.; Lui, G. M.; Szoka, F. C., Gene delivery and expression in human retinal pigment epithelial cells: effects of synthetic carriers, serum, extracellular matrix and viral promoters. *Journal of drug targeting* **2000**, *7* (6), 413-421.
37. Tang, M. X.; Redemann, C. T.; Szoka, F. C., In vitro gene delivery by degraded polyamidoamine dendrimers. *Bioconjugate chemistry* **1996**, *7* (6), 703-714.
38. Li, J.-J.; Zhou, Y.-N.; Luo, Z.-H., Smart fiber membrane for pH-induced oil/water separation. *ACS applied materials & interfaces* **2015**, *7* (35), 19643-19650.
39. Cao, Y.; Liu, N.; Fu, C.; Li, K.; Tao, L.; Feng, L.; Wei, Y., Thermo and pH dual-responsive materials for controllable oil/water separation. *ACS applied materials & interfaces* **2014**, *6* (3), 2026-2030.
40. Zhou, Y. N.; Li, J. J.; Luo, Z. H., Toward efficient water/oil separation material: Effect of copolymer composition on pH-responsive wettability and separation performance. *AIChE Journal* **2016**. *62*(5), 1758-1771.
41. Shiga, T.; Hirose, Y.; Okada, A.; Kurauchi, T., Bending of ionic polymer gel caused by swelling under sinusoidally varying electric fields. *Journal of Applied Polymer Science* **1993**, *47* (1), 113-119.
42. Gong, J. P.; Nitta, T.; Osada, Y., Electrokinetic modeling of the contractile

- phenomena of polyelectrolyte gels-one-dimensional capillary model. *Journal of Physical Chemistry* **1994**, *98* (38), 9583-9587.
43. Lahann, J.; Mitragotri, S.; Tran, T.-N.; Kaido, H.; Sundaram, J.; Choi, I. S.; Hoffer, S.; Somorjai, G. A.; Langer, R., A reversibly switching surface. *Science* **2003**, *299* (5605), 371-374.
  44. Porcar, I.; Perrin, P.; Tribet, C., UV– Visible Light: A Novel Route to Tune the Type of an Emulsion. *Langmuir* **2001**, *17* (22), 6905-6909.
  45. Higashi, N.; Shimizu, K.; Niwa, M., Surface monolayers of poly (L-glutamic acid)-functionalized amphiphiles: effect of attachment of spiropyran to the polymer segment. *Journal of colloid and interface science* **1997**, *185* (1), 44-48.
  46. Suzuki, A.; Tanaka, T., Phase transition in polymer gels induced by visible light. *Nature* **1990**, *346* (6282), 345.
  47. Wang, R.; Hashimoto, K.; Fujishima, A.; Chikuni, M.; Kojima, E.; Kitamura, A.; Shimohigoshi, M.; Watanabe, T., Light-induced amphiphilic surfaces. *Nature* **1997**, *388* (6641), 431.
  48. Wang, R.; Sakai, N.; Fujishima, A.; Watanabe, T.; Hashimoto, K., Studies of surface wettability conversion on TiO<sub>2</sub> single-crystal surfaces. *The Journal of Physical Chemistry B* **1999**, *103* (12), 2188-2194.
  49. Machida, M.; Norimoto, K.; Watanabe, T.; Hashimoto, K.; Fujishima, A., The effect of SiO<sub>2</sub> addition in super-hydrophilic property of TiO<sub>2</sub> photocatalyst. *Journal of Materials science* **1999**, *34* (11), 2569-2574.
  50. Miyauchi, M.; Nakajima, A.; Hashimoto, K.; Watanabe, T., A highly hydrophilic thin film under 1  $\mu\text{W}/\text{cm}^2$  UV illumination. *Advanced Materials* **2000**, *12* (24), 1923-1927.
  51. Sakai, N.; Fujishima, A.; Watanabe, T.; Hashimoto, K., Enhancement of the photoinduced hydrophilic conversion rate of TiO<sub>2</sub> film electrode surfaces by anodic polarization. *The Journal of Physical Chemistry B* **2001**, *105* (15), 3023-3026.
  52. Qi, K.; Xin, J. H., Room-temperature synthesis of single-phase anatase TiO<sub>2</sub>

- by aging and its self-cleaning properties. *ACS applied materials & interfaces* **2010**, *2* (12), 3479-3485.
53. Wang, R.; Wang, X.; Xin, J. H., Advanced visible-light-driven self-cleaning cotton by Au/TiO<sub>2</sub>/SiO<sub>2</sub> photocatalysts. *ACS Applied Materials & Interfaces* **2009**, *2* (1), 82-85.
  54. Kong, Y.; Liu, Y.; Xin, J. H., Fabrics with self-adaptive wettability controlled by “light-and-dark”. *Journal of Materials Chemistry* **2011**, *21* (44), 17978-17987.
  55. Emeline, A. V.; Rudakova, A. V.; Sakai, M.; Murakami, T.; Fujishima, A., Factors affecting UV-induced superhydrophilic conversion of a TiO<sub>2</sub> surface. *The Journal of Physical Chemistry C* **2013**, *117* (23), 12086-12092.
  56. Shull, K. R.; Karis, T. E., Dewetting dynamics for large equilibrium contact angles. *Langmuir* **1994**, *10* (1), 334-339.
  57. Tretinnikov, O. N.; Ikada, Y., Hydrogen bonding and wettability of surface-grafted organophosphate polymer. *Macromolecules* **1997**, *30* (4), 1086-1090.
  58. de Crevoisier, G.; Fabre, P.; Corpart, J.-M.; Leibler, L., Switchable tackiness and wettability of a liquid crystalline polymer. *Science* **1999**, *285* (5431), 1246-1249.
  59. Rieutord, F.; Salmeron, M., Wetting properties at the submicrometer scale: A scanning polarization force microscopy study. *The Journal of Physical Chemistry B* **1998**, *102* (20), 3941-3944.
  60. Yoo, D.; Shiratori, S. S.; Rubner, M. F., Controlling bilayer composition and surface wettability of sequentially adsorbed multilayers of weak polyelectrolytes. *Macromolecules* **1998**, *31* (13), 4309-4318.
  61. Thünemann, A. F.; Schnöller, U.; Nuyken, O.; Voit, B., Diazosulfonate polymer complexes: Structure and wettability. *Macromolecules* **2000**, *33* (15), 5665-5671.
  62. Thünemann, A. F., Complexes of polyethyleneimine with perfluorinated carboxylic acids: wettability of lamellar structured mesophases. *Langmuir*

- 2000**, *16* (2), 824-828.
63. Ichimura, K.; Oh, S.-K.; Nakagawa, M., Light-driven motion of liquids on a photoresponsive surface. *Science* **2000**, *288* (5471), 1624-1626.
  64. Tadmor, R., Line energy and the relation between advancing, receding, and young contact angles. *Langmuir* **2004**, *20* (18), 7659-7664.
  65. Young, T., An essay on the cohesion of fluids. *Philosophical Transactions of the Royal Society of London* **1805**, *95*, 65-87.
  66. Liu, X.; Liang, Y.; Zhou, F.; Liu, W., Extreme wettability and tunable adhesion: biomimicking beyond nature? *Soft matter* **2012**, *8* (7), 2070-2086.
  67. Nishino, T.; Meguro, M.; Nakamae, K.; Matsushita, M.; Ueda, Y., The lowest surface free energy based on- CF<sub>3</sub> alignment. *Langmuir* **1999**, *15* (13), 4321-4323.
  68. Wenzel, R. N., Resistance of solid surfaces to wetting by water. *Industrial & Engineering Chemistry* **1936**, *28* (8), 988-994.
  69. Dorrer, C.; R uhe, J., Some thoughts on superhydrophobic wetting. *Soft Matter* **2009**, *5* (1), 51-61.
  70. Cassie, A. B. D.; Baxter, S., Wettability of porous surfaces. *Transactions of the Faraday society* **1944**, *40*, 546-551.
  71. Vogler, E. A., Structure and reactivity of water at biomaterial surfaces. *Advances in colloid and interface science* **1998**, *74* (1), 69-117.
  72. Yoon, R.-H.; Flinn, D. H.; Rabinovich, Y. I., Hydrophobic interactions between dissimilar surfaces. *Journal of colloid and interface science* **1997**, *185* (2), 363-370.
  73. Berg, J. M.; Eriksson, L. G.; Claesson, P. M.; Borve, K. G., 3-component Langmuir-Blodgett-films with a controllable degree of polarity. *Langmuir* **1994**, *10* (4), 1225-1234.
  74. Wang, S.; Jiang, L., Definition of superhydrophobic states. *Advanced Materials* **2007**, *19* (21), 3423-3424.
  75. Ball, P., Engineering shark skin and other solutions. *Nature* **1999**, *400* (6744), 507-509.

76. Barthlott, W.; Neinhuis, C., Purity of the sacred lotus, or escape from contamination in biological surfaces. *Planta* **1997**, *202* (1), 1-8.
77. Neinhuis, C.; Barthlott, W., Characterization and distribution of water-repellent, self-cleaning plant surfaces. *Annals of botany* **1997**, *79* (6), 667-677.
78. Zhai, J.; Li, H. J.; Li, Y. S.; Li, S. H.; Jiang, L., Discovery of super-amphiphobic properties of aligned carbon nanotube films. *PHYSICS-BEIJING*- **2002**, *31* (8), 483-486.
79. Feng, L.; Li, S.; Li, Y.; Li, H.; Zhang, L.; Zhai, J.; Song, Y.; Liu, B.; Jiang, L.; Zhu, D., Super-hydrophobic surfaces: from natural to artificial. *Advanced materials* **2002**, *14* (24), 1857-1860.
80. Feng, L.; Zhang, Y.; Xi, J.; Zhu, Y.; Wang, N.; Xia, F.; Jiang, L., Petal effect: a superhydrophobic state with high adhesive force. *Langmuir* **2008**, *24* (8), 4114-4119.
81. Öner, D.; McCarthy, T. J., Ultrahydrophobic surfaces. Effects of topography length scales on wettability. *Langmuir* **2000**, *16* (20), 7777-7782.
82. Chen, W.; Fadeev, A. Y.; Hsieh, M. C.; Öner, D.; Youngblood, J.; McCarthy, T. J., Ultrahydrophobic and ultralyophobic surfaces: some comments and examples. *Langmuir* **1999**, *15* (10), 3395-3399.
83. Li, S.; Li, H.; Wang, X.; Song, Y.; Liu, Y.; Jiang, L.; Zhu, D., Super-hydrophobicity of large-area honeycomb-like aligned carbon nanotubes. *The journal of physical chemistry B* **2002**, *106* (36), 9274-9276.
84. Yoshimitsu, Z.; Nakajima, A.; Watanabe, T.; Hashimoto, K., Effects of surface structure on the hydrophobicity and sliding behavior of water droplets. *Langmuir* **2002**, *18* (15), 5818-5822.
85. Extrand, C. W., Model for contact angles and hysteresis on rough and ultraphobic surfaces. *Langmuir* **2002**, *18* (21), 7991-7999.
86. Herminghaus, S., Roughness-induced non-wetting. *EPL (Europhysics Letters)* **2000**, *52* (2), 165.
87. Bormashenko, E.; Stein, T.; Whyman, G.; Bormashenko, Y.; Pogreb, R.,

- Wetting properties of the multiscaled nanostructured polymer and metallic superhydrophobic surfaces. *Langmuir* **2006**, *22* (24), 9982-9985.
88. Marmur, A., Wetting on hydrophobic rough surfaces: to be heterogeneous or not to be? *Langmuir* **2003**, *19* (20), 8343-8348.
  89. Kennedy, R. J., Directional water-shedding properties of feathers. *Nature* **1970**, *227*, 736-737.
  90. Zheng, Y.; Gao, X.; Jiang, L., Directional adhesion of superhydrophobic butterfly wings. *Soft Matter* **2007**, *3* (2), 178-182.
  91. Gao, X.; Jiang, L., Biophysics: water-repellent legs of water striders. *Nature* **2004**, *432* (7013), 36-36.
  92. Parker, A. R.; Lawrence, C. R., Water capture by a desert beetle. *Nature* **2001**, *414* (6859), 33-34.
  93. Seely, M. K.; Hamilton, W. J., Fog catchment sand trenches constructed by tenebrionid beetles, *Lepidochora*, from the Namib Desert. *Science* **1976**, *193* (4252), 484-486.
  94. Seely, M. K., Irregular fog as a water source for desert dune beetles. *Oecologia* **1979**, *42* (2), 213-227.
  95. Chaudhury, M. K.; Whitesides, G. M. *How to make water run uphill*; DTIC Document: 1992.
  96. Daniel, S.; Chaudhury, M. K.; Chen, J. C., Fast drop movements resulting from the phase change on a gradient surface. *Science* **2001**, *291* (5504), 633-636.
  97. Lorenceau, É.; Quéré, D., Drops on a conical wire. *Journal of Fluid Mechanics* **2004**, *510*, 29-45.
  98. Bai, H.; Tian, X.; Zheng, Y.; Ju, J.; Zhao, Y.; Jiang, L., Direction controlled driving of tiny water drops on bioinspired artificial spider silks. *Advanced materials* **2010**, *22* (48), 5521-5525.
  99. Zheng, Y.; Bai, H.; Huang, Z.; Tian, X.; Nie, F.-Q.; Zhao, Y.; Zhai, J.; Jiang, L., Directional water collection on wetted spider silk. *Nature* **2010**, *463* (7281), 640-643.

100. Andrews, H. G.; Eccles, E. A.; Schofield, W. C. E.; Badyal, J. P. S., Three-dimensional hierarchical structures for fog harvesting. *Langmuir* **2011**, *27* (7), 3798-3802.
101. Manoj, K.; Chaudhury, M. K.; George, M. W., How to make water run uphill. *Science* **1992**, *256* (5063), 1539-1541.
102. Ju, J.; Bai, H.; Zheng, Y.; Zhao, T.; Fang, R.; Jiang, L., A multi-structural and multi-functional integrated fog collection system in cactus. *Nature communications* **2012**, *3*, 1247.
103. Xue, Y.; Wang, T.; Shi, W.; Sun, L.; Zheng, Y., Water collection abilities of green bristlegrass bristle. *RSC Advances* **2014**, *4* (77), 40837-40840.
104. Furmidge, C. G. L., Studies at phase interfaces. I. The sliding of liquid drops on solid surfaces and a theory for spray retention. *Journal of colloid science* **1962**, *17* (4), 309-324.
105. Bhushan, B.; Jung, Y. C.; Koch, K., Micro-, nano-and hierarchical structures for superhydrophobicity, self-cleaning and low adhesion. *Philosophical Transactions of the Royal Society of London A: Mathematical, Physical and Engineering Sciences* **2009**, *367* (1894), 1631-1672.
106. Bohn, H. F.; Federle, W., Insect aquaplaning: Nepenthes pitcher plants capture prey with the peristome, a fully wettable water-lubricated anisotropic surface. *Proceedings of the National Academy of Sciences of the United States of America* **2004**, *101* (39), 14138-14143.
107. Wong, T.-S.; Kang, S. H.; Tang, S. K. Y.; Smythe, E. J.; Hatton, B. D.; Grinthal, A.; Aizenberg, J., Bioinspired self-repairing slippery surfaces with pressure-stable omniphobicity. *Nature* **2011**, *477* (7365), 443-447.
108. Jiang, L.; Zhao, Y.; Zhai, J., A lotus-leaf-like superhydrophobic surface: a porous microsphere/nanofiber composite film prepared by electrohydrodynamics. *Angewandte Chemie* **2004**, *116* (33), 4438-4441.
109. Liu, Y.; Chen, X.; Xin, J. H., Can superhydrophobic surfaces repel hot water? *Journal of Materials Chemistry* **2009**, *19* (31), 5602-5611.
110. Wang, B.; Li, J.; Wang, G.; Liang, W.; Zhang, Y.; Shi, L.; Guo, Z.; Liu, W.,

- Methodology for robust superhydrophobic fabrics and sponges from in situ growth of transition metal/metal oxide nanocrystals with thiol modification and their applications in oil/water separation. *ACS applied materials & interfaces* **2013**, 5 (5), 1827-1839.
111. Li, J.; Shi, L.; Chen, Y.; Zhang, Y.; Guo, Z.; Su, B.-l.; Liu, W., Stable superhydrophobic coatings from thiol-ligand nanocrystals and their application in oil/water separation. *Journal of Materials Chemistry* **2012**, 22 (19), 9774-9781.
112. Dong, H.; Wang, N.; Wang, L.; Bai, H.; Wu, J.; Zheng, Y.; Zhao, Y.; Jiang, L., Bioinspired electrospun knotted microfibers for fog harvesting. *ChemPhysChem* **2012**, 13 (5), 1153-1156.
113. Tian, X.; Chen, Y.; Zheng, Y.; Bai, H.; Jiang, L., Controlling water capture of bioinspired fibers with hump structures. *Advanced Materials* **2011**, 23 (46), 5486-5491.
114. Bai, H.; Ju, J.; Zheng, Y.; Jiang, L., Functional fibers with unique wettability inspired by spider silks. *Advanced materials* **2012**, 24 (20), 2786-2791.
115. Chen, Y.; He, J.; Wang, L.; Xue, Y.; Zheng, Y.; Jiang, L., Excellent bead-on-string silkworm silk with drop capturing abilities. *Journal of Materials Chemistry A* **2014**, 2 (5), 1230-1234.
116. Hou, Y.; Chen, Y.; Xue, Y.; Wang, L.; Zheng, Y.; Jiang, L., Stronger water hanging ability and higher water collection efficiency of bioinspired fiber with multi-gradient and multi-scale spindle knots. *Soft Matter* **2012**, 8 (44), 11236-11239.
117. Sahni, V.; Labhasetwar, D. V.; Dhinojwala, A., Spider silk inspired functional microthreads. *Langmuir* **2011**, 28 (4), 2206-2210.
118. Tian, X.; Bai, H.; Zheng, Y.; Jiang, L., Bio-inspired Heterostructured Bead-on-String Fibers That Respond to Environmental Wetting. *Advanced Functional Materials* **2011**, 21 (8), 1398-1402.
119. Yuan, W.; Zhang, K.-Q., Structural evolution of electrospun composite fibers from the blend of polyvinyl alcohol and polymer nanoparticles. *Langmuir*

- 2012**, 28 (43), 15418-15424.
120. Feng, S.; Hou, Y.; Chen, Y.; Xue, Y.; Zheng, Y.; Jiang, L., Water-assisted fabrication of porous bead-on-string fibers. *Journal of Materials Chemistry A* **2013**, 1 (29), 8363-8366.
121. Wang, L.; Ji, X.-Y.; Wang, N.; Wu, J.; Dong, H.; Du, J.; Zhao, Y.; Feng, X.-Q.; Jiang, L., Biaxial stress controlled three-dimensional helical cracks. *NPG Asia Materials* **2012**, 4 (4), e14.
122. Hou, Y.; Chen, Y.; Xue, Y.; Zheng, Y.; Jiang, L., Water collection behavior and hanging ability of bioinspired fiber. *Langmuir* **2012**, 28 (10), 4737-4743.
123. Hou, Y.; Gao, L.; Feng, S.; Chen, Y.; Xue, Y.; Jiang, L.; Zheng, Y., Temperature-triggered directional motion of tiny water droplets on bioinspired fibers in humidity. *Chemical Communications* **2013**, 49 (46), 5253-5255.
124. Heng, X.; Xiang, M.; Lu, Z.; Luo, C., Branched ZnO wire structures for water collection inspired by cacti. *ACS applied materials & interfaces* **2014**, 6 (11), 8032-8041.
125. Ju, J.; Xiao, K.; Yao, X.; Bai, H.; Jiang, L., Bioinspired conical copper wire with gradient wettability for continuous and efficient fog collection. *Advanced Materials* **2013**, 25 (41), 5937-5942.
126. Zhai, L.; Berg, M. C.; Cebeci, F. Ç.; Kim, Y.; Milwid, J. M.; Rubner, M. F.; Cohen, R. E., Patterned superhydrophobic surfaces: toward a synthetic mimic of the Namib Desert beetle. *Nano Letters* **2006**, 6 (6), 1213-1217.
127. Ishii, D.; Yabu, H.; Shimomura, M., Novel biomimetic surface based on a self-organized metal– polymer hybrid structure. *Chemistry of Materials* **2009**, 21 (9), 1799-1801.
128. Chen, R.; Zhang, X.; Su, Z.; Gong, R.; Ge, X.; Zhang, H.; Wang, C., Perfectly hydrophobic silicone nanofiber coatings: preparation from methyltrialkoxysilanes and use as water-collecting substrate. *The Journal of Physical Chemistry C* **2009**, 113 (19), 8350-8356.
129. Thickett, S. C.; Neto, C.; Harris, A. T., Biomimetic surface coatings for

- atmospheric water capture prepared by dewetting of polymer films. *Advanced Materials* **2011**, *23* (32), 3718-3722.
130. Wang, B.; Zhang, Y.; Liang, W.; Wang, G.; Guo, Z.; Liu, W., A simple route to transform normal hydrophilic cloth into a superhydrophobic–superhydrophilic hybrid surface. *Journal of Materials Chemistry A* **2014**, *2* (21), 7845-7852.
131. Bai, H.; Wang, L.; Ju, J.; Sun, R.; Zheng, Y.; Jiang, L., Efficient water collection on integrative bioinspired surfaces with star-shaped wettability patterns. *Advanced Materials* **2014**, *26* (29), 5025-5030.
132. Leslie, D. C.; Waterhouse, A.; Berthet, J. B.; Valentin, T. M.; Watters, A. L.; Jain, A.; Kim, P.; Hatton, B. D.; Nedder, A.; Donovan, K., A bioinspired omniphobic surface coating on medical devices prevents thrombosis and biofouling. *Nature biotechnology* **2014**, *32* (11), 1134-1140.
133. Kratochvil, M. J.; Welsh, M. A.; Manna, U.; Ortiz, B. J.; Blackwell, H. E.; Lynn, D. M., Slippery Liquid-Infused Porous Surfaces that Prevent Bacterial Surface Fouling and Inhibit Virulence Phenotypes in Surrounding Planktonic Cells. *ACS Infectious Diseases* **2016**, *2* (7), 509-517.
134. Wei, C.; Zhang, G.; Zhang, Q.; Zhan, X.; Chen, F., Silicone Oil-Infused Slippery Surfaces Based on Sol–Gel Process-Induced Nanocomposite Coatings: A Facile Approach to Highly Stable Bioinspired Surface for Biofouling Resistance. *ACS Applied Materials & Interfaces* **2016**, *8* (50), 34810-34819.
135. Aizenberg, J., Slippery interfaces: A new concept in anti-biofouling materials. *European Cells and Materials* **2016**, *32* (5), 7.
136. Manna, U.; Raman, N.; Welsh, M. A.; Zayas-Gonzalez, Y. M.; Blackwell, H. E.; Palecek, S. P.; Lynn, D. M., Slippery Liquid-Infused Porous Surfaces that Prevent Microbial Surface Fouling and Kill Non-Adherent Pathogens in Surrounding Media: A Controlled Release Approach. *Advanced Functional Materials* **2016**, *26* (21), 3599-3611.
137. Stamatopoulos, C.; Hemrle, J.; Wang, D.; Poulikakos, D., Exceptional

- Anti-Icing Performance of Self-Impregnating Slippery Surfaces. *ACS Applied Materials & Interfaces* **2017**, 9(11), 10233-10242.
138. Kreder, M. J.; Alvarenga, J.; Kim, P.; Aizenberg, J., Design of anti-icing surfaces: smooth, textured or slippery? *Nature Reviews Materials* **2016**, 1, 15003.
139. Wang, N.; Xiong, D.; Lu, Y.; Pan, S.; Wang, K.; Deng, Y.; Shi, Y., Design and fabrication of the lyophobic slippery surface and its application in anti-Icing. *The Journal of Physical Chemistry C* **2016**, 120 (20), 11054-11059.
140. Dou, R.; Chen, J.; Zhang, Y.; Wang, X.; Cui, D.; Song, Y.; Jiang, L.; Wang, J., Anti-icing coating with an aqueous lubricating layer. *ACS applied materials & interfaces* **2014**, 6 (10), 6998-7003.
141. Liu, Q.; Yang, Y.; Huang, M.; Zhou, Y.; Liu, Y.; Liang, X., Durability of a lubricant-infused Electrospray Silicon Rubber surface as an anti-icing coating. *Applied Surface Science* **2015**, 346, 68-76.
142. Lv, J.; Song, Y.; Jiang, L.; Wang, J., Bio-inspired strategies for anti-icing. *ACS nano* **2014**, 8 (4), 3152-3169.
143. Wei, Q.; Schlaich, C.; Prévost, S.; Schulz, A.; Böttcher, C.; Gradzielski, M.; Qi, Z.; Haag, R.; Schalley, C. A., Supramolecular polymers as surface coatings: rapid fabrication of healable superhydrophobic and slippery surfaces. *Advanced Materials* **2014**, 26 (43), 7358-7364.
144. Aizenberg, J.; Aizenberg, M.; Kang, S. H.; Wong, T. S.; Kim, P., Slippery surfaces with high pressure stability, optical transparency, and self-healing characteristics. Google Patents: 2015.
145. Vogel, N.; Belisle, R. A.; Hatton, B.; Wong, T.-S.; Aizenberg, J., Transparency and damage tolerance of patternable omniphobic lubricated surfaces based on inverse colloidal monolayers. *Nature communications* **2013**, 4, 2176.
146. Wang, L.; McCarthy, T. J., Covalently attached liquids: instant omniphobic surfaces with unprecedented repellency. *Angewandte Chemie* **2016**, 128 (1), 252-256.

147. Liu, P.; Zhang, H.; He, W.; Li, H.; Jiang, J.; Liu, M.; Sun, H.; He, M.; Cui, J.; Jiang, L., Development of “Liquid-like” Copolymer Nanocoatings for Reactive Oil-Repellent Surface. *ACS nano* **2017**.
148. De Gennes, P.-G.; Brochard-Wyart, F.; Quéré, D., *Capillarity and wetting phenomena: drops, bubbles, pearls, waves*. Springer Science & Business Media: 2013.
149. Yao, X.; Hu, Y.; Grinthal, A.; Wong, T.-S.; Mahadevan, L.; Aizenberg, J., Adaptive fluid-infused porous films with tunable transparency and wettability. *Nature materials* **2013**, *12* (6), 529-534.
150. Park, K.-C.; Kim, P.; Grinthal, A.; He, N.; Fox, D.; Weaver, J. C.; Aizenberg, J., Condensation on slippery asymmetric bumps. *Nature* **2016**, *531*(7592), 78-82.
151. Kase, S.; Matsuo, T., Studies on melt spinning. I. Fundamental equations on the dynamics of melt spinning. *Journal of Polymer Science Part A: General Papers* **1965**, *3* (7), 2541-2554.
152. Jalili, R.; Aboutalebi, S. H.; Esrafilzadeh, D.; Shepherd, R. L.; Chen, J.; Aminorroaya-Yamini, S.; Konstantinov, K.; Minett, A. I.; Razal, J. M.; Wallace, G. G., Scalable one-step wet-spinning of graphene fibers and yarns from liquid crystalline dispersions of graphene oxide: towards multifunctional textiles. *Advanced Functional Materials* **2013**, *23* (43), 5345-5354.
153. Zhang, M.; Ogale, A. A., Carbon fibers from dry-spinning of acetylated softwood kraft lignin. *Carbon* **2014**, *69*, 626-629.
154. Wang, X.; Ding, B.; Sun, G.; Wang, M.; Yu, J., Electro-spinning/netting: a strategy for the fabrication of three-dimensional polymer nano-fiber/nets. *Progress in Materials Science* **2013**, *58* (8), 1173-1243.
155. Kim, M.; Beskok, A.; Kihm, K., Electro-osmosis-driven micro-channel flows: a comparative study of microscopic particle image velocimetry measurements and numerical simulations. *Experiments in Fluids* **2002**, *33* (1), 170-180.

156. Nguyen, D. D.; Tai, N.-H.; Lee, S.-B.; Kuo, W.-S., Superhydrophobic and superoleophilic properties of graphene-based sponges fabricated using a facile dip coating method. *Energy & Environmental Science* **2012**, *5* (7), 7908-7912.
157. Wang, R.; Xin, J. H.; Tao, X. M.; Daoud, W. A., ZnO nanorods grown on cotton fabrics at low temperature. *Chemical Physics Letters* **2004**, *398* (1), 250-255.
158. Tsubokawa, N.; Hosoya, M.; Yanadori, K.; Sone, Y., Grafting onto carbon black: Reaction of functional groups on carbon black with acyl chloride-capped polymers. *Journal of Macromolecular Science-Chemistry* **1990**, *27* (4), 445-457.
159. Benoit, D.; Chaplinski, V.; Braslau, R.; Hawker, C. J., Development of a universal alkoxyamine for "living" free radical polymerizations. *Journal of the American Chemical Society* **1999**, *121* (16), 3904-3920.
160. Kenausis, G. L.; Vörös, J.; Elbert, D. L.; Huang, N.; Hofer, R.; Ruiz-Taylor, L.; Textor, M.; Hubbell, J. A.; Spencer, N. D., Poly (L-lysine)-g-poly (ethylene glycol) layers on metal oxide surfaces: attachment mechanism and effects of polymer architecture on resistance to protein adsorption. *The Journal of Physical Chemistry B* **2000**, *104* (14), 3298-3309.
161. Biesalski, M.; Johannsmann, D.; Rühle, J., Synthesis and swelling behavior of a weak polyacid brush. *The Journal of chemical physics* **2002**, *117* (10), 4988-4994.
162. Biesalski, M.; Rühle, J., Synthesis of a poly (p-styrenesulfonate) brush via surface-initiated polymerization. *Macromolecules* **2003**, *36* (4), 1222-1227.
163. Fan, X.; Xia, C.; Fulghum, T.; Park, M.-K.; Locklin, J.; Advincula, R. C., Polymer brushes grafted from clay nanoparticles adsorbed on a planar substrate by free radical surface-initiated polymerization. *Langmuir* **2003**, *19* (3), 916-923.
164. Zhou, Q.; Fan, X.; Xia, C.; Mays, J.; Advincula, R., Living anionic surface initiated polymerization (SIP) of styrene from clay surfaces. *Chemistry of*

*materials* **2001**, *13* (8), 2465-2467.

165. Advincula, R.; Zhou, Q.; Park, M.; Wang, S.; Mays, J.; Sakellariou, G.; Pispas, S.; Hadjichristidis, N., Polymer brushes by living anionic surface initiated polymerization on flat silicon (SiO<sub>2</sub>) and gold surfaces: homopolymers and block copolymers. *Langmuir* **2002**, *18* (22), 8672-8684.
166. Quirk, R. P.; Mathers, R. T.; Cregger, T.; Foster, M. D., Anionic synthesis of block copolymer brushes grafted from a 1, 1-diphenylethylene monolayer. *Macromolecules* **2002**, *35* (27), 9964-9974.
167. Yang, H.; Zhu, H.; Hendrix, M. M. R. M.; Lousberg, N. J.; de With, G.; Esteves, A.; Xin, J. H., Temperature-Triggered Collection and Release of Water from Fogs by a Sponge-Like Cotton Fabric. *Advanced Materials* **2013**, *25* (8), 1150-1154.
168. Ju, H.; McCloskey, B. D.; Sagle, A. C.; Wu, Y.-H.; Kusuma, V. A.; Freeman, B. D., Crosslinked poly (ethylene oxide) fouling resistant coating materials for oil/water separation. *Journal of Membrane Science* **2008**, *307* (2), 260-267.
169. Zhu, X.; Tu, W.; Wee, K.-H.; Bai, R., Effective and low fouling oil/water separation by a novel hollow fiber membrane with both hydrophilic and oleophobic surface properties. *Journal of Membrane Science* **2014**, *466*, 36-44.
170. An, J.; Cui, J. F.; Zhu, Z. Q.; Liang, W. D.; Pei, C. J.; Sun, H. X.; Yang, B. P.; Li, A., Conductive polymer-coated mesh films with tunable surface wettability for separation of oils and organics from water. *Journal of Applied Polymer Science* **2014**, *131* (18).
171. Cao, Y.; Zhang, X.; Tao, L.; Li, K.; Xue, Z.; Feng, L.; Wei, Y., Mussel-inspired chemistry and michael addition reaction for efficient oil/water separation. *ACS applied materials & interfaces* **2013**, *5* (10), 4438-4442.
172. Xu, L.-P.; Wu, X.; Meng, J.; Peng, J.; Wen, Y.; Zhang, X.; Wang, S., Papilla-like magnetic particles with hierarchical structure for oil removal

- from water. *Chemical Communications* **2013**, 49 (78), 8752-8754.
173. Novio, F.; Ruiz-Molina, D., Hydrophobic coordination polymer nanoparticles and application for oil–water separation. *RSC Advances* **2014**, 4 (29), 15293-15296.
174. Zhang, J.; Seeger, S., Polyester materials with superwetting silicone nanofilaments for oil/water separation and selective oil absorption. *Advanced Functional Materials* **2011**, 21 (24), 4699-4704.
175. Zhang, M.; Wang, C.; Wang, S.; Li, J., Fabrication of superhydrophobic cotton textiles for water–oil separation based on drop-coating route. *Carbohydrate polymers* **2013**, 97 (1), 59-64.
176. Zhang, L.; Zhang, Z.; Wang, P., Smart surfaces with switchable superoleophilicity and superoleophobicity in aqueous media: toward controllable oil/water separation. *NPG Asia Materials* **2012**, 4 (2), e8.
177. Kwon, G.; Kota, A.; Li, Y.; Sohani, A.; Mabry, J. M.; Tuteja, A., On-demand separation of oil-water mixtures. *Advanced Materials* **2012**, 24 (27), 3666-3671.
178. Janout, V.; Myers, S. B.; Register, R. A.; Regen, S. L., Self-cleaning resins. *Journal of the American Chemical Society* **2007**, 129 (17), 5756-5759.
179. Zhang, L.; Zhong, Y.; Cha, D.; Wang, P., A self-cleaning underwater superoleophobic mesh for oil-water separation. *Scientific reports* **2013**, 3.
180. Gao, S. J.; Shi, Z.; Zhang, W. B.; Zhang, F.; Jin, J., Photoinduced superwetting single-walled carbon nanotube/TiO<sub>2</sub> ultrathin network films for ultrafast separation of oil-in-water emulsions. *Acs Nano* **2014**, 8 (6), 6344-6352.
181. Krogman, K. C.; Lowery, J. L.; Zacharia, N. S.; Rutledge, G. C.; Hammond, P. T., Spraying asymmetry into functional membranes layer-by-layer. *Nature materials* **2009**, 8 (6), 512-518.
182. Menkhaus, T. J.; Varadaraju, H.; Zhang, L.; Schneiderman, S.; Bjustrom, S.; Liu, L.; Fong, H., Electrospun nanofiber membranes surface functionalized with 3-dimensional nanolayers as an innovative adsorption medium with

- ultra-high capacity and throughput. *Chemical Communications* **2010**, *46* (21), 3720-3722.
183. Subbiah, T.; Bhat, G. S.; Tock, R. W.; Parameswaran, S.; Ramkumar, S. S., Electrospinning of nanofibers. *Journal of Applied Polymer Science* **2005**, *96* (2), 557-569.
184. Gautam, A. K.; Lai, C.; Fong, H.; Menkhaus, T. J., Electrospun polyimide nanofiber membranes for high flux and low fouling microfiltration applications. *Journal of Membrane Science* **2014**, *466*, 142-150.
185. Doshi, J.; Reneker, D. H., Electrospinning process and applications of electrospun fibers. *Journal of electrostatics* **1995**, *35* (2-3), 151-160.
186. Braun, P. V., and Biologically Inspired Nanocomposites. *PM Ajayan, LS Schadler, PV Braun* **2003**, 155.
187. Carlmark, A.; Malmström, E., Atom transfer radical polymerization from cellulose fibers at ambient temperature. *Journal of the American Chemical Society* **2002**, *124* (6), 900-901.
188. Carlmark, A.; Malmström, E. E., ATRP grafting from cellulose fibers to create block-copolymer grafts. *Biomacromolecules* **2003**, *4* (6), 1740-1745.
189. Singh, N.; Chen, Z.; Tomer, N.; Wickramasinghe, S. R.; Soice, N.; Husson, S. M., Modification of regenerated cellulose ultrafiltration membranes by surface-initiated atom transfer radical polymerization. *Journal of Membrane Science* **2008**, *311* (1), 225-234.
190. Ono, Y.; Shikata, T., Hydration and dynamic behavior of poly (N-isopropylacrylamide) s in aqueous solution: A sharp phase transition at the lower critical solution temperature. *Journal of the American Chemical Society* **2006**, *128* (31), 10030-10031.
191. Tai, M. H.; Gao, P.; Tan, B. Y. L.; Sun, D. D.; Leckie, J. O., Highly efficient and flexible electrospun carbon–silica nanofibrous membrane for ultrafast gravity-driven oil–water separation. *ACS applied materials & interfaces* **2014**, *6* (12), 9393-9401.
192. Si, Y.; Fu, Q.; Wang, X.; Zhu, J.; Yu, J.; Sun, G.; Ding, B., Superelastic and

- superhydrophobic nanofiber-assembled cellular aerogels for effective separation of oil/water emulsions. *ACS nano* **2015**, *9* (4), 3791-3799.
193. Obaid, M.; Barakat, N. A. M.; Fadali, O. A.; Motlak, M.; Almajid, A. A.; Khalil, K. A., Effective and reusable oil/water separation membranes based on modified polysulfone electrospun nanofiber mats. *Chemical Engineering Journal* **2015**, *259*, 449-456.
194. Xue, B.; Gao, L.; Hou, Y.; Liu, Z.; Jiang, L., Temperature controlled water/oil wettability of a surface fabricated by a block copolymer: application as a dual water/oil on-off switch. *Advanced Materials* **2013**, *25* (2), 273-277.
195. Xu, L.; Liu, N.; Cao, Y.; Lu, F.; Chen, Y.; Zhang, X.; Feng, L.; Wei, Y., Mercury ion responsive wettability and oil/water separation. *ACS applied materials & interfaces* **2014**, *6* (16), 13324-13329.
196. Zhang, L.; Menkhaus, T. J.; Fong, H., Fabrication and bioseparation studies of adsorptive membranes/felts made from electrospun cellulose acetate nanofibers. *Journal of Membrane Science* **2008**, *319* (1), 176-184.
197. Pan, Y. V.; Wesley, R. A.; Luginbuhl, R.; Denton, D. D.; Ratner, B. D., Plasma polymerized N-isopropylacrylamide: synthesis and characterization of a smart thermally responsive coating. *Biomacromolecules* **2001**, *2* (1), 32-36.
198. Kaholek, M.; Lee, W.-K.; Ahn, S.-J.; Ma, H.; Caster, K. C.; LaMattina, B.; Zauscher, S., Stimulus-responsive poly (N-isopropylacrylamide) brushes and nanopatterns prepared by surface-initiated polymerization. *Chemistry of Materials* **2004**, *16* (19), 3688-3696.
199. Schild, H. G.; Tirrell, D. A., Microcalorimetric detection of lower critical solution temperatures in aqueous polymer solutions. *Journal of Physical Chemistry* **1990**, *94* (10), 4352-4356.
200. Cho, E. C.; Lee, J.; Cho, K., Role of bound water and hydrophobic interaction in phase transition of poly (N-isopropylacrylamide) aqueous solution. *Macromolecules* **2003**, *36* (26), 9929-9934.

201. Jung, Y. C.; Bhushan, B., Wetting behavior of water and oil droplets in three-phase interfaces for hydrophobicity/philicity and oleophobicity/philicity. *Langmuir* **2009**, *25* (24), 14165-14173.
202. Plunkett, K. N.; Zhu, X.; Moore, J. S.; Leckband, D. E., PNIPAM chain collapse depends on the molecular weight and grafting density. *Langmuir* **2006**, *22* (9), 4259-4266.
203. Short, J., Long-term effects of crude oil on developing fish: lessons from the Exxon Valdez oil spill. *Energy Sources* **2003**, *25* (6), 509-517.
204. Dubansky, B.; Whitehead, A.; Miller, J. T.; Rice, C. D.; Galvez, F., Multitissue molecular, genomic, and developmental effects of the Deepwater Horizon oil spill on resident Gulf killifish (*Fundulus grandis*). *Environmental science & technology* **2013**, *47* (10), 5074-5082.
205. Shannon, M. A.; Bohn, P. W.; Elimelech, M.; Georgiadis, J. G.; Marinas, B. J.; Mayes, A. M., Science and technology for water purification in the coming decades. *Nature* **2008**, *452* (7185), 301-310.
206. Xue, Z.; Cao, Y.; Liu, N.; Feng, L.; Jiang, L., Special wettable materials for oil/water separation. *Journal of Materials Chemistry A* **2014**, *2* (8), 2445-2460.
207. Quéré, D., Wetting and roughness. *Annu. Rev. Mater. Res.* **2008**, *38*, 71-99.
208. Bonn, D.; Eggers, J.; Indekeu, J.; Meunier, J.; Rolley, E., Wetting and spreading. *Reviews of modern physics* **2009**, *81* (2), 739.
209. Gao, N.; Yan, Y., Characterisation of surface wettability based on nanoparticles. *Nanoscale* **2012**, *4* (7), 2202-2218.
210. Liang, W.; Guo, Z., Stable superhydrophobic and superoleophilic soft porous materials for oil/water separation. *RSC Advances* **2013**, *3* (37), 16469-16474.
211. Zhou, X.; Zhang, Z.; Xu, X.; Guo, F.; Zhu, X.; Men, X.; Ge, B., Robust and durable superhydrophobic cotton fabrics for oil/water separation. *ACS applied materials & interfaces* **2013**, *5* (15), 7208-7214.
212. Xue, Z.; Wang, S.; Lin, L.; Chen, L.; Liu, M.; Feng, L.; Jiang, L., A novel superhydrophilic and underwater superoleophobic hydrogel-coated mesh for

- oil/water separation. *Advanced Materials* **2011**, *23* (37), 4270-4273.
213. Zhang, F.; Zhang, W. B.; Shi, Z.; Wang, D.; Jin, J.; Jiang, L., Nanowire-Haired Inorganic Membranes with Superhydrophilicity and Underwater Ultralow Adhesive Superoleophobicity for High-Efficiency Oil/Water Separation. *Advanced Materials* **2013**, *25* (30), 4192-4198.
214. Chen, P.-C.; Xu, Z.-K., Mineral-coated polymer membranes with superhydrophilicity and underwater superoleophobicity for effective oil/water separation. *Scientific reports* **2013**, *3*, 2776.
215. Feng, X.; Feng, L.; Jin, M.; Zhai, J.; Jiang, L.; Zhu, D., Reversible super-hydrophobicity to super-hydrophilicity transition of aligned ZnO nanorod films. *Journal of the American Chemical Society* **2004**, *126* (1), 62-63.
216. Daoud, W. A.; Xin, J. H., Nucleation and growth of anatase crystallites on cotton fabrics at low temperatures. *Journal of the American Ceramic Society* **2004**, *87* (5), 953-955.
217. Daoud, W. A.; Leung, S. K.; Tung, W. S.; Xin, J. H.; Cheuk, K.; Qi, K., Self-cleaning keratins. *Chemistry of Materials* **2008**, *20* (4), 1242-1244.
218. Qi, K.; Xin, J. H.; Daoud, W. A.; Mak, C. L., Functionalizing Polyester Fiber with a Self-Cleaning Property Using Anatase TiO<sub>2</sub> and Low-Temperature Plasma Treatment. *International Journal of Applied Ceramic Technology* **2007**, *4* (6), 554-563.
219. Qi, K.; Wang, X.; Xin, J. H., Photocatalytic self-cleaning textiles based on nanocrystalline titanium dioxide. *Textile Research Journal* **2010**, 0040517510383618.
220. Chowdhury, D.; Paul, A.; Chattopadhyay, A., Photocatalytic Polypyrrole–TiO<sub>2</sub>– Nanoparticles Composite Thin Film Generated at the Air– Water Interface. *Langmuir* **2005**, *21* (9), 4123-4128.
221. Tsunoyama, H.; Sakurai, H.; Negishi, Y.; Tsukuda, T., Size-specific catalytic activity of polymer-stabilized gold nanoclusters for aerobic alcohol oxidation in water. *Journal of the American Chemical Society* **2005**, *127* (26),

9374-9375.

222. Horikoshi, S.; Serpone, N.; Hisamatsu, Y.; Hidaka, H., Photocatalyzed degradation of polymers in aqueous semiconductor suspensions. 3. Photooxidation of a solid polymer: TiO<sub>2</sub>-blended poly (vinyl chloride) film. *Environmental science & technology* **1998**, *32* (24), 4010-4016.
223. Liu, F.; Hashim, N. A.; Liu, Y.; Abed, M. R. M.; Li, K., Progress in the production and modification of PVDF membranes. *Journal of membrane science* **2011**, *375* (1), 1-27.
224. Kang, G.-d.; Cao, Y.-m., Application and modification of poly (vinylidene fluoride)(PVDF) membranes—A review. *Journal of Membrane Science* **2014**, *463*, 145-165.
225. Damodar, R. A.; You, S.-J.; Chou, H.-H., Study the self cleaning, antibacterial and photocatalytic properties of TiO<sub>2</sub> entrapped PVDF membranes. *Journal of Hazardous Materials* **2009**, *172* (2), 1321-1328.
226. Rahimpour, A.; Jahanshahi, M.; Rajaeian, B.; Rahimnejad, M., TiO<sub>2</sub> entrapped nano-composite PVDF/SPES membranes: preparation, characterization, antifouling and antibacterial properties. *Desalination* **2011**, *278* (1), 343-353.
227. Moghadam, M. T.; Lesage, G.; Mohammadi, T.; Mericq, J. P.; Mendret, J.; Heran, M.; Faur, C.; Brosillon, S.; Hemmati, M.; Naeimpoor, F., Improved antifouling properties of TiO<sub>2</sub>/PVDF nanocomposite membranes in UV-coupled ultrafiltration. *Journal of Applied Polymer Science* **2015**, *132* (21).
228. Che, H.; Huo, M.; Peng, L.; Fang, T.; Liu, N.; Feng, L.; Wei, Y.; Yuan, J., CO<sub>2</sub>-Responsive Nanofibrous Membranes with Switchable Oil/Water Wettability. *Angewandte Chemie* **2015**, *127* (31), 9062-9066.
229. Borrás, A.; Barranco, A.; González-Elipe, A. R., Reversible superhydrophobic to superhydrophilic conversion of Ag@ TiO<sub>2</sub> composite nanofiber surfaces. *Langmuir* **2008**, *24* (15), 8021-8026.
230. Xu, Q. F.; Liu, Y.; Lin, F.-J.; Mondal, B.; Lyons, A. M., Superhydrophobic

- TiO<sub>2</sub>-polymer nanocomposite surface with UV-induced reversible wettability and self-cleaning properties. *ACS applied materials & interfaces* **2013**, 5 (18), 8915-8924.
231. Cheng, L.-P., Effect of temperature on the formation of microporous PVDF membranes by precipitation from 1-octanol/DMF/PVDF and water/DMF/PVDF systems. *Macromolecules* **1999**, 32 (20), 6668-6674.
232. Yee, W. A.; Kotaki, M.; Liu, Y.; Lu, X., Morphology, polymorphism behavior and molecular orientation of electrospun poly (vinylidene fluoride) fibers. *Polymer* **2007**, 48 (2), 512-521.
233. Wang, X.; Wang, X.; Zhang, L.; An, Q.; Chen, H., Morphology and formation mechanism of poly (vinylidene fluoride) membranes prepared with immerse precipitation: effect of dissolving temperature. *Journal of Macromolecular Science, Part B* **2009**, 48 (4), 696-709.
234. Lee, M. S.; Lee, T. S.; Park, W. H., Highly hydrophobic nanofibrous surfaces generated by poly (vinylidene fluoride). *Fibers and Polymers* **2013**, 14 (8), 1271-1275.
235. Lafuma, A.; Quéré, D., Superhydrophobic states. *Nature materials* **2003**, 2 (7), 457-460.
236. Woodward, I.; Schofield, W. C. E.; Roucoules, V.; Badyal, J. P. S., Super-hydrophobic surfaces produced by plasma fluorination of polybutadiene films. *Langmuir* **2003**, 19 (8), 3432-3438.
237. Xue, Z.; Liu, M.; Jiang, L., Recent developments in polymeric superoleophobic surfaces. *Journal of Polymer Science Part B: Polymer Physics* **2012**, 50 (17), 1209-1224.
238. Boulangé-Petermann, L.; Debaq, C.; Poiret, P.; Cromières, B., Effect of the physical chemistry of polymeric coating surfaces on fouling and cleanability with particular reference to the food industry. *Contact angle, wettability and adhesion. Philadelphia, PA, USA: VPS* **2003**, 501-519.
239. Liu, J.; Wang, L.; Guo, F.; Hou, L.; Chen, Y.; Liu, J.; Wang, N.; Zhao, Y.; Jiang, L., Opposite and complementary: a

- superhydrophobic–superhydrophilic integrated system for high-flux, high-efficiency and continuous oil/water separation. *Journal of Materials Chemistry A* **2016**, *4* (12), 4365-4370.
240. Rana, D.; Matsuura, T., Surface modifications for antifouling membranes. *Chemical reviews* **2010**, *110* (4), 2448-2471.
241. Srijaroonrat, P.; Julien, E.; Aurelle, Y., Unstable secondary oil/water emulsion treatment using ultrafiltration: fouling control by backflushing. *Journal of Membrane Science* **1999**, *159* (1), 11-20.
242. Hilal, N.; Ogunbiyi, O. O.; Miles, N. J.; Nigmatullin, R., Methods employed for control of fouling in MF and UF membranes: a comprehensive review. *Separation Science and Technology* **2005**, *40* (10), 1957-2005.
243. Chen, Y.; Zheng, Y., Bioinspired micro-/nanostructure fibers with a water collecting property. *Nanoscale* **2014**, *6* (14), 7703-7714.
244. Ju, J.; Yao, X.; Yang, S.; Wang, L.; Sun, R.; He, Y.; Jiang, L., Cactus Stem Inspired Cone-Arrayed Surfaces for Efficient Fog Collection. *Advanced Functional Materials* **2014**, *24* (44), 6933-6938.
245. Chen, X.; Liu, Y.; Lu, H.; Yang, H.; Zhou, X.; Xin, J. H., In-situ growth of silica nanoparticles on cellulose and application of hierarchical structure in biomimetic hydrophobicity. *Cellulose* **2010**, *17* (6), 1103-1113.
246. Neuvonen, S.; Suomela, J., The effect of simulated acid rain on pine needle and birch leaf litter decomposition. *Journal of applied ecology* **1990**, 857-872.
247. Franklin, W. E.; Rowland, S. P., Thermogravimetric analysis and pyrolysis kinetics of cotton fabrics finished with THPOH-NH<sub>3</sub>. *Journal of Macromolecular Science—Chemistry* **1983**, *19* (2), 265-282.
248. Price, D.; Horrocks, A. R.; Akalin, M.; Farooq, A. A., Influence of flame retardants on the mechanism of pyrolysis of cotton (cellulose) fabrics in air. *Journal of Analytical and Applied pyrolysis* **1997**, *40*, 511-524.
249. Lu, Y.; Sathasivam, S.; Song, J.; Crick, C. R.; Carmalt, C. J.; Parkin, I. P., Robust self-cleaning surfaces that function when exposed to either air or oil.

- Science* **2015**, *347* (6226), 1132-1135.
250. Yao, L.; He, J., Recent progress in antireflection and self-cleaning technology—From surface engineering to functional surfaces. *Progress in Materials Science* **2014**, *61*, 94-143.
251. Chu, Z.; Feng, Y.; Seeger, S., Oil/water separation with selective superantirewetting/superwetting surface materials. *Angewandte Chemie International Edition* **2015**, *54* (8), 2328-2338.
252. Wang, B.; Liang, W.; Guo, Z.; Liu, W., Biomimetic super-lyophobic and super-lyophilic materials applied for oil/water separation: a new strategy beyond nature. *Chemical Society Reviews* **2015**, *44* (1), 336-361.
253. Du, M.; Zhao, Y.; Tian, Y.; Li, K.; Jiang, L., Electrospun Multiscale Structured Membrane for Efficient Water Collection and Directional Transport. *Small* **2016**, *12* (8), 1000-1005.
254. Liu, X.; Li, Y.; Hu, J.; Jiao, J.; Li, J., Smart moisture management and thermoregulation properties of stimuli-responsive cotton modified with polymer brushes. *RSC advances* **2014**, *4* (109), 63691-63695.
255. Miljkovic, N.; Enright, R.; Nam, Y.; Lopez, K.; Dou, N.; Sack, J.; Wang, E. N., Jumping-droplet-enhanced condensation on scalable superhydrophobic nanostructured surfaces. *Nano letters* **2012**, *13* (1), 179-187.
256. Ma, X.; Cao, M.; Teng, C.; Li, H.; Xiao, J.; Liu, K.; Jiang, L., Bio-inspired humidity responsive switch for directional water droplet delivery. *Journal of Materials Chemistry A* **2015**, *3* (30), 15540-15545.
257. Kamei, J.; Yabu, H., On-Demand Liquid Transportation Using Bioinspired Omniphobic Lubricated Surfaces Based on Self-Organized Honeycomb and Pincushion Films. *Advanced Functional Materials* **2015**, *25* (27), 4195-4201.
258. Liu, Y.; Wang, X.; Fei, B.; Hu, H.; Lai, C.; Xin, J. H., Bioinspired, Stimuli-Responsive, Multifunctional Superhydrophobic Surface with Directional Wetting, Adhesion, and Transport of Water. *Advanced Functional Materials* **2015**, *25* (31), 5047-5056.
259. Kim, P.; Wong, T.-S.; Alvarenga, J.; Kreder, M. J.; Adorno-Martinez, W. E.;

- Aizenberg, J., Liquid-infused nanostructured surfaces with extreme anti-ice and anti-frost performance. *ACS nano* **2012**, *6* (8), 6569-6577.
260. Liu, H.; Zhang, P.; Liu, M.; Wang, S.; Jiang, L., Organogel-based Thin Films for Self-Cleaning on Various Surfaces. *Advanced Materials* **2013**, *25* (32), 4477-4481.
261. Salem, L., Attractive forces between long saturated chains at short distances. *The Journal of Chemical Physics* **1962**, *37* (9), 2100-2113.
262. Greenberg, S. A.; Alfrey, T., Side chain crystallization of n-alkyl polymethacrylates and polyacrylates<sup>1</sup>. *Journal of the American Chemical Society* **1954**, *76* (24), 6280-6285.
263. Jakubowski, W.; Juhari, A.; Best, A.; Koynov, K.; Pakula, T.; Matyjaszewski, K., Comparison of thermomechanical properties of statistical, gradient and block copolymers of isobornyl acrylate and n-butyl acrylate with various acrylate homopolymers. *Polymer* **2008**, *49* (6), 1567-1578.
264. Mazurek, M.; Kinning, D. J.; Kinoshita, T., Novel materials based on silicone-acrylate copolymer networks. *Journal of applied polymer science* **2001**, *80* (2), 159-180.
265. Howland, C. J.; Antkowiak, A.; Castrejón-Pita, J. R.; Howison, S. D.; Oliver, J. M.; Style, R. W.; Castrejón-Pita, A. A., It's Harder to Splash on Soft Solids. *Physical review letters* **2016**, *117* (18), 184502.